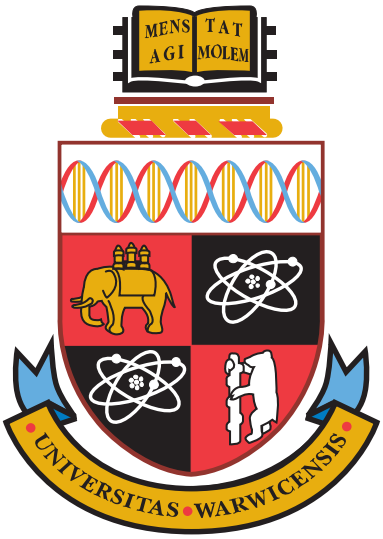

Theory of X-ray Thomson Scattering in Warm Dense Matter

by

Kathrin Wünsch

Thesis

Submitted to the University of Warwick

for the degree of

Doctor of Philosophy

Department of Physics

September 2011

THE UNIVERSITY OF WARWICK

Contents

List of Tables

List of Figures

Acknowledgments

Such a work would not have been possible without the collaboration of many people during the last years. At first, I would like to thank my supervisor, Dr D.O. Gericke, for his guidance and support throughout my PhD. I would also like to acknowledge all my colleagues of the CFSA group for the very good working atmosphere. In particular, I would like to thank Dr J. Vorberger for providing the DFT-MD simulation data presented in this work and his patience with my numberless questions. Furthermore, I would like to mention D.J. Edie and D.A. Chapman for their proof-reading skills in the last minute.

I am very grateful to the experimental groups of Dr G. Gregori from Oxford and Dr S.H. Glenzer from the Lawrence Livermore National Laboratory who gave me the required insight as a theorist into the experimental background. I would also like to acknowledge their kind hospitality during my research visit at Livermore. Furthermore, I would like to thank Dr Z. Donkó from the Hungarian Academy of Sciences in Budapest, for the MD simulation data presented in this work. I also acknowledge the financial support from the Engineering and Physical Science Council.

Moreover, a special thanks for all my friends for their continuous support here in England and back home in Germany. In particular, I wish to thank my boyfriend, Giannis, for his understanding for my work demands and his encouraging help in any kind of programming issues. And last, but not least, I would like to thank my family for their unconditional support, their visits and the numberless phone calls in all these years.

Declarations

I declare that the work presented in this thesis is my own except where stated otherwise, and was carried out at the University of Warwick under the supervision of Dr D.O. Gericke. The work has not been submitted in this or any other academic institution for admission to a higher degree.

Some parts of the work reported in this thesis have been published, as listed below:

- *X-ray Scattering as a probe for warm dense mixtures and high-pressure miscibility*,
  K. Wünsch, J. Vorberger, G. Gregori, and D.O. Gericke,
  EPL **94**, 25001 (2011)
- *Screening of ionic cores in partially ionized plasmas within linear response*,
  D.O. Gericke, J. Vorberger, K. Wünsch, and G. Gregori,
  Phys. Rev. E **81**, 065401(R) (2010)
- *Structural Properties of Warm Dense Matter*,
  D.O. Gericke, K. Wünsch, A. Grinenko and J. Vorberger,
  J. Phys. (Conf. Series) **220**, 012001 (2010)
- *Measurements of Ionic Structure in Shock Compressed Lithium Hydride from Ultrafast X-Ray Thomson Scattering*,
  A.L. Kritcher, P. Neumayer, C.R.D. Brown, P. Davis, T. Döppner, R.W. Falcone, D.O. Gericke, G. Gregori, B. Holst, O.L. Landen, H.J. Lee, E.C. Morse, A. Pelka, R. Redmer, M. Roth, J. Vorberger, K. Wünsch and S.H. Glenzer,
  Phys. Rev. L **103**, 245004 (2009)

- *Measurement of short-range electron correlations in shock-compressed plastic by short-pulse x-ray scattering*,
  B. Barbrel, M. Koenig, A. Benuzzi-Mounaix, E. Brambrink, C.R.D. Brown, D.O. Gericke, B. Nagler, M. Rabec le Gloahec, D. Riley, C. Spindloe, S.M. Vinko, J. Vorberger, J. Wark, K. Wünsch, and G. Gregori,
  Phys. Rev. L **102**, 165004 (2009)
- *Modelling the Scattering of X-Rays in Warm Dense Matter*,
  D.O. Gericke, K. Wünsch, and J. Vorberger,
  Nucl. Instrum. Methods Phys. Res. A **606**, 142 (2009)
- *Ion Structure in Warm Dense Matter: Benchmarking hypernetted-chain equations by first-principle simulations*,
  K. Wünsch, J. Vorberger, and D.O. Gericke,
  Phys. Rev. E **79**, 010201(R) (2009)
- *Ion Structure in Dense Plasmas: MSA versus HNC*,
  K. Wünsch, J. Vorberger, G. Gregori and D.O. Gerickes,
  J. Phys. A: Math. Theor. **42**, 214053 (2009)
- *Probing Warm Dense Lithium by Inelastic X-Ray Scattering*,
  E. Garcia Saiz, G. Gregori, D.O. Gericke, J. Vorberger, B. Barbrel, R.J. Clarke, R.R. Freeman, S.H. Glenzer, F.Y. Khattak, M. Koenig, O.L. Landen, D. Neely, P. Neumayer, M.M. Notley, A. Pelka, D. Price, M. Roth, M. Schollmeier, R.L. Weber, L. van Woerkom, K. Wünsch, and D. Riley,
  Nature Physics **4**, 940 (2008)
- *Structure of Strongly Coupled, Multi-Component Plasmas*,
  K. Wünsch, P. Hilse, M. Schlanges, and D.O. Gericke,
  Phys. Rev. E **77**, 056404 (2008)
- *Ion Structure for X-Ray Thomson Scattering in Dense Fusion Plasmas*,
  K. Wünsch, J. Vorberger, M. Schlanges, and D.O. Gericke,
  J. Phys. (Conf. Series) **112**, 032077 (2008)

Abstract

This thesis presents the theoretical framework required to apply spectrally resolved x-ray Thomson scattering (XRTS) as a diagnostic method for warm dense matter. In particular, the theory is generalised to allow for the description of systems with multiple ion species where all mutual correlations are taken into account within the new approach. Supplemented with the theory presented, XRTS is now a promising diagnostics for high-energy-density matter containing different chemical elements or mixtures of different materials.

The signal measured at XRTS contains the unshifted Rayleigh peak and frequency-shifted features. The first is related to elastic scattering from electrons co-moving with the ions whilst the second occurs due to scattering from free electrons and excitation/ionisation events. The focus of this thesis lies on the elastic scattering feature which requires the ion structure and the electron density around the ion as input for the theoretical modelling. The ion structure is obtained from quantum simulations (DFT-MD) and classical hypernetted-chain (HNC) equations. The analysis of the DTF-MD simulation data reveals that partial ionisation yields strong modifications of the ion-ion interactions. Similar effects are found for the form of the electron screening cloud around an ion.

On the basis of the newly developed theory and structural models, multi-component effects on the XRTS signal are studied. It is shown that the Rayleigh feature is very sensitive to the ratio of the elements in the scattering volume and their mutual correlations. These results indicate that XRTS is well-suited to probe the properties of complex materials and the process of mixing in the WDM regime.

The advanced theories are finally applied to experimental spectra. The procedure allows for both extracting the basic plasma parameters and assessing the quality of the theoretical models applied. Comparisons with several experiments demonstrated that the non-collective regime (large scattering angle) is reasonably well understood whereas the collective regime (small scattering angle/long wavelength limit) still holds challenges. The collective regime is problematic as here strong correlations and screening are highly relevant and, thus, a yet unknown description for fully coupled quantum systems needs to be applied.

Abbreviations

Acronyms

DFT-MD	Density functional molecular dynamics
FEL	Free electron laser
FWHM	Full width at half maximum
HNC	Hypernetted-chain
ICF	Inertial confinement fusion
KK	Klimontovich-Kraeft
MD	Molecular dynamics
MSA	Mean spherical approximation
OCP	One component plasma
RPA	Random phase approximation
SRR	Short range repulsion
WDM	Warm dense matter
XRTS	X-ray Thomson scattering
Y	Yukawa

Indices

'a'	species
'α'	ion species
'i'	initial quantity
's'	scattered quantity

Math symbols

δ	Delta distribution
$[A, B]$	Commutator with $[A, B] = AB - BA$
$\{A, B\}$	Poisson brackets with $\{A, B\} = \sum_i \left(\frac{\partial A}{\partial \mathbf{r}_i} \frac{\partial B}{\partial \mathbf{p}_i} - \frac{\partial A}{\partial \mathbf{p}_i} \frac{\partial B}{\partial \mathbf{r}_i} \right)$
$\underset{N}{\mathrm{Tr}}\,(A)$	Trace of A
$\langle A \rangle$	Ensemble average of A
$\|\psi\rangle$	State vector

Symbols

$B(r)$	Bridge function	
d_a	Mean inter-particle distance	(1.5)
E	Energy	
$\mathbf{E}(\mathbf{r}, t)$	Electromagnetic wave	
$f(k)$	Form factor	(3.36)
$f_a(\mathbf{p})$	Energy distribution function	(1.2)
F	Helmholtz free energy	
$F(\mathbf{k}, t)$	Intermediate scattering function	(2.57)
$\hat{F}_s$	Reduced density operator	(2.17)
$\mathbf{k}$	Wave vector	
$I_\nu(x)$	Fermi integral	(1.11)
$g(\mathbf{r})$	Pair distribution function	(2.40)
$G(\mathbf{r}, t)$	Generalised pair distribution function	(2.54)
$\hat{H}$	Hamiltonian	
m	Mass	
N	Particle number	
n	Density	
$n_B(\omega)$	Bose function	(2.66)
n_i	Total ion density	
$P(\omega)$	Power	
$\mathbf{p}$	Momentum vector	
q	Particle charge	
$q(k)$	Screening function	(3.61)
$\mathbf{r}$	Position vector	
r_s	Brückner parameter	(1.6)
s	Spin	
S	Entropy	(2.9)
$S(\mathbf{k})$	Static structure factor	(2.48)
$S(\mathbf{k}, \omega)$	Dynamic structure factor	(2.60)
t	Time	
T	Temperature	
V	Volume	
$V(\mathbf{r})$	Potential	
$\mathbf{v}$	Velocity vector	
w	Probability	
$\mathbf{x}$	$(\mathbf{r}, \mathbf{p})$	
Z	Ionisation degree	
Z_{can}	Canonic partition function	(2.11)
α	Scattering parameter	(1.9)
$\beta = 1/k_B T$	Inverse temperature	
Γ	Coupling parameter	(1.5)
$\Gamma(\nu)$	Gamma function	

$\epsilon_a(\mathbf{p})$	Energy per particle a	
$\varepsilon(\mathbf{k},\omega)$	Dielectric function	(2.64)
ϵ_F	Fermi energy	(1.3)
Θ	Scattering angle	
Λ	Thermal wavelength	(1.1)
λ	Wavelength	
λ_s	Screening length	(1.10)
λ_D	Debye screening length	(1.12)
λ_{TF}	Thomas-Fermi screening length	(1.13)
κ_s	Inverse screening length	(1.10)
μ	Chemical potential	
ϱ	Phase space probability	
ϱ_s	Reduced phase space probability	(2.31)
$\hat{\varrho}$	Probability density operator	(2.5)
$\hat{\varrho}_s$	Reduced probability density operator	(2.16)
σ	Cross section	
σ_{Th}	Thomson cross section	(3.10)
$\Phi(\mathbf{r})$	Electrostatic potential	
$\chi(\mathbf{k},\omega)$	Susceptibility	(2.62)
ω	Frequency	
ω_{Pl}	Plasma frequency	(1.7)
Ω	Solid angle	

Constants

a_B	Bohr radius
e	Elementary charge
k_B	Boltzmann constant
$h = 2\pi\hbar$	Planck constant
m_e	Electron mass
m_p	Proton mass
r_e	Classical electron radius

Chapter 1

Introduction

Driven by the impressive progress in experimental possibilities and computing power, research related to dense matter with high energy density has significantly changed over the last decade. In particular, the availability of large-scale experimental laser and pulse-power facilities has made it possible to investigate extreme states of matter that naturally only occur in stars or large planets. Recent developments include the completion of the National Ignition Facility (NIF) at the Lawrence Livermore National Laboratory, USA [Moses and Wuest, 2005], the upgrade of the Omega Laser Facilities in Rochester, USA [Soures et al., 1993] as well as the innovative high intensity schemes developed at LULI 2000, France [Koenig et al., 2006] and the Central Laser Facility at the Rutherford Appleton Laboratory (RAL) in the UK [Danson et al., 1998]. The largest facilities, particularly NIF, can compress matter up to a few hundred times solid or fluid density and reach temperatures above ten million degrees needed to initiate thermonuclear fusion. Moreover, it has been demonstrated that much smaller facilities can reach the interesting parameter region of the warm dense matter (WDM) regime, with densities comparable to solids and temperatures of a few electron volts.

These new experimental possibilities also drive improvements in theory and simulations as they provide high-quality data for tests. On the other hand, most experimental investigations also require intensive theoretical support for both the design of the set-up and the interpretation of the data. This fact is particularly true for WDM, which covers states between traditional fields of interest like condensed matter and hot plasmas. Contrary to the parameter regimes of solids and plasmas, WDM has neither a well-defined long-range structure, nor can temperature, correlation and degeneracy effects be neglected [Drake, 2006]. Nevertheless, it retains some properties common to both solids and plasmas. The most similarities can be

found when comparing its properties with those of strongly coupled fluids. Due to this complex nature of WDM, a wide range of interesting physical phenomena arise [Council, 2003; Koenig et al., 2005]. Their investigation needs the combined efforts of experimental, theoretical and simulation approaches.

1.1 Warm dense matter

The investigation of WDM is of significant importance for planetary science and astrophysics as it naturally occurs in the interior of giant gas planets [Guillot, 1999; Militzer et al., 2008; Nettelmann et al., 2008], in white dwarfs [Dufour et al., 2007] or the outer crust of neutron stars [Daligault and Gupta, 2009]. To understand the interior structure of giant gas planets, which might also shed some light on the creation and evolution of planetary systems, material properties like the equation of state of hydrogen [Vorberger et al., 2004; Holst et al., 2008, 2011; Lorenzen et al., 2010], helium [Khairallah and Militzer, 2008; Militzer, 2009], water [French et al., 2009, 2010] and, more realistically, mixtures of many elements and substances needs to be known [Huser et al., 2005]. Moreover, demixing and segregation of heavy elements play an important rule for the energy balance [Guillot, 1999]. In particular, mixing properties of helium and hydrogen under high pressures are of great interest for the modelling of giant gas planets such as Jupiter, Saturn and Uranus [Vorberger et al., 2007; Lorenzen et al., 2009; Wilson and Militzer, 2010].

WDM research is also driven by the grand challenge of achieving energy production by means of inertial confinement fusion (ICF) [Lindl, 1998; Atzeni and Meyer-ter-Vehn, 2004]. Here, WDM occurs in the Hohlraum walls and as a transient state in the fusion pellets during the compression phase [Atzeni and Meyer-ter-Vehn, 2004]. With the commissioning of NIF, a platform to create conditions required to ignite and burn deuterium-tritium mixtures is now available. During the compression, extreme states of matter with up to 1000 times solid density and temperatures in excess of 10 keV are generated [Glenzer et al., 2010]. This type of matter, including all states along the compression path, needs to be understood for successful progression of fusion research [Lindl et al., 2004]. The absorption of driver energy [Grinenko and Gericke, 2009], hydrodynamic instabilities [Regan et al., 2002, 2004; Welser-Sherrill et al., 2007], the equation of state of the fuel materials [Grinenko et al., 2008; Hu et al., 2010], temperature relaxation [Glosli et al., 2008; Daligault and Dimonte, 2009; Vorberger et al., 2010] and α-particle heating [Gauthier et al., 2004; Barriga-Carrasco, 2010; Edie et al.] are only a few examples of physical properties that are of significant interest in connection with the ICF research.

From the theoretical point of view, the description of WDM is challenging as it is characterised by partial ionisation, arbitrary degeneracy and strong ionic correlations [Council, 2003; Koenig et al., 2005]. Each feature alone can be well described by theoretical means. For example, strong coupling can be handled reasonably well by integral equations from classical fluid theory, by Monte Carlo or by molecular dynamics simulations. The only input is the interaction potential which is reasonable well understood in classical systems [Ornstein and Zernike, 1914; Baus and Hansen, 1980; Hansen and McDonald, 1990]. On the other hand, degeneracy can be treated well for weakly coupled systems by incorporating correlations in a perturbative way [Bohm and Pines, 1953; Pines, 1953]. However, the various energy scales, namely, the thermal, the electron Fermi and the correlation energy, are of the same order of magnitude in WDM, yielding a complex, strongly coupled quantum system [Council, 2003]. Accordingly, traditional techniques as used in fluids, solids and hot matter become inapplicable or, at least, have to be re-evaluated in the light of the new requirements.

The definition of WDM above is rather qualitative. Indeed, a commonly excepted definition does not exist. However, one may use dimensionless parameters to quantify the ratios of thermal, Fermi and correlation energies. In WDM, these parameters are typically of the order of unity. The importance of degeneracy effects may be estimated by [Kremp et al., 2005; Kraeft et al., 1986]

$$n_a \Lambda_a^3 = n_a \left(\frac{2\pi\hbar^2}{m_a k_B T} \right)^{\frac{3}{2}} , \tag{1.1}$$

where Λ_a is the thermal wavelength of the particle of species a [1], with the mass, m_a, and the density, n_a. Furthermore, $k_B T$ denotes the temperature scale with the Boltzmann constant k_B. For $n_e \Lambda_e^3 \gtrsim 1$, the probability clouds of the electrons overlap. In this case, the behaviour of the many-particle system is drastically changed from the classical prediction by the fact that the electrons are indistinguishable and obey the spin-statistic theorem [Mahan, 2000]. The main effect of the spin statistics is that fermions obey Pauli's exclusion principle, that is, two identical fermions cannot occupy the same quantum state simultaneously [Pauli, 1925], while bosons are free to occupy the same state, allowing the Bose-Einstein condensation for low temperatures [Anderson et al., 1995; Mahan, 2000]. In WDM, the electrons are typically partially degenerate whilst the ions can be treated classically.

In equilibrium, the different statistics are expressed in the energy distribution

[1] The thermal de Broglie wavelength at mean thermal speed, $v_{th} = \sqrt{k_B T/m}$, is defined as $\lambda_a = \hbar/\sqrt{k_B T m_a} = \Lambda_a/\sqrt{2\pi}$ [de Broglie, 1927].

functions. For fermions (plus sign) [Fermi, 1926; Dirac, 1926] and bosons (minus sign) [Bose, 1924; Einstein, 1924] one has

$$f_a(\mathbf{p}) = \frac{1}{\mathrm{e}^{\beta(\epsilon_a(\mathbf{p})-\mu_a)} \pm 1} \,, \tag{1.2}$$

where the plus sign Here, $\epsilon_a(\mathbf{p})$ is the energy and μ_a the chemical potential of particle of species a. $\beta = 1/(k_B T)$ characterises the inverse temperature scale. For highly degenerate systems, with $n_e \Lambda_e^3 \gg 1$, the thermal energy is very small compared to the Fermi energy

$$\epsilon_F = \frac{\hbar^2}{2m_e} \left(3\pi^2 n_e\right)^{2/3} \,. \tag{1.3}$$

In this case, the Fermi distribution (1.2) is a step function and the electrons can be treated in the $T = 0$ limit. In non-degenerate systems, where $n_e \Lambda_e^3 \ll 1$, both the Fermi and the Bose distributions (1.2) coincide with the non-degenerate Boltzmann distribution function

$$f_a(\mathbf{p}) = \frac{n_a \Lambda_a^3}{2s_a + 1} \, \mathrm{e}^{-\beta \epsilon_a(\mathbf{p})} \,. \tag{1.4}$$

The factor $2s_a + 1$ accounts for the spin statistics. The line $n_e \Lambda_e^3 = 1$ in Fig. 1.1 roughly labels the boundary between systems with degenerate and non-degenerate electrons. A similar line for the ion component is shifted to much higher densities due to their large masses.

The strength of the inter-particle interactions is usually estimated by the coupling parameter, Γ_a, which is given by the ratio of the mean potential energy, $\langle V_a \rangle$, to the mean kinetic energy, $\langle T_a \rangle$ [Kremp et al., 2005]

$$\Gamma_a = \frac{\langle V_a \rangle}{\langle T_a \rangle} \xrightarrow{n_e \Lambda_e^3 \to 0} \frac{Z_a^2 e_a^2}{k_B T d_a} \,. \tag{1.5}$$

In the non-degenerate case, the classical coupling parameter emerges, which is determined by the charge of the species, Ze, the mean particle distance, $d_a = (3/4\pi n_a)^{1/3}$, and the temperature, T. For sufficiently high temperatures and low densities, the particles in the plasma become uncorrelated and, thus, randomly distributed. Here, the coupling parameter is $\Gamma_a \ll 1$ (see Fig. 1.1) and the plasma shows the properties of an ideal gas. In contrast, correlation effects significantly influence the system if the correlation energy exceeds the thermal energy, leading to a non-ideal plasma state. Here, the particles establish a short-range structure well-known from fluid systems.

To determine the coupling strength in degenerate systems, the kinetic energy in the definition of the coupling parameter (1.5) has to be calculated from an ap-

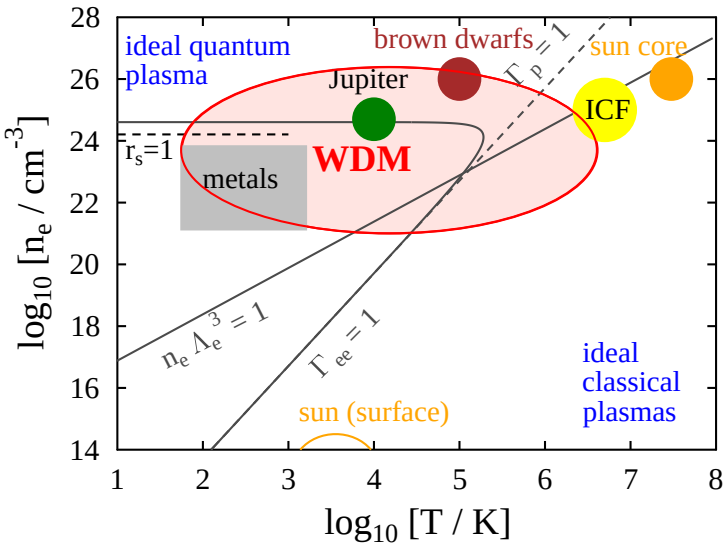

Figure 1.1: Density-temperature phase space for fully ionised hydrogen, highlighting the areas of interest. Indicated are the ideal classical plasma, the ideal quantum plasmas and the WDM region. Furthermore, contours are given where important dimensionless parameters, namely, the coupling, Γ, the degeneracy, $n_e\Lambda_e$, and the Brückner parameter, r_s, are constant. Furthermore, the location of astrophysical objects and technical applications are shown.

propriate expression for quantum systems. In the $T = 0$ limit, this is the Fermi energy (1.3). Another useful parameter to classify the correlation strength in the quantum regime is the Brückner parameter [Kraeft et al., 1986]

$$r_s = \frac{d_a}{a_B} \,. \tag{1.6}$$

This parameter quantifies the ratio of the mean particle distance and the Bohr radius, $a_B = \hbar^2/(e^2 m_e)$ [2]. Both, the coupling parameter (1.5) and the Brückner parameter indicate an ideal quantum plasma for very high densities. Here, the kinetic energy of the electrons, given by the Fermi energy, exceeds the potential energy due to Coulomb interactions.

Fig. 1.1 presents the characteristic parameters discussed above in the density-temperature plane for fully ionised hydrogen. In particular, the region of WDM is highlighted. As shown, WDM includes states with weakly coupled, but partially degenerate electrons as well as classical, but strongly coupled ions. Furthermore,

[2] In this thesis, the Gaussian unit system (cgs) will be used [Jackson, 1999]

the ions of heavier elements are usually only partially ionised due to the moderate temperatures in WDM. The temperature- and density-dependent ionisation degrees add an additional complexity to both the degeneracy and the coupling parameters, which modifies the simple lines in Fig. 1.1. Moreover, strong coupling may play a crucial role in multicomponent systems. Here, one has to consider the different coupling strengths for the pairwise interactions.

1.2 X-ray Thomson scattering as a diagnostic tool in warm dense matter

Any theoretical investigation of WDM properties requires knowledge of the basic system parameters, e.g., electron density, mass density, temperature, and ionisation state, for a comparison with measured data. One of the few experimental tools available to measure these quantities is based on the scattering of light or particles. Light scattering is a widely used diagnostic method in various fields of physics [van de Hulst, 1981; Attwood, 1999; Als-Nielsen and McMorrow, 2001; Santra, 2009] particularly, to determine the structural properties of the material under investigation. A main advantage of this method lies in the fact that it can be performed in a non-perturbative way.

For the application of the scattering process as diagnostics in plasmas, the frequency of the incident radiation has to be higher than the plasma frequency [Ichimaru, 2004a]

$$\omega_{Pl} = \sqrt{\sum_a \frac{4\pi n_a (Z_a e)^2}{m_a}} \,, \tag{1.7}$$

which is dominated by the electron contribution. For lower frequencies, reflection and absorption are the main processes of the light-matter interaction and, thus, any scattered light will be attenuated before it reaches the detector. Consequently, x-rays must be used for the diagnostics of dense plasmas and warm dense matter which are of interest here. Nowadays, intense x-ray pulses can be generated at high-energy laser facilities [Kritcher et al., 2008; García Saiz et al., 2008] and with free electron lasers (FELs) [Höll et al., 2007]. These developments have opened the possibility of probing heated matter at solid density and beyond.

X-ray radiation has further advantages as a diagnostic tool. The probe beam can be focused to a very small spot size for high spatial resolution [Santra, 2009]. X-ray pulses with 10 ps duration from laser-based sources [Barbrel et al., 2009; Kritcher et al., 2008] and 10 fs flashes of x-rays from FELs [Altarelli et al., 2006; Arthur, 2002] allow the study of the dynamic response of the system as well as vari-

ous relaxation processes in dense plasmas. The currently used x-ray sources also fulfil the stringent requirements [Urry et al., 2006] of sufficiently high photon numbers, with energies in the keV range, and an adequate bandwidth to access the motions of the electrons. Successfully applied x-ray sources created by high-power lasers include sources that employ the titanium Ly-α, He-α and K-α line [Glenzer et al., 2003a; Kritcher et al., 2008], the manganese He-α line [Lee et al., 2009] and chlorine Ly-α line [Glenzer et al., 2007; García Saiz et al., 2008].

The dynamics of the ion motion can, however, not be resolved with the bandwidths achieved by current laser-based sources [Gregori and Gericke, 2009] as the ion acoustic modes have frequencies lower than the ion plasma frequency. Thus, such measurements would require a bandwidth which is, at least, a factor $\frac{1}{\sqrt{m_p/m_e}} \sim \frac{1}{43}$ smaller than for a source that can resolve the collective electron dynamics. An alternative is the use of FELs, as their wavelengths, low bandwidth and high brilliance might allow access to the low frequency dynamics dominated by the ion motion in the near future [Gregori and Gericke, 2009]. FELs in the VUV and x-ray range are operational at DESY in Hamburg, Germany [Altarelli et al., 2006] and SLAC at Stanford, USA [Arthur, 2002], respectively.

For the interpretation of measured spectra, an appropriate theory is required. The interaction of electromagnetic radiation with matter containing free electrons can be described qualitatively in the following way: The free particles are accelerated in the field of the incoming electromagnetic wave and self-consistently radiate [Hutchinson, 2005]. Electrons at rest would not change the radiation field since the emitted field is identical to the incident field. A moving electron, however, scatters the radiation due to the Doppler shift. On a macroscopic scale, plasmas are quasi-neutral systems with uniformly distributed particles. As a result, the scattered fields would cancel each other. However, significant density fluctuations arise on a microscopic scale. These fluctuations then lead, finally, to a detectable scattering signal. Although often stated otherwise, this picture makes it clear that the incident radiation field is scattered on density fluctuations rather than on the particles [Sheffield, 1975].

The scattering of light on matter is often classified by the mechanism and depending on whether or not the photon energy is conserved during the scattering process. Rayleigh scattering describes the elastic scattering of electromagnetic radiation on microscopic particles, such as, atoms or electrons [Rayleigh, 1899; Jackson, 1999] if the wavelength of the initial radiation is larger than the particles size. In the case of probed particles with a size comparable or larger than the wavelength of the radiation field, e.g., dust particles or molecules, the process is referred to as

Mie scattering [Mie, 1908]. The atoms and molecules in the matter probed can also be excited by the incident radiation. Then, the scattered photon shows a frequency shift according to the change of energy levels in the atom or the molecule. This inelastic process is called Raman scattering [Raman and Krishnan, 1928]. The inelastic scattering of light on charged particles, that is, the electrons in a plasma, is referred to as Compton scattering [Sheffield, 1975; Santra, 2009]. Here, the photons experience a frequency shift due to the finite energy transfer to the electron (Compton effect) [Compton, 1923; Schwabel, 2002]. The non-relativistic, classical limit of Compton scattering, where the photon energy is much less than the rest energy of the electrons, is called Thomson scattering [Sheffield, 1975]. Here, the energy transfer during the scattering process is negligible and, thus, this contribution is then referred to as elastic Rayleigh scattering.

For the diagnostics of WDM, frequency resolved x-ray scattering is applied in most experiments. This approach is commonly referred to as x-ray Thomson scattering (XRTS) within the scientific community. Due to the use of x-rays, the energy of the initial photon is much larger than the ionisation energy of most bound electrons, that is, $\hbar\omega_i \gg E_I$. In these cases, photo-absorption can be neglected. Of course, this statement is not true for x-rays matching the energies of the K-shell electrons or the energies of the L-shell electrons for heavier elements. Thus, the K-edge and the L-edge in the absorption spectra are carefully avoided in XRTS studies. The momentum transferred to the scattered photon during the scattering process is given by $\hbar\mathbf{k} = \hbar\mathbf{k}_s - \hbar\mathbf{k}_i$ and $\hbar\omega = \hbar\omega_s - \hbar\omega_i$ is the energy change of the photon. Here, ω_i and ω_s denote the frequency and $\mathbf{k}_i$ and $\mathbf{k}_s$ characterise the wave vector of the incident and the scattered wave, respectively. For energy transfers that are small compared to the photon energy and in the non-relativistic limit, the wave vector change, k, is approximated well by

$$k = |\mathbf{k}| = \frac{4\pi}{\lambda_i} \sin(\theta/2) \; . \tag{1.8}$$

Here, θ denotes the scattering angle and λ_i is the wavelength of the incident photon. The scattering geometry of XRTS is shown in Fig. 1.2.

The scattering process can be distinguished with respect to the number of electrons that scatter coherently, that is, between the non-collective and the collective scattering regime. In the first case, the incident photons scatter on independent, uncorrelated electrons whereas the probe beam interacts with an ensemble of correlated electrons in the Debye sphere in the second case. The different scattering

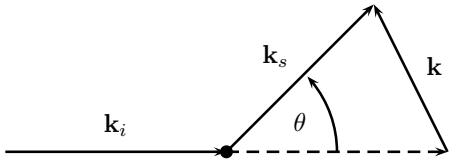

Figure 1.2: Schematics of the scattering geometry where $\mathbf{k}_i$ and $\mathbf{k}_s$ are the incident and the scattered wave vector, respectively. θ is the scattering angle.

regimes can be distinguished via the scattering parameter, α, which is defined as

$$\alpha = \frac{1}{k\lambda_s} \,. \tag{1.9}$$

For $\alpha > 1$, the electrons scatter the light collectively, whereas $\alpha \ll 1$ indicates scattering by single electrons. The scale length of electron correlations in a gas of free electrons is given by the screening length, λ_s. For electrons with arbitrary degeneracy, as in WDM, the latter is given by [Kremp et al., 2005]

$$\lambda_s^{-2} = \kappa_s^2 = 4\pi \sum_a (Z_a e)^2 \frac{2s_a + 1}{\Lambda_a} \frac{\mathrm{d}}{\mathrm{d}\mu_a} I_{1/2}(\beta\mu) \,, \tag{1.10}$$

where κ_s denotes the inverse screening length. Here, $I_{1/2}(x)$ characterises the Fermi integral [Kremp et al., 2005]

$$I_\nu(x) = \frac{1}{\Gamma(\nu+1)} \int_0^\infty \mathrm{d}t \, \frac{t^\nu}{\mathrm{e}^{t-x} + 1} \tag{1.11}$$

with the Gamma function, $\Gamma(\nu)$ [Abramowitz and Stegun, 1965]. In general, the screening length must be calculated numerically. In the classical limit, it coincides with the well-known Debye length [Kremp et al., 2005],

$$\lambda_s \xrightarrow{n_a \Lambda_a^3 \ll 1} \lambda_D = \sqrt{\sum_a \frac{k_B T}{4\pi n_a (Z_a e)^2}} \,, \tag{1.12}$$

whereas the Thomas-Fermi screening length, λ_{TF}, follows in the limit of highly degenerate systems, that is,

$$\lambda_s \xrightarrow{n_a \Lambda_a^3 \gg 1} \lambda_{TF} = \sqrt{\sum_a \frac{\hbar^2}{4 m_a (Z_a e)^2} \left(\frac{\pi}{3 n_a}\right)^{1/3}} \,. \tag{1.13}$$

Thus, it depends on the incident photon energy, the scattering geometry and the

plasma conditions as to whether the collective or the non-collective scattering regime can be accessed in a particular experiment. A scattering process at a large scattering angle yields usually a large k vector and, therefore, a small scattering parameter ($\alpha < 1$). In this backscattering geometry, the frequency spectrum shows the typical characteristics of single-particle behaviour, that is, a Rayleigh peak at the incident frequency caused by the elastic scattering on bound electrons and a frequency down-shifted feature associated with inelastic Compton scattering. In forward geometry at small scattering angles, the scattering parameter is mostly larger than unity and the probe radiation interacts with a cloud of correlated electrons in the Debye sphere. In this case, information on collective properties, such as plasmons, can be obtained from the scattering spectrum. Spectrally resolved scattering experiments showed that the different features in the spectrum can be resolved for both the non-collective and the collective scattering regime. The combination of such geometries then allows for an extraction of basic plasma parameters as well as the microscopic structure from the scattering signal [Glenzer and Redmer, 2009; Froula et al., 2011].

Fünfer *et al.* and Kunze *et al.* first applied spectrally-resolved optical Thomson scattering for inferring the basic plasma parameters from low-density plasmas [Fünfer et al., 1963; Kunze et al., 1964]. Followed by many theoretical and experimental studies (see, e.g., [Evans and Katzenstein, 1969; Salpeter, 1960; Sheffield, 1975]), Thomson scattering in the optical regime has now been developed to be a reliable diagnostic tool for plasmas in the low-density regime.

Riley *et al.* extended the parameter region where light scattering can be used to infer plasma properties into dense plasmas with frequency-integrated x-ray diffraction experiments [Riley et al., 2000]. The extension of spectrally-resolved Thomson scattering to investigate the microscopic structure in dense plasmas by applying highly energetic x-rays was first proposed by Landen *et al.* in 2001 [Landen et al., 2001]. This concept was experimentally demonstrated by the group of Glenzer on isochorically-heated beryllium, first in backscattering geometry in 2003 [Glenzer et al., 2003a] and then also for forward scattering where plasmons could be observed [Glenzer et al., 2007]. After these proof-of-principle experiments, XRTS was applied as diagnostic tool to address a wide range of topics including shock-compressed matter [Ravasio et al., 2007; Lee et al., 2009], the investigation of the ion structure in the long-wavelength limit [García Saiz et al., 2008], the coalescence of shock waves [Kritcher et al., 2008], temperature measurements through the detailed balance [Döppner et al., 2009] and the position of plasmons in strongly coupled, shock-compressed matter [Neumayer et al., 2010]. Recent investigations are focussing on more complex, composite materials which is, of course, related to

the fact that most materials in nature and technical applications consist of multiple chemical elements. For instance, XRTS experiments were performed on plastics [Barbrel et al., 2009; Sawada et al., 2007], plastics with impurities [Gregori et al., 2006] and lithium-hydride [Kritcher et al., 2009].

The plasma parameters are usually extracted from the measured scattering signal by fitting a theoretically generated spectrum. The fit is obtained by varying the plasma parameters, that is, electron density, charge state and temperature. The parameters giving the smallest statistical errors are considered to be the plasma conditions of the material under investigation. So far, the theoretical models are mainly based on the work of Chihara [Chihara, 1987, 2000], which was first used in the context of XRTS by Gregori *et al.* [Gregori et al., 2003]. Here, a decomposition of the total electron densities in partially ionised plasma, that is, the definition of kinetically free and bound electrons, is used to describe the different scattering features. The inelastic scattering feature created by the free electrons is described using quantum statistical perturbation theory (random phase approximation - RPA). A pseudo-potential approach was applied in the first works to calculate the ion structure needed for the determination of the Rayleigh peak that is caused by elastic scattering on bound electrons.

Later, significant improvements were introduced in those descriptions. For the free electrons, the effect of electron-ions collisions was incorporated within the Born-Mermin approach for the dynamic electron response [Redmer et al., 2005; Höll et al., 2007; Fortmann et al., 2009]. Our group contributed to the theoretical description of the elastic Rayleigh peak. To this goal, we investigated the structural properties in strongly coupled multicomponent plasmas on the basis of integral equations [Wünsch et al., 2008a] and benchmarked the results with *ab initio* simulations (DFT-MD) [Wünsch et al., 2009a]. Furthermore, we discussed many-body corrections to the screening cloud [Gericke et al., 2010] in partially ionised plasmas.

For the analysis of the scattering signal from composite materials, Gregori *et al.* extended the Chihara formula based on a model that implied an average charge state of the ions that is only strictly valid in the RPA limit [Gregori et al., 2006]. To overcome these restrictions, we fully generalised the Chihara formula by including all mutual correlations between the different ion species and the electrons [Wünsch et al., 2011]. This approach allows now to described also strongly coupled systems with an arbitrary number of ion species as it occurs in many WDM experiments and natural environments.

1.3 Models for the structure in warm dense matter

X-ray Thomson scattering as a diagnostic tool uses a fitting procedure to match the experimentally measured data and the calculated scattering spectra. As it will be shown later, the theoretical description of XRTS requires knowledge of the structural properties of the matter under investigation. Thus, one needs well-tested theoretical models for the electron and ion structure to extract the plasma conditions correctly. Unfortunately, WDM is a complex and highly non-ideal state and a general theory for WDM is still missing. However, several reduced models were developed to describe the ion structure in dense plasmas. These models can serve as a simple estimate for the structural properties of WDM. Essential comparisons with full scale quantum simulations then allow for deeper understanding of the underlying mechanisms and, thus, provide additional insights.

Widely used are the one-component plasma (OCP) and the Yukawa models for classical particles [Baus and Hansen, 1980]. In both descriptions, only the ion species are considered explicitly. The electrons in the plasma are treated either as a uniform neutralising background (OCP) or as a polarisable fluid (Yukawa). Thus, the ions interact through the Coulomb potential [Kremp et al., 2005]

$$V_{ab}(r) = \frac{Z_a Z_b \, e^2}{r} \tag{1.14}$$

in the OCP model. As the electrons are considered here to not react to the electrostatic field of the ions, they form a structureless background only ensuring charge neutrality in the plasma.

If the polarisation of the electron component is taken into account in linear response, the long-range nature of the Coulomb force leads to screening of the bare forces [Kraeft et al., 1986; Kremp et al., 2005]. As a result, the bare Coulomb interactions must be replaced by a statically screened Coulomb (Debye) potential [Kremp et al., 2005]

$$V_{ab}(r) = \frac{Z_a Z_b \, e^2}{r} \mathrm{e}^{-r\kappa_s} \, . \tag{1.15}$$

Here, κ_s denotes the inverse screening length which can be calculated by Eq. (1.10) to account for partially degenerate electrons in WDM. Using such a statically screened potential to describe the ion properties is usually referred to as the Yukawa model. In this case, the polarisation of the electron background must be also taken into account when calculating the thermodynamics of the total system [Hamaguchi et al., 1997; Vorberger et al., 2011].

Within these models, it is now possible to apply integral equations developed

in fluid theory to describe the strongly coupled ions in WDM. This technique is based on a classical approach and, thus, appropriate only for the ions. Nevertheless, this method provides high numerical efficiency. In contrast, *ab initio* simulations, such as, density functional molecular dynamics (DFT-MD), aim to describe fully interacting quantum systems [Martin, 2004]. This method, first developed in solid state physics for the $T = 0$ limit and later extended to finite temperatures, can describe strongly coupled ions consistent with degenerate electrons. Therefore, it exactly meets the requirements of WDM, but such simulations demand much computing power.

1.4 Outline of the thesis

The objective of this thesis is to develop the theoretical framework for the analysis of experimentally obtained x-ray scattering spectra. In particular, a generalisation of the description for systems with multiple ion species is presented. Thus, the structural properties of strongly coupled multicomponent systems are investigated first. These input quantities are then combined to create artificial scattering spectra which finally allow for comparisons with experiments.

Chapter 2 gives a short introduction to the basics of the statistical description of many-particle systems. First, the general quantum mechanical description is introduced. Then, the main results will also be presented in the classical limit as special attention is given to strongly coupled, but classical ions in WDM.

The theoretical basis to describe light scattering in WDM is presented in chapter 3. Here, the coherent and incoherent scattering regime are characterised and it is shown that the scattering signal is directly proportional to the microscopic electron structure in the plasma. To determine the microscopic structure in partially ionised systems, the description follows the idea of Chihara who decomposed the total electron density into contributions from bound and free electrons. On this basis, a formula for the dynamic electron-electron structure factor will be derived. Finally, the original work considering only one ion component is generalised for systems with an arbitrary number of ion species.

In chapter 4, several methods to determine the static ion structure are introduced and compared to each other in various plasma regimes. In particular, the effect of multiple ion species is discussed and the need of a full multicomponent treatment for strongly coupled systems is shown. The electronic structure in partially, ionised plasmas is studied in chapter 5. In this respect, the dynamic response of kinetically free electrons and the static structure of electrons following the ion motion have to be distinguished. The latter can again be decomposed into bound electrons and free

electrons forming the screening cloud. Theoretical models for all three contributions are presented.

Chapter 6 shows how the electronic and ionic structure can be combined to generate theoretical scattering spectra. On this basis, the sensitivity of the scattering signal to different plasma parameters is studied. Afterwards, the elastic Rayleigh peak is discussed in more detail. Here, the influence on the different theoretical models for the ion structure is highlighted. For mixtures, it is demonstrated that the Rayleigh peak is very sensitive to the ratio of different elements in the probe volume. This fact indicates that XRTS can be used as a diagnostics of warm dense mixtures as well as for pure elements.

The last chapter presents a comparison of the theory developed with a few examples of experimentally obtained data. Based on these examples, the general fitting process to extract the basic plasma parameters is discussed and the challenges which arise are highlighted. It is also shown how additional information, e.g., on plasmons or the inter-particle interactions, can be derived from the scattering spectra.

Chapter 2

The statistical description of plasmas

The equilibrium and non-equilibrium properties of a many-particle system with a large number of degrees of freedom, such as a plasma, must be described by statistical mechanics. This chapter will introduce the main quantities and establishes the theoretical foundation for the following chapters. While the electrons require a fully quantum mechanical description, the ions are sufficiently well characterised by a purely classical treatment in most cases. Following the derivation of the quantum mechanical description, the main results will thus also be presented in the classical limit. In particular, the pair distribution function and the static structure factor will be defined as key quantities to describe the microscopic structure of many-particle systems.

To allow for a description of dynamical systems, the explicit temporal dependence of all quantities will be introduced, and consequently the dynamic structure factor is defined as correlation function of density fluctuations in time and space. This quantity plays a central role for the description of the scattering process of light in matter. At the end of the chapter, the plasma will be considered as an ensemble of freely moving, charged particles subject to several electromagnetic phenomena, like dynamic screening and plasma oscillations. To describe such phenomena, quantities like response functions and the dielectric function will be introduced. Finally, the fluctuation-dissipation theorem yields the link between the microscopic density fluctuations and the dynamic response of the system to an external perturbation.

2.1 Quantum statistics and the classical limit

A plasma is a many-particle system consisting of electrons, ions and neutral particles which mutually interact via electromagnetic forces. To fully describe such a complex system by theoretical methods, the microscopic behaviour of each individual particle in the electromagnetic field of the surrounding medium has to be considered. This task is not only computationally impractical, even in the era of high performance computing, but also in principle impossible as one never has full information of the initial conditions. However, it is unnecessary to have this full information as statistical physics links the microscopic behaviour of the particles to macroscopic properties of the system by applying methods from probability and statistical theories.

The basis for the quantum statistical description is given by the N-particle Hamiltonian of the form [Kremp et al., 2005]

$$\hat{H}_N = \hat{T}_N + \hat{V}_N = \sum_{i=1}^{N} \frac{\mathbf{p}_i^2}{2m} + \sum_{i<j}^{N} V_{ij}(\mathbf{r}_i - \mathbf{r}_j) \; . \tag{2.1}$$

The Hamiltonian is split into the operator of the kinetic energy $\hat{T}_N$ and the operator of the potential energy $\hat{V}_N$ which is characterised by the pairwise inter-particle potential V_{ij}. Here, $\mathbf{r}_i$ and $\mathbf{p}_i$ denote the position and the momentum operators of the particle i. The sum runs over all particles in the system. In the case of a plasma, the interaction between the particles is given by the Coulomb potential

$$V_{ij}(\mathbf{r}_i - \mathbf{r}_j) = \frac{Z_i Z_j e^2}{|\mathbf{r}_i - \mathbf{r}_j|} \; . \tag{2.2}$$

The microscopic state of the N-particle system is fully specified if a complete set of one-particle observables can be determined. A one-particle observable b_i is a set of simultaneously measurable physical quantities [Kraeft et al., 1986], as for example, the position vector with the spin component, $b_i = (\mathbf{r}_i, s_i^z)$, or the momentum plus spin, $b_i = (\mathbf{p}_i, s_i^z)$. In this case, the complete description of the system is represented by the state vector $|\psi_N\rangle = |b_1\, b_2\, \ldots\, b_N\rangle$ in the N-particle Hilbert space $\mathcal{H}_N$. The N-particle Schrödinger equation determining this state vector,

$$i\hbar \frac{\partial}{\partial t} |\psi_N(t)\rangle = \hat{H}_N |\psi_N(t)\rangle \; , \tag{2.3}$$

describes the microscopic dynamics of the system. Please note that the state vector $|\psi_N\rangle$ has to be symmetrised or anti-symmetrised depending if bose or fermi-particles are considered as a result of the spin-statistic postulate [Kremp et al., 2005].

The knowledge of the state vector also allows for the determination of the expectation value of any observable. If the latter is described by the operator $\hat{A}$, one has

$$\langle \hat{A} \rangle = \langle \psi_N | \hat{A} \, | \psi_N \rangle \ . \tag{2.4}$$

In the case that the quantum system can be described by a single state vector $|\psi(t)\rangle$, this state is called a "pure state". Otherwise, the system is in a "mixed" state, described by the superposition of pure states having well-defined properties.

2.1.1 Probability density operator

Due to the large number of particles, it is impossible to determine a pure microscopic quantum state for macroscopic systems such as fluids, gases or plasmas, or even its initial conditions. Furthermore, the interaction and the coupling with the surrounding medium causes a permanent variation of the microscopic state. Hence, the system must be described as a "mixed state", that is, a statistical ensemble of pure states $|\psi_N^l(t)\rangle$, where each state occurs with a certain possibility w_l. A quantity that combines the information of a mixed quantum state in a macroscopic system is the probability density operator [Kremp et al., 2005]

$$\hat{\varrho}_N = \sum_l w_l |\psi_N^l\rangle\langle\psi_N^l| \ , \tag{2.5}$$

where the sum runs over all possible states l. It is a positive defined Hermitian operator, $\hat{\varrho}^+ = \hat{\varrho}$, which simplifies for a pure quantum state to $\hat{\varrho} = |\psi_N\rangle\langle\psi_N|$. Due to the fact that the sum of all the weights must be unity, i.e. $\sum_l w_l = 1$, the probability density operator is normalised by taking the trace $\mathrm{Tr}\,\hat{\varrho} = 1$.

To obtain the time evolution of the density operator, it is of advantage to use the Schrödinger picture where the state ψ_N is the time-dependent quantity. Applying the Schrödinger equation (2.3), the density operator can be found to obey

$$i\hbar \frac{\partial}{\partial t} \hat{\varrho}_N = \left[\hat{H}_N, \hat{\varrho}_N \right] \ . \tag{2.6}$$

This equation is known as the von-Neumann equation [Kraeft et al., 1986]. The bracket denotes the commutator defined as

$$\left[\hat{H}_N, \hat{\varrho}_N \right] = \hat{H}_N \hat{\varrho}_N - \hat{\varrho}_N \hat{H}_N \ . \tag{2.7}$$

The average value of any observable in a mixed state is given by means of the density

operator as

$$\langle \hat{A}_N \rangle = \sum_l w_l \langle \psi_N^l | \hat{A}_N | \psi_N^l \rangle = \operatorname*{Tr}_N \left(\hat{A}_N \hat{\varrho}_N \right) . \tag{2.8}$$

The density operator is thus essential in connecting microstates of the system to the observable macrostates. The entropy S, which plays a central role in the thermodynamic description, is connected to the probability density operator via [Reichl, 2004]

$$S = -k_B \operatorname*{Tr}_N \left(\hat{\varrho}_N \ln \hat{\varrho}_N \right) . \tag{2.9}$$

For systems in thermodynamic equilibrium, the entropy is maximal ($S = S_{\max}$) and the von-Neumann equation simplifies to $[\hat{H}_N, \hat{\varrho}_N] = 0$.

Considering a canonical ensemble, that is, a closed system that exchanges energy with the surrounding medium but has a fixed particle number, the density operator is given as [Reichl, 2004]

$$\hat{\varrho}_N = \frac{1}{Z_{\text{can}}} \, \mathrm{e}^{-\beta \hat{H}_N} \tag{2.10}$$

with the partition function

$$Z_{\text{can}} = \operatorname*{Tr}_N \left(\mathrm{e}^{-\beta \hat{H}_N} \right) . \tag{2.11}$$

In the canonical ensemble, the Helmholtz free energy F is the thermodynamic potential and fully defines its thermodynamics. Using Eq. (2.9) one finds that it is connected to the statistical description via the relation

$$F(T, N, V) = -k_B T \ln Z_{\text{can}}(T, N, V) . \tag{2.12}$$

Further thermodynamic quantities can then be calculated by partial derivatives. For instance, the pressure and the chemical potential are given by

$$p(T, N, V) = -\left(\frac{\partial F}{\partial V} \right)_{T,N} \quad \text{and} \quad \mu(T, N, V) = \left(\frac{\partial F}{\partial N} \right)_{V,T} . \tag{2.13}$$

Thus, the many-particle system can be fully described by the probability density operator, which contains all the statistical and dynamical information.

2.1.2 Reduced probability density operator

The full information in the density operator is in most cases not required as many physical observables are represented by one-, two-particle or s-particle functions

[Kraeft et al., 1986]. A N-particle function is thus for instance given by

$$\hat{A}_N = \sum_{\{s\}} \hat{A}_{\{s\}} \; . \tag{2.14}$$

Important examples are the kinetic energy which is given by a sum over 1-particle operators $\hat{T}_N = \sum_i \hat{T}_i$ or the potential energy which is expressed as a sum over binary operators $\hat{V}_N = \sum_{i<j} \hat{V}_{ij}$. To calculate the mean value of such additive or binary quantities only the reduced 1-particle or 2-particle density operator is required [Reichl, 2004]

$$\hat{\varrho}_1(b_1) = \int \mathrm{d}b_2 \ldots \mathrm{d}b_N \, \hat{\varrho}_N(b_2, \ldots, b_N) \; , \tag{2.15a}$$

$$\hat{\varrho}_{12}(b_1, b_2) = \int \mathrm{d}b_3 \ldots \mathrm{d}b_N \, \hat{\varrho}_N(b_3, \ldots, b_N) \; . \tag{2.15b}$$

More generally, the reduced s-particle density operator is given as

$$\hat{\varrho}_s(b_1, \ldots, b_s) = \int \mathrm{d}b_{s+1} \ldots \mathrm{d}b_N \, \hat{\varrho}_N(b_{s+1}, \ldots, b_N) = \operatorname*{Tr}_{s+1 \ldots N} \hat{\varrho}_N \; . \tag{2.16}$$

with a complete set of observables b_i. Thus, a reduction of information is achieved by taking the trace over observables of the particles which are not considered.

For many approaches, it is more convenient to introduce the reduced density operator $\hat{F}_s$ defined by Bogolyubov [Kraeft et al., 1986]

$$\hat{F}_s = V^s \hat{\varrho}_s \quad \text{with} \quad \operatorname*{Tr}_{1 \ldots s} \hat{F}_s = V^s \; . \tag{2.17}$$

Here, V denotes the volume of the system. With the reduced density operator, the mean values of the s-particle observables are then obtained via

$$\langle A_N \rangle = \binom{N}{s} \frac{1}{V^s} \operatorname*{Tr}_{1 \ldots s} \left(\hat{F}_s \hat{A}_s \right) = \frac{n^s}{s!} \operatorname*{Tr}_{1 \ldots s} \left(\hat{F}_s \hat{A}_s \right) \; , \tag{2.18}$$

where the well-justified relation $s \ll N$ is used for the second step. In the case of the 1- or 2-particle observable, the expectation values simplify

$$\langle \hat{A}_1 \rangle = n \operatorname*{Tr}_1 \left(\hat{F}_1 \hat{A}_1 \right) \; , \tag{2.19a}$$

$$\langle \hat{A}_{12} \rangle = \frac{n^2}{2} \operatorname*{Tr}_{12} \left(\hat{F}_{12} \hat{A}_{12} \right) \; , \tag{2.19b}$$

with the reduced 1- and 2-particle density operator, $\hat{F}_1$ and $\hat{F}_{12}$, respectively.

2.1.3 Equation of motion for the reduced density operator

The equation of motion for the reduced density operator $\hat{F}_s$ can be obtained from the von-Neumann equation (2.6) for the probability density operator. Here, the trace over the $(N-s)$ particle states has to be evaluated

$$\underset{s+1\ldots N}{\mathrm{Tr}} \left\{ i\hbar \frac{\partial}{\partial t} \hat{\varrho}_N \right\} = \underset{s+1\ldots N}{\mathrm{Tr}} \left\{ \left[\hat{H}_N, \hat{\varrho}_N \right] \right\} . \tag{2.20}$$

On the left hand side, the derivative and the trace can be exchanged as both are linear operators and thus the reduced density operator occurs directly. To evaluate the right hand side, it is convenient to split the Hamiltonian into three terms [Kraeft et al., 1986]

$$\hat{H}_N = \hat{H}_s + \hat{H}_{N-s} + \hat{V}_{s,N-s} . \tag{2.21}$$

The first two terms express the Hamiltonian of the isolated s- and $(N-s)$-particle subsystems, respectively. The last term characterises the interaction between the two subsystems. Thus, the three contributions are given as

$$\hat{H}_s = \sum_{i=1}^{s} \frac{\hat{p}_i^2}{2m} + \sum_{i<j}^{s} \hat{V}_{ij} , \tag{2.22a}$$

$$\hat{H}_{N-s} = \sum_{i=s+1}^{N} \frac{\hat{p}_i^2}{2m} + \sum_{i<j=s+1}^{N} \hat{V}_{ij} , \tag{2.22b}$$

$$\hat{V}_{s,N-s} = \sum_{i=1}^{s} \sum_{j=s+1}^{N} \hat{V}_{ij} . \tag{2.22c}$$

With these definitions, equation (2.20) leads to

$$i\hbar \frac{1}{V^s} \frac{\partial}{\partial t} \hat{F}_s = \underset{s+1\ldots N}{\mathrm{Tr}} \left[\hat{H}_s, \hat{\varrho}_N \right] + \underset{s+1\ldots N}{\mathrm{Tr}} \left[\hat{H}_{N-s}, \hat{\varrho}_N \right] + \underset{s+1\ldots N}{\mathrm{Tr}} \left[\hat{V}_{s,N-s}, \hat{\varrho}_N \right] . \tag{2.23}$$

The first term on the right hand side directly yields $[\hat{H}_s, \hat{F}_s]/V^s$ as the trace only affects the density operator. The second term vanishes as the trace is invariant under cyclic permutations. The last term needs to be rearranged. One obtains

$$\underset{s+1\ldots N}{\mathrm{Tr}} \sum_{i=1}^{s} \sum_{j=s+1}^{N} \left[\hat{V}_{ij}, \hat{\varrho}_N \right] = \frac{N-s}{V^{s+1}} \underset{s+1}{\mathrm{Tr}} \left[\sum_{i=1}^{s} \hat{V}_{i,s+1}, \hat{F}_{s+1} \right] \tag{2.24}$$

as the interaction is equal between the two subsystems. Under the condition $s \ll N$, the equation of motion for the density operators follows to be

$$i\hbar\frac{\partial}{\partial t}\hat{F}_s - \left[\hat{H}_s, \hat{F}_s\right] = n \operatorname*{Tr}_{s+1} \left[\sum_{i=1}^{N} \hat{V}_{i,s+1}, \hat{F}_{s+1}\right] . \tag{2.25}$$

This is the quantum version of the BBGKY hierarchy named after the authors which first derived the hierarchy, namely, Bogolyubov, Born, Green, Kirkwood and Yvon [Kraeft et al., 1986]. It represents the kinetic equation of the reduced density operator. The first equations for the reduced 1- and 2-particle density operator are

$$i\hbar\frac{\partial}{\partial t}\hat{F}_1 - \left[\hat{H}_1, \hat{F}_1\right] = n \operatorname*{Tr}_{2} \left[\hat{V}_{12}, \hat{F}_{12}\right] , \tag{2.26a}$$

$$i\hbar\frac{\partial}{\partial t}\hat{F}_{12} - \left[\hat{H}_{12}, \hat{F}_{12}\right] = n \operatorname*{Tr}_{3} \left[\hat{V}_{12} + \hat{V}_{23}, \hat{F}_{123}\right] . \tag{2.26b}$$

A specific characteristics of the above set of integro-differential equations is the coupling between successive equations of motion, that means, the equation for $\hat{F}_s$ is expressed in terms of $\hat{F}_{s+1}$. This coupling makes it impossible to solve this set of equations unless a relation between the functions $\hat{F}_{s+1}$ and $\hat{F}_s$ can be introduced and the hierarchy of equations is closed.

The most simple closure relation for the hierarchy (2.25) assumes independent particles. In this case, the reduced 2-particle density operator is given as

$$\hat{F}_{12} \simeq \hat{F}_1 \cdot \hat{F}_2 . \tag{2.27}$$

This approximation yields the Vlasov equation which can be used to describe collisionless systems [Kremp et al., 2005].

2.1.4 The classical limit for the reduced density operator

While the electrons in dense plasmas require a fully quantum statistical description, the ions are sufficiently well characterised within classical statistics due to their large masses. It is only for systems with extremely high densities that quantum effects must also be considered for the ions. Furthermore, there are several methods available which include quantum effects approximately into classical calculations. Although these approximations are mostly limited to weakly degenerate systems, comparisons with full quantum mechanical methods show that the results are often sufficient to characterise the main feature within the warm dense matter regime. This fact will be verified in more detail later in the thesis.

For these reasons, the statistical description will also be presented here in the classical limit. The main difference to quantum statistics follows from the fact that the phase space variables $\mathbf{r}$ and $\mathbf{p}$ commute within the classical treatment. Therefore, the N-particle system is described in the $6N$-dimensional phase phase $\mathbf{x}^N = (\mathbf{r}^N, \mathbf{p}^N)$ which is spanned by $3N$ position variables $\mathbf{r}^N = (\mathbf{r}_1, \mathbf{r}_2, \dots \mathbf{r}_N)$ and $3N$ momentum variables $\mathbf{p}^N = (\mathbf{p}_1, \mathbf{p}_2, \dots \mathbf{p}_N)$. The quantity which contains the statistical information is the phase space probability density $\varrho_N(\mathbf{x}_1, \mathbf{x}_2, \dots \mathbf{x}_N, t)$, where $\varrho_N \, \mathrm{d}\mathbf{r}^N \mathrm{d}\mathbf{p}^N$ defines the probability that the system is in the microscopic state characterised by $\mathbf{r}^N$ and $\mathbf{p}^N$ at the time t [Hansen and McDonald, 1990]. With this central quantity, the ensemble average of a macroscopic property $A(t)$ is given by

$$\langle A(t) \rangle = \int \mathrm{d}\mathbf{x}_1 \dots \mathrm{d}\mathbf{x}_N \; A(\mathbf{x}_1, \dots, \mathbf{x}_N, t) \; \varrho_N(\mathbf{x}_1, \dots, \mathbf{x}_N, t) \; . \tag{2.28}$$

The equation of motion of the phase space probablility density is described by the Liouville equation [Hansen and McDonald, 1990]

$$\frac{\partial \varrho_N}{\partial t} = \{ H_N, \varrho_N \} \; , \tag{2.29}$$

which is the classical version of the von-Neumann equation (2.6). Here, the brackets are the Poisson brackets defined by

$$\{ H_N, \varrho_N \} = \sum_{i=1}^{N} \left(\frac{\partial H_N}{\partial \mathbf{r}_i} \frac{\partial \varrho_N}{\partial \mathbf{p}_i} - \frac{\partial H_N}{\partial \mathbf{p}_i} \frac{\partial \varrho_N}{\partial \mathbf{r}_i} \right) \; , \tag{2.30}$$

with H_N being the Hamiltonian for the classical N-particle system.

The introduction of reduced phase space probability densities are convenient for classical systems as well. One defines the reduced s-particle probability density within the classical limit via

$$\varrho_s(\mathbf{x}_1, \dots, \mathbf{x}_s, t) = \frac{N!}{(N-s)!} \int \mathrm{d}\mathbf{x}_{s+1} \dots \mathrm{d}\mathbf{x}_N \; \varrho_N(\mathbf{x}_1, \dots, \mathbf{x}_N, t) \; . \tag{2.31}$$

Analogous to quantum statistics (see Eq. (2.25)), the equation of motion for the reduced probability density can be derived by decomposing the Hamiltonian in terms describing the s-particle and the remaining $(N-s)$-particle subsystem and the additional potential term to account for the interaction between the two subsystems. The result is given by the classical BBGKY-Hierarchy [Kraeft et al., 1986]

$$\frac{\partial}{\partial t} \varrho_s = \{ H_s, \varrho_s \} + (N-s) \sum_{1 \leq i \leq s} \int \mathrm{d}\mathbf{x}_{s+1} \; \{ V_{i,s+1}, \varrho_{s+1} \} \; . \tag{2.32}$$

Again, it can be seen that the equation of motion couples the reduced s-particle function ϱ_s with the reduced $(s+1)$-particle probability density ϱ_{s+1} .

In equilibrium, the probability density function can be factorised into terms containing position and momentum vectors, respectively. It is often useful to integrate over the momentum variables. The remaining particle density is then a function of the position coordinates only [1]

$$\tilde{\varrho}(\mathbf{r}) = \int \mathrm{d}\mathbf{p}\, \varrho(\mathbf{r}, \mathbf{p}) \; . \tag{2.33}$$

The particle density provides the complete information on the microscopic structure in the many-particle system.

To connect the microscopic probability density with macroscopic properties, the canonical ensemble will be considered again. In thermodynamic equilibrium, the canonical partition function is given by [Hansen and McDonald, 1990]

$$Z_{\mathrm{can}} = \frac{1}{h^{3N} N!} \int \mathrm{d}\mathbf{r}^N \mathrm{d}\mathbf{p}^N \mathrm{e}^{-\beta H_N} \; . \tag{2.34}$$

The inclusion of the coefficient $1/h^{3N}N!$, with Planck's constant h, ensures the correct treatment of possible positions in phase space (uncertainty relation) and indistinguishable particles. In this way, it is the classical limit of the quantum mechanical expression (2.11).

As already pointed out, the kinetic and the potential part of the Hamiltonian can be separated in the classical limit which makes it possible to perform the integration over the momenta. Thus, the canonical partition function can be expressed as

$$Z_{\mathrm{can}} = \frac{\Lambda^{-3N}}{N!} \int \mathrm{d}\mathbf{r}_1 \ldots \mathrm{d}\mathbf{r}_N \; \exp\left[-\beta V_N(\mathbf{r}_1, \ldots, \mathbf{r}_N)\right] \; . \tag{2.35}$$

The reduced s-particle density is then given by the partition function via

$$\varrho_s(\mathbf{r}^s) = \frac{N!}{(N-s)!} \frac{1}{Z_{\mathrm{can}}} \int \mathrm{d}\mathbf{r}^{(N-s)} \exp\left[-\beta V_N(\mathbf{r}^N)\right] \; . \tag{2.36}$$

Another useful quantity in the description of the microscopic structure is the s-particle distribution function, which is defined as [Hansen and McDonald, 1990]

$$F_s(\mathbf{r}_s) = \frac{\varrho_s(\mathbf{r}_1, \ldots, \mathbf{r}_s)}{\prod_{i=1}^{s} \varrho_1(\mathbf{r}_i)} = \frac{\varrho_s(\mathbf{r}_1, \ldots, \mathbf{r}_s)}{n^s} \; . \tag{2.37}$$

[1] For simplification in the notation, the symbol $\tilde{\varrho}(\mathbf{r})$ will be renamed to $\varrho(\mathbf{r})$.

The reduced 1-particle density is normalised in a way that it yields the density in homogeneous systems, that is, $\varrho_1(\mathbf{r}) = N/V = n$ holds in this case.

2.2 Radial distribution function and structure factor

The pair distribution function plays a central role for the description of the structural properties in a plasma. This quantity is defined by (see. Eq. (2.36))

$$g(\mathbf{r}, \mathbf{r}') = \frac{\varrho_2(\mathbf{r}, \mathbf{r}')}{n^2} \ . \tag{2.38}$$

For an isotropic, homogeneous system, the inter-particle potential depends only on the separation $r = |\mathbf{r} - \mathbf{r}'|$ and the system is thus fully determined by the radial distribution function $g(r)$.

In the classical limit, the particles in the system are considered as point particles and their local phase density is given by delta functions in position space, i.e., $\varrho = \sum_i \delta(\mathbf{r} - \mathbf{r}_i)$. This description was introduced by Klimontovich [Kremp et al., 2005] and thus this form is often referred to as the Klimontovich densities. To account for the statistical ensemble, the reduced 1-particle density is given by the average particle density

$$\varrho_1(\mathbf{r}) = \left\langle \sum_{i=1}^{N} \delta(\mathbf{r} - \mathbf{r}_i) \right\rangle \ . \tag{2.39}$$

Here, the brackets $\langle \dots \rangle$ denote the ensemble average with respect to the canonical partition function of the system.

The connection to the 2-particle density matrix is obtained by considering the statistical average of the product of two local particle densities within the canonical description [Hansen and McDonald, 1990]

$$\begin{aligned}
\left\langle \sum_{ij} \delta(\mathbf{r} - \mathbf{r}_i)\delta(\mathbf{r}' - \mathbf{r}_j) \right\rangle &= \frac{1}{Z_{\text{can}}} \sum_{ij} \int \mathrm{d}\mathbf{r}_N \ \delta(\mathbf{r} - \mathbf{r}_i)\delta(\mathbf{r}' - \mathbf{r}_j) \exp\left[-\beta V_N(\mathbf{r}_N)\right] \\
&= \frac{N(N-1)}{Z_{\text{can}}} \int \mathrm{d}\mathbf{r}_N \ \delta(\mathbf{r} - \mathbf{r}_1)\delta(\mathbf{r}' - \mathbf{r}_2) \exp\left[-\beta V_N(\mathbf{r}_N)\right] \\
&= \frac{N(N-1)}{Z_{\text{can}}} \int \mathrm{d}\mathbf{r}_3 \dots \mathrm{d}\mathbf{r}_N \ \exp\left[-\beta V_N(\mathbf{r}, \mathbf{r}', \mathbf{r}_3, \dots, \mathbf{r}_N)\right] \\
&= \varrho_2(\mathbf{r}, \mathbf{r}') \ .
\end{aligned}$$

In the last step, the definition (2.36) was used. This result allows for the connection

of the pair distribution function with the Klimontovich densities

$$g(\mathbf{r},\mathbf{r}') = \frac{1}{n^2}\left\langle \sum_{\substack{i,j=1\\ i\neq j}}^{N} \delta(\mathbf{r}-\mathbf{r}_i)\;\delta(\mathbf{r}'-\mathbf{r}_j)\right\rangle \;. \tag{2.40}$$

This pair distribution function characterises the microscopic structure in many-particle systems like gases, fluids or plasmas. Often the radial distribution function is sufficient. It depends only of the separation $r = |\mathbf{r}-\mathbf{r}'|$ and the term $4\pi r^2\, n\, g(r)\,\mathrm{d}r$ gives the average number of particles in the spherical shell of width $\mathrm{d}r$ at the distance r from a central particle.

As the effects of multiple species in the systems will be studied extensively in this thesis, the partial pair distributions between the various species a and b are required which are defined by [Hansen and McDonald, 1990; Wünsch et al., 2008a]

$$g_{ab}(\mathbf{r},\mathbf{r}') = \frac{\varrho_N^{(ab)}(\mathbf{r},\mathbf{r}')}{n_a n_b} = \frac{1}{n_a n_b}\left\langle \sum_{\substack{i=1\\ i\neq j\,\forall\, a=b}}^{N_a}\sum_{j=1}^{N_b} \delta(\mathbf{r}-\mathbf{r}_i)\delta(\mathbf{r}'-\mathbf{r}_j)\right\rangle \;. \tag{2.41}$$

Here, n_a and N_a characterise the densities and particle numbers associated with the particles of species a, respectively.

The pair distribution function also links the microscopic structure to macroscopic and thermodynamic quantities. For example, the internal energy of a classical system is given by [Reichl, 2004]

$$\langle E_{pot}\rangle = \frac{1}{2}\frac{N^2}{V}\int_0^\infty \mathrm{d}r\; 4\pi r^2\, V(r)\, g(r)\;, \tag{2.42}$$

and the pressure can be obtained via

$$\frac{p}{k_B T} = \frac{N}{V} - \frac{2\pi n^2}{3k_B T}\int_0^\infty \mathrm{d}r\; r^3\;\frac{\partial V(r)}{\partial r} g(r)\;. \tag{2.43}$$

For direct comparisons with experimental results, the static structure factor $S(k)$ is a very useful quantity as it is directly related to the intensity of light or particles scattered by the system. $S(k)$ is defined as the ensemble average of two local particle densities in k-space [Hansen and McDonald, 1990]

$$S(k) = \frac{1}{N}\left\langle \varrho(\mathbf{k})\varrho^*(\mathbf{k})\right\rangle \;, \tag{2.44}$$

where the densities in the Fourier space are given by

$$\varrho(\mathbf{k}) = \int\limits_V \mathrm{d}\mathbf{r}\, \varrho(\mathbf{r}) \mathrm{e}^{-i\mathbf{r}\cdot\mathbf{k}} = \sum_{i=1}^{N} \mathrm{e}^{-i\mathbf{k}\cdot\mathbf{r}_i} \ . \tag{2.45}$$

The structure factor can also be expressed via the Fourier transformation of the pair distribution function [Reichl, 2004]

$$\begin{aligned} S(k) &= \frac{1}{N} \left\langle \sum_i \sum_j \mathrm{e}^{-i\mathbf{k}\cdot\mathbf{r}_i}\, \mathrm{e}^{i\mathbf{k}\cdot\mathbf{r}_j} \right\rangle \\ &= \frac{1}{N} \sum_{i=j} \left\langle \mathrm{e}^{-i\mathbf{k}(\mathbf{r}_i - \mathbf{r}_i)} \right\rangle + \frac{1}{N} \sum_{i\neq j} \left\langle \mathrm{e}^{-i\mathbf{k}(\mathbf{r}_i - \mathbf{r}_j)} \right\rangle \\ &= 1 + \frac{1}{N} \left\langle \sum_{i\neq j} \int \mathrm{d}\mathbf{r}\, \mathrm{d}\mathbf{r}' \mathrm{e}^{-i\mathbf{k}(\mathbf{r}-\mathbf{r}')} \delta(\mathbf{r} - \mathbf{r}_i) \delta(\mathbf{r}' - \mathbf{r}_j) \right\rangle \\ &= 1 + \frac{1}{N} \int \mathrm{d}\mathbf{r}\, \mathrm{d}\mathbf{r}' \mathrm{e}^{-i\mathbf{k}(\mathbf{r}-\mathbf{r}')} \varrho_2(\mathbf{r}, \mathbf{r}') \\ &= 1 + n \int \mathrm{d}\mathbf{r}\, \mathrm{e}^{-i\mathbf{k}\cdot\mathbf{r}} g(\mathbf{r}) \ . \end{aligned} \tag{2.46}$$

This equation can also be written in the more convenient form [Reichl, 2004]

$$S(k) = 1 + n\delta(\mathbf{k}) + n \int \mathrm{d}\mathbf{r}\, \mathrm{e}^{-i\mathbf{k}\cdot\mathbf{r}} \left[g(\mathbf{r}) - 1 \right] \ . \tag{2.47}$$

The delta function characterises the coherent contribution accounting for $\mathbf{k} = 0$. This term will be neglected in the following as finite k vectors are considered.

If a system consists of multiple species, the definition for the static structure factor has to be generalised to account for all mutual correlations between the various species. The partial structure factors are then defined by

$$S_{ab}(\mathbf{k}) = \frac{1}{\sqrt{N_a N_b}} \left\langle \varrho_a(\mathbf{k}) \varrho_b^*(\mathbf{k}) \right\rangle = \delta_{ab} + \sqrt{n_a n_b} \int \mathrm{d}\mathbf{r} \left[g_{ab}(\mathbf{r}) - 1 \right] \exp(-i\mathbf{k}\cdot\mathbf{r}) \tag{2.48}$$

via the partial pair distribution function $g_{ab}(\mathbf{r})$. For isotropic systems the equation simplifies to

$$S_{ab}(k) = \delta_{ab} + \frac{4\pi}{k} \sqrt{n_a n_b} \int\limits_0^\infty \mathrm{d}r\, r \sin(kr) [g_{ab}(r) - 1] \ . \tag{2.49}$$

In the limiting case of uncorrelated particles, the structure factor $S(k)$ is unity. This value is also reached in the limit of large wave vectors k.

2.3 Time-dependent correlation functions

The static quantities $S(k)$ and $g(r)$ can be generalised to account for the fact that, even in thermodynamic equilibrium, the particles are constantly moving and, thus, cause time-dependent density fluctuations. The study of these fluctuations is essential for the understanding of the dynamic response of many-particle systems.

Time-dependent density fluctuations $\delta\varrho$ are defined as [Ichimaru, 2004a]

$$\delta\varrho(\mathbf{r},t) = \varrho(\mathbf{r},t) - n \;, \tag{2.50}$$

where $\varrho(\mathbf{r},t)$ denotes the local particle density now given by

$$\varrho(\mathbf{r},t) = \sum_{j=1}^{N} \delta(\mathbf{r} - \mathbf{r}_j(t)) \;. \tag{2.51}$$

$n = N/V$ denotes the mean particle density for a system with N particles within the volume V. $\mathbf{r}_j(t)$ reflects the spatial trajectory of the $j-$th particle including the time dependency. The Fourier components of the density are determined by

$$\delta\varrho(\mathbf{k},t) = \int\limits_V \mathrm{d}\mathbf{r}\, \delta\varrho(\mathbf{r},t)\mathrm{e}^{-i\mathbf{r}\cdot\mathbf{k}} = \sum_j \exp\left[-i\mathbf{k}\cdot\mathbf{r}_j(t)\right] - N\delta(\mathbf{k}) \;. \tag{2.52}$$

The difference between $\varrho(\mathbf{k},t)$ and $\delta\varrho(\mathbf{k},t)$ is only given by the contribution at $\mathbf{k} = 0$. Thus, it is convenient for simplicity of the notation to use the symbol $\varrho(\mathbf{k},t)$ for the definition of density fluctuations in k-space.

The generalisation of the well-known pair distribution function (2.40) to a time-dependent distribution function was introduced by von Hove [van Hove, 1954]

$$G(\mathbf{r},\mathbf{r}',t,t') = \frac{1}{N}\left\langle \varrho(\mathbf{r}'+\mathbf{r},t+t')\varrho(\mathbf{r}',t')\right\rangle \;. \tag{2.53}$$

This quantity has a direct physical interpretation as it characterises the correlations between two particles where the one particle is located at $\mathbf{r}'+\mathbf{r}$ at the time $t+t'$ and the other particle is located at the position $\mathbf{r}'$ at the time t'. In equilibrium, it is possible to set the time $t' = 0$. Furthermore it is useful, to integrate over the original position $\mathbf{r}'$ to be independent of the coordinate system. After these transformations, the generalised pair distribution function is given as

$$G(\mathbf{r},t) = \frac{1}{N}\sum_{i,j=1}^{N}\int \mathrm{d}\mathbf{r}' \left\langle \delta(\mathbf{r}+\mathbf{r}_i(0)-\mathbf{r}')\delta(\mathbf{r}'-\mathbf{r}_j(t))\right\rangle \;. \tag{2.54}$$

In the special case of $t = 0$, the integration can be performed leading to

$$\begin{aligned} G(\mathbf{r},0) &= \frac{1}{N}\left\langle \sum_{i,j=1}^{N} \delta(\mathbf{r}+\mathbf{r}_i(0)-\mathbf{r}_j(0)) \right\rangle \\ &= \delta(\mathbf{r}) + \frac{1}{N}\left\langle \sum_{i\neq j}^{N} \delta(\mathbf{r}+\mathbf{r}_i(0)-\mathbf{r}_j(0)) \right\rangle \\ G(\mathbf{r},0) &= \delta(\mathbf{r}) + n\, g(\mathbf{r}) \ , \end{aligned} \tag{2.55}$$

showing the connection to the radial distribution function (2.40) for the special case of isotropic, homogeneous systems.

Similar to the static case, the von Hove function for multicomponent systems is defined by [Chávez-Rojo and Medina-Noyola, 2006]

$$G_{ab}(\mathbf{r},t) = \frac{1}{\sqrt{N_a N_b}} \int \mathrm{d}\mathbf{r}' \left\langle \varrho_a(\mathbf{r}'+\mathbf{r},t)\varrho_b(\mathbf{r}',0)\right\rangle \ . \tag{2.56}$$

It is often convenient to consider the density-density correlation functions in Fourier space. This function is called the intermediate scattering function

$$F_{ab}(\mathbf{k},t) = \frac{1}{\sqrt{N_a N_b}} \left\langle \varrho_a(\mathbf{k},t)\varrho_b^*(\mathbf{k},0)\right\rangle = \int \mathrm{d}\mathbf{r}\, G_{ab}(\mathbf{r},t)\mathrm{e}^{i\mathbf{k}\cdot\mathbf{r}} \ . \tag{2.57}$$

It can be split into two terms: the "self" and the "distinct" part, corresponding to the case where the same particle is considered at different times or if the two different Klimontovich densities correspond to different particles

$$F_{ab}(k,t) = F_{ab}^s(k,t) + F_{ab}^d(k,t) \ . \tag{2.58}$$

The two parts are given by [Chávez-Rojo and Medina-Noyola, 2006]

$$F_{ab}^s(\mathbf{k},t) = \delta_{ab}\frac{1}{N_a}\left\langle \sum_{i=1}^{N_a} \exp\left[i\mathbf{k}(\mathbf{r}_i^{(a)}(t)-\mathbf{r}_i^{(a)}(0))\right]\right\rangle = \delta_{ab}F_a^s(k,t) \ , \tag{2.59a}$$

and

$$\begin{aligned} F_{ab}^d(\mathbf{k},t) = {} & \frac{1-\delta_{ab}}{\sqrt{N_a N_b}}\left\langle \sum_{i=1}^{N_a}\sum_{j=1}^{N_b} \exp\left[i\mathbf{k}(\mathbf{r}_i^{(a)}(t)-\mathbf{r}_j^{(b)}(0))\right]\right\rangle \\ & + \delta_{ab}\frac{1}{N_a}\left\langle \sum_{i=1}^{N_a}\sum_{i\neq j} \exp\left[i\mathbf{k}(\mathbf{r}_i^{(a)}(t)-\mathbf{r}_j^{(a)}(0))\right]\right\rangle \ . \end{aligned} \tag{2.59b}$$

The self part (2.59a) describes single-particle dynamics, for example, self-diffusion, while the distinct part describes correlations between distinct particles. The two terms in the distinct part account for the fact that the two particles can be from the same species, that is $a = b$, or that both particles belong to different species.

The Fourier transformation of the intermediate scattering function with respect to time gives its power spectrum. The resulting quantity is called the dynamic structure factor [Ichimaru, 2004a,b]

$$S_{ab}(\mathbf{k},\omega) = \frac{1}{2\pi}\int \mathrm{d}t\, F_{ab}(\mathbf{k},t)\mathrm{e}^{i\omega t} = \frac{1}{2\pi\sqrt{N_a N_b}}\int \mathrm{d}t\ \langle \delta\varrho_a(\mathbf{k},t)\delta\varrho_b^*(\mathbf{k},0)\rangle\, \mathrm{e}^{i\omega t}\ . \tag{2.60}$$

The static structure factor is then obtained by integrating over the frequency

$$S_{ab}(\mathbf{k}) = \int \mathrm{d}\omega\, S_{ab}(\mathbf{k},\omega)\ , \tag{2.61}$$

which is in agreement with the definition (2.48). As the structure factor can be accessed directly via scattering experiments, the definitions of the dynamic quantities provide the foundation for the description of dynamic properties, such as electron plasma oscillations or ion acoustic modes.

2.4 Susceptibility and dielectric function

A plasma is an ensemble of freely moving particles with charge Ze which respond to an externally applied electrostatic potential, Φ^{ext}, via density fluctuations. Within the linear response theory, the induced density fluctuations in a multicomponent system are given by [Ichimaru, 2004b]

$$\delta\varrho_a^{\mathrm{ind}}(\mathbf{k},\omega) = \sum_b \chi_{ab}(\mathbf{k},\omega) Z_b e\, \Phi^{\mathrm{ext}}(\mathbf{k},\omega)\ . \tag{2.62}$$

$\chi_{ab}(\mathbf{k},\omega)$ characterises the density-density response function or susceptibility. In an ideal, uncorrelated system, like a free electron gas, the density response is given by an analytic formula (see section 5.1.1). However the dynamic susceptibility is in general not known in strongly coupled many-particle systems. Several approximation have been investigated to account for this physics.

The density fluctuations cause an induced electrostatic field in the plasma of the form [Ichimaru, 2004a]

$$\Phi^{\mathrm{ind}}(\mathbf{k},\omega) = \sum_a \frac{4\pi Z_a e}{k^2}\delta\varrho_a^{\mathrm{ind}}(\mathbf{k},\omega)\ . \tag{2.63}$$

The dielectric function, $\varepsilon(\mathbf{k},\omega)$, represents the changes of the total electrostatic field, $\Phi^{\mathrm{tot}} = \Phi^{\mathrm{ind}} + \Phi^{\mathrm{ext}}$, due to the external perturbation [Murillo and Weisheit, 1998]

$$\varepsilon(\mathbf{k},\omega)\Phi^{\mathrm{tot}}(\mathbf{k},\omega) = \Phi^{\mathrm{ext}}(\mathbf{k},\omega) \; . \tag{2.64}$$

Substitution of Eqs. (2.62) and (2.63) in this expression yields [Ichimaru, 2004b]

$$\varepsilon^{-1}(\mathbf{k},\omega) = 1 + \frac{\Phi^{\mathrm{ind}}}{\Phi^{\mathrm{ext}}} = 1 + \sum_{ab} V_{ab}(\mathbf{k})\chi_{ab}(\mathbf{k},\omega) \tag{2.65}$$

with the Coulomb potential in Fourier space $V_{ab}(k) = 4\pi Z_a Z_b e^2/k^2$. This expression connects the dielectric function with the density response of the system.

The fluctuation-dissipation theorem presents a general relation between the response of the system to an external perturbation and the microscopic correlation functions of the density fluctuations, characterised by the dynamic structure factor [Kubo, 1966]. For multicomponent systems, the theorem is given by [Kremp et al., 2005]: [2]

$$S_{ab}(\mathbf{k},\omega) = \frac{1}{\pi} n_{\mathrm{B}}(\omega)\, \mathrm{Im}\, \chi_{ab}(\mathbf{k},\omega) \; . \tag{2.66}$$

Here, the imaginary part of the susceptibility is relevant as it describes the absorption of the radiation energy and, thus, characterises the dissipative quantity. The Bose function $n_{\mathrm{B}}(\omega) = \left[\mathrm{e}^{-\beta\hbar\omega} - 1\right]^{-1}$ describes the occupation probability of collective oscillations.

[2] Often the definition of the dynamic structure factor via the fluctuation-dissipation theorem is given with an additional factor of density n. In this thesis, the density will be included in the definition of the static structure factor.

Chapter 3

The theory of x-ray Thomson scattering

Light scattering, particularly in the case when x-rays are applied, is of great interest as a plasma diagnostic because it is one of a few non-perturbing methods well-suited for warm dense matter. In principle, all basic plasma parameters, such as temperature, density and charge state, can be obtained from the measured scattering signal. Furthermore, the microscopic structure of the material can be inferred.

In the beginning of this chapter, the theoretical framework of the scattering process will be derived. Therein, it will be distinguished between the non-coherent and the coherent scattering process. In the first case, the electrons in the scattering volume considered are uncorrelated, yielding the total scattered field from the sum of the electromagnetic fields of all individual electrons. In the coherent case, the correlations between the electrons have to be included by considering their distribution functions to account for the position and the velocity of each electron. It will be shown that the scattering signal in this case is directly proportional to the total dynamic electron structure factor.

The scattering signal of a partially ionised plasma has two distinct features, namely, a frequency-shifted part, related to the dynamically free electrons, and an unshifted one (Rayleigh peak), due to scattering from electrons that follow the ion motion. Following ideas originally developed by Chihara [Chihara, 1987, 2000], it will be shown that the electron structure factor can be decomposed into different parts associated with these distinct features. After the derivation for an electron-ion system, the treatment will be generalised to systems with multiple ion species [Wünsch et al., 2011]. This is of particular interest as recent scattering experiments have been performed on composite materials, such as plastic [Barbrel et al., 2009]

and lithium hydride [Kritcher et al., 2009, 2008]. At the end of this chapter, simplifications of the scattering formula that have been used will be highlighted based on the elements investigated and the constraints of current laser-driven x-ray sources.

3.1 Light scattering as plasma diagnostics

The scattering process of light in matter is here described by considering the incoming photons as a classical electromagnetic wave and the plasma as a fully interacting system consisting of electrons and ions [1]. For the theoretical description of this process a few reasonable assumptions have to be made. Firstly, only radiation with high enough frequencies to penetrate the plasma with negligible attenuation are considered. This is particularly challenging in the case of warm dense matter with near solid-state density and above where x-rays are required. Furthermore, the scattering volume has to be small enough to avoid multiple scattering. The use of x-rays however reduces this problem due to the small scattering cross section.

As it will be shown later, the scattering process is inversely proportional to the mass of the particles and, thus, the ion contribution to the scattering process can be neglected. Nevertheless, the ions have an indirect effect on the coherent scattering process as bound electrons as well as free electrons forming the screening cloud, are following the ion motion and, thus, reflect the ion properties. The entire derivation is also restricted to the non-relativistic case, where the momentum of the photon can be neglected. This is sufficient as long as the photon energy is much less than the rest mass of the electron or the fraction of energy transferred is small.

3.1.1 Thomson cross section and incoherent scattering

The basic scattering process can be described in a classical way as follows: an electromagnetic wave impinges on a free particle with charge q and mass m. The particle will be accelerated and self-consistently radiates. In the non-relativistic case, the contribution of the magnetic field can be neglected and the emitted radiation, that is the scattered wave, has the same frequency as the incident wave if the particle was initially at rest.

Scattering by a single electron

First the scattered power of a single electron in an electromagnetic field will be derived. The incident electromagnetic field is described by a monochromatic plane

[1] A fully quantum mechanical derivation of the x-ray scattering process can be found in Ref. [Santra, 2009].

wave of the form [Jackson, 1999]

$$\mathbf{E}_i(\mathbf{r},t) = \hat{\boldsymbol{\epsilon}}_{i0}\, E_{i0}\, \mathrm{e}^{i(\mathbf{k}_i\mathbf{r}-\omega_i t)} \tag{3.1}$$

with the amplitude E_{i0}, the wavenumber $\mathbf{k}_i$, the frequency ω_i and the polarisation vector $\hat{\boldsymbol{\epsilon}}_{i0}$ [2]. The electron with position $\mathbf{r}$ and velocity $\mathbf{v}$ gets accelerated in this electric field. Its equation of motion in the non-relativistic case is given by

$$m_e \frac{\mathrm{d}\mathbf{v}}{\mathrm{d}t} = -e\mathbf{E}_i(\mathbf{r},t)\ . \tag{3.2}$$

Applying the dipole approximation, the emitted radiation of the electron can be derived to be [Jackson, 1999]

$$\mathbf{E}_s(R,t) = \frac{-e}{Rc^2}\left[\hat{\mathbf{n}}_s \times (\hat{\mathbf{n}}_s \times \dot{\mathbf{v}})\right]\ . \tag{3.3}$$

Here, R denotes the distance between the charge and the observation point and $\hat{\mathbf{n}}_s$ is the unit vector in the direction where the scattered radiation is detected (see Fig. 3.2). A combination of the last three equations leads to the scattered electric field on the observation point

$$\mathbf{E}_s(R,t) = \frac{e^2 E_{i0}}{m_e R c^2}\left[\hat{\mathbf{n}}_s \times (\hat{\mathbf{n}}_s \times \hat{\boldsymbol{\epsilon}}_{i0})\right] \mathrm{e}^{i(\mathbf{k}_i\mathbf{r}-\omega_i t)}\ . \tag{3.4}$$

The double vector product $[\hat{\mathbf{n}}_s \times (\hat{\mathbf{n}}_s \times \hat{\boldsymbol{\epsilon}}_{i0})]$ defines the polarisation of the scattered wave, which depends on the polarisation of the incident wave. The time-averaged power at the scattered wave per unit solid angle is then [Sheffield, 1975]

$$\frac{\mathrm{d}P_s}{\mathrm{d}\Omega} = \frac{cR^2}{4\pi} \lim_{T\to\infty} \frac{1}{T} \int_{-\infty}^{\infty} \mathrm{d}t\ |E_S(R,t)|^2 = \frac{r_e^2 c}{8\pi} |E_{i0}|^2 \left[\hat{\mathbf{n}}_s \times (\hat{\mathbf{n}}_s \times \hat{\boldsymbol{\epsilon}}_{i0})\right]^2\ , \tag{3.5}$$

where the classical electron radius, $r_e = e^2/(m_e c^2)$, is introduced. T denotes the macroscopic time duration of the scattering process.

The polarisation term can be simplified to

$$\left[\hat{\mathbf{n}}_s \times (\hat{\mathbf{n}}_s \times \hat{\boldsymbol{\epsilon}}_{i0})\right]^2 = \left[(\hat{\mathbf{n}}_s \cdot \hat{\boldsymbol{\epsilon}}_{i0})\cdot \hat{\mathbf{n}}_s - \hat{\boldsymbol{\epsilon}}_{i0}\right]^2 = 1 - (\hat{\mathbf{n}}_s \cdot \hat{\boldsymbol{\epsilon}}_{i0})^2\ , \tag{3.6}$$

whereas the unit vector pointing in the direction of the observation detector can be expressed in Cartesian coordinates $(\hat{\mathbf{x}}, \hat{\mathbf{y}}, \hat{\mathbf{z}})$ as $\hat{\mathbf{n}}_s = (\sin\theta\cos\phi\ \hat{\mathbf{x}}, \sin\theta\sin\phi\ \hat{\mathbf{y}}, \cos\theta\ \hat{\mathbf{z}})$, as illustrated in Fig. 3.1. If the incident monochromatic wave is linearly polarised

[2] The indices 'i' and 's' label incident and scattered quantities, respectively.

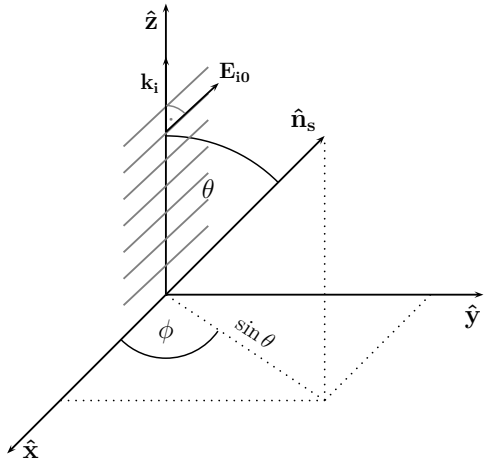

Figure 3.1: Scattering geometry in the Cartesian coordinate system to illustrate the calculation of the polarisation term from the scattered wave observed in the $\hat{\mathbf{n}}_s$ direction. The incident radiation is presented as a wave propagating in the $\hat{\mathbf{z}}$ direction and having a linear polarisation along the $\hat{\mathbf{x}}$-axis. The scattering geometry is defined by the scattering angle, θ, and the azimuthal angle, ϕ, lying in the $\hat{\mathbf{x}}-\hat{\mathbf{y}}$ plane.

along the $\hat{\mathbf{x}}-$axis ($\hat{\boldsymbol{\epsilon}}_{i0} = \hat{\mathbf{x}}$), as it can be realised in a free electron laser, the polarisation term is finally given as

$$[\hat{\mathbf{n}}_s \times (\hat{\mathbf{n}}_s \times \hat{\boldsymbol{\epsilon}}_{i0})]^2 \Big|_{\text{lin.pol.}} = 1 - \sin^2\theta\cos^2\phi \; . \tag{3.7}$$

In laser produced x-ray sources, the radiation is however fully unpolarised and, thus, an average over the azimuthal angle ϕ has to be performed

$$[\hat{\mathbf{n}}_s \times (\hat{\mathbf{n}}_s \times \hat{\boldsymbol{\epsilon}}_{i0})]^2 \Big|_{\text{unpol.}} = 1 - \sin^2\theta\,\overline{\cos^2\phi} = 1 - \frac{\sin^2\theta}{2} = \frac{1}{2}\left(1 + \cos^2\theta\right) \; . \tag{3.8}$$

An experimentally useful quantity is the differential scattering cross section that defines the ratio of the scattered power per unit time and solid angle to the incident energy flux per unit area and time, i.e. $c|E_{i0}|^2/(8\pi)$ [Jackson, 1999]. In the case of an unpolarised incident wave, this quantity is given by

$$\frac{\mathrm{d}\sigma}{\mathrm{d}\Omega} = \frac{1}{2}r_e^2(1 + \cos^2\theta) \; . \tag{3.9}$$

The integration over the solid angle $\mathrm{d}\Omega$ leads to the total Thomson cross section for

a single electron

$$\sigma_{\mathrm{Th}} = \frac{1}{2} r_e^2 \int \mathrm{d}\Omega (1 + \cos^2\theta) = \frac{8}{3} \pi r_e^2 \,, \tag{3.10}$$

where $\mathrm{d}\Omega = 2\pi \,\mathrm{d}\cos\theta$ is used. This Thomson formula is strictly valid only for such low frequencies where the momentum of the photon can be neglected. For higher frequencies, the Compton effect gives significant contributions to the scattering process and a full quantum mechanical description has to be applied. A suitable approach was given by Klein and Nishina who derived an approximate total cross section formula based on the Dirac equation, which also allows relativistic effects to be included [Klein and Nishina, 1929].

Incoherent scattering

To describe the scattering process within a plasma, the individual contributions of the electrons have to be added. First, only incoherent scattering will be considered. This approach is valid when the scattering parameter (1.9) is much smaller than unity. In this case, the scale length of the scattering volume is smaller than the characteristic screening length (1.10) and the light scatters on single, randomly distributed electrons.

In experimental set-ups the detector measures the scattered radiation spectrally resolved around the scattered frequency $[\omega_s - \frac{\mathrm{d}\omega_s}{2}, \omega_s + \frac{\mathrm{d}\omega_s}{2}]$. Thus, the spectral scattered power is introduced, which can be obtained by Parseval's theorem [Jackson, 1999]

$$\frac{\mathrm{d}P_s(R,\omega)}{\mathrm{d}\Omega} = \frac{cR^2}{4\pi} \lim_{T\to\infty} \frac{1}{T\pi} \int_{\omega_s - \mathrm{d}\omega_s/2}^{\omega_s + \mathrm{d}\omega_s/2} \mathrm{d}\omega_s \left| E_s^{\mathrm{T}}(R,\omega_s) \right|^2 \,, \tag{3.11}$$

where

$$E_s^{\mathrm{T}}(R,\omega_s) = \int_{-\infty}^{\infty} \mathrm{d}t \, E_s^{\mathrm{T}}(R,t) \mathrm{e}^{-i\omega_s t} \tag{3.12}$$

is the Fourier transform of the scattered field.

To determine this quantity, the equation of the electric field caused by the scattering on a single electron, j, with position, $\mathbf{r}_j$, (see eq. (3.4)) is considered

$$\mathbf{E}_{sj}(R,t) = \frac{e^2 E_{i0}}{m_e R c^2} \left[\hat{\mathbf{n}}_s \times (\hat{\mathbf{n}}_s \times \hat{\boldsymbol{\epsilon}}_{i0}) \right] \mathrm{e}^{i(\mathbf{k}_i \mathbf{r}_j(t') - \omega_i t')} \,. \tag{3.13}$$

Note that on the right hand side the retarded time, t', was introduced to account for the time delay between emission of the wave due to the moving electron and the detection at the observation point at time t, i.e. $t' = t - \frac{R}{c}$, where c is the speed of

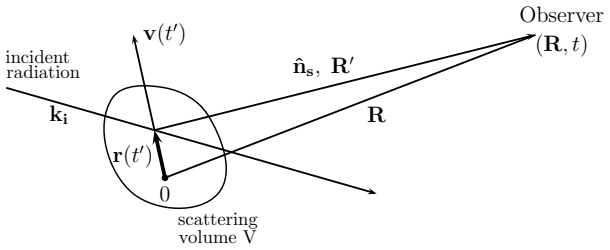

Figure 3.2: Illustration of the scattering geometry of an electron moving with velocity $\mathbf{v}(t')$ in the scattering volume, V, at the retarded time, t'. The observation point at time, t, is far enough to neglect the distance the electron will move over the observation time, $\mathbf{r}(t')$, that is, $R' \simeq R$.

light [Sheffield, 1975]. If the distance to the observation point R (see Fig. 3.2) is significantly larger than the distance that the electron will travel during the observation time, the retarded time can be approximately written as [Sheffield, 1975]

$$t' \simeq t - \frac{1}{c}\left[R - \hat{\mathbf{n}}_s \cdot \mathbf{r}_j(t')\right] \ . \tag{3.14}$$

The above condition is always fulfilled in the experiments that will be discussed within this thesis.

To evaluate the scattered electric field in frequency space, it is convenient to also introduce the retarded time in the Fourier transformation (3.12). The field is then given by [Hutchinson, 2005]

$$\begin{aligned} \mathbf{E}_{sj}(R, w_s) &= \frac{r_e}{R} E_{i0} \left[\hat{\mathbf{n}}_s \times (\hat{\mathbf{n}}_s \times \hat{\boldsymbol{\epsilon}}_{i0})\right] \int \mathrm{d}t' \mathrm{e}^{i\left[\omega_s\left(t' + \frac{R}{c} - \frac{\hat{\mathbf{n}}_s \mathbf{r}_j(t')}{c}\right)\right]} \mathrm{e}^{i[\mathbf{k}_i \mathbf{r}_j(t') - \omega_i t']} \\ &= \frac{r_e}{R} E_{i0}\, \mathrm{e}^{ik_s R} \left[\hat{\mathbf{n}}_s \times (\hat{\mathbf{n}}_s \times \hat{\boldsymbol{\epsilon}}_{i0})\right] \int \mathrm{d}t' \mathrm{e}^{-i[\omega t' - \mathbf{k}\mathbf{r}_j(t')]} \end{aligned} \tag{3.15}$$

where $\omega = \omega_s - \omega_i$ and $\mathbf{k} = \mathbf{k}_s - \mathbf{k}_i$ are the frequency and wavenumber shifts of the incident photons, respectively and $k_s = \omega_s/c$. In the non-relativistic case, the velocity is constant and thus the time integration can be performed

$$\mathbf{E}_{sj}(R, w_s) = \frac{r_e}{R} E_{i0}\, \mathrm{e}^{ik_s R} \left[\hat{\mathbf{n}}_s \times (\hat{\mathbf{n}}_s \times \hat{\boldsymbol{\epsilon}}_{i0})\right] \delta\left(\mathbf{k} \cdot \mathbf{v} - \omega\right) \ . \tag{3.16}$$

The scattered frequency,

$$\omega_s = \omega_i - \mathbf{k} \cdot \mathbf{v} = \omega_i - (\mathbf{k}_s - \mathbf{k}_i) \cdot \mathbf{v} \ , \tag{3.17}$$

is thus Doppler-shifted from the incident frequency depending on the electron velocity in the **k**-direction.

In incoherent scattering, the single electrons are uncorrelated and, thus, the total spectral power is given by the sum of the individual electric fields multiplied with a distribution of the electron velocities. As the scattered power is considered within a frequency range $\omega_s \rightarrow \mathrm{d}\omega_s$, only the electrons with the velocity $\mathbf{v} + \mathrm{d}\mathbf{v}$ that fulfil Eq. (3.17) are relevant, which can be expressed by the velocity distribution function $N_e\, f(\mathbf{v})\mathrm{d}\mathbf{v}$. Therefore, the scattered power per unit solid angle and frequency is [Hutchinson, 2005]

$$\frac{\mathrm{d}^2 P_s(R,\omega_s)}{\mathrm{d}\Omega \mathrm{d}\omega_s} = N_e \frac{P_i}{A} r_e^2 \left[\hat{\mathbf{n}}_s \times (\hat{\mathbf{n}}_s \times \hat{\boldsymbol{\epsilon}}_{i0})\right]^2 \int \mathrm{d}\mathbf{v}\, f(\mathbf{v}) \delta\left(\mathbf{k}\cdot\mathbf{v} - \omega\right) \ . \tag{3.18}$$

$P_i = cE_{i0}^2 A/(8\pi)$ denotes here the incident power with the cross section of the incident beam A. The scattered power can be simplified if the velocity components are split in the directions of the scattered wave vector **k** and perpendicular to it, i.e., one within the scattering plane and one perpendicular to the scattering plane. Then the integral can be simplified to [Sheffield, 1975]

$$\frac{\mathrm{d}^2 P_s(R,\omega_s)}{\mathrm{d}\Omega \mathrm{d}\omega_s} = N_e \frac{P_i}{A} r_e^2 \left[\hat{\mathbf{n}}_s \times (\hat{\mathbf{n}}_s \times \hat{\boldsymbol{\epsilon}}_{i0})\right]^2 f\left(\frac{\omega}{k}\right) \frac{1}{k} \ , \tag{3.19}$$

where $f(\omega/k)$ is the one-dimensional velocity distribution in the **k** direction.

In conclusion, the scattered frequency spectrum is directly proportional to the velocity distribution of the electrons for non-relativistic conditions and as long as the incident wave scatters incoherently on the sample. The latter condition can be realised in experiments via a backscattering geometry where k is large and the scattering volume is small.

3.1.2 Coherent scattering

If the incident wave interacts with several electrons simultaneously, their correlations have to be taken into account. In this case, the scattering parameter (1.9) is roughly unity or above, that means, the scale length of the measured scattering volume is comparable to or greater than the characteristic screening length.

The starting point for the derivation of the power spectrum is Eq. (3.15), the scattered electric field of a single electron in frequency space. To determine the total electric field generated by the electron ensemble in the scattering volume, the individual contributions have to be summed in a coherent way, that is, multiplied by the distribution function accounting for the positions, $\mathbf{r}(t)$, and the velocities, $\mathbf{v}(t)$,

of the particles at time, t. This property is given by the Klimontovich distribution function which is introduced as [Klimontovich, 1975]

$$f_e(\mathbf{r}, \mathbf{v}, t) = \sum_{j=1}^{N_e} \delta(\mathbf{r} - \mathbf{r}_j(t))\delta(\mathbf{v} - \mathbf{v}_j(t)) \ . \tag{3.20}$$

This function describes the microscopic density of the electrons in phase space.

The total scattered field is given by integration over the phase space of the individual electric fields multiplied by the distribution function [Sheffield, 1975]

$$E_s^{\mathrm{T}}(\omega_s, R) = \int \mathrm{d}\mathbf{r}\, \mathrm{d}\mathbf{v}\, E_s(\omega_s, R) f_e(\mathbf{r}, \mathbf{v}, t') \ . \tag{3.21}$$

Please note, that the Klimontovich distribution function is also written with the retarded time, t'. In the non-relativistic dipole approximation, the scattered field is independent of the velocity and thus the integral regarding $\mathbf{v}$ is trivial

$$E_s^{\mathrm{T}}(\omega_s, R) = \int \mathrm{d}\mathbf{r}\, E_s(\omega_s, R)\, \varrho_e(\mathbf{r}, t') \ , \tag{3.22}$$

where

$$\varrho_e(\mathbf{r}, t') = \int \mathrm{d}\mathbf{v} f_e(\mathbf{r}, \mathbf{v}, t') = \sum_{j=1}^{N_e} \delta(\mathbf{r} - \mathbf{r}_j(t')) \tag{3.23}$$

is the Klimontovich density. The power spectrum per solid angle and frequency is then given as [Hutchinson, 2005; Sheffield, 1975](see Eq. (3.11))

$$\begin{aligned} \frac{\mathrm{d}^2 P_s(R, \omega_s)}{\mathrm{d}\Omega\, \mathrm{d}\omega_s} = \frac{cR^2}{4\pi} \lim_{T\to\infty} \frac{1}{\pi T} \\ \times \left| \int \mathrm{d}t'\, \mathrm{d}\mathbf{r} \frac{r_e}{R} \mathrm{e}^{ik_s R} E_{i0} \left[\hat{\mathbf{n}}_s \times (\hat{\mathbf{n}}_s \times \hat{\boldsymbol{\epsilon}}_{i0})\right] \varrho_e(\mathbf{r}, t') \mathrm{e}^{i[\omega t' - \mathbf{k}\cdot\mathbf{r}_j(t')]} \right|^2 \ . \end{aligned} \tag{3.24}$$

As used before, ω and $\mathbf{k}$ in the exponential function represent the wavenumber and frequency shift during the scattering process. To evaluate the integral, the Klimontovich densities have to be expressed in the $k-$ and $\omega-$space, i.e.

$$\varrho_e(\mathbf{r}, t') = \int \frac{\mathrm{d}\mathbf{k}}{(2\pi)^3} \frac{\mathrm{d}\omega}{2\pi} \varrho_e(\mathbf{k}, \omega) \mathrm{e}^{-i(\mathbf{k}\cdot\mathbf{r} - \omega t')} \ , \tag{3.25}$$

which leads to

$$\frac{\mathrm{d}^2 P_s(R,\omega_s)}{\mathrm{d}\Omega\,\mathrm{d}\omega_s} = \frac{cR^2}{4\pi}\lim_{T\to\infty}\frac{1}{\pi T}\left|\frac{r_e}{R}\mathrm{e}^{ik_sR}E_{i0}\left[\hat{\mathbf{n}}_s\times(\hat{\mathbf{n}}_s\times\hat{\boldsymbol{\epsilon}}_{i0})\right]\right|^2 \times\left|\int \mathrm{d}t'\,\mathrm{d}\omega\,\mathrm{d}\mathbf{r}\,\mathrm{d}\mathbf{k}\,\varrho_e(\mathbf{k},\omega)\mathrm{e}^{i[\omega-(\omega_s-\omega_i)]t'}\mathrm{e}^{i[\mathbf{k}-(\mathbf{k}_s-\mathbf{k}_i)]\cdot\mathbf{r}_i(t')}\right|^2 . \quad (3.26)$$

Now, the following properties of the delta distribution can be used

$$\int \mathrm{d}t\,\mathrm{e}^{i(x-x_0)t} = 2\pi\,\delta(x-x_0) \quad \text{and} \quad \int \mathrm{dx}\ \mathrm{f(x)}\delta(\mathrm{x}-\mathrm{x}_0) = \mathrm{f}(\mathrm{x}_0)\ . \quad (3.27)$$

Applying these forms to introduce δ-distributions in ω- and k-space, one obtains for the scattered power of the electron ensemble

$$\begin{aligned}\frac{\mathrm{d}^2 P_s(R,\omega_s)}{\mathrm{d}\Omega\,\mathrm{d}\omega_s} &= \frac{cR^2}{4\pi}\lim_{T\to\infty}\frac{1}{\pi T}\left|\frac{r_e}{R}\mathrm{e}^{ik_sR}E_{i0}\left[\hat{\mathbf{n}}_s\times(\hat{\mathbf{n}}_s\times\hat{\boldsymbol{\epsilon}}_{i0})\right]\right|^2 \\ &\quad\times\left|\int \mathrm{d}\omega\,\mathrm{d}\mathbf{k}\,\varrho_e(\mathbf{k},\omega)\delta(\omega-(\omega_s-\omega_i))\delta(\mathbf{k}-(\mathbf{k}_s-\mathbf{k}_i))\right|^2 \\ &= \frac{c\,r_e^2E_{i0}^2}{4\pi^2}\left[\hat{\mathbf{n}}_s\times(\hat{\mathbf{n}}_s\times\hat{\boldsymbol{\epsilon}}_{i0})\right]^2\lim_{T\to\infty}\frac{1}{T}\left|\varrho_e(\mathbf{k}_s-\mathbf{k}_i,\omega_s-\omega_i)\right|^2 . \quad (3.28)\end{aligned}$$

Again, the statistical ensemble average has to be considered, that is, $|\varrho_e(\mathbf{k},\omega)|^2$ is replaced with $\left\langle|\varrho_e(\mathbf{k},\omega)|^2\right\rangle$. Thus, the scattered power is characterised by the correlation function of the density fluctuations [Hutchinson, 2005]

$$\frac{\mathrm{d}^2 P_s(R,\omega_s)}{\mathrm{d}\Omega\,\mathrm{d}\omega_s} = \frac{r_e^2P_i}{2\pi A}\left[\hat{\mathbf{n}}_s\times(\hat{\mathbf{n}}_s\times\hat{\boldsymbol{\epsilon}}_{i0})\right]^2 NS_{ee}(\mathbf{k},\omega)\ , \quad (3.29)$$

with

$$S_{ee}(\mathbf{k},\omega) = \lim_{T\to\infty,V\to\infty}\frac{1}{TV}\left\langle\frac{|\varrho_e(\mathbf{k},\omega)|^2}{n_e}\right\rangle\ . \quad (3.30)$$

The last line is equivalent to the definition of the dynamic structure factor (2.60). The macroscopic variables T and V characterise the time of the probing and the scattering volume, respectively.

3.2 Electronic structure for partially ionised plasmas

As shown above, the dynamic electron structure factor, which characterises the microscopic density fluctuations in a many particle system, plays a crucial role in the description of the light-plasma scattering process. In equilibrium, this quantity

is given by the fluctuation-dissipation theorem (see Eq. (2.66)). This approach is well-suited for parameter regimes where well-developed approximations for the susceptibility, $\chi(\mathbf{k},\omega)$, exist, particularly for fully ionised, weakly coupled plasmas. For other systems a more direct approach has to be developed.

3.2.1 Partially ionised, strongly coupled plasmas

In a fully ionised plasma, the electromagnetic wave interacts with the free electrons and the scattering process is well described within the random phase approximation (RPA) for weakly coupled electrons, which will be discussed in section 5.1.1. In a strongly coupled plasma, a theory beyond RPA is required to account for correlation effects. Furthermore, many plasmas which are of interest here are only partially ionised and, thus, the bound electrons have to be included in the description. A formula considering all mutual correlations between free, weakly and strongly bound electrons as well as strongly coupled ions was first derived by Chihara 1987 for metallic fluids and later extended to plasmas [Chihara, 1987, 2000]. Here, this description is presented. The original concept will then be generalised to systems with multiple ion species in the following section.

A partially ionised system of N_i nuclei of one species with atomic number Z_A is considered. The total electron number is split into $Z_b N_i$ bound electrons and $Z_f N_i$ free electrons. Following this decomposition, the total electron density, ϱ_e, can similarly be split into bound and free contributions ϱ_b and ϱ_f, respectively,

$$\varrho_e(\mathbf{k},t) = \sum_{j=1}^{Z_A N_i} \exp\left(i\mathbf{k}\cdot\mathbf{r}_j(t)\right) = \varrho_b(\mathbf{k},t) + \varrho_f(\mathbf{k},t)\,. \tag{3.31}$$

The total intermediate scattering function $F^{\mathrm{tot}}(\mathbf{k},t)$, defined by Eq. (2.57), describes the density fluctuations in the plasma and can now be expressed as

$$\begin{aligned}
N_e F_{ee}^{\mathrm{tot}}(\mathbf{k},t) &= \Big\langle \varrho_e(\mathbf{k},t)\varrho_e^*(\mathbf{k},0)\Big\rangle = \Big\langle \varrho_e(\mathbf{k},t)\varrho_e(-\mathbf{k},0)\Big\rangle \\
&= \Big\langle \left[\varrho_b(\mathbf{k},t)+\varrho_f(\mathbf{k},t)\right]\left[\varrho_b(-\mathbf{k},0)+\varrho_f(-\mathbf{k},0)\right]\Big\rangle \\
&= \Big\langle \varrho_b(\mathbf{k},t)\varrho_b(-\mathbf{k},0)\Big\rangle + \Big\langle \varrho_f(\mathbf{k},t)\varrho_b(-\mathbf{k},0)\Big\rangle + \Big\langle \varrho_b(\mathbf{k},t)\varrho_f(-\mathbf{k},0)\Big\rangle \\
&\quad + \Big\langle \varrho_f(\mathbf{k},t)\varrho_f(-\mathbf{k},0)\Big\rangle \\
&= \underbrace{\Big\langle \varrho_b(\mathbf{k},t)\varrho_b(-\mathbf{k},0)\Big\rangle}_{(1)} + \underbrace{2\Big\langle \varrho_f(\mathbf{k},t)\varrho_b(-\mathbf{k},0)\Big\rangle}_{(2)} + \underbrace{\Big\langle \varrho_f(\mathbf{k},t)\varrho_f(-\mathbf{k},0)\Big\rangle}_{(3)}\,.
\end{aligned} \tag{3.32}$$

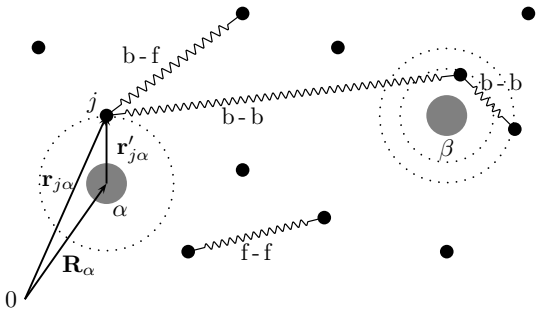

Figure 3.3: Schematic illustration of the inter-particle correlations in a partially ionised plasma. The gray dots labelled with α and β denote the ions, whereas the black dots mark the electrons classified as bound electrons moving around the ions and free electrons. The corrugated lines indicate the correlations, whereas the symbols $f-f$, $b-f$ and $b-b$ stands for free-free, bound-free and bound-bound, respectively, according to the correlations between the various electrons.

In the last step, it is used that a time shift can be performed within the ensemble average. Furthermore, the intermediate scattering function is a real function and symmetric in the wavenumber domain, i.e., $F(\mathbf{k}) = F(-\mathbf{k})$. For partially ionised plasmas, the intermediate scattering function consists of three contributions describing the various inter-particle correlations in the system: (1) the correlations between bound electrons, (2) the correlations between free and bound electrons and finally, (3) the correlations between free electrons as illustrated in Fig. 3.3.

Correlations between bound electrons

In the following, the contribution describing the mutual correlations between the bound electrons will be considered in more detail. The total bound electron among the nuclei, labelled α, is given by

$$\varrho_b(\mathbf{k},t) = \sum_{\alpha=1}^{N_i}\sum_{j=1}^{Z_b} \exp\left[i\mathbf{k}\cdot\mathbf{r}_{j\alpha}(t)\right] . \tag{3.33}$$

$\mathbf{r}_{j\alpha}(t)$ characterises the trajectory of a bound electron, j, around the ion, α. The introduction of relative coordinates of the electrons to the ion position $\mathbf{R}_\alpha$, that is

$\mathbf{r}'_{j\alpha}(t) = \mathbf{r}_{j\alpha}(t) - \mathbf{R}_\alpha(t)$, leads to

$$\varrho_b(\mathbf{k},t) = \sum_{\alpha=1}^{N_i}\sum_{j=1}^{Z_b} \exp\left[i\mathbf{k}(\mathbf{r}'_{j\alpha}+\mathbf{R}_\alpha)\right] = \sum_{\alpha=1}^{N_i}\left(\sum_{j=1}^{Z_b}\exp\left[i\mathbf{k}\cdot\mathbf{r}'_{j\alpha}\right]\right)\exp\left[i\mathbf{k}\cdot\mathbf{R}_\alpha\right] . \quad (3.34)$$

Due to the large mass difference, it is convenient to apply the Born-Oppenheimer approximation, that is, the electron motion can be separated from the motion of the nucleus [Martin, 2004]. Furthermore, the bound electron density around any nucleus is the same as identical ions are considered. This will be visualised in the following steps of the derivation by setting $\alpha = 1$ as the representative ion [3]. Thus, the bound electron distribution can be approximately described as

$$\varrho_b(\mathbf{k},t) \simeq f_i(k)\sum_{\alpha=1}^{N_i}\exp\left[i\mathbf{k}\cdot\mathbf{R}_\alpha(t)\right] , \quad (3.35)$$

where the ionic form factor $f_i(k)$ characterises the form of the bound state density,

$$f_i(k) = \left\langle \sum_{j=1}^{Z_b}\exp\left[i\mathbf{k}\cdot\mathbf{r}'_{j\alpha}(t)\right]\right\rangle = \left\langle \sum_{j=1}^{Z_b}\exp\left[i\mathbf{k}\cdot\mathbf{r}'_{j1}(t)\right]\right\rangle . \quad (3.36)$$

This quantity has to be calculated from an appropriate quantum theory taking shell effects into account for heavier species (see section 5.2).

To determine the correlations between the bound electrons, the ensemble average of the product of two densities has to be taken

$$\left\langle \varrho_b(\mathbf{k},t)\varrho_b(-\mathbf{k},0)\right\rangle = \left\langle \sum_{\alpha=1}^{N_i}\sum_{j=1}^{Z_b}\exp\left[i\mathbf{k}\left(\mathbf{r}'_{j\alpha}(t)+\mathbf{R}_\alpha(t)\right)\right] \times \sum_{\beta=1}^{N_i}\sum_{l=1}^{Z_b}\exp\left[-i\mathbf{k}\left(\mathbf{r}'_{l\beta}(0)+\mathbf{R}_\beta(0)\right)\right]\right\rangle . \quad (3.37)$$

Here, α and β account for the ions while j and l label the electrons in the many-particle system. This expression can be split into a part where two different ions are considered ($\alpha \neq \beta$) and a part where the electrons are bound to the same ion ($\alpha = \beta$)

[3] Atoms or ions with a different internal structure must be described by the multicomponent formula derived in the following section 3.2.2

$$\left\langle |\varrho_b(\mathbf{k},t)|^2 \right\rangle = \sum_{\substack{\alpha,\beta \\ \alpha\neq\beta}} \sum_{j,l} \left\langle \exp\left[i\mathbf{k}\cdot\mathbf{r}'_{j\alpha}(t)\right] \exp\left[-i\mathbf{k}\cdot\mathbf{r}'_{l\beta}(0)\right] \exp\left[i\mathbf{k}(\mathbf{R}_\alpha(t)-\mathbf{R}_\beta(0))\right] \right\rangle + \sum_{\substack{\alpha,\beta \\ \alpha=\beta}} \sum_{j,l} \left\langle \exp\left[i\mathbf{k}\cdot\mathbf{r}'_{j\alpha}(t)\right] \exp\left[-i\mathbf{k}\cdot\mathbf{r}'_{l\alpha}(0)\right] \exp\left[i\mathbf{k}(\mathbf{R}_\alpha(t)-\mathbf{R}_\alpha(0))\right] \right\rangle . \quad (3.38)$$

After decoupling the ion motion from the electron motion, the first part becomes

$$\left\langle |\varrho_b(\mathbf{k},t)|^2 \right\rangle \Big|_{\alpha\neq\beta} = \sum_{\substack{\alpha,\beta \\ \alpha\neq\beta}} \sum_{j,l} \left\langle \exp\left[i\mathbf{k}\cdot\mathbf{r}'_{j\alpha}(t)\right] \exp\left[-i\mathbf{k}\cdot\mathbf{r}'_{l\beta}(0)\right] \right\rangle \times \left\langle \exp\left[i\mathbf{k}(\mathbf{R}_\alpha(t)-\mathbf{R}_\beta(0))\right] \right\rangle . \quad (3.39)$$

The distributions of the electron densities are not correlated to each other here. Thus, the ensemble average can be separated

$$\left\langle \exp\left[i\mathbf{k}\cdot\mathbf{r}'_{j\alpha}(t)\right] \exp\left[-i\mathbf{k}\cdot\mathbf{r}'_{l\beta}(0)\right] \right\rangle = \left\langle \exp\left[i\mathbf{k}\cdot\mathbf{r}'_{j\alpha}(t)\right] \right\rangle \left\langle \exp\left[-i\mathbf{k}\cdot\mathbf{r}'_{l\beta}(0)\right] \right\rangle . \quad (3.40)$$

These two terms describe the ionic form factor for the ions α and β (3.36) which are equal as the same ion species is considered. The form factors can be treated statically as the electrons move instantly with respect to the ionic motion.

$$\left\langle |\varrho_b(\mathbf{k},t)|^2 \right\rangle \Big|_{\alpha\neq\beta} = f_i(\mathbf{k})\ f_i(-\mathbf{k}) \sum_{\substack{\alpha,\beta \\ \alpha\neq\beta}} \left\langle \exp\left[i\mathbf{k}(\mathbf{R}_\alpha(t)-\mathbf{R}_\beta(0))\right] \right\rangle . \quad (3.41)$$

The remaining ensemble average describes the autocorrelation function of the ion distribution, which can be described by the ion-ion intermediate scattering function (see Eq. (2.57))

$$F_{ii}(\mathbf{k},t) = \frac{1}{N_i} \sum_{\alpha,\beta} \left\langle \exp\left[i\mathbf{k}(\mathbf{R}_\alpha(t)-\mathbf{R}_\beta(0))\right] \right\rangle . \quad (3.42)$$

Here, different ions must be considered. Thus, the single particle dynamics, i.e., the correlations between positions of one and the same particle at different times, have to be subtracted [Hansen and McDonald, 1990; Chávez-Rojo and Medina-Noyola, 2006], yielding

$$\left\langle |\varrho_b(\mathbf{k},t)|^2 \right\rangle \Big|_{\alpha\neq\beta} = |f_i(\mathbf{k})|^2 \left[N_i F_{ii}(\mathbf{k},t) - N_i F^s_{ii}(\mathbf{k},t)\right] \quad (3.43)$$

with

$$F_{ii}^{\mathrm{s}}(\mathbf{k},t) = \frac{1}{N_i}\sum_{\alpha=1}^{N_i}\Big\langle \exp\left[i\mathbf{k}(\mathbf{R}_\alpha(t) - \mathbf{R}_\alpha(0))\right]\Big\rangle \,. \tag{3.44}$$

Eq. (3.44) is the self-part of the ion-ion intermediate scattering function.

To determinate the correlations between electrons bound to the same nucleus, that is the second part of (3.38), the electron motion will be separated again from the ion motion which leads to

$$\Big\langle |\varrho_b(\mathbf{k},t)|^2\Big\rangle\Big|_{\alpha=\beta} = \sum_{j,l=1}^{Z_b}\Big\langle \exp\left[i\mathbf{k}\left(\mathbf{r}'_{j0}(t) - \mathbf{r}'_{l0}(0)\right]\Big\rangle \sum_{\alpha=1}^{N_i}\Big\langle \exp\left[i\mathbf{k}(\mathbf{R}_\alpha(t) - \mathbf{R}_\alpha(0))\right]\Big\rangle \,. \tag{3.45}$$

The first term describes the correlations of bound electrons within the same ion, which is expressed over the intermediate scattering function $F_{ce}(\mathbf{k},t)$, whereas the second term yields the self-part of the ion-ion intermediate scattering function (3.44)

$$\Big\langle |\varrho_b(\mathbf{k},t)|^2\Big\rangle\Big|_{\alpha=\beta} = Z_b F_{ce}(\mathbf{k},t) \times N_i F_{ii}^{\mathrm{s}}(\mathbf{k},t) \,. \tag{3.46}$$

Finally, the density-density correlation of two bound electrons in a plasma with a single ion component is given by the sum of (3.43) and (3.46), that is,

$$\Big\langle |\varrho_b(\mathbf{k},t)|^2\Big\rangle = N_i|f_i(\mathbf{k})|^2 F_{ii}(\mathbf{k},t) + N_i\left[Z_b F_{ce}(\mathbf{k},t) - |f_i(\mathbf{k})|^2\right] F_{ii}^{S}(\mathbf{k},t) \,. \tag{3.47}$$

Correlations between free electrons

To describe the correlations between free electrons, the definition of the appropriate intermediate scattering function can be used directly

$$F_{ee}(\mathbf{k},t) = \frac{1}{Z_f N_i}\Big\langle \varrho_f(\mathbf{k},t)\varrho_f(-\mathbf{k},0)\Big\rangle \,. \tag{3.48}$$

Thus, the correlations are directly given by

$$\Big\langle \varrho_f(\mathbf{k},t)\varrho_f(-\mathbf{k},0)\Big\rangle = Z_f N_i F_{ee}(\mathbf{k},t) \,. \tag{3.49}$$

Here, it should be mentioned that the free electrons also form the screening cloud. Thus, this contribution still contains ionic information as the screening cloud follows the ion motion.

Correlations between free and bound electrons

The last contribution of the inter-particle correlations in the plasma is the bound-free term. To determine this part, the description of the bound electron distribution (3.35) can be used which yields

$$\begin{aligned}\Big\langle \varrho_b(\mathbf{k},t)\varrho_f(-\mathbf{k},0)\Big\rangle &= f_i(\mathbf{k})\left\langle \sum_{\alpha=1}^{N_i} \exp\left(i\mathbf{k}\cdot\mathbf{R}_\alpha\right)\varrho_f(-\mathbf{k},0)\right\rangle \\ &= f_i(\mathbf{k})\Big\langle \varrho_i(\mathbf{k},t)\varrho_f(-\mathbf{k},0)\Big\rangle \,, \end{aligned} \tag{3.50}$$

where $\varrho_i(\mathbf{k},t)$ denotes the ionic density distribution. The average can be expressed as an electron-ion intermediate scattering function

$$F_{ei}(\mathbf{k},t) = \frac{1}{\sqrt{Z_f}N_i}\Big\langle \varrho_i(\mathbf{k},t)\varrho_f(-\mathbf{k},0)\Big\rangle \,, \tag{3.51}$$

and one obtains

$$\Big\langle \varrho_b(\mathbf{k},t)\varrho_f(-\mathbf{k},0)\Big\rangle = N_i\sqrt{Z_f}f_i(\mathbf{k})F_{ei}(\mathbf{k},t) \,. \tag{3.52}$$

Total electron-electron structure factor

After the decomposition derived above, the total intermediate scattering function of bound and free electrons (3.32) is given by

$$\begin{aligned} N_e F^{tot}(\mathbf{k},t) = N_i|f_i(\mathbf{k})|^2 F_{ii}(\mathbf{k},t) + N_i\left[Z_b F_{ce}(\mathbf{k},t) - |f_i(\mathbf{k})|^2\right] F_{ii}^S(\mathbf{k},t) \\ + Z_f N_i F_{ee}(\mathbf{k},t) + N_i\sqrt{Z_f}f_i(\mathbf{k})F_{ei}(\mathbf{k},t) \,. \end{aligned} \tag{3.53}$$

To obtain the power spectrum of the electron density-density correlation, the Fourier transformation with respect to time has to be taken

$$S_{ee}^{tot}(\mathbf{k},\omega) = \frac{1}{2\pi}\int_\infty^\infty \mathrm{d}t\; F^{tot}(\mathbf{k},t)\exp(i\omega t) \,,$$

and it follows

$$\begin{aligned} N_e S_{ee}^{tot}(\mathbf{k},\omega) = N_i|f_i(\mathbf{k})|^2 S_{ii}(\mathbf{k},\omega) + Z_f N_i S_{ee}(\mathbf{k},\omega) + N_i\sqrt{Z_f}f_i(\mathbf{k})S_{ei}(\mathbf{k},\omega) \\ + \frac{N_i Z_b}{2\pi}\int_\infty^\infty \mathrm{d}t\, F_{ce}(\mathbf{k},t)F_{ii}^S(\mathbf{k},t) - N_i|f_i(\mathbf{k})|^2 S_{ii}^S(\mathbf{k},\omega) \,. \end{aligned} \tag{3.54}$$

The remaining integral can be expressed as a convolution in the frequency space:

$$\begin{aligned} N_e S_{ee}^{tot}(\mathbf{k},\omega) &= N_i |f_i(\mathbf{k})|^2 S_{ii}(\mathbf{k},\omega) + Z_f N_i S_{ee}(\mathbf{k},\omega) + N_i \sqrt{Z_f} f_i(\mathbf{k}) S_{ei}(\mathbf{k},\omega) \\ &\quad + Z_b N_i \int \mathrm{d}\omega' S_{ce}(\mathbf{k},\omega-\omega') S_{ii}^S(\mathbf{k},\omega') - N_i |f_i(\mathbf{k})|^2 S_{ii}^S(\mathbf{k},\omega) \quad (3.55) \\ &= N_i |f_i(\mathbf{k})|^2 S_{ii}(\mathbf{k},\omega) + Z_f N_i S_{ee}(\mathbf{k},\omega) + N_i \sqrt{Z_f} f_i(\mathbf{k}) S_{ei}(\mathbf{k},\omega) \\ &\quad + Z_b N_i \int \mathrm{d}\omega' \tilde{S}_{ce}(\mathbf{k},\omega-\omega') S_{ii}^S(\mathbf{k},\omega') \; . \quad (3.56) \end{aligned}$$

In the last step, the dynamic structure factor of the bound electrons of each ion was introduced

$$\tilde{S}_{ce}(\mathbf{k},\omega) = S_{ce}(\mathbf{k},\omega) - \frac{1}{Z_b} |f_i(\mathbf{k})|^2 \, \delta(\omega) \; . \quad (3.57)$$

The expression for the total electronic structure factor (3.56) is still not applicable as all partial structure factors are still inter-connected. As already mentioned in the paragraph on the correlations between free electrons, the electron-electron dynamic structure factor $S_{ee}(\mathbf{k},\omega)$ still contains correlations of free electrons forming the screening cloud and thus ionic properties. The same applies for the electron-ion structure factor $S_{ei}(\mathbf{k},\omega)$. Indeed, the structure factors in a many-particle system form a set of $\frac{1}{2}K(K+1)$ equations where K represents the number of the different species.

To decouple the different contributions, it is convenient to consider the density response function, $\chi(\mathbf{k},\omega)$, related to the structure factor via the fluctuation-dissipation theorem (2.66). The response function of a fully ionised plasma is given by a matrix equation [Chihara, 1987]

$$\underline{\underline{\chi}}(\mathbf{k},\omega) = \underline{\underline{\chi}}^0(\mathbf{k},\omega) \left[\mathbb{1} - \sqrt{\underline{\underline{\mathcal{D}}}} \, \underline{\underline{\mathcal{C}}}(\mathbf{k},\omega) \sqrt{\underline{\underline{\mathcal{D}}}} \, \underline{\underline{\chi}}^0(\mathbf{k},\omega) \right]^{-1} \quad (3.58)$$

with the components being defined as

$$[\,\underline{\underline{\mathcal{D}}}\,]_{ab} = \delta_{ab} n_a, \; [\,\underline{\underline{\mathcal{C}}}\,]_{ab} = C_{ab}(\mathbf{k},\omega), \; [\,\underline{\underline{\chi}}\,]_{ab} = \chi_{ab}(\mathbf{k},\omega), \; \text{and} \; [\,\underline{\underline{\chi}}^0\,]_{ab} = \delta_{ab}\chi_a^0(\mathbf{k},\omega) \; .$$

The indices a and b denote the species in the system, that is, electrons and ions. $\mathbb{1}$ describes the identity matrix and $\mathcal{D}$ the density matrix with the particle densities n_a. $\chi(\mathbf{k},\omega)^0$ and $\chi(\mathbf{k},\omega)$ capture the physics of the non-interacting and the interacting systems, respectively. $C(\mathbf{k},\omega)$ characterises the dynamic direct correlation function, which was first introduced by Ornstein and Zernike [Ornstein and Zernike, 1914]. It represents the total correlations between two particles over an effective potential

which includes the effect of the surrounding medium.

For a system with a single ion species, that is a two-component system with $a = e$ and $b = i$, the different dynamical response functions are given by [4]

$$\chi_{ee} = \frac{1}{\Delta}\left(1 - n_i\, C_{ii}\chi_i^0\right)\chi_e^0 \,, \tag{3.59a}$$

$$\chi_{ei} = \frac{1}{\Delta}\sqrt{n_e n_i}\, C_{ei}\chi_e^0\,\chi_i^0 \,, \tag{3.59b}$$

$$\chi_{ie} = \frac{1}{\Delta}\sqrt{n_e n_i}\, C_{ei}\chi_e^0\,\chi_i^0 \,, \tag{3.59c}$$

$$\chi_{ii} = \frac{1}{\Delta}\left(1 - n_e\, C_{ee}\chi_e^0\right)\chi_i^0 \,, \tag{3.59d}$$

with the abbreviation

$$\Delta = \left(1 - n_e\, C_{ee}\chi_e^0\right)\left(1 - n_i\, C_{ii}\chi_i^0\right) - n_e n_i C_{ei}^2 \chi_e^0\,\chi_i^0 \,.$$

Note, that the symmetry $C_{ei} = C_{ie}$ is used which is valid in translate invariant systems such as plasmas. In the system of equations (3.59), the mutual connection between the response functions can be easily seen. For example, the electron-electron response function (3.59a) depends on all three direct correlation functions, namely, C_{ee}, C_{ei} and C_{ii}, as well as on the non-interacting response function of the electrons, χ_e^0, and the ions, χ_i^0. This function can be rearranged to give two contributions describing electrons that follow the ion motion (and forming the screening cloud) and electrons that move independent of the ions. The matrix relation can be inverted and, applying the fluctuation-dissipation theorem (Eq. (2.66)), finally yields

$$S_{ee}(\mathbf{k},\omega) = \frac{q^2(k)}{Z_f} S_{ii}(\mathbf{k},\omega) + S_{ee}^0(\mathbf{k},\omega) \,, \tag{3.60a}$$

$$S_{ei}(\mathbf{k},\omega) = \frac{q(k)}{\sqrt{Z_f}} S_{ii}(\mathbf{k},\omega) \,, \tag{3.60b}$$

with the expression for the screening function

$$q(\mathbf{k}) = \frac{n_e C_{ei}\,\chi_e^0}{1 - n_e C_{ee}\chi_e^0} \,. \tag{3.61}$$

Here, $S_{ee}^0(\mathbf{k},\omega)$ is the structure factor of a free electron gas. A more detailed description of the calculation above can be found in the appendix A.

With the relations (3.60), the electron-electron structure factor (3.60a) can be expressed via the ion-ion structure factor, $S_{ii}(\mathbf{k},\omega)$, modulated by the screening

[4] For simplicity of the notation, the wavenumber and frequency arguments are suppressed.

function, $q(\mathbf{k})$, and the structure factor for a free electron gas, $S^0_{ee}(\mathbf{k},\omega)$. In the same manner, the correlation between electrons and ions (3.60b) is given by the microscopic structure of the ions, $S_{ii}(\mathbf{k},\omega)$, which is again modified by the screening function, $q(\mathbf{k})$, to account for the electrons forming the screening cloud. The screening function (3.61) is defined by the direct electron-electron and electron-ion correlation functions, C_{ee} and C_{ei}, respectively.

Using equation (3.56) and inserting the definition of the partial structure factors $S_{ee}(\mathbf{k},\omega)$ and $S_{ei}(\mathbf{k},\omega)$ from Eqs. (3.60), the results can be summarised in the total electronic structure factor for an electron-ion plasma of the form

$$\frac{N_e}{N_i}\, S^{tot}_{ee}(k,\omega) = |f_i(k) + q(k)|^2\, S_{ii}(k,\omega) + Z_f S^0_{ee}(\mathbf{k},\omega) + Z_b \int \mathrm{d}\omega'\, \tilde{S}_{ce}(\mathbf{k},\omega-\omega') S_s(\mathbf{k},\omega')\ . \quad (3.62)$$

As the scattered power is directly proportional to the dynamic structure factor (see Eq. (3.29)), the spectrum contains three distinct features characterised by each term of the equation above. The first contribution describes the domain of the x-ray Thomson scattering signal with small frequency shifts, which strongly depends on the correlated ions. Here, electrons bound to the nucleus, characterised by the atomic/ionic form factor $f_i(\mathbf{k})$, and the electrons in the screening cloud, described by $q(\mathbf{k})$, contribute to the scattering of the probe beam. The ion-ion structure factor, $S_{ii}(\mathbf{k},\omega)$, reflects the spatial arrangement and thermal motion of the ions. The second part of Eq. (3.62) describes the scattering due to the free electrons that do not follow the ion motion. This part contributes at large frequency shifts where the inelastic Compton feature as well as collective excitations (plasmons) can be observed. The last term characterises the inelastic scattering by weakly bound electrons due to excitations of the inner core electrons to higher lying bound states or into the continuum (Raman-like scattering).

3.2.2 Generalisation for multiple ion species

Equation (3.62) is limited to an electron-ion system with one ion species. However, there are many kinds of charge states possible in a plasma. Such a situation can only be described with Eq. (3.62) by introducing an average charge state. Furthermore, x-ray scattering experiments have moved to more complex, composite matter due to the fact that most materials in nature and technological applications consists of multiple chemical elements. Therefore, to fully study and understand mixtures, a more general expression for the total electronic structure is required. Within this

thesis, the Chihara formula (3.62) will be generalised to allow the description of the x-ray scattering signal for systems with multiple ion species and takes all mutual correlations, in particular between different ion species, fully into account [Wünsch et al., 2011]. Here, the different steps needed will be presented and the terms that have to be treated in a more general way will be highlighted.

Consider a plasma consisting of electrons and N_i ions of K species (labelled $\alpha, \beta = 1, 2, \ldots, K$) with N_α being the particle number of the ion species α and $N_1 + N_2 + \cdots + N_K = \sum_\alpha N_\alpha = N_i$. Then the total electron density can be split into the free part and contributions of bound electrons associated with the K different ion species

$$\varrho_e^{\mathrm{tot}}(\mathbf{k}, t) = \sum_{\alpha=1}^{K} \varrho_\alpha^b(\mathbf{k}, t) + \varrho_f(\mathbf{k}, t) \; . \tag{3.63}$$

The total intermediate scattering function is then given by

$$\begin{aligned} N_e F^{\mathrm{tot}}(\mathbf{k}, t) &= \Big\langle \varrho_e(\mathbf{k}, t) \varrho_e(-\mathbf{k}, 0) \Big\rangle \\ &= \left\langle \left[\sum_{\alpha=1}^{K} \varrho_\alpha^b(\mathbf{k}, t) + \varrho_f(\mathbf{k}, t) \right] \left[\sum_{\beta=1}^{K} \varrho_\beta^b(-\mathbf{k}, 0) + \varrho_f(-\mathbf{k}, 0) \right] \right\rangle \\ &= \left\langle \sum_{\alpha=1}^{K} \varrho_\alpha^b(\mathbf{k}, t) \sum_{\beta=1}^{K} \varrho_\beta^b(-\mathbf{k}, 0) \right\rangle + \left\langle \sum_{\alpha=1}^{K} \varrho_\alpha^b(\mathbf{k}, t) \varrho_f(-\mathbf{k}, 0) \right\rangle \\ &\quad + \left\langle \varrho_f(\mathbf{k}, t) \sum_{\beta=1}^{K} \varrho_\beta^b(-\mathbf{k}, 0) \right\rangle + \Big\langle \varrho_f(\mathbf{k}, t) \varrho_f(-\mathbf{k}, 0) \Big\rangle \end{aligned}$$

The two terms describing correlations between bound and free electrons can be combined. Furthermore, the first contribution characterising the correlations between bound electrons has to be split depending on whether the same ion species is considered in both densities or if the electrons belong to different ion species. This yields

$$\begin{aligned} N_e F^{\mathrm{tot}}(\mathbf{k}, t) = &\underbrace{\left\langle \sum_{\substack{\alpha,\beta \\ \alpha=\beta}} \varrho_\alpha^b(\mathbf{k}, t) \varrho_\alpha^b(-\mathbf{k}, 0) \right\rangle}_{(1)} + \underbrace{\left\langle \sum_{\substack{\alpha,\beta \\ \alpha\neq\beta}} \varrho_\alpha^b(\mathbf{k}, t) \varrho_\beta^b(-\mathbf{k}, 0) \right\rangle}_{(2)} \\ &+ 2 \underbrace{\left\langle \sum_{\alpha} \varrho_\alpha^b(\mathbf{k}, t) \varrho_f(-\mathbf{k}, 0) \right\rangle}_{(3)} + \underbrace{\Big\langle \varrho_f(\mathbf{k}, t) \varrho_f(-\mathbf{k}, 0) \Big\rangle}_{(4)} \; . \end{aligned} \tag{3.64}$$

The different contributions reflect the various inter-particle correlations that can be

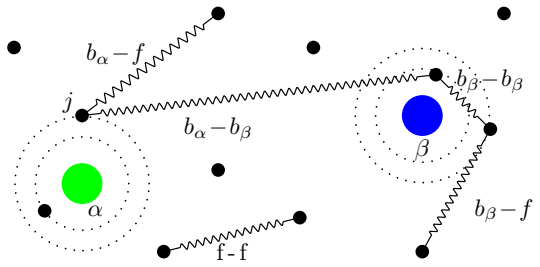

Figure 3.4: Schematic illustration of the inter-particle correlations in a plasma with two ion species, depicted as blue and green dots. The black dots mark the electrons classified as bound electrons moving around the ions and free electrons. The corrugated lines indicate the correlations, whereas the symbols $f - f$, $b_\alpha - f$ and $b_\alpha - b_\alpha$ stands for free-free, bound-free and bound-bound, respectively, where the index denotes the belongings of the bound electrons to the according ion species α.

observed in a multicomponent plasma (see Fig. 3.4), that is,

(1) correlations between electrons bound to the same ion species,

(2) correlations between electrons bound to different ion species,

(3) correlations between bound electrons and free electrons and

(4) correlations between free electrons.

If K different ion species are considered, then K^2 bound-bound terms (including (1) and (2)), K bound-free terms (3) and one free-free term (4) will be obtained.

Correlations between bound electrons

The first contribution of the intermediate scattering function (3.64), which describes the density correlations between bound electrons belonging to the same ion species, can be treated exactly like in the case for a single ion species. For generalisation, the sum over the ion species has to be taken to account for multiple elements in the system

$$\left\langle \sum_{\substack{\alpha,\beta \\ \alpha=\beta}} \varrho_\alpha^b(\mathbf{k},t)\varrho_\alpha^b(-\mathbf{k},0) \right\rangle = \sum_\alpha N_\alpha \left|f_\alpha(\mathbf{k})\right|^2 F_{\alpha\alpha}(\mathbf{k},t) + N_\alpha \left[Z_\alpha^b F_\alpha^{ce}(\mathbf{k},t) - \left|f_\alpha(\mathbf{k})\right|^2 \right] F_{\alpha\alpha}^{\mathrm{s}}(\mathbf{k},t)\ . \quad (3.65)$$

Here, N_α denotes the number of ions, f_α is the atomic/ionic form factor and Z_α^b is the number of electrons bound to ions of species labelled α. $F_{\alpha\alpha}(\mathbf{k},t)$ and $F_{\alpha\alpha}^{\mathrm{s}}(\mathbf{k},t)$ are the ion-ion intermediate scattering functions between ions of the same species and its self-part, whereas $F_\alpha^{ce}(\mathbf{k},t)$ characterises the correlations of the bound electrons within the ions of species α.

If bound electrons of different ion species are considered, which is the second part of Eq. (3.64), then no self-part occurs. The equation simplifies in this case to

$$\left\langle \sum_{\substack{\alpha,\beta \\ \alpha\neq\beta}} \varrho_\alpha^b(\mathbf{k},t)\varrho_\beta^b(-\mathbf{k},0) \right\rangle = \sum_{\alpha,\beta} \sqrt{N_\alpha N_\beta}\; f_\alpha(\mathbf{k}) f_\beta(\mathbf{k}) F_{\alpha\beta}(\mathbf{k},t)\;. \tag{3.66}$$

The partial ion-ion intermediate scattering function $F_{\alpha\beta}(\mathbf{k},t)$ describes the ensemble average between the microscopic ion density distributions ϱ_α^i and ϱ_β^i of the corresponding ion species α and β.

Correlations between free electrons

The result which describes the interaction between free electrons can be directly copied from the single ion approach (3.49), that is

$$\Big\langle \varrho_f(\mathbf{k},t)\varrho_f(-\mathbf{k},0) \Big\rangle = Z_f N_i F_{ee}(\mathbf{k},t)\;. \tag{3.67}$$

Here, $Z_f N_i = Z_f \sum_\alpha N_\alpha$ denotes the total number of free electrons in the system.

Correlations between bound and free electrons

The correlations of free electrons with bound electrons can be derived in the same manner as a single ion species and only need to be generalised by summing over all species considered in the system

$$\left\langle \sum_{\alpha} \varrho_\alpha^b(\mathbf{k},t)\varrho_f(-\mathbf{k},0) \right\rangle = \sum_{\alpha} \sqrt{N_\alpha}\sqrt{Z_f N_i}\; f_\alpha(\mathbf{k}) F_{e\alpha}(\mathbf{k},t)\;. \tag{3.68}$$

Here, the electron-ion intermediate scattering function, $F_{e\alpha}(\mathbf{k},t)$, is modulated with the form factor, $f_\alpha(\mathbf{k})$, of bound states of component α and the corresponding particle number, the free electrons, $Z_f N_i$, and the ions of the species α, N_α, respectively.

Total electronic structure factor in a multicomponent system

Finally, all contributions from above can be combined and a Fourier transformation with respect to time yields the total electron-electron structure factor

$$\begin{aligned} N_e^{\mathrm{tot}} S_{ee}^{\mathrm{tot}}(\mathbf{k},\omega) &= \sum_\alpha N_\alpha \left|f_\alpha(\mathbf{k})\right|^2 S_{\alpha\alpha}(\mathbf{k},\omega) + \sum_{\substack{\alpha,\beta \\ \alpha\neq\beta}} \sqrt{N_\alpha N_\beta} f_\alpha(\mathbf{k}) f_\beta(\mathbf{k}) S_{\alpha\beta}(\mathbf{k},\omega) \\ &\quad + \sum_\alpha \sqrt{N_\alpha}\sqrt{Z_f N_i} f_\alpha(\mathbf{k}) S_{e\alpha}(\mathbf{k},\omega) + \sum_\alpha Z_f N_i S_{ee}(\mathbf{k},\omega) \\ &\quad + \sum_\alpha N_\alpha Z_\alpha^b \int \mathrm{d}\omega'\, \tilde{S}_\alpha^{ce}(\mathbf{k},\omega-\omega') S_\alpha^s(\mathbf{k},\omega') \,. \end{aligned} \tag{3.69}$$

The first two terms can be merged. With the total electron number $N_e^{\mathrm{tot}} = \overline{Z_A} N_i$, where $\overline{Z_A}$ is the average atomic number, the structure factor is given by

$$\begin{aligned} \overline{Z_A} S_{ee}^{\mathrm{tot}}(\mathbf{k},\omega) &= \sum_{\alpha,\beta} \sqrt{x_\alpha x_\beta} f_\alpha(\mathbf{k}) f_\beta(\mathbf{k}) S_{\alpha\beta}(\mathbf{k},\omega) + \sum_\alpha \sqrt{Z_f x_\alpha} f_\alpha(\mathbf{k}) S_{e\alpha}(\mathbf{k},\omega) \\ &\quad + Z_f S_{ee}(\mathbf{k},\omega) + \sum_\alpha x_\alpha Z_\alpha^b \int \mathrm{d}\omega'\, \tilde{S}_\alpha^{ce}(\mathbf{k},\omega-\omega') S_\alpha^s(\mathbf{k},\omega') \,. \end{aligned} \tag{3.70}$$

Here, the concentrations $x_\alpha = n_\alpha / \sum_\alpha n_\alpha$ were introduced.

Again, both the electron-electron as well as the electron-ion structure factor contain ionic information as they include correlations between free electrons forming the screening cloud. To decouple the partial structure factor, the expression for the density response function (3.58) has to be considered in a more general way. Such a treatment leads to (see appendix A for a detailed calculation)

$$S_{ee}(\mathbf{k},\omega) = \sum_{\alpha,\beta} \frac{\sqrt{x_\alpha x_\beta}}{Z_f} q_\alpha(\mathbf{k}) q_\beta(\mathbf{k}) S_{\alpha\beta}(\mathbf{k},\omega) + S_{ee}^0(\mathbf{k},\omega) \,, \tag{3.71a}$$

$$S_{e\alpha}(\mathbf{k},\omega) = \sqrt{\frac{x_\alpha}{Z_f}}\, q_\alpha(\mathbf{k}) S_{\alpha\alpha}(\mathbf{k},\omega) + \sum_{\beta\neq\alpha} \sqrt{\frac{x_\beta}{Z_f}}\, q_\beta(\mathbf{k}) S_{\alpha\beta}(\mathbf{k},\omega) \,, \tag{3.71b}$$

where the generalised expression for the screening functions is defined as

$$q_\alpha(\mathbf{k}) = \frac{n_e C_{e\alpha}(\mathbf{k})\, \chi_e^0(\mathbf{k})}{1 - n_e C_{ee}(\mathbf{k}) \chi_e^0(\mathbf{k})} \,. \tag{3.72}$$

$C_{ea}(\mathbf{k})$ characterises the direct electron-ion correlation function describing the correlations between electrons and ions of species α. The electron-electron structure factor (3.71a) can be separated in an electron-ion correlation, determined by the structural

properties of the ions and the correlations of the free electrons to the ions contained in the screening function $q(k)$, and a contribution of a free electron gas describing the kinetically free electrons in the system. The free-bound structure factors (3.71b) can furthermore be described by the microscopic structure of the several ions in the system modulated by the screening function. It should be pointed out here, that the structure factors $S_{e\alpha}(\mathbf{k},\omega)$ are not only defined by microscopic properties of the ion species α, which is given by the first part of Eq. (3.71b). Moreover, they also contain structural information associated with the other ion species as the various ions may strongly interact. In appendix A, the equations are explicitly given for a system with two ion species as an example.

The final results can be summarized in the total electron-electron structure factor of a multicomponent system

$$\overline{Z_A} S_{ee}^{\mathrm{tot}}(\mathbf{k},\omega) = \sum_{\alpha,\beta} \sqrt{x_\alpha x_\beta}\,[f_\alpha(\mathbf{k}) + q_\alpha(\mathbf{k})]\,[f_\beta(\mathbf{k}) + q_\beta(\mathbf{k})]\,S_{\alpha\beta}(\mathbf{k},\omega) + Z_f S_{ee}^{0}(\mathbf{k},\omega) + \sum_{\alpha} x_\alpha Z_\alpha^b \int \mathrm{d}\omega'\; \tilde{S}_\alpha^{ce}(\mathbf{k},\omega-\omega') S_\alpha^s(\mathbf{k},\omega')\;. \quad (3.73)$$

This equation reflects again the three distinct features in the x-ray scattering signal. The first term describes quasi-elastic scattering of bound and screening electrons associated with different ion species. The second term contains the full dynamic response of the kinetically free electrons, whereas the contribution of the last term is from excitations or ionisations of bound electrons by the x-rays.

Expression (3.73) allows to analyse x-ray scattering experiments of strongly, coupled plasmas with multiple ion species. Therefore, it will be the central equation of this thesis. Due to the novel decomposition, all mutual correlations can be taken fully into account which opens the way to observe and study mixtures under extreme conditions. It contains the well-known result (3.62) derived by Chihara [Chihara, 1987, 2000] by setting $\alpha = \beta$. Moreover, it reduces to the approximate description of Gregori *et. al.* for weakly coupled systems described within RPA [Gregori et al., 2006].

3.3 Current experimental limitations

To generate the probe beam for the scattering experiment, laser-produced x-ray sources are applied. They allow for sufficiently high photon energies that can penetrate plasmas at solid densities and also have enough flexibility to adjust the wavenumber in angularly resolved measurements. Successfully tested experimental platforms are, e.g., titanium Ly-α, He-α and K-α lines [Glenzer et al., 2003a;

Kritcher et al., 2008], manganese He-α line [Lee et al., 2009], chlorine Ly-α line [Glenzer et al., 2007; García Saiz et al., 2008] and copper K-α line [Barbrel et al., 2009]. The bandwidth of these x-ray sources are narrow enough to observe collective oscillations of the electrons which arise as plasmon peaks shifted by around $20-60\,\mathrm{eV}$ from the elastic Rayleigh peak for solid densities [Urry et al., 2006]. In contrast, the collective oscillations of the ions appear in the vicinity of the ion plasma frequency ω^i_{Pl} or at even lower frequencies determined by the ion acoustic wave [Gregori and Gericke, 2009]. Thus, for the best case of a hydrogen plasma with solid density ($n_i = 5 \times 10^{22}\,\mathrm{cm}^{-3}$) the ion acoustic modes could be observed at an energy shift of around $\hbar\omega^i_{\mathrm{Pl}} \approx 0.2\,\mathrm{eV}$ in the scattering signal. This low frequency part cannot be resolved in current laser experiments and, hence, it is sufficient to treat the partial ion-ion structure factors in Eq. (3.73) statically, that is, $S_{\alpha\beta}(k,\omega) = S_{\alpha\beta}(k)\delta(\omega)$. Please note that, $S_{\alpha\beta}(k)$ is a frequency-integrated quantity. For this reason, the static ion structure will be discussed in detail in section 4. The future use of free electron lasers might allow for experimental access to the frequency scale relevant for $S_{\alpha\beta}(k,\omega)$. Then, the full dynamic response of the ions has to be included in the description.

The x-ray probe beam can also excite tightly bound electrons. This process contributes to the inelastic scattering of the x-rays [Issolah et al., 1991]. This scattering contribution is a Raman transition which occurs if the energy transfer during the scattering process is higher than the binding energy of the inner core electrons. Theoretically, it is described by the last term of Eq. (3.73). Here, $\tilde{S}^{ce}(k,\omega)$ accounts for the correlations between bound electrons and $S^s(k,\omega)$ represents the thermal motion of the ions. Approximations to calculate these quantities can be found in e.g. Refs. [Gregori et al., 2003; Sahoo et al., 2008].

For light elements, such as beryllium, the contribution is small compared to the inelastic Compton feature of the free electrons [Gregori et al., 2003]. As most materials investigated by current scattering experiments are low Z materials, this contribution will be neglected in the following. Furthermore, the main focus of this thesis is the elastic Rayleigh peak, which is not affected by the Raman transition as it contributes to the high-frequency part of the x-ray scattering signal.

Chapter 4

Static ion structure in warm dense matter

Structural properties in warm dense matter are of great importance for the analysis of the x-ray scattering signal as presented in the previous section. In particular, the elastic Rayleigh feature strongly depends on the microscopic arrangement of the ions. The nature of warm dense matter, that is, strongly coupled but fluid-like ions and partially degenerate electrons, makes the theoretical description challenging, as standard plasma or solid state theories, mainly based on perturbation theories, lose their applicability.

In the beginning of this chapter, several methods to determine the microscopic structure in WDM will be introduced. Mainly the integral equation approach from classical fluid theory will be described. The following section presents first results and highlights the characteristics in strongly coupled systems. Furthermore, the section will validate the different methods introduced in various plasma regimes mainly by comparisons with MD simulations. Effective quantum potentials will then be investigated which are derived to mimic quantum effects in the classical calculations [Wünsch et al., 2008a]. To discuss their applicability in WDM, a comparison with full quantum simulations (DFT-MD) will be presented. This also allows to study the effective ion-ion interaction in WDM. It will be shown that derivations from the screened Coulomb potential arise for partially ionised plasmas [Wünsch et al., 2009a]. In the final section, the effect of several ions species in more complex, composite plasmas will be discussed and the need of a full multicomponent treatment will be presented for strongly coupled systems.

4.1 Methods to determine the structural properties of classical particles

In the beginning, analytical expressions for the structural properties will be presented which are valid in weakly coupled systems, such as, high temperature plasmas with low densities. For denser and more strongly coupled systems, the rising correlations cannot be treated as a small perturbation. Thus, an integral equation derived in fluid theory will be introduced. The Ornstein-Zernike relation can, in principle, describe all mutual correlation in the system. However, a closure relation is required to solve the system. Here, the hypernetted-chain (HNC) and the mean spherical approximation (MSA) will be presented as useful closure relations for systems with long-range Coulomb interactions. A short introduction to simulations, in particular *ab initio* simulations, will be presented as further methods to study the microscopic structure in WDM. The latter one is the most accurate method, however, the high computational demand limits its applicability, making the integral equations a valuable everyday tool.

4.1.1 The limiting case of weakly coupled systems

In the limiting case of weakly coupled systems, approximate closure relations for the BBGKY hierarchy (2.32) can be found to determine analytical solutions for the reduced distribution function. In the case of the pair distribution function $g(r)$, the equation of motion in thermodynamic equilibrium is given by [Ichimaru, 2004a]

$$k_B T \frac{\partial g(r_{12})}{\partial \mathbf{r}_1} + g(r_{12}) \frac{\partial V_{12}(r_{12})}{\partial \mathbf{r}_1} = -n \int \mathrm{d}\mathbf{r}_3 \frac{\partial V_{13}(r_{13})}{\partial \mathbf{r}_3} F_{123}(r_{12}, r_{23}, r_{13}) \; . \tag{4.1}$$

Here, $g(r)$ is coupled with the reduced 3-particle distribution function F_{123}. The closure relation $F_{123} = 0$ which considers only binary interactions but neglects the surrounding medium, leads to

$$g(r) = \exp\left\{-\beta V_{12}(r)\right\} \; . \tag{4.2}$$

This approximation yields sufficient results for short range potentials and weakly coupled systems. However, in a plasma featuring the long-range Coulomb potential, this equation leads to non-physical behaviour as, for example, the potential energy calculated within this approximation diverges. In a plasma, screening effects play a crucial rule. To incorporate them in the description an improved closure relation for

F_{123} is required to account for the surrounding medium [Kremp et al., 1997]

$$F_{123} \simeq F_1 \cdot F_2 \cdot F_3 + F_1 g_{23} + F_2 g_{13} + F_3 g_{12} = 1 + g_{12} + g_{13} + g_{23} \; . \tag{4.3}$$

Such ansatz will give a sufficient approximation for the pair distribution function in the weakly coupled regime [Ichimaru, 2004b], namely

$$g(r) = \exp\left\{ \frac{-\beta q^2}{r} \exp\left(-\kappa_s r\right) \right\} = \exp\left\{ -\beta V^D(r) \right\} \; . \tag{4.4}$$

This expression was first derived by Debye and Hückel [Debye and Hückel, 1923]. Here, the Coulomb potential between two ions is linearly screened as the electrons are considered as a polarisable background, which is described by the Debye potential $V^D(r)$ (1.15). κ_s denotes the inverse screening length, which is defined over the Fermi integral for the electrons (1.10). For very weakly coupled systems, the exponential function can be expanded to

$$g(r) = 1 - \beta \frac{q^2}{r} \exp\left(-\kappa_s r\right) \; . \tag{4.5}$$

The static structure factor, defined by Eq. (2.49), for an isotropic system is then given by

$$\begin{aligned} S(k) &= 1 + \frac{4\pi}{k} n \int_0^\infty \mathrm{d}r \, r \sin\left(kr\right) [g(r) - 1] \; , \\ &= 1 - 4\pi\beta q^2 n \frac{1}{k} \frac{k}{k^2 + \kappa_s^2} \; , \\ S(k) &= \frac{k^2}{k^2 + \kappa_D^2} \; . \end{aligned} \tag{4.6}$$

In the last step, the definition of the inverse screening length in the classical limit, κ_D (1.12), was used.

Now, a two component system consisting of electrons and ions will be studied. To calculate the static ion structure factor in the weakly coupled limit, the ion-ion pair distribution (2.41) is required

$$g_{ii}(r) = 1 - \frac{\beta (Z_i e)^2}{r} \exp\left(-\kappa_D r\right) \; . \tag{4.7}$$

Moreover, the inverse screening length is now a sum over the particles, which is given

in the non-degenerate limit as

$$\kappa_D = \sqrt{\sum_a \kappa_a^2} = \sqrt{\sum_a \frac{4\pi n_a q_a^2}{k_B T}} \tag{4.8}$$

with $a = e, i$ characterising electron and ion properties, respectively. Similar to the calculation from the one-component system, the static ion-ion structure factor is given by [Kremp et al., 2005]

$$S_{ii}(k) = \frac{k^2 + \kappa_e^2}{k^2 + \kappa_e^2 + \kappa_i^2} \, . \tag{4.9}$$

As the ions in WDM can be treated as classical particles, the expression above describes the ionic system sufficiently as long as the inter-particle forces are weak.

4.1.2 Ornstein-Zernike relation

The weak-coupling approximations (4.4) or (4.5) fail for strongly coupled ions, where the correlations cannot be treated as a small perturbation to the thermal energy. To include higher-order correlations, an integral equation approach developed in fluid theory can be used. Here, a multicomponent version based on the well-known Ornstein-Zernike relation that connects the direct correlation function, c_{ab}, with the total correlation function $h_{ab} = g_{ab}(r) - 1$ is applied [Ornstein and Zernike, 1914; Hansen and McDonald, 1990; Kremp et al., 2005]

$$h_{ab}(\mathbf{r}) = c_{ab}(\mathbf{r}) + \sum_c n_c \int \mathrm{d}\mathbf{r}' c_{ac}(\mathbf{r}') \; h_{cb}(|\mathbf{r} - \mathbf{r}'|) \, . \tag{4.10}$$

The Ornstein-Zernike relation is an integral equation determining the total correlations between particles, which can be decomposed into a direct and an indirect contribution. The first part describes the direct correlations between two particles, represented by $c_{ab}(r)$. The second term in the Orstein-Zernike equation characterises the indirect influence of the medium via correlations to all components.

A Fourier transformation of the Ornstein-Zernike relation (4.10) leads to an algebraic expression that can be easily inverted

$$h_{ab}(\mathbf{k}) = c_{ab}(\mathbf{k}) + \sum_c n_c \, c_{ac}(\mathbf{k}) \, h_{cb}(\mathbf{k}) \, . \tag{4.11}$$

With the aid of the Ornstein-Zernike relation, the BBGKY-hierarchy (2.32) can be formally decoupled [Kremp et al., 2005; Schwarz et al., 2007]. It is an exact

expression defining the direct correlation function, $c(r)$, which requires, however, a second equation, the so-called closure relation, to determine both $h(r)$ and $c(r)$. Several approximations for such a closure relation were developed. Depending on the system considered, they can describe the structural and thermodynamic properties sufficiently well. In general, the Ornstein-Zernike equation must be solved numerically. However, a few closures were developed for simple model systems which can be solved analytically.

4.1.3 Mean spherical approximation (MSA)

One of the approximations, which allows for an analytical solution, is the mean spherical approximation (MSA) designed for systems with charged hard spheres [Hansen and McDonald, 1990]. The inter-ionic potential is here given by

$$V(r) = \begin{cases} \infty & \text{for } r < \sigma_c \\ V_{ii}(r) = \frac{Z_i^2 e^2}{r} & \text{for } r > \sigma_c \end{cases} \tag{4.12}$$

with the particle diameter, σ_c. In MSA, the radial distribution function and the direct correlation functions are set to

$$g_{ii}(r) = 0 \quad \text{for } r < \sigma_c \qquad \text{and} \qquad c_{ii}(r) = -\beta V_{ii}^C(r) \quad \text{for } r > \sigma_c \,. \tag{4.13}$$

Thus, this model considers the plasma ions as positively charged hard spheres with a diameter σ_c, that interact via Coulomb forces in a uniform, neutralising background of the electrons. For such a OCP-like model system, one can find an analytical solution [Palmer and Weeks, 1973; Singh and Holz, 1983]. The ion-ion structure factor is then given by the relation [Gregori et al., 2007]

$$S_{ii}^{\mathrm{OCP}}(k) = \frac{1}{1 - c_{ii}(k;\sigma_c)} \,, \tag{4.14}$$

where the direct correlation function is a functional of the cut-off parameter σ_c

$$\begin{aligned} c_{ii}(k;\sigma_c) = \frac{24\eta}{k^6} \Big\{ & y_0 k^3 \left(\sin k - k\cos k\right) + y_1 k^2 \left[2k\sin k - \left(q^2-2\right)\cos k - 2\right] \\ & + y_2 k \left[\left(3k^2-6\right)\sin k - \left(k^2-6\right) k\cos k\right] \\ & + y_3 \left[\left(4k^2-24\right) k\sin k - \left(k^4 - 12k^2 + 24\right)\cos k + 24\right] \\ & + \frac{y_4}{k^2} \left[6\left(k^4 - 20k^2 + 120\right) k\sin k \right. \\ & \left. - \left(k^6 - 30k^4 + 360k^2 - 720\right)\cos k - 720\right] - \gamma k^4 \cos k \Big\} \,, \end{aligned} \tag{4.15}$$

with

$$y_0 = -\frac{(1+2\eta)^2}{(1-\eta)^4} + \frac{h_0^2}{4(1-\eta)^2} - \frac{(1+\eta)\,h_0\chi}{12\eta} - \frac{\left(5+\eta^2\right)\chi^2}{60\eta}\,, \tag{4.16}$$

$$y_1 = 6\eta h_1^2\,, \tag{4.17}$$

$$y_2 = \frac{\chi^2}{6}\,, \tag{4.18}$$

$$y_3 = \frac{\eta}{2}\left(y_0 + \chi^2 h_2\right)\,, \tag{4.19}$$

$$y_4 = \frac{\eta\chi^2}{60}\,. \tag{4.20}$$

Further abbreviations are defined as

$$h_0 = \frac{1+2\eta}{1-\eta}\left[1 - \sqrt{1 + \frac{2(1-\eta)^3\chi}{(1+2\eta)^2}}\right]\,, \tag{4.21}$$

$$h_1 = \frac{h_0^2}{24\eta} - \frac{1+\frac{\eta}{2}}{(1-\eta)^2}\,, \tag{4.22}$$

$$h_2 = -\frac{1+\eta-\frac{\eta^2}{5}}{12\eta} - \frac{(1-\eta)\,h_0}{12\eta\chi}\,. \tag{4.23}$$

The model is fully determined by the following dimensionless parameters

$$\eta = \frac{\pi}{6} n_i \sigma_c^3\,, \qquad \gamma = \frac{Z^2 e^2}{\sigma_c k_B T} \qquad \text{and} \qquad \chi = \sqrt{24\eta\gamma}\,. \tag{4.24}$$

The particle diameter, σ_c, is the only free parameter in this model. It can either be obtained by the best fit in comparison with experimental results or by other considerations. A sensible approach is to request that the radial distribution function should be continuous at the hard-sphere boundary, which can be achieved by setting $h_1 = 0$ [Gillian, 1974]. This yields a conditional equation for the particle's diameter.

The upper solution must be modified if screening by the electrons should be incorporated in the MSA. To retain the analytical solution, one applies a weak empty-core pseudo-potential of the form $V_{ei}(k) = -(Ze^2/k^2)\cos(k\sigma_c/2)$ for the electron-ion interactions. This potential yields the screening function [Ashcroft, 1966; Gregori et al., 2007; Chaturvedi et al., 1981]

$$f(k) = \frac{\kappa_i^2}{k^2}\cos^2(k\sigma_c/2)\left[\frac{1}{\varepsilon(k)} - 1\right] = -\frac{\kappa_i^2}{k^2}\cos^2(k\sigma_c/2)\left[\frac{\kappa_e^2}{k^2+\kappa_e^2}\right]\,, \tag{4.25}$$

where κ_i and κ_e are the inverse ion and electron screening length (1.10), respectively.

$\varepsilon(k)$ characterises the static dielectric function of the electrons, which is given in the weakly coupled limit as $\varepsilon(k) = 1 + (\kappa_e^2/k^2)$.

The ion-ion structure factor for the screened ionic subsystem is then given by

$$S_{ii}(k) = \frac{S_{ii}^{\mathrm{OCP}}(k)}{1 + f(k) S_{ii}^{\mathrm{OCP}}(k)} \,. \tag{4.26}$$

To avoid any unphysical behaviour of $S_{ii}(k)$ and to ensure smooth electron wave functions, the electron-ion pseudo-potential, $V_{ei}(k)$, is usually truncated after the first node [Chaturvedi et al., 1981].

4.1.4 Hypernetted-chain approach (HNC)

A general closure relation for the Ornstein-Zernike relation can be determined by the diagrammatic method, which is a series expansion into powers of the density based on an idea of Mayer and Montroll [Mayer and Montroll, 1941]. Thereby, the various integrals can be expressed as diagrams which are sorted by different features [Hansen and McDonald, 1990]. A detailed analysis of the diagrammatic expansion of the pair distribution function was provided by [van Leeuwen et al., 1959] and is given by

$$g_{ab}(\mathbf{r}) = \exp\left[-\beta V_{ab}(\mathbf{r}) + N_{ab}(\mathbf{r}) + B_{ab}(\mathbf{r})\right] \,. \tag{4.27}$$

Here, $B_{ab}(r)$ expresses a special type of diagrams which are known as bridge diagrams. In the context of this method, the Ornstein-Zernike relation (4.10) is often written as

$$h_{ab}(\mathbf{r}) = c_{ab}(\mathbf{r}) + \sum_c n_c \int \mathrm{d}\mathbf{r}' c_{ac}(\mathbf{r}')\; h_{cb}(|\mathbf{r} - \mathbf{r}'|) = c_{ab}(\mathbf{r}) + N_{ab}(\mathbf{r}) \,, \tag{4.28}$$

where the nodal diagrams, $N_{ab}(r)$, characterise the contributions of the indirect correlations between the particles. This system of equations, that is, the closure equation and the Ornstein-Zernike relation, are an exact integral representation of the BBGKY hierarchy that fully determines the structure in classical systems. Unfortunately, the form of the bridge functions, $B_{ab}(r)$, is unknown and, therefore, different approximations have been applied.

The hypernetted-chain (HNC) approximation, which neglects the bridge diagrams ($B_{ab} = 0$), yields very good results for Coulomb-like systems [Baus and Hansen, 1980]. This closure relation is then given by

$$g_{ab}^{\mathrm{HNC}}(\mathbf{r}) = \exp\left[-\beta V_{ab}(\mathbf{r}) + N_{ab}(\mathbf{r})\right] \,. \tag{4.29}$$

For a single component system, the HNC equations, (4.28) and (4.29), can be solved by iteration going back and forth from real to Fourier space and vice versa. For systems with K components, the system of equations is more complex as $K(K+1)/2$ different correlation functions have to be considered. This number already accounts for the symmetry, $h_{ab} = h_{ba}$ and $c_{ab} = c_{ba}$, which follows from translational invariance. Therefore, it is convenient to express the Ornstein Zernike relation in the form of a matrix equation

$$\underline{\underline{\mathcal{H}}}(k) = \underline{\underline{\mathcal{C}}}(k) + \underline{\underline{\mathcal{D}}}\,\underline{\underline{\mathcal{C}}}(k)\,\underline{\underline{\mathcal{H}}}(k)\;, \tag{4.30}$$

whereby the matrices are defined as

$$\underline{\underline{\mathcal{H}}}(k) = \begin{pmatrix} h_{11}(k) & h_{12}(k) & \dots & h_{1b}(k) \\ h_{21}(k) & h_{22}(k) & \dots & h_{2b}(k) \\ \vdots & \vdots & \ddots & \vdots \\ h_{a1}(k) & h_{a2}(k) & \dots & h_{ab}(k) \end{pmatrix}, \; \underline{\underline{\mathcal{C}}}(k) = \begin{pmatrix} c_{11}(k) & c_{12}(k) & \dots & c_{1b}(k) \\ c_{21}(k) & c_{22}(k) & \dots & c_{2b}(k) \\ \vdots & \vdots & \ddots & \vdots \\ c_{a1}(k) & c_{a2}(k) & \dots & c_{ab}(k) \end{pmatrix}$$

with the density matrix $\underline{\underline{\mathcal{D}}} = \delta_{ab} n_a$. With these definitions, the following system of equations determines the HNC approximation for multicomponent systems

$$\underline{\underline{\mathcal{G}}}(r) = \underline{\underline{\mathcal{H}}}(r) - 1 = \left(\exp\left\{-\beta V_{ab}(r) + N_{ab}(r)\right\}\right)_{ab}\;, \tag{4.31a}$$

$$\underline{\underline{\mathcal{C}}}(r) = \underline{\underline{\mathcal{H}}}(r) - \underline{\underline{\mathcal{N}}}(r) \quad \text{or} \quad \underline{\underline{\mathcal{C}}}(k) = \underline{\underline{\mathcal{H}}}(k) - \underline{\underline{\mathcal{N}}}(k)\;, \tag{4.31b}$$

$$\underline{\underline{\mathcal{H}}}(k) = \left[\mathbb{1} - \underline{\underline{\mathcal{C}}}(k)\underline{\underline{\mathcal{D}}}\right]^{-1} \underline{\underline{\mathcal{C}}}(k)\;. \tag{4.31c}$$

These equations are the HNC closure relation, the definition of the nodal diagrams based on the Ornstein-Zernike relation and the Ornstein-Zernike equation itself, rearranged to express the total correlation function in Fourier space. To solve this set of equations, an iterative method can be used. As a start solution, the weakly coupled limit for the pair distribution function is applied, that is, $g^0_{ab}(r) = \exp\left(-\beta V_{ab}(r)\right)$, and the contributions from the nodal diagrams are set to zero. With Eq. (4.31c), an improved pair distribution can be calculated by applying a numerical matrix inversion for each k-value. The resulting matrix $\underline{\underline{\mathcal{C}}}(k)$ is then reassembled into functions $c_{ab}(k)$ and transformed back to real space. Here, the closure relation is used to calculate new total correlation functions, $h_{ab}(r)$. These newly obtained functions are now used as an improved form and the loop runs again until convergence is achieved.

To make the method reliable for Coulomb systems, further consideration are needed. The asymptotic behaviour for the pair distribution function and the total

correlation functions are

$$\lim_{r\to\infty} g(r) = 1 \implies \lim_{r\to\infty} h(r) = 0 \,, \tag{4.32}$$

which leads for Coulomb systems to a long range term for the nodal diagrams,

$$\lim_{r\to\infty} N(r) \sim V(r) \sim \frac{1}{r} \,. \tag{4.33}$$

This behaviour prohibits a direct numerical Fourier transformation. To overcome this problem, [Springer et al., 1973] defined the auxiliary short-range functions

$$N^s(r) = N(r) - \beta V^l(r) \,, \tag{4.34a}$$
$$c^s(r) = c(r) + \beta V^l(r) \,, \tag{4.34b}$$
$$V^s(r) = V(r) - V^l(r) \,, \tag{4.34c}$$

which allow a numerical Fourier transformation. The indices 'l' and 's' characterise the long-range and short-range functions, respectively. The long-range potential, $V^l(r)$, is defined in such a way that it has the same asymptotic behaviour as the Coulomb potential, whereas the short range potential $V^s(r)$ should only contribute for small distances. Examples of such potentials can be [Springer et al., 1973]

$$V^l(r) = \frac{q^2}{r}\left[1 - \exp(-\alpha r)\right] \,, \tag{4.35a}$$
$$V^s(r) = \frac{q^2}{r}\exp(-\alpha r) \,, \tag{4.35b}$$

where α is a free parameter defining the range of the short range function. These potentials also have the advantage of an analytical form in the Fourier space

$$V^l(k) = 4\pi q^2 \frac{\alpha^2}{k^2(k^2+\alpha^2)} \,. \tag{4.36}$$

The system of equations for the HNC approximation (4.31) is now modified by applying the short range defined functions above

$$\underline{\underline{\mathcal{G}}}(r) = \underline{\underline{\mathcal{H}}}(r) - 1 = \left(\exp\left\{-\beta V^s_{ij}(r) + N^s_{ab}(r)\right\}\right)_{ab} \,, \tag{4.37a}$$
$$\underline{\underline{\mathcal{C}}}^s(r) = \underline{\underline{\mathcal{H}}}(r) - \underline{\underline{\mathcal{N}}}^s(r) \,, \tag{4.37b}$$
$$\underline{\underline{\mathcal{H}}}(k) = \left[\mathbb{1} - \underline{\underline{\mathcal{C}}}(k)\underline{\underline{\mathcal{D}}}\right]^{-1} \underline{\underline{\mathcal{C}}}(k) \,. \tag{4.37c}$$

A flow diagram of the implemented iterative HNC process is shown in Fig. 4.1.

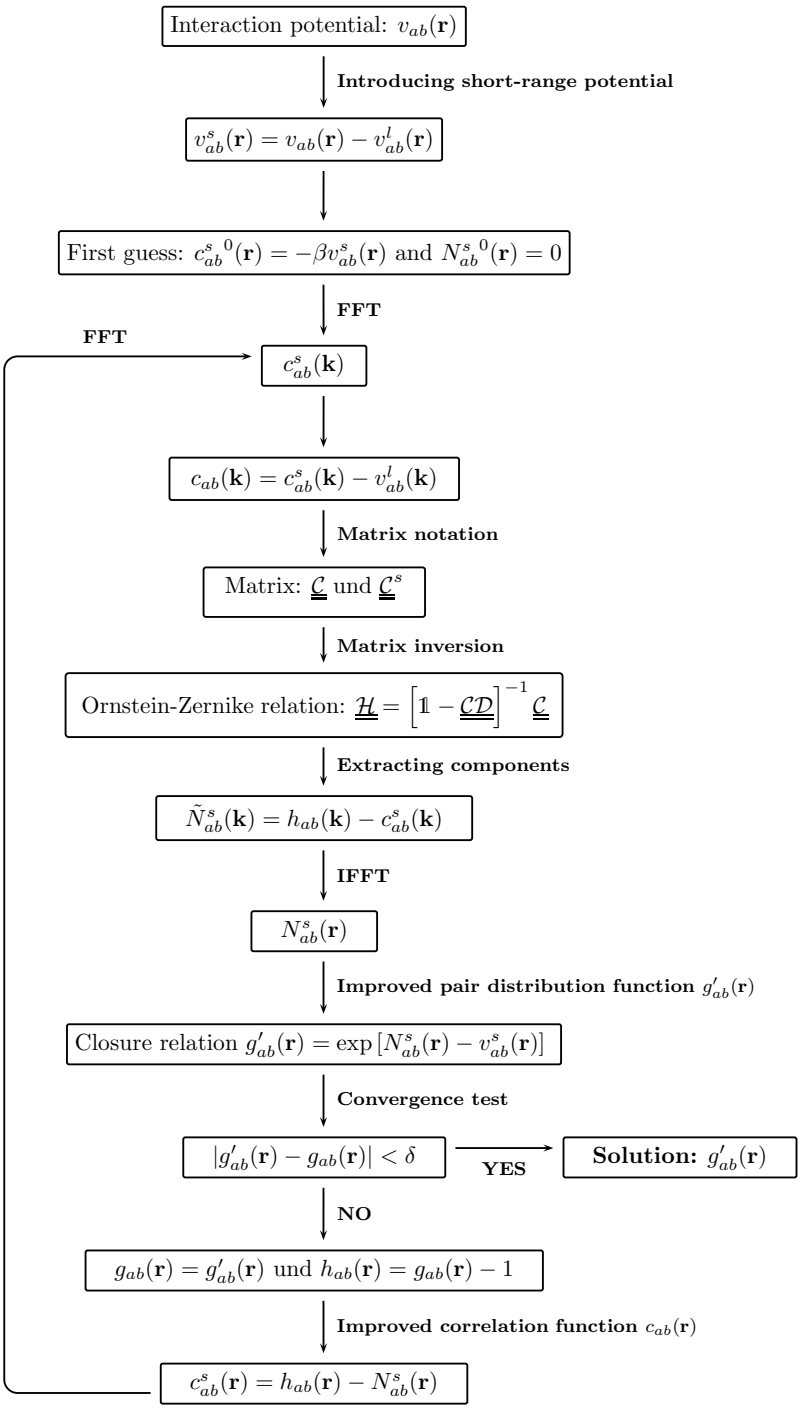

Figure 4.1: Flow diagram of the iterative HNC process.

For the transformations from real to Fourier space, a fast Fourier transformation (FFT) has been implemented. This tool, as well as the technique for the matrix inversion, was taken from the Numerical Recipes [Press et al., 1994].

The HNC method above is limited to within the convergence area of the iterative process, which is practical given by the coupling strength as expressed in the classical coupling parameter Γ (see Eq. (1.5)). For systems with purely repulsive forces, such as the ion components in a plasma, the full fluid region is accessible. In contrast, attractive electron-ion interactions pose a considerable problem which is mitigated by the use of weaker pseudo-potentials that are employed to mimic quantum effects in classical systems (see section 4.3). Such a treatment allows HNC solutions up to moderately coupled plasmas with $\Gamma_i \approx 1$.

4.1.5 Numerical simulation techniques

Numerical simulations, such as molecular dynamics (MD), can precisely predict the ionic structure in strongly coupled systems but require large numerical efforts [Hansen and McDonald, 1978, 1981]. With a given inter-particle potential, the MD method simulates the time dependent behaviour on a microscopic scale by solving the classical equation of motion in the force field considered [Fehske et al., 2008]. The simulations were used here to verify the accuracy of the HNC results since they intrinsically include all correlations, especially the bridge diagrams neglected in the HNC approach. All simulations were performed by Dr Zoltán Donkó from the Hungarian Academy of Sciences in Budapest. For each set-up, several thousand ions contained in a cubic volume with periodic boundary conditions were considered. When extracting the structural information, the average over many independent configurations was taken to reduce the numerical noise due to finite system size.

The accuracy of MD simulations strongly depends on the chosen interaction potential, which limits its capability in the WDM regime as the effective potential it not exactly known for such complex many-particle systems. An alternative way is the combination of electronic structure methods and MD simulations. Based on the Born-Oppenheimer approximation, the electron motion can be decoupled from the ion motion. This allows the calculation of the forces acting on the nuclei from a given electronic structure which can be directly used in the MD simulations. The electron configuration for a given ion arrangement is calculated, e.g., by density-functional theory. This method is know as *ab initio* MD simulations as the effective interaction potential is directly obtained from the electron configuration. Thus, no further approximations are required which made this method a powerful tool in many scientific areas [Marx and Hutter, 2005].

To calculate the electronic structure in the WDM regime, density functional theory (DFT) has proven to yield accurate results as it incorporates quantum effects as well as correlation effects between the electrons. The basic principle of DFT is the Hohenberg-Kohn theorem which proves that the physical system is completely determined by the ground state density [Hohenberg and Kohn, 1964]. With this "basic variable" all properties of the many-particle system can be written as a functional of the density, for example, the many-body wave function $\psi = \psi[n]$. The practical application of this fundamental theorem was dramatically improved by the Kohn-Sham ansatz, which connects the original interacting many-particle system with an auxiliary, non-interacting system by demanding that the ground state density is kept [Kohn and Sham, 1965]. The Hamiltonian of the auxiliary, non-interacting system is then given by (in atomic units) [Martin, 2004]

$$\hat{H}^{\sigma}_{\mathrm{KS}} = -\frac{1}{2}\nabla^2 + V^{\sigma}_{\mathrm{KS}}(\mathbf{r}) \; , \tag{4.38}$$

where $V^{\sigma}_{\mathrm{KS}}(\mathbf{r})$ characterises the effective potential of the Kohn-Sham system, which reproduces the exact ground state density of the original interaction system. This can be decomposed as

$$V^{\sigma}_{\mathrm{KS}}(\mathbf{r}) = V_{\mathrm{ext}}(\mathbf{r}) + V_{\mathrm{Hartree}}[n] + V^{\sigma}_{xc}[n] \; . \tag{4.39}$$

The first term describes the external potential due to the nuclei or any other external fields, the second contribution is the Hartree potential and the last term characterises the exchange-correlation potential. This approach is an exact description as long as the exchange-correlation potential, which contains all the many-body effects, is known. However, in most correlated systems this quantity is not known and must be approximated. Many studies have been made to find reasonable approximations for the exchange-correlation potential which leads to sufficient results for various systems. Some widely used approximations are the local density approximation (LDA) and the generalised gradient approximation (GGA) [Martin, 2004]. The first approach assumes that the exchange-correlation energy for each particle is equivalent to the energy of a homogeneous electron gas with the same density. This can be expanded to the more general local spin density approximation (LSDA). The GGA still approximates the exchange-correlation energy locally, but it takes the gradient of the density into account. This leads to improvements for many cases. With an approximate exchange-correlation potential, the Kohn-Sham equations can be solved in a self-consistent way: with an initial ground state density, the effective potential

(4.39) can be estimated. Then, the generalised Schrödinger equation [Martin, 2004]

$$\left[-\frac{1}{2}\nabla^2 + V_{\mathrm{KS}}^{\sigma}(\mathbf{r})\right]\psi_i^{\sigma}(\mathbf{r}) = \epsilon_i^{\sigma}\psi_i^{\sigma}(\mathbf{r}) \tag{4.40}$$

can be solved which leads to a new expression for the electron density. These newly obtained functions can be used as an improved guess until convergence is achieved.

The original DFT approach was derived for a pure ground state in the $T = 0$ limit, which is not applicable in the WDM regime. Here, temperature effects have to be included, which can be done based on the work of Mermin [Mermin, 1965], who expanded the Hohenberg-Kohn theorem to non-zero temperature systems.

R. Car and M. Parrinello combined later the electron structure calculation DFT with MD simulations [Car and Parrinello, 1985]. For an initial ionic structure, the electron configuration is calculated via DFT, which allows the determination of the interaction potentials required for the MD simulations. According to the forces, the ions are moved to a new configuration and the loop can start again. As for classical MD simulations, the system needs to reach thermodynamic equilibrium in the beginning of each run, before physical properties can be extracted.

All the DFT-MD simulations presented in this thesis were performed by J. Vorberger applying several packages, such as VASP [Blöchl, 1994; Kresse and Hafner, 1993, 1994a,b; Kresse and Furthmüller, 1996a,b; Kresse and Joubert, 1999; Perdew and Zunger, 1981; Perdew et al., 1992, 1993, 1996, 1997; Vanderbilt, 1990] and abinit [Gonze et al., 2002, 2005, 2009] which implement density functional theory and combine it with a MD solver for the ions. DFT-MD exactly meets the requirements to describe fully interacting quantum systems such as WDM, but it is a very computationally intensive method. Run times of DFT-MD simulations on high performance computers can easily exceed a couple of days, which limits their applicability as an analysis tool for experimental support. Here, DFT-MD simulations are mainly used to benchmark the HNC results and, thus, investigate the effective inter-particle potential in WDM.

4.2 First results for the ionic structure

After the introduction of the techniques to calculate the structural properties in a plasma, this section presents results for the pair distribution function or the structure factor. At the beginning, a system with only one ion species will be studied within two models: i) the one-component plasma (OCP) and the ii) the Yukawa model. In the first approximation the ions interact exclusively through the Coulomb potential

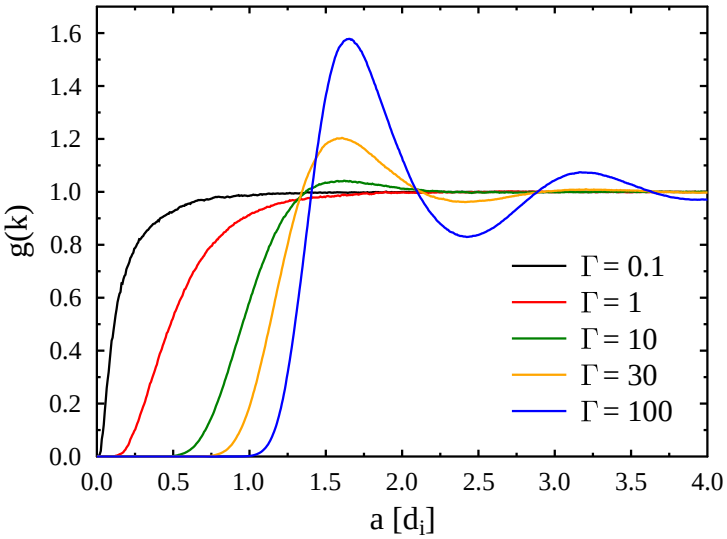

Figure 4.2: Radial pair distribution functions for a hydrogen plasma obtained by MD simulations applying the Yukawa model for different coupling strengths. The inverse screening length is set to $\kappa = 2\, d_i^{-1}$. (Courtesy of Dr. Z. Donkó).

whereas the electrons are considered as a uniform and structureless background to ensure the charge neutrality in the plasma. In the Yukawa model the electrons are described as a polarisable background resulting in a statically screened ion-ion Coulomb potential.

Figure 4.2 presents pair distribution functions in the Yukawa model obtained by MD simulations for a plasma at various coupling strengths. The inverse screening length is set to be $\kappa = 2\, d_i^{-1}$ where d_i denotes the mean inter-particle distance. The different curves illustrate the appearance of a short-range structure with increasing coupling strength characterised by the classical coupling parameter, Γ (1.5). For weakly coupled systems, that is, $\Gamma = 0.1$, the pair distribution function shows nearly a constant value of unity. This is the typical characteristics for uncorrelated systems such as an ideal gas. For small distances, the Coulomb interactions lead to a repulsion between the ions causing a decrease of the probability density. Thus, the pair distribution function goes to zero at the origin. For moderately coupled plasmas with $\Gamma \geq 1$, the correlation hole for small separations increases due to the rising interaction strength between the ions. For $\Gamma \geq 10$ the pair distribution functions exhibit oscillations which indicate the formation of a short-range structure in the plasma. With further increases of the coupling strength, the oscillations become more pronounced until maxima and minima are well formed to indicate high probabilities for next neighbours at these positions.

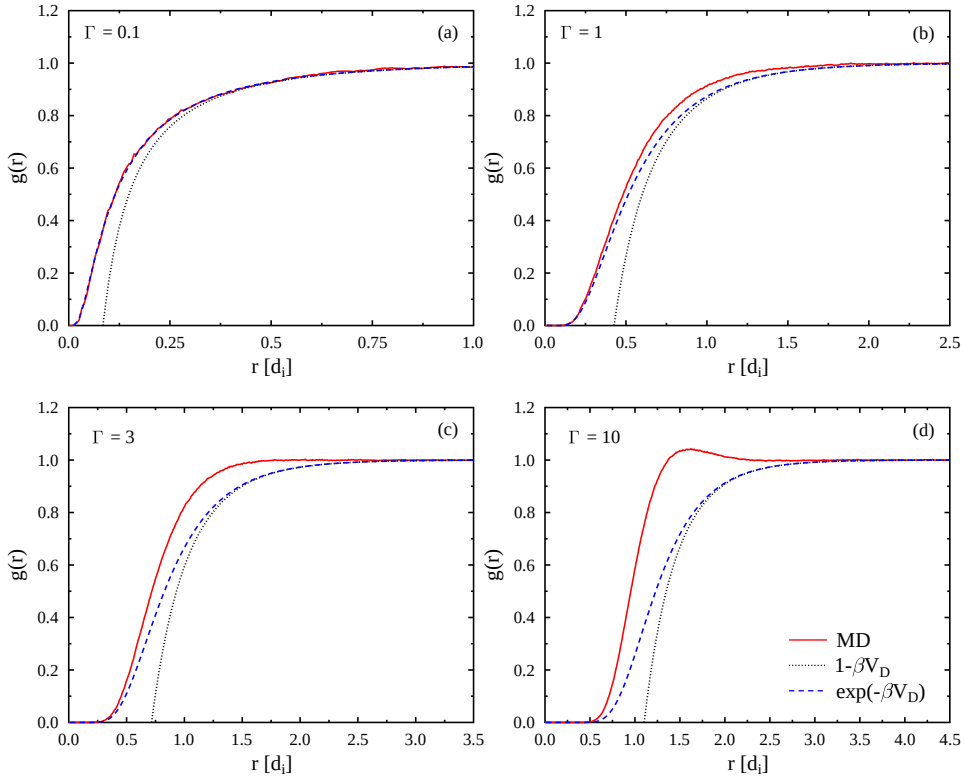

Figure 4.3: Pair distribution functions of a hydrogen plasma calculated in the Debye-Hückel limit (4.4) and its linear expansion (4.5) for different coupling strengths in comparison with results obtained by MD simulations to discuss the area of validation. Please note, the variations in the x-axis indicate the appearance of a short-range structure with the increase of the coupling strength.

In the following sections, the limits and accuracy of the techniques mentioned above to calculate the microscopic structure in a plasma will be discussed for different systems, mainly by comparisons with results from MD simulations.

4.2.1 Limit of the weak coupling theories

For weakly coupled plasmas, expressions for the radial distribution function can be derived analytically. To discuss the area of validity, these solutions will be compared with results obtained by MD simulations which accurately describe the microscopic structure. Fig. 4.3 presents the pair distribution functions for a hydrogen plasma with different coupling strengths: (a) a weakly coupled plasmas, i.e. $\Gamma = 0.1$, (b)-(c) moderately coupled plasmas, with $\Gamma = 1$ to 3, and (d) a strongly coupled plasma with $\Gamma = 10$. A screened Coulomb potential (1.15) is used as effective inter-particle

potential with a fixed inverse screening length of $\kappa = 2\, d_i^{-1}$. In addition to the results from the MD simulations, the pair distribution calculated in the Deby-Hückel limit (4.4) and its linear expansion (4.5) are plotted.

As expected, the analytical expressions for the pair distribution function are in very good agreement with the results from the simulations for weakly coupled systems with $\Gamma = 0.1$. The linear expansion of the Debye-Hückel expression (4.5), however, cannot describe the microscopic structure for small distances as it is only a linear approximation resulting in a divergent behaviour for $r \to 0$. Already for small, but finite, distances both approximations merge with the pair distribution function obtained by the MD simulation and thus, show the correct long-range behaviour.

For moderate coupling strength, shown in Fig. 4.3 (b), the analytical expressions still show the correct long-range behaviour of the pair distribution function. However, for small distances, the discrepancies between the models increase with higher coupling strength. Again, the linear expansion of the Debye-Hückel limit shows the divergent behaviour for $r \to 0$ but it still merges in the curves obtained by the simulations at larger distances.

For strongly coupled plasma with $\Gamma \geq 3$, the weak coupling theories present significant qualitative differences to the simulation results, which get more pronounced for $\Gamma = 10$ as seen in Fig. 4.3 (d). The radial distribution function, obtained by MD simulations, shows a steep slope for small distances with the appearance of a peak. In contrast, the weak coupling approximations cannot reproduce the formation of the short-range structure as they do not incorporate higher order inter-particle correlations. This yields a significant underestimation of the correlation strength.

In summary, the Debye-Hückel approximation can be used to characterise the structure of the plasma, up to moderate coupling strength with $\Gamma \lesssim 1$, whereas the linear expansion should only be applied for weakly coupled systems with $\Gamma \ll 1$.

4.2.2 The validation of the HNC method

Although MD simulations can accurately describe the structure in strongly coupled plasmas [Hansen and McDonald, 1978, 1981], the numerical effort limits its applicability as an efficient analysis tool. In contrast, the HNC approach is a much less computationally intensive method, which makes access to high performance computing facilities unnecessary. Furthermore, noisy results, due to a poor statistics in the simulations, are not an issue, as the method works in the thermodynamic limit.

To verify the accuracy of the HNC method and, in particular, to estimate the error due to the neglect of the bridge diagrams, Fig. 4.4 presents a comparison with MD simulation data for a fully ionised hydrogen plasma with various coupling

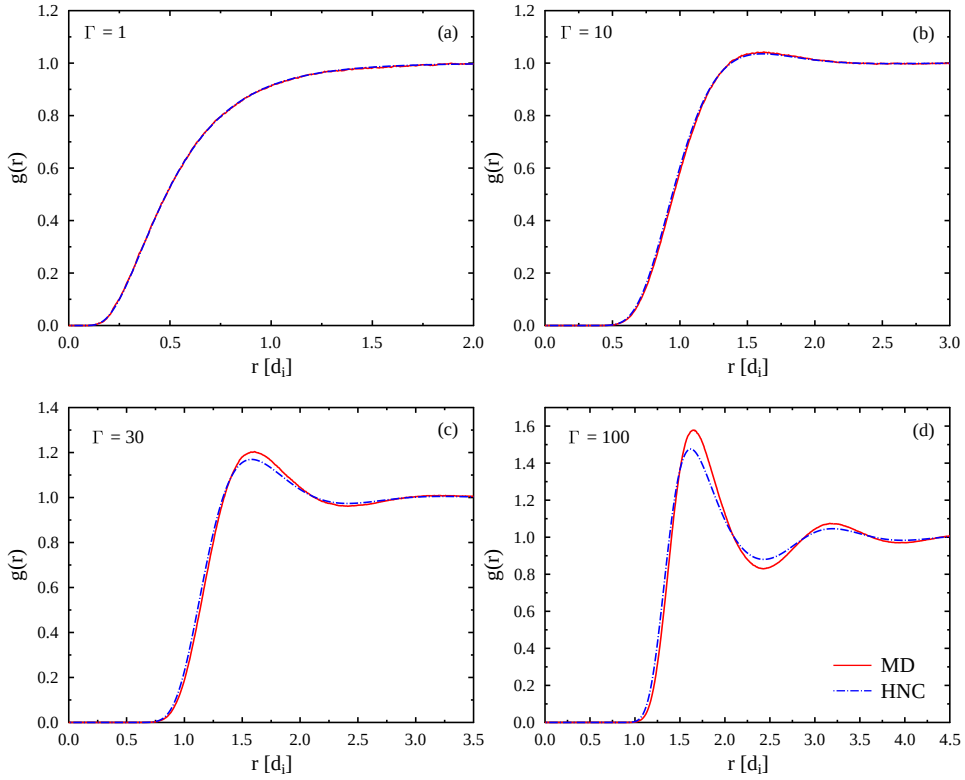

Figure 4.4: Comparison of HNC results with pair distribution functions obtained by MD simulation data for different coupling strengths of fully ionised hydrogen plasma. The effective interaction potential is a statically screened Coulomb potential with $\kappa = 2\,d_i^{-1}$. Please note, the variations in the x-axis indicate the appearance of a short-range structure with the increase of the coupling strength.

strengths. Again, the interaction potential is a statically screened Coulomb potential (1.15) with a fixed inverse screening length $\kappa = 2\,d_i^{-1}$. In a moderately coupled plasma, see figures 4.4 (a) and (b), the pair distribution functions obtained by the HNC approach are in an excellent agreement with the MD simulation data [Hansen and McDonald, 1981].

For a coupling strength of $\Gamma = 30$, small differences between HNC results and MD simulation data arise. These are caused by the fact that the correlations described by the bridge diagrams are neglected within the HNC approach. This leads to an underestimation of the coupling strength, which is well known for strongly coupled Coulomb systems [Baus and Hansen, 1980]. These differences become more pronounced for more strongly coupled systems, like that presented in the last panel of Fig. 4.4. To overcome this problem, several approximations for the Bridge diagrams

have been suggested. These models are often based on fits to simulation results [Iyetomi et al., 1992].

Nevertheless, the accuracy of the HNC method emphasises its applicability for the determination of the microscopic structure for a wide range of conditions, including strongly coupled plasmas. Moreover, this method can easily be expanded to treat multiple species, which hardly increases the numerical effort. This allows for the study of the influence of electrons or various ion species in the system. Consequently, the HNC method will be the main analysis tool for the study of the ionic structure in warm dense matter in this thesis.

4.2.3 Limits of the mean spherical approximation (MSA)

Another closure relation for the Ornstein Zernike equation (4.10) that has been used is the mean spherical approximation (MSA), which was derived for systems with hard core repulsions. Although it introduces further drastic approximations, it has the advantage of an analytical solution while the HNC approach relies on an iterative numerical treatment. In the following, a comparison of results obtained by MSA and HNC calculations will show under which conditions MSA can be used and when the HNC method must be applied.

MSA does not compute pair distribution functions, rather it calculates the structure factors directly. Therefore, static structure factors for systems of different coupling strengths, due to a variation in temperature, are compared in Fig. 4.5. The inverse screening length is calculated self-consistently for the temperatures given via the definition (1.10), applying the Fermi distribution to account for the partially degenerate electrons in warm dense matter. In the comparisons, the OCP and the Yukawa model, that is, a pure Coulomb and a screened Coulomb system, will be considered respectively.

In the OCP model, the structure factors from HNC and MSA calculations are in good agreement for all coupling strengths considered. The more approximated MSA gives slightly higher and shifted peaks. This documents that the extra cut-off in the MSA only has a minor effect on the ionic structure. Since direct classical simulations, such as MD, showed good agreement with HNC results, as shown in the last section, the MSA can be considered to be reasonably accurate for OCPs up to high coupling strengths.

The screening of the Coulomb interactions introduces new characteristics: the structure factors increase for small wave vectors, k, and the oscillations for larger k are damped due to the weaker interactions. In general, the structure is more affected by screening when calculated by the HNC equations than within the MSA

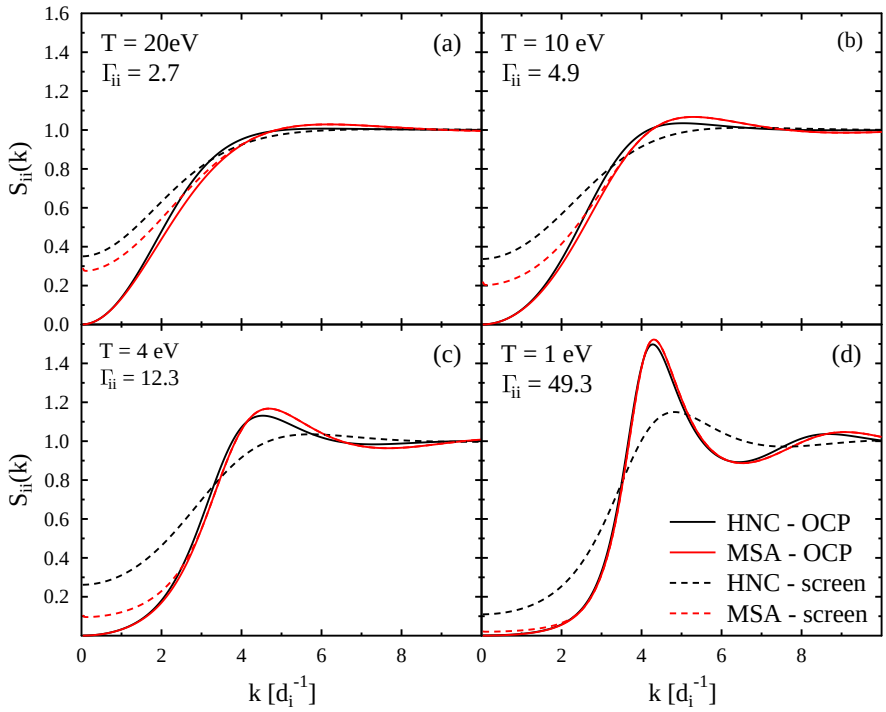

Figure 4.5: Static ion-ion structure factore $S_{ii}(k)$ for doubly charged ions with a density of $n_i = 1.5 \times 10^{23}\,\mathrm{cm}^{-3}$ at different temperatures obtained by MSA and HNC calculations. The effective ionic coupling strengths according to the plasma parameters are displayed in each figure by the classical coupling parameter, Γ_{ii}.

approach. These differences increase strongly with the coupling strength where the screening by the electrons becomes stronger as well. For the moderately coupled ions in Figs. 4.5(a) and (b), both approaches give similar results. On the other hand, the results shown in Figs. 4.5(c) and (d) display qualitative differences between the two approaches. This behaviour is connected to the way screening is treated within the MSA. Here, the highest wavenumber, where the structure factor is screened (first node in the electron-ion pseudo-potential), becomes smaller with coupling strength. In Figs. 4.5(c) and (d), this cut-off is already less than the first peak of the structure factor, $S_{ii}(k)$. Accordingly, the screened MSA coincides with the OCP result for most k values and spatial correlations are vastly overestimated.

These results show that MSA fails to incorporate the crucial effect of screening for plasmas with strongly coupled and screened ions in the entire wavenumber space. This effect occurs due to the early truncation of the screening function at very small k. Thus, the determination of the microscopic structure appling MSA should be limited to moderately coupled or weakly screened plasmas [Wünsch et al., 2009b].

4.3 Results for electron-ion systems

The HNC approach can describe the microscopic structure of classical plasmas in the strongly coupled regime. So far, the electrons were only considered implicitly via their effect on the ion-ion interaction within a linear screening model. To improve this description, and thus go beyond linear screening, the electrons can be included as a separate species in a multicomponent version of the HNC method which allows the treatment of electrons and ions on equal footing. However, quantum diffraction or exchange effects, that are intrinsic for the electrons, must be incorporated into the classical scheme. Several efforts were made in the past to integrate quantum effects approximately, mainly based on the use of effective quantum potentials which were designed to mimic the quantum behaviour in classical calculations.

Quantum diffraction effects must be incorporated in the system if the thermal de Broglie wavelength, $\lambda_{ee} = \hbar/(\sqrt{m_e k_B T})$ [Kraeft et al., 1986], of the electrons is of the magnitude of the inter-particle interaction characterised by the screening length.

Such potentials can be obtained by identifying the two-particle Slater sum with an auxiliary quantum potential in the classical partition function [Kraeft et al., 1986]. This procedure follows the original idea of Morita [Morita, 1959]. In the limiting case of weak degeneracy and small coupling strength, Kelbg and co-workers evaluated the sum with a perturbation theory for a Coulomb system and obtained [Kelbg, 1964b,a]

$$V_{ab}^{\mathrm{Kelbg}}(r) = \frac{q_a q_b}{r}\left[1 - \exp\left(-\frac{r^2}{\lambda_{ab}^2}\right) + \frac{\sqrt{\pi} r}{\lambda_{ab}}\left(1 - \Phi\left(\frac{r}{\lambda_{ab}}\right)\right)\right] . \tag{4.41}$$

$\Phi(x) = \frac{2}{\sqrt{\pi}} \int_0^x \mathrm{d}t \exp(-t^2)$ denotes the Gaussian error function. The Kelbg-potential neglects higher-order interactions and thus, is only applicable for weakly coupled systems with $\Gamma < 1$.

Another widely used quantum pseudo-potential was derived by Klimontovich und Kraeft [Klimontovich and Kraeft, 1974]. In the original work, a screened Coulomb system is studied. However, as HNC self-consistently incorporates screening effects within the species considered, the potential was modified to be used in multicomponent HNC calculations, which leads to [Schwarz et al., 2007]

$$V_{ei}^{\mathrm{KK}}(r) = -\frac{k_B T \xi_{ei}^2}{16}\left[1 + \frac{k_B T \xi_{ei}^2}{16 Z e^2} r\right]^{-1} , \tag{4.42}$$

where $\xi_{ei} = (Z e^2 \beta)/(\lambda_{ei})$. This form, however, was only derived for the electron-ion interaction.

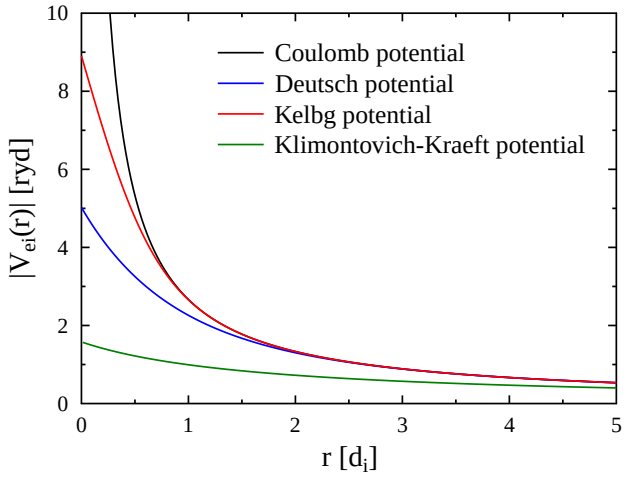

Figure 4.6: Comparison of the effective quantum potentials used with the classical Coulomb potential for a plasma with $T = 10^5\,\mathrm{K}$, $n_i = 1.23 \cdot 10^{23}\,\mathrm{cm}^{-3}$ and $Z = 2$.

A further effective quantum potential which describes quantum diffraction approximately was suggested by Deutsch [Deutsch, 1977]

$$V_{ab}^{\mathrm{Deutsch}}(r) = \frac{q_a q_b}{r}\left[1 - \exp\left(-\frac{r}{\lambda_{ab}}\right)\right] \quad . \tag{4.43}$$

This form simplifies the Kelbg-potential.

In Fig. 4.6, the potentials discussed are plotted for a plasma with $T = 10^5\,\mathrm{K}$, $n_i = 1.23{\cdot}10^{23}\,\mathrm{cm}^{-3}$ and $Z = 2$. The main difference between the quantum potentials and the classical Coulomb potential is the finite value at the origin. This fact is due to the Heisenberg uncertainty principle in the quantum mechanical description. Thus, the singularity of the Coulomb potential for $r \to 0$ is removed. The smallest value at the origin is obtained by the Klimontovich-Kraeft (KK) potential, that means, it generates a very weak electron-ion interaction. In contrast, the Kelbg potential leads to the strongest interaction between electrons and ions. For large distances, all effective potentials coincide with the Coulomb potential.

Radial distribution functions $g_{ei}(r)$ and $g_{ii}(r)$ and static structure factors $S_{ei}(k)$ and $S_{ii}(k)$ obtained by HNC calculations applying the different effective quantum potentials, defined above, are presented in Fig. 4.7 for a hydrogen plasma with density $n_i = 10^{22}\,\mathrm{cm}^{-3}$ and temperatures of $T = 4.5 \times 10^4\,\mathrm{K}$. As the Klimontovich-Kraeft potential is only defined for the electron-ion interaction, a Kelbg potential is used for the interaction between two electrons and a Coulomb potential for the ion interaction.

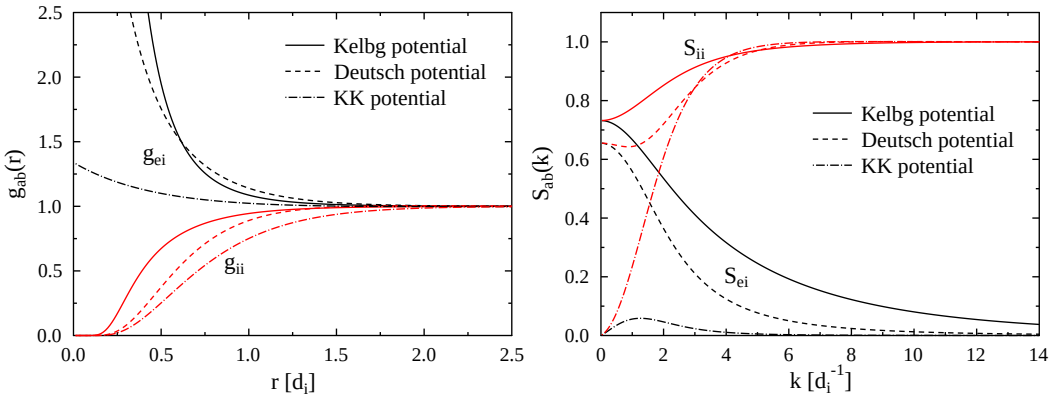

(a) pair distribution functions (b) static structure factors

Figure 4.7: Pair distribution functions and static structure factors for an electron-ion system obtained by HNC method applying various effective quantum potentials. The plasma parameters for the hydrogen system considered are $n_i = 10^{22}\,\mathrm{cm}^{-3}$ and $T = 4.5 \times 10^4\,\mathrm{K}$.

Due to the attractive interaction, the electron-ion pair distribution function, $g_{ei}(r)$ increases for values smaller then the mean particle distance, d_i. The slope here is directly related to the strength of the effective quantum potential applied. Therefore, the radial distribution function obtained by the HNC calculation applying the Kelbg potential presents the steepest rise, whereas the use of the Klimontovich-Kraeft potential yields only a gradual increase. The differences in the ion-ion pair distribution functions, $g_{ii}(r)$, are an indirect effect since, for the ions, quantum effects are negligible and, hence, the ion-ion potential is pure Coulomb. The Kelbg potential, which is characterised by a strong electron-ion interaction, leads to a strong shielding of the ions by the electrons resulting in a weak effective ion-ion interaction. This can be seen as the corresponding ion-ion distribution function shows a weak coupling behaviour with a small correlation hole. In contrast, the $g_{ii}(r)$ obtained by calculations using the Klimontovich-Kraeft potential shows the strongest coupling strength of all the curves presented. This is related to the weak electron-ion interaction which causes almost no screening between the ions due to the electrons.

The partial structure factors for this example are shown in Fig. 4.7 (b). Note that the structure factor, $S_{ei}(k)$, is defined as the Fourier transformation of $g_{ei}(r)$ without adding unity (see Eq. (2.48)). That leads to a decrease of the function in the limit, $\lim_{k\to\infty} S_{ei}(k) = 0$. The small k-behaviour of the ionic structure factor, $S_{ii}(k)$, gives an indication of the strength of the effective screening in the system considered. The $S_{ii}(k)$ obtained by HNC calculations using the Klimontovich-Kraeft potential

nearly goes to zero at the origin, which is a typical OCP-like behaviour, that is, there is effectively no screening. In contrast, the magnitude of the ion-ion structure factor at the origin, $S_{ii}(k = 0)$, has the highest value for the calculation using the Kelbg potential. This consistently indicates that the Kelbg potential yields the strongest screening between the ions of the quantum potentials considered.

In summary, the effects of the various quantum potentials on the predicted partial pair distribution and structure factors yield significant differences for small distances, r, or wavenumbers k, in warm dense matter. To study the effective inter-particle potential, comparisons with either experimental results or full quantum simulations are necessary. The experimental access to the microscopic structure in warm dense matter is still a challenging task as it relies on the theoretical models of the material under consideration. As the different quantum potentials yield very different results, and are known to be applicable in a small parameter regime only, we have to conclude that these calculations have small predictive value [Wünsch et al., 2008a]. In contrast, *ab initio* simulations, such as density functional molecular dynamics (DFT-MD), aim to describe fully interacting quantum systems.

4.4 Comparison with quantum simulations

Density functional molecular dynamics (DFT-MD) (see section 4.1.5) describe the strong correlations of the ions as well as the degeneracy of the electrons in a consistent way. As it is an *ab initio* simulation, it uses Coulomb forces modified for technical applicability only. It self-consistently calculates the effective inter-particle forces from electronic structure methods. This treatment meets the requirements of warm dense matter exactly, but such simulations demand high computing power.

By benchmarking the results of the HNC approach against DFT-MD data, the effective inter-particle potential within the system can be investigated [Schwarz et al., 2010]. In particular, the applicability of the effective quantum potentials, introduced in the previous section, can be studied. Once the effective interaction is understood, the ionic structure in WDM can be determined very efficiently by the HNC approach.

Fig. 4.8 presents ionic radial distribution functions obtained by HNC and DFT-MD simulations for warm dense beryllium under several compression levels changing its density. The temperature and the ion charge state for the HNC runs are set to $T = 13\,\mathrm{eV}$ and $Z = 2$ which gives plasma parameters similar to recently performed scattering experiments on beryllium [Glenzer et al., 2003a, 2007; Lee et al., 2009].

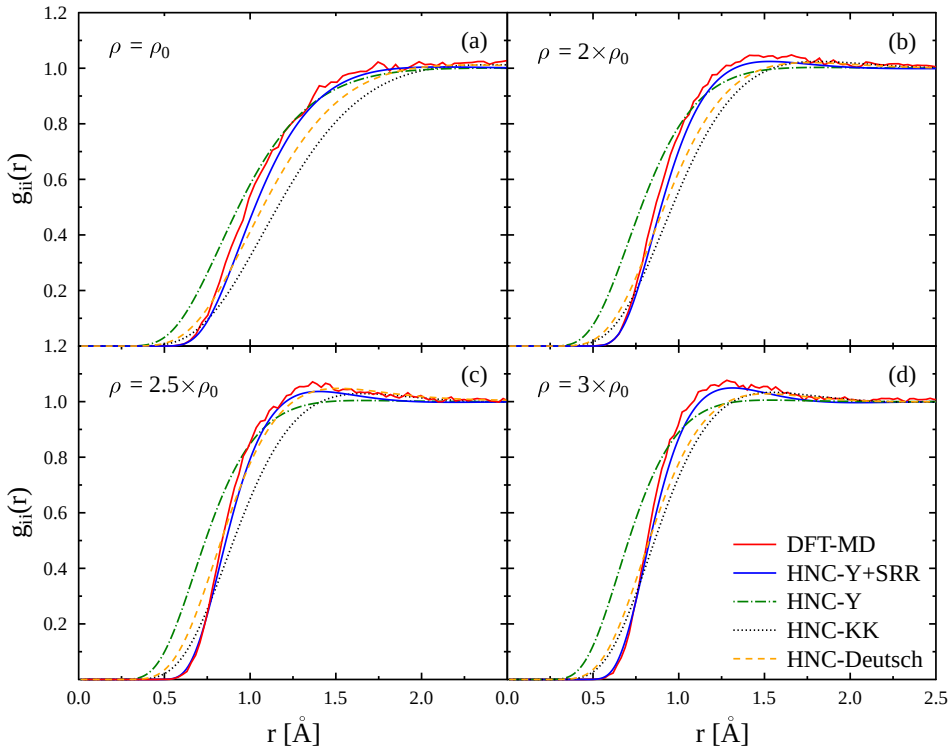

Figure 4.8: Ion-ion pair distribution functions for warm dense beryllium with different densities obtained by HNC calculations applying different effective interaction potentials and DFT-MD simulations. The normal solid density is ϱ_0 =1.848 g/cm^3, temperature is $T = 13\,\mathrm{eV}$ and the ion charge is $Z = 2$.

The HNC calculation applying the Klimontovich-Kraeft potential uses the Kelbg potential between the electrons and the Coulomb potential between the ions as the Klimontovich-Kraeft potential can describe only the electron-ion interactions. It can be seen, that the results from the two-component HNC method using effective quantum potentials lead to pair distributions that rise less sharply than the data obtained by the DFT-MD simulations. Furthermore, the pair distribution function, $g_{ii}(r)$, are shifted to the right. This is the typical behaviour for too strongly coupled ions or, equivalently, less effectively screened ions. As already discussed in the previous section, the quantum potentials, in particular the Klimontovich-Kraeft potential, generate weak electron-ion interactions, yielding almost OCP-like result where no screening is incorporated.

In contrast, the model which considers only ions via linearly screened Coulomb forces, that is, the Yukawa model (labelled HNC-Y), works rather well when com-

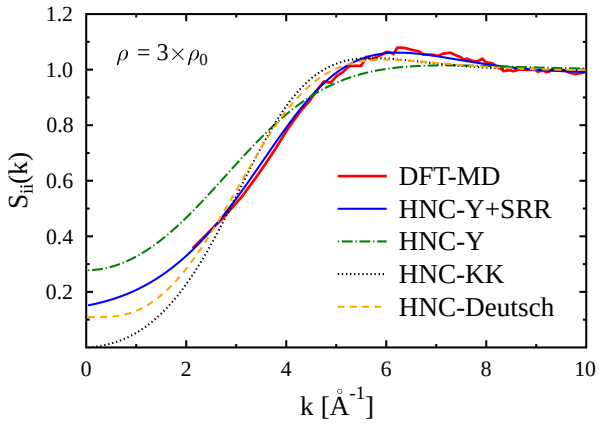

Figure 4.9: Ion-ion static structure factor for threefold compressed warm dense beryllium obtained by HNC calculations applying different effective interaction potentials and DFT-MD simulations. The plasma conditions are the same as in Fig. 4.8 (d).

paring its outcome to the DFT-MD data for lower densities. As it can be seen in Fig. 4.8 (a), the large distance behaviour as well as the shoulder of the pair distribution function is well described. With the increase of the density, however, the Yukawa model seems to underestimated the coupling for smaller distances, as it cannot reproduce the rising peak. Nevertheless, the results from the comparison indicates that screening can be considered to be linear for larger distances.

The underestimation of the small r behaviour can be understood by considering the electronic configuration of warm beryllium: with the degree of ionisation $Z = 2$, the beryllium ions still have an intact $1s^2$ shell. In simple terms, the wave functions of the core electrons are not allowed to overlap due to the Pauli exclusion principle. Therefore, an additional repulsion force occurs for distances smaller than the binding radius of the $1s$ states. This effect can be modelled by an additional short-range repulsion (SRR) term added to the Debye potential. We suggested a Lennard-Jones-like structure of the form [Wünsch et al., 2009a]

$$V_{ij}^{Y+SRR}(r) = \left(\frac{a}{r}\right)^4 + \frac{Z_i Z_j e^2}{r} \exp\left(-\kappa r\right) . \tag{4.44}$$

A fit to the potential directly extracted from the DFT-MD simulations yields the power of the SRR contribution. The parameter, a, is a fit parameter to match the HNC results to the DFT-MD data. It defines the strength of the short-range repulsion and stays constant for the same material under conditions where the charge state does not change.

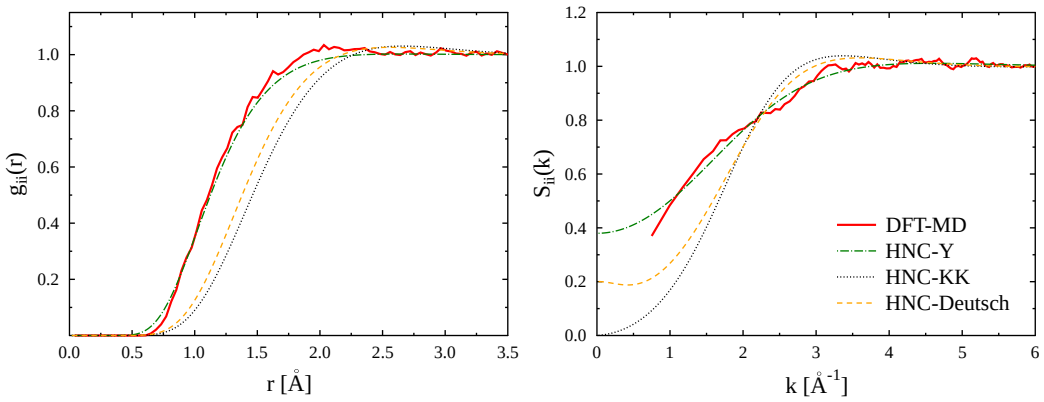

(a) pair distribution functions (b) static structure factors

Figure 4.10: Pair distribution functions and static structure factors for the ions in a lithium plasma obtained by HNC calculations applying different effective interaction potentials and DFT-MD simulations. The plasma parameters are given by $T = 5\,\mathrm{eV}$, $\varrho = 0.85\,\mathrm{g/cm^3}$ and $Z = 1.6$.

Applying the modified Debye potential (4.44) in the HNC approach (labelled HNC-Y+SRR) yields $g(r)$'s with a larger correlation hole and a steeper rise at small distances. In particular, for the highly compressed beryllium in Fig. 4.8 (d), the additional repulsion is sufficient to reproduce the correct inter-particle spacing and, thus, a pair distribution function which is now in very good agreement with results from DFT-MD simulations.

In Fig. 4.9, the static ion-ion structure factor for beryllium with three-times the solid density, that is, the case from Fig. 4.8(d), is displayed. The data from the DFT-MD simulations cannot describe the very small k-behaviour as the simulations are restricted to k values larger then $2\pi/L$, where L characterises the length of the simulation box. Therefore, HNC calculations are a valuable method if the effective ionic interaction is understood as they can predict the small wavelength behaviour.

The Klimontovich-Kraeft potential used in the HNC method leads a OCP-like behaviour as already described, that is, $S_{ii}(k = 0) \approx 0$. Similarly, the application of the Deutsch potential in the HNC calculations yields a structure factor with a small value at the origin. As for the pair distribution function, the best agreement with the DFT-MD data can be achieved by the use of the Debye potential with an additional short-range repulsion (labelled HNC-Y+SRR).

Fig. 4.10 shows the predicted microscopic structure of warm dense lithium obtained by DFT-MD simulations and HNC calculations applying various inter-particle potentials. The plasma parameters are $\varrho = 0.85\,\mathrm{g/cm^3}$, $T = 5\,\mathrm{eV}$ and $Z = 1.6$. These were taken from recent scattering experiment on shock compressed

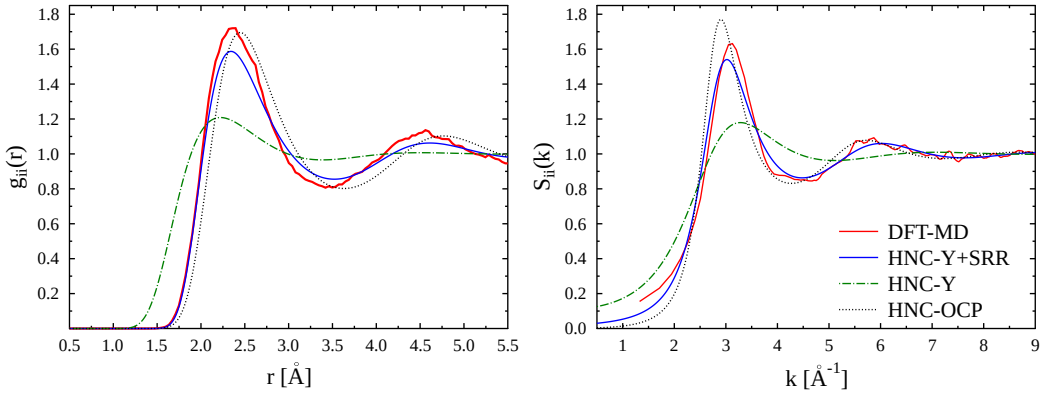

(a) pair distribution functions (b) static structure factors

Figure 4.11: Pair distribution functions and static structure factors for the ions in an aluminium plasma obtained by HNC calculations applying different effective interaction potentials and DFT-MD simulations. The plasma parameters are given by $T = 1.1\,\mathrm{eV}$, $\varrho = 3.4\,\mathrm{g/cm^3}$ and $Z = 3$.

matter [García Saiz et al., 2008]. Once more, the HNC results applying the quantum potentials, namely, the Klimontovich-Kraeft potential and the Deutsch potential, yield distribution functions and structure factors which are too strongly coupled. Thus, these potentials fail to describe the effective screening in warm dense lithium correctly. In contrast, the HNC approach with the Debye interaction leads to results that are in very good agreement to the simulation data. Here, a modification of the Debye potential with an additional short-range repulsion is not required as the lithium ions do not have an intact inner $1s^2$ shell for the charge state considered.

As a last example, warm dense aluminium is considered for plasma parameters $\varrho = 3.4\,\mathrm{g/cm^3}$, $T = 1.1\,\mathrm{eV}$ and $Z = 3$. The corresponding pair distribution functions and static structure factors for the ions are presented in Fig. 4.11. The DFT-MD simulation leads to a pair distribution function with well-pronounced maxima and a large correlation hole which is a typical behaviour for strongly coupled systems expected under the plasma parameter considered. A similar shape, however slightly shifted to the right, is obtained by HNC calculations when unscreened Coulomb interactions are applied between the ions (labelled HNC-OCP).

The negligence of screening effects in the OCP model systems seems, however, physically questionable. Thus, HNC calculations were performed for the Yukawa model to account for linear screening. The resulting pair distribution strongly underestimates the correlations in warm dense aluminium when being compared to DFT-MD data. However, so far the effects of the inner shells of the aluminium ions were neglected. These bound electrons lead, in the same way as discussed for

the beryllium plasma, to an additional repulsion for small distances. After taking the SRR contribution (4.44) into account, the ion-ion pair distribution functions, obtained by the HNC approach, also show the typical characteristics of strongly coupled systems and agree well with the simulation data. Thus, core electrons in warm dense aluminium influence the ionic structure by raising correlations for small distances if the inter-particle distance is comparable to the bound state radius.

In summary, the comparisons presented here lead to two main conclusions: Firstly, the quantum potentials, which mimic quantum effects in classical methods like HNC, exceed their applicability in the warm dense matter region. They strongly underestimate the effective screening in the system due to a weak electron-ion interaction. This effect then leads to too strongly coupled ions. Secondly, the ionic structure in WDM can be described by a simple linearly screened Coulomb potential. If partially ionised ions are considered, an additional short range repulsion due to the forbidden overlap of the wave functions of bound electrons has to be incorporated in the description. An easy algebraic expression is capable to mimicking this effect and, thus, allows the application of the HNC approach to efficiently calculate the microscopic structure in warm dense matter.

4.5 Extension to multiple ion species

So far, the microscopic structure of simple materials, that is, plasmas with a single ion species, has been considered. However, most materials in nature consist of ions in different charge states or with multiple chemical elements. Accordingly, the partial ionic structure factors are required (see Eq. (3.73)) to account for all mutual correlations and to allow for an interpretation of the x-ray scattering signal in mixtures or composite materials.

The HNC approach can be used to study multicomponent effects as all the various ion species can be included as further components in the generalised multicomponent version. Fig. 4.12 shows the microscopic ionic structure of a strongly coupled CH plasma obtained by a two-component HNC calculation. Here, hydrogen is fully ionised and the carbon ions are fourfold charged. Both were taken as separate components. The densities of hydrogen and carbon ions are $n_H = n_C = 2.5 \times 10^{23}\,\mathrm{cm}^{-3}$ and the temperature is set to be $T = 2 \times 10^4\,\mathrm{K}$. As a comparison, the results from a further HNC run for an isolated hydrogen plasma under the same conditions are plotted in the figure as a green dashed line.

All three partial pair distribution functions show the typical behaviour of a strongly coupled system: a correlation hole, a sharp rise and well-pronounced

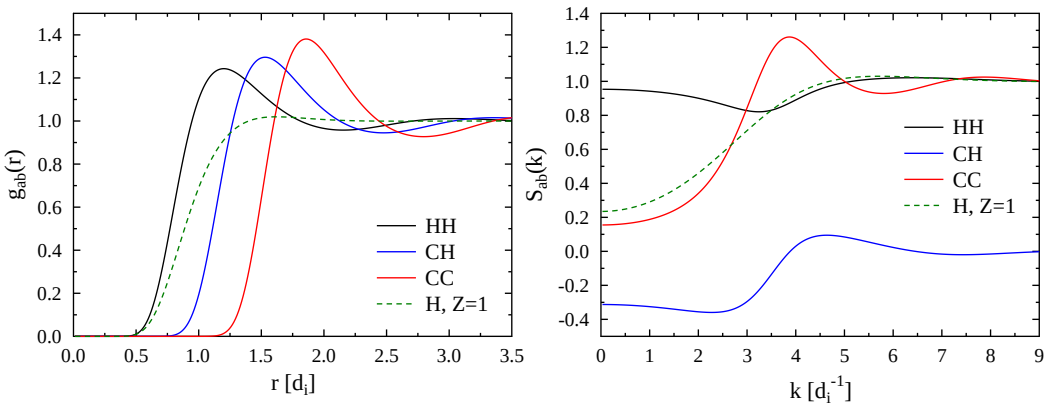

(a) partial pair distribution functions (b) partial static structure factors

Figure 4.12: Partial pair distribution functions and partial static structure factors for ions in a CH plasma obtained by HNC calculations. The plasma parameters are given by $T = 2 \times 10^4\,\mathrm{K}$ and $n_H = n_C = 2.5 \times 10^{23}\,\mathrm{cm}^{-3}$ whereas the hydrogen and carbon ions are fully and fourfold ionised, respectively. The dashed line, labelled "$H, Z = 1$", shows results for an isolated hydrogen plasma under the same conditions.

oscillations indicating the occurrence of a short-range structure in the system. As the carbon ions are fourfold ionised, the carbon-carbon coupling is the strongest, yielding a pair distribution function and a structure factor with the most pronounced maxima. In contrast, the pair distribution function obtained by the one-component HNC calculation of isolated hydrogen plasma presents only a moderately coupled system with a monotonically rising function without further oscillations. Thus, the comparison in Fig. 4.12 shows that the highly charged carbon ions imprint their structure onto the proton subsystem in the CH mixture. These results illustrate the requirement for a full multicomponent description as such an effect cannot be described by a single-ion approach, using an average state of the system.

The partial structure factors, shown in Fig. 4.12 (b), illustrate the highly non-linear coupling of the carbon ions in the mixture as well. Whereas the large k-behaviour of the hydrogen structure factor obtained by a single-ion approach is in agreement with the data from the multicomponent version, the small k characteristics presents qualitative differences. The screening of the hydrogen ions due to the carbon ions modifies the long-range part of the proton-proton potential yielding an increase of the hydrogen-hydrogen structure factor, $S_{HH}(k)$, for small wavenumbers. The partial structure factor, $S_{CH}(k)$, between protons and carbon ions presents the typical characteristic with the large k limit of zero. Due to the definition of the partial structure factors (see Eq. (2.48)), negative values for small k can occur for the cross terms showing the repulsive correlations.

As the HNC approach self-consistently includes the screening contributions of all species considered, all mutual correlations can be described within the system. This is significant as highly charged ions imprint their structure onto the subsystem of the ions with lower charge states. The generalisation of the HNC approach to multiple ion species is theoretically unlimited. The only practical restriction might come from run time issues which will be significant for a large number of species ($K \gtrsim 100$).

Although a full multicomponent description is required, present theoretical descriptions of the microscopic structure in complex systems often rely on an approximate treatment based on a one component system via relation [Gregori et al., 2006]

$$S_{\alpha\beta}(k) = \delta_{\alpha\beta} + \frac{\sqrt{n_\alpha n_\beta}}{n} \frac{Z_\alpha Z_\beta}{Z_f^2} \left[S_{ii}^{\mathrm{1comp}}(k) - 1 \right] . \tag{4.45}$$

$S_{ii}^{\mathrm{1comp}}(k)$ characterises the single-ion structure factor calculated for an average state of $Z_f = \sum_\alpha n_\alpha Z_\alpha / \sum_\alpha n_\alpha$. The expression (4.45) is exact in the limit of weakly coupled systems where the random phase approximation is valid.

Most x-ray scattering experiments are nowadays performed in moderately to strongly coupled systems. Therefore, the approximation (4.45) should be validated by comparisons with results from full multicomponent calculations. Such a comparison can be found in Fig. 4.13 where a CH plasma is considered again. The different temperatures generate moderately coupled (Fig. 4.13 (a)) and strongly coupled (Fig. 4.13 (b)) systems. The effective inter-ionic potential used here is a linearly screened Coulomb potential. The dashed lines are the partial structure factors obtained by relation (4.45) after a single-ion HNC calculation was performed for the system with an average ion charge state of $Z_f = 2.5$. In contrast, the solid lines illustrate the outcome from the multicomponent HNC calculations.

In the moderately coupled system, that is Fig. 4.13 (a), differences can be observed in the carbon-carbon structure factor, $S_{CC}(k)$, only. Here, the function is shifted down and to the right. For small k values, the partial structure factor obtained by the approximation is negative, which is an unphysical behaviour. This effect gets more pronounced for the strongly coupled case presented in Fig. 4.13 (b). Furthermore, the position of the peak is significantly shifted to the right. For strong coupling, the hydrogen-hydrogen structure factor presents qualitative differences as well. Whereas the structure factor obtained by the multicomponent approach has a minimum, the approximate treatment predicts a maximum. These differences occur as the intrinsic mutual correlations in the complex CH plasma cannot be described by the relation (4.45). Again, this approach being based on the one-component

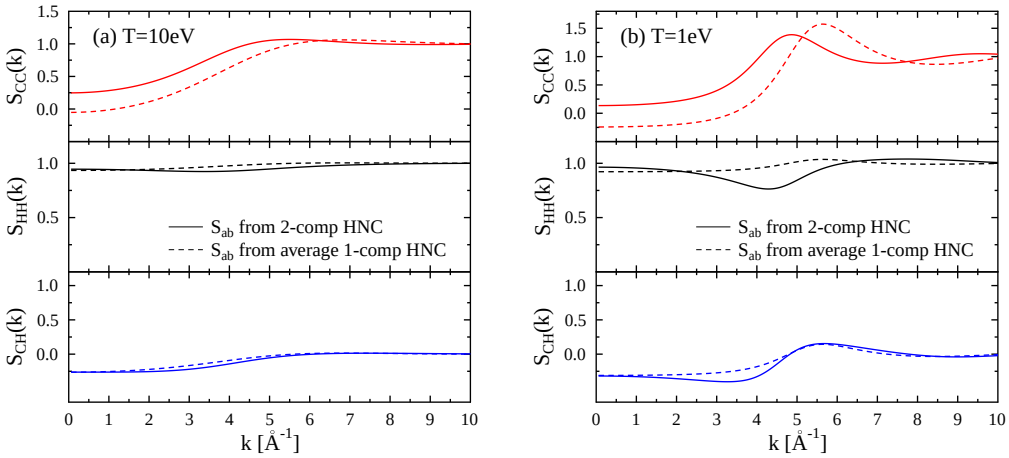

(a) moderately coupled system (b) strongly coupled system

Figure 4.13: Comparison of partial static structure factors for a CH plasma using the full multicomponent description and calculations applying an average charge state. The plasma has a density of $n_i = 5{\times}10^{23}\,\mathrm{cm}^{-3}$ and an average ion charge of $Z_f = 2.5$. In the two-component calculation, fully ionised hydrogen and fourfold ionised carbon ions with $n_H = n_C = 2.5 \times 10^{23}\,\mathrm{cm}^{-3}$ are considered. The temperatures used are $T = 10\,\mathrm{eV}$(left) and $T = 1\,\mathrm{eV}$ (right).

treatment is unable to account for the non-linear effects in strongly coupled plasmas.

As a result, we find that the partial structure factors can be deduced from single-ion calculations only in weakly to moderately coupled plasmas. In strongly coupled systems, however, a multicomponent description is essential.

Chapter 5

Electronic structure in warm dense matter

Chihara suggested an artificial decomposition of the electron densities to describe the total electronic structure in a plasma, which is the key quantity for the description of the x-ray scattering signal. Based on this idea, Chihara split the electrons into free and bound electrons, where the latter are considered to be tightly bound core electrons. Furthermore, free electrons form the screening cloud around the ions. As these are co-moving with the ions, their contributions can be treated statically as the ion dynamic cannot be resolved in current scattering experiments using laser produced x-ray sources. The response of kinetically free electrons, however, requires a dynamic description as it gives rise to collective excitations.

In this chapter, the electronic structure in warm dense matter will be studied, starting with the dynamic description of the free electrons. As the electrons are partially degenerate and only weakly coupled, they are described well within the random phase approximation (RPA). This approach is one of the most commonly used standard approximations in many particle systems. Based on RPA, collective properties of the free electron structure factor will be discussed, such a plasma oscillations, and the application for x-ray scattering will be highlighted. An outlook at the end of the section gives suggestions to go beyond RPA and improve the description for more coupled and collisional systems.

Afterwards, the electrons following the ion motion will be considered: firstly the tightly bound core electrons which are characterised by the atomic form factor. Then the screening cloud is considered. The latter one can be described using the linear response theory whereas a pseudo-potential approach is applied to account for additional core electrons in partially ionised plasmas [Gericke et al., 2010].

5.1 Description of the free electron feature

The response of the kinetically free electrons in a plasma to the x-ray probe beam is given by $Z_f S^0_{ee}(\mathbf{k},\omega)$ (see eq. (3.73)). To calculate the dynamic structure factor, the fluctuation-dissipation theorem (2.66) can be used

$$S^0_{ee}(\mathbf{k},\omega) = \frac{1}{\pi}\frac{1}{\exp\left(-\beta\hbar\omega\right)-1}\,\mathrm{Im}\;\chi_{ee}(\mathbf{k},\omega)\;,$$

where $\chi_{ee}(\mathbf{k},\omega)$ characterises the density response function of the free electrons in the system. As already pointed out, the response function in a many-particle system is difficult to determine. However, useful approximations can often be applied that sufficiently describe the physical properties. For instance, the electrons in warm dense matter are partially degenerate and only weakly coupled. This fact makes it possible to apply a linear response theory, which was first developed by Bohm and Pines [Bohm and Pines, 1953; Pines, 1953]. This theory, known as the random phase approximation (RPA), was applied for a degenerate electron gas to described the collective density response in a Coulomb force field.

In the beginning of this section, the susceptibility in the random phase approximation will be studied, yielding a suitable expression for the dynamic structure factor. This allows the determination of the free electron feature in the x-ray scattering signal. Based on this theory, the typical characteristics in the various plasma regimes considered will be highlighted [Gregori et al., 2003; Redmer et al., 2005]. Thereby, it will be demonstrated how basic plasma parameters, namely the electron density and the electron temperature, influence the behaviour of the response function and the dynamic structure factor providing a sensitive method for their measurements.

5.1.1 Susceptibility within random phase approximation (RPA)

The random phase approximation (RPA) is a linear response theory which neglects non-linear interactions between the density fluctuations [Ichimaru, 2004a]. Therefore, it cannot describe collisions in the system, which significantly influence the behaviour of strongly coupled plasmas, and thus, limits its applicability to weakly coupled systems. Nevertheless, it is capable of capturing essential properties of a free electron gas, as for instance collective plasma oscillations (plasmons).

In RPA, the susceptibility is determined by the response of an uncorrelated

system, χ_a^0, and the Coulomb potential in Fourier space, $V(\mathbf{k})$ [Kremp et al., 2005]

$$\chi_{ab}^{\mathrm{RPA}}(\mathbf{k},\omega) = \chi_a^0(\mathbf{k},\omega) + \sum_c \chi_a^0(\mathbf{k},\omega) V_{ac}(\mathbf{k}) \chi_{ab}^{\mathrm{RPA}}(\mathbf{k},\omega) \; . \tag{5.1}$$

This relation is the general expression for multicomponent systems where the indices 'a', 'b' and 'c' account for the particle species in the systems. In the case of a free electron gas, this equation simplifies to

$$\begin{aligned} \chi_{ee}^{\mathrm{RPA}}(\mathbf{k},\omega) &= \chi_e^0(\mathbf{k},\omega) + \chi_e^0(\mathbf{k},\omega) V_{ee}(\mathbf{k}) \chi_{ee}^{\mathrm{RPA}}(\mathbf{k},\omega) \\ \chi_{ee}^{\mathrm{RPA}}(\mathbf{k},\omega) &= \frac{\chi_e^0(\mathbf{k},\omega)}{1 - V_{ee}(\mathbf{k}) \chi_e^0(\mathbf{k},\omega)} = \frac{\chi_e^0(\mathbf{k},\omega)}{\varepsilon_{ee}^{\mathrm{RPA}}(\mathbf{k},\omega)} \; . \end{aligned} \tag{5.2}$$

Here, $\varepsilon^{\mathrm{RPA}}(\mathbf{k},\omega)$ is the dielectric function in RPA which can be generally expressed via the susceptibility by [Ichimaru, 2004a]

$$\varepsilon^{\mathrm{RPA}}(\mathbf{k},\omega) = 1 - \sum_a V_{aa}(\mathbf{k}) \chi_{ab}^0(\mathbf{k},\omega) \; . \tag{5.3}$$

The response function of an uncorrelated system is given by [Kremp et al., 2005]

$$\chi_{ab}^0(\mathbf{k},\omega) = \chi_a^0(\mathbf{k},\omega)\delta_{ab} = \delta_{ab} \int \frac{\mathrm{d}\mathbf{k}}{(2\pi)^3} \frac{f_a(\mathbf{k}) - f_a(\mathbf{k}+\mathbf{k}')}{\hbar\omega + E_a(\mathbf{k}) - E_a(\mathbf{k}+\mathbf{k}') + i\epsilon} \; . \tag{5.4}$$

Here, $E_a(\mathbf{k})$ denotes the kinetic energy of the particle a. Applying the Fermi distribution in thermodynamic equilibrium (1.2), the real and the imaginary part of the susceptibility for an electron gas is given by

$$\begin{aligned} \mathrm{Re}\,\chi_a^0(k) = \frac{(2s_a+1)\sigma_a^2}{16\pi^2 k_B T k} \, \mathcal{P} \int_{-\infty}^{\infty} \frac{\mathrm{d}k'}{k'} \Bigg\{ &\ln\left[1 + \mathrm{e}^{-\frac{\left(k'+\Delta_a^+\right)^2}{\sigma_a} + \beta\mu_a}\right] \\ &+ \ln\left[1 + \mathrm{e}^{-\frac{\left(k'+\Delta_a^-\right)^2}{\sigma_a} + \beta\mu_a}\right] \Bigg\} \end{aligned} \tag{5.5}$$

$$\mathrm{Im}\,\chi_a^0(k) = \frac{(2s_a+1)\sigma_a^2}{16\pi k_B T k} \left\{ \ln\left[1 + \mathrm{e}^{-\frac{\left(\Delta_a^+\right)^2}{\sigma_a} + \beta\mu_a}\right] - \ln\left[1 + \mathrm{e}^{-\frac{\left(\Delta_a^-\right)^2}{\sigma_a} + \beta\mu_a}\right] \right\} \tag{5.6}$$

with the abbreviations

$$\sigma_a = \frac{m_a k_B T}{m_e} \quad \text{and} \quad \Delta_a^{\pm}(k,\omega) = \frac{k}{2} \pm \frac{m_a}{m_e} \frac{\omega}{2k} \; . \tag{5.7}$$

For the calculation of the real part, the Chauchy mean value integral, $\mathcal{P}$, with the singularity at $k = 0$ has to be solved.

As the susceptibility is a complex quantity, the response function between the free electrons can be rearranged to

$$\chi_{ee}^{\mathrm{RPA}}(\mathbf{k},\omega) = \frac{\mathrm{Re}\,\chi_e^0 - V_{ee}\left[\left(\mathrm{Re}\,\chi_e^0\right)^2 + \left(\mathrm{Im}\,\chi_e^0\right)^2\right] + i\,\mathrm{Im}\,\chi_e^0}{\left(1 - V_{ee}\,\mathrm{Re}\,\chi_e^0\right)^2 + \left(V_{ee}\,\mathrm{Im}\,\chi_e^0\right)^2} \,. \tag{5.8}$$

Applying the fluctuation-dissipation theorem (2.66) leads to the following expression of the dynamic structure factor

$$S_{ee}^0(\mathbf{k},\omega) = \frac{1}{\pi}\frac{1}{\exp\left(-\beta\hbar\omega\right) - 1}\frac{\mathrm{Im}\,\chi_e^0}{\left(1 - V_{ee}\,\mathrm{Re}\,\chi_e^0\right)^2 + \left(V_{ee}\,\mathrm{Im}\,\chi_e^0\right)^2} \tag{5.9}$$

within the random phase approximation.

In many cases, it is convenient to rewrite this expression in terms of the dielectric function, $\varepsilon(\mathbf{k},\omega)$. In RPA, the dielectric function and the susceptibility are connected by Eq. (5.3) which can be simplified in a free electron gas to $\varepsilon^{\mathrm{RPA}}(\mathbf{k},\omega) = 1 - V_{ee}(\mathbf{k})\chi_{ee}^0(\mathbf{k},\omega)$. The electronic dynamic structure factor is then given by

$$S_{ee}^0(\mathbf{k},\omega) = -\frac{1}{\pi V_{ee}}\frac{1}{\exp\left(-\beta\hbar\omega\right) - 1}\,\mathrm{Im}\left(\varepsilon^{\mathrm{RPA}}\right)^{-1} \,. \tag{5.10}$$

For the numerical evaluation of the principle value integral for the real part of the susceptibility (5.5), the idea of [Longman, 1958] for a decomposition of the integral together with a Gaussian quadrature [Press et al., 1994] was implemented. The imaginary part of $\chi_a^0(\mathbf{k},\omega)$ can be directly computed from the analytical expression (5.6). The required chemical potential was calculated from the ideal relation for the temperature and densities given. To this end, the function [Kremp et al., 2005]

$$n_a = \frac{2s_a + 1}{\Lambda_a^3} I_{\frac{1}{2}}\left(\frac{\mu_a}{k_B T}\right) \,, \tag{5.11}$$

has to be inverted. For fermionic systems, one has to account for the spin degeneracy, $2s + 1 = 2$, here. $I_\nu(x)$ is the Fermi integral defined by Eq. (1.11). The chemical potential is analytically known for non-degenerate (Boltzmann statistics), $\beta\mu = \ln\frac{1}{2}n\Lambda^3$, and highly degenerate (Fermi statistics), $\mu = \epsilon_F = \frac{\hbar^2}{2m_e}(3\pi^2 n_e)^{2/3}$ (1.3), electrons [Kremp et al., 2005]. To avoid numerical issues, the exponential functions in the real and imaginary part of $\chi_a^0(\mathbf{k},\omega)$, Eqs. (5.5) and (5.6), need to be treated with care for extreme cases.

5.1.2 Results for the dynamic structure factor of the free electrons

Characteristics in collective and non-collective regimes

Depending on the wave vector considered, the frequency spectrum of the dynamic response of a plasma possesses two different behaviours, namely, the collective and the non-collective regime. In the short-wavelength regime, that is, $k \gg \kappa_s$, where κ_s denotes the inverse screening length (1.10), the plasma particles are uncorrelated. The associated frequency spectrum shows the characteristics of a single-particle behaviour, that is, the shape of the spectrum is proportional to the velocity distribution of the particles. However, if the wave vector k is of the order of the inverse screening length or smaller ($k \ll \kappa_s$), the probed density fluctuations show collective behaviour. Two peaks arise in the spectrum near the plasma frequency which are collective modes with quasi-particle characteristics (plasmons).

The two different frequency spectra of the plasma excitations are presented in Fig. 5.1 for a free electron gas with $n_e = 10^{20}\,\mathrm{cm}^{-3}$ and $T = 10\,\mathrm{eV}$. The inverse screening length for this system is $\kappa_s = 0.0224\,\mathrm{a_B^{-1}}$. The wave vectors were chosen in such a way, that Fig. 5.1a presents the non-collective regime with $\frac{k}{\kappa_s} > 1$ and Fig. 5.1b the collective region with $\frac{k}{\kappa_s} < 1$.

The spectral function of longitudinal excitations (collective or otherwise) is given by

$$\mathrm{Im}\left(\varepsilon^{\mathrm{RPA}}\right)^{-1} = \frac{-\,\mathrm{Im}\,\varepsilon^{\mathrm{RPA}}}{\left(\mathrm{Re}\,\varepsilon^{\mathrm{RPA}}\right)^2 + \left(\mathrm{Im}\,\varepsilon^{\mathrm{RPA}}\right)^2}\,. \tag{5.12}$$

The real and the imaginary part of the dielectric function as well as the imaginary part of the inverse dielectric function are also plotted in Fig. 5.1 for the collective and the non-collective regime. All quantities were calculated within RPA. In the non-collective regime of Fig. 5.1a, the real part of the dielectric function is only slowly varying over the entire frequency space. Therefore, the frequency spectrum is dominated by the characteristics of the imaginary part of the dielectric function. In the collective regime (see Fig. 5.1b), $\mathrm{Re}\,\varepsilon(\mathbf{k},\omega)$ features two zeros. The first zero occurs when the imaginary part of $\varepsilon(\mathbf{k},\omega)$ is large. As $\mathrm{Im}\,\varepsilon(\mathbf{k},\omega)$ indicates the damping in the system, this mode is strongly damped and no excitations arise. However, the second zero is located in the high frequency part where the imaginary part of the dielectric function is small. This causes a sharp rise in the imaginary part of the inverse dielectric function yielding the plasmon peaks in the frequency spectrum.

The plasmon resonance ω_{res} is given by the plasma dispersion relation which can be approximately calculated using the relation $\mathrm{Re}\,\varepsilon(\mathbf{k},\omega) = 0$. A calculation

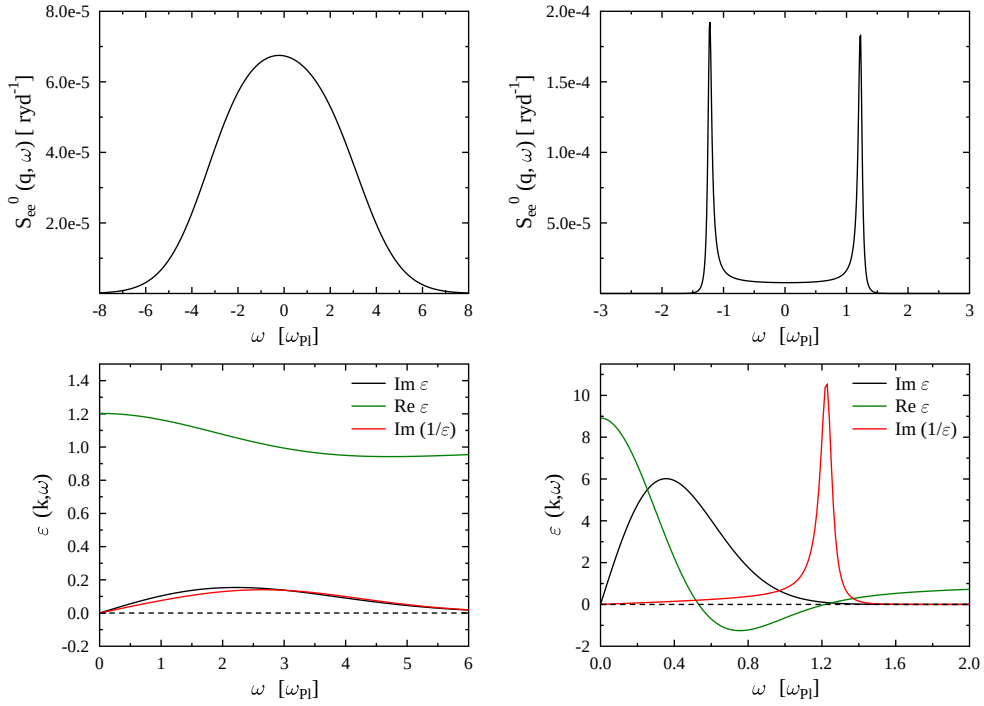

(a) non-collective regime

(b) collective regime

Figure 5.1: Dynamic structure factor, the real- and the imaginary part of the dielectric function as well as the imaginary part of the inverse dielectric function calculated in RPA for an electron gas with $n_e = 10^{20}\,\mathrm{cm}^{-3}$ and $T = 10\,\mathrm{eV}$. In panel (a), the wave vector is $k = 0.05\,\mathrm{a_B^{-1}}$ and it is $k = 0.008\,\mathrm{a_B^{-1}}$ on the right. The inverse screening length for this system is $\kappa_s = 0.0224\,\mathrm{a_B^{-1}}$.

based on RPA leads to [Kremp et al., 2005]

$$\omega_{\mathrm{res}} = \omega_{Pl}\left(1 + \frac{1}{2}\frac{k^2}{\hbar^2 m_e^2}\frac{\langle p^2\rangle}{\omega_{Pl}^2}\right) \tag{5.13}$$

with the plasma frequency ω_{Pl} (1.7) and the average of the square of the momentum $\langle p^2\rangle$. The latter one can be analytically calculated in limiting cases. For example, for classical systems $\langle p^2\rangle = 3m_e k_B T$ [Kremp et al., 2005]. The second term in the dispersion relation takes the thermal motions of the electrons into account, which was first derived by Bohm and Gross [Bohm and Gross, 1949]. An improvement including quantum diffraction was given in Ref. [Höll et al., 2007; Thiele et al., 2008]. From Eq. (5.13), it can be seen that the plasmon resonance position is mainly determined by the plasma frequency. Therefore, the plasmon frequency shift provides a sensitive method for the determination of the free electron density if small k values are used.

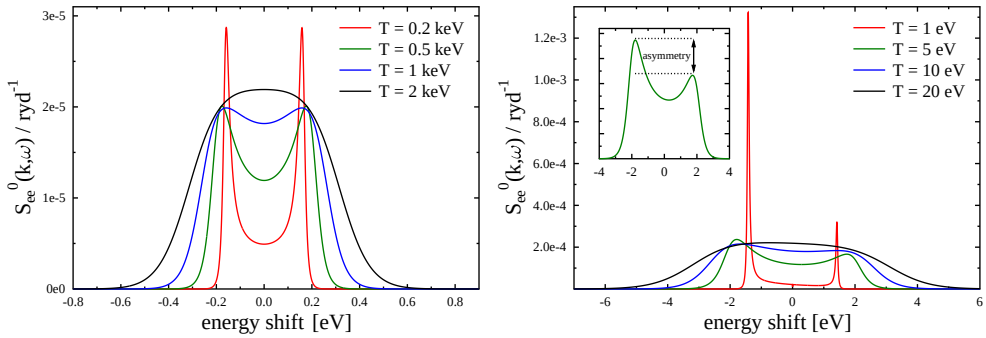

(a) weakly non-ideal plasma (b) warm dense plasma

Figure 5.2: Dynamic structure factors of a free electron gas (a) for a weakly coupled, non-degenerate system with $n_e = 10^{19}\,\mathrm{cm}^{-3}$ and (b) warm dense matter with $n_e = 10^{21}\,\mathrm{cm}^{-3}$ calculated in RPA for various electron temperatures. The scattering angle is $\theta = 90\,^\circ$. The plasma parameters are given in table 5.1.

It is important to notice that this method is independent of any models for the ion structure properties in dense plasmas.

Temperature dependency in weakly non-ideal and WDM plasmas

In the following, the temperature dependency of the dynamic structure factor will be studied. Here, the dynamic structure factor of a free electron gas is calculated for (a) a weakly coupled, non-degenerate plasma and (b) warm dense matter which is partially degenerate and moderately coupled. The results are presented in Fig. 5.2 and the plasma parameters are listed in table 5.1.

The lower density system is accessible with optical lasers, that is, wavelength of $\lambda_0 = 500\,\mathrm{nm}$, whereas for probing the denser plasma a wavelength of below $\lambda_0 = 4\,\mathrm{nm}$ is required. The scattering angle is set to $\theta = 90\,^\circ$ for both systems. In the collective regime, that is, the red curve in Fig. 5.2a, the structure factor of the weakly non-ideal plasma shows the two distinct symmetric plasmon peaks in the vicinity of the plasma frequency $\hbar\omega_{Pl} = 0.12\,\mathrm{eV}$. With the increase of the temperature, the maxima broaden as the characteristic screening length κ_s (1.10) decreases. Thus, the electrons start to behave like uncorrelated scatterers. For temperatures above $T = 2\,\mathrm{keV}$, the well-known individual particle-like spectra is obtained (black curve in Fig. 5.2a).

With the higher density used in Fig. 5.2b, the plasma frequency increases and the quantum effects contained in the Bose function become more important. As an effect the plasmon peaks become asymmetric where the red shifted peak ($\omega < 0$)

Table 5.1: Plasma parameters as used for the calculation of the dynamic structure factors in Fig. 5.2. α is the scattering parameter (1.9) for 90° scattering.

n_e / cm^{-3}	T / eV	$n_e\Lambda^3$	Γ	α	λ / nm
10^{19}	200	1.1×10^{-6}	2.5×10^{-3}	2.1	500
10^{19}	500	2.9×10^{-7}	1.0×10^{-3}	1.3	500
10^{19}	1000	1.0×10^{-7}	5.0×10^{-4}	0.9	500
10^{19}	2000	3.7×10^{-8}	2.0×10^{-4}	0.6	500
10^{21}	1	0.330	2.30	2.9	4
10^{21}	5	0.025	0.46	1.3	4
10^{21}	10	0.010	0.23	0.9	4
10^{21}	20	0.004	0.11	0.6	4

is more pronounced. This asymmetry depends on the equilibrium temperature, T, of the relevant frequency. It is referred to as detailed balance

$$\frac{S(\mathbf{k},\omega)}{S(-\mathbf{k},-\omega)} = \exp\left(\frac{\hbar\omega}{k_B T}\right) . \tag{5.14}$$

This relation reflects that the ratio of the cross-section for the scattering process of a photon with initial momentum, $\mathbf{k}_i$, and frequency, ω_i, into the final state: $(\mathbf{k}_i, \omega_i) \rightarrow (\mathbf{k}_s, \omega_s)$ and reverse, $(\mathbf{k}_s, \omega_s) \rightarrow (\mathbf{k}_i, \omega_i)$, is equal to the ratio of the statistic weights of the states $|i\rangle$ and $|s\rangle$, which is given by the Boltzmann factor [Höll et al., 2007; Hansen and McDonald, 1990].

In principle, the detailed balance relation can be used as a measurement tool to determine the temperature in the system, as it is independent of any model assumption for the structural properties in the dense plasma. However, only few experiments fulfil the requirements of sufficient temperatures, densities and signal-to-noise ratios to resolve the blue shifted ($\omega > 0$) plasmon needed for this relation.

Dependency on the scattering angle

In Fig. 5.3, the dependency of the dynamic structure factor on the scattering angle is studied. Here, an electron gas with a density of $n_e = 10^{23}\,\mathrm{cm}^{-3}$ and a temperature of $T = 5\,\mathrm{eV}$ is considered. To access this strongly coupled ($\Gamma = 2.15$) and degenerate system ($n_e\Lambda^3 = 2.96$), hard x-ray radiation with a wavelength of $\lambda_0 = 0.26\,\mathrm{nm}$ are required. In this case, scattering at a small angle accesses the collective scattering

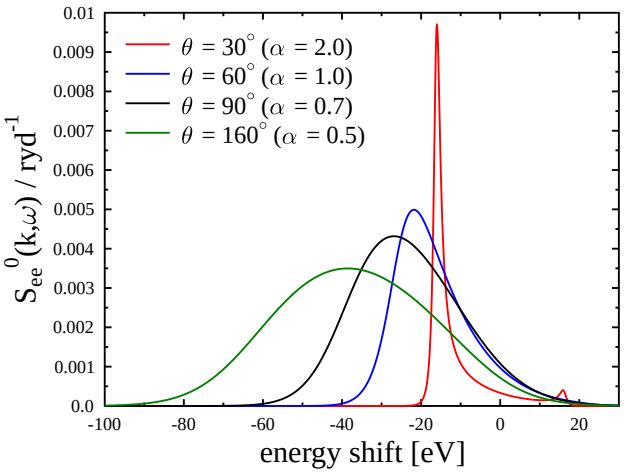

Figure 5.3: Dynamic structure factors for a free electron gas calculated in RPA for various scattering angles. Considered is a plasma with electron density $n_e = 10^{23}\,\mathrm{cm}^{-3}$, temperature $T = 5\,\mathrm{eV}$ and initial photon energy of $E_0 = 2.96\,\mathrm{keV}$. The legend labels the scattering angles with the associated scattering parameters.

regime and collective behaviour of the plasma can be studied. Due to the initial photon energy and the temperature of the system, the blue shifted plasmon peak can only be observed for very small scattering angles (see red curve in Fig. 5.3). With the increase of the scattering angle, the dynamic structure factor is red-shifted and broadened.

For scattering angles from $\theta \geq 90°$, the non-collective scattering regime is reached. Examples for the structure factor in this case are given by the black and the green curves in Fig. 5.3. The scattering parameter is $\alpha < 1$ giving a backscattering geometry. As presented in the previous section 3.1.1, the scattering signal is in this case proportional to the velocity distribution function and down-shifted due to the Compton effect [Glenzer and Redmer, 2009]

$$\Delta E_\mathrm{C} = \frac{\hbar^2 k^2}{2m} \,. \tag{5.15}$$

By varying the scattering angle, the collective or the non-collective mode can be accessed, which allows to study various features of the system under investigation.

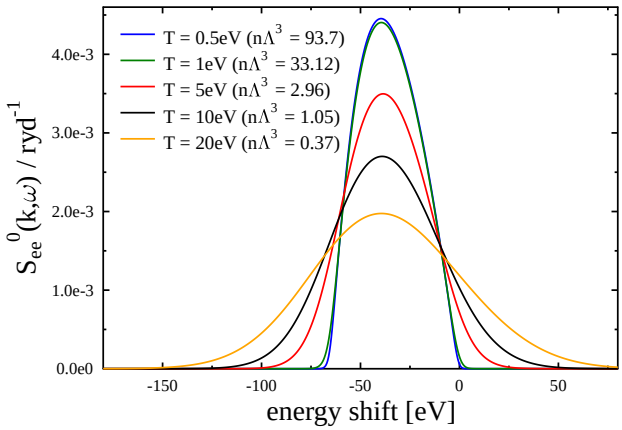

Figure 5.4: Dynamic structure factors for a free electron gas calculated in RPA for various degeneracy parameters. Considered is a plasma with electron density $n_e = 10^{23}\,\mathrm{cm}^{-3}$, initial photon energy $E_0 = 2.96\,\mathrm{keV}$ and angle $\theta = 160°$. The legend labels the electron temperature with the associated degeneracy parameters.

Influence of the degeneracy parameter

As mentioned above, the scattering spectrum in the non-collective scattering regime is proportional to the velocity distribution of the electrons, which is a Maxwell-Boltzmann function for classical plasmas and a Fermi distribution function for highly degenerate plasmas [Glenzer and Redmer, 2009]. The influence of the degeneracy parameter, $n\Lambda^3$, of the dynamic structure factor is presented in Fig. 5.4. Here, $S(k,\omega)$ of a free electron gas is calculated in RPA for various temperatures and, thus, different degeneracy parameters. The probe beam is considered to be detected in backward scattering geometry with $\theta = 160°$ and an initial energy of $E_0 = 2.96\,\mathrm{keV}$.

For small temperatures, the system is highly degenerate and the shape of the scattering spectrum is parabolic. For sufficiently high degeneracy, the parabolic form becomes temperature independent, as presented by the almost identical curves associated to the electron temperatures $T = 1\,\mathrm{eV}$ and $T = 0.5\,\mathrm{eV}$. Therefore, the Compton line provides a sensitive measurement method to obtain the electron density in highly degenerate systems.

An increase of the temperature, and thus a decrease of the degeneracy parameter, causes a lowering and broadening of the peak. For non-degenerate systems, the scattering signal reflects the exponential shape of the Maxwell-Boltzmann function, which is temperature but not density dependent. Thus, in the non-degenerate case, the electron temperature can be determined by the spectrum of the down-shifted Compton line.

5.1.3 Improvements of the description

The RPA is a linear response theory which neglects higher-order terms in the density fluctuations. These neglected correlations are, however, essential to describe inter-particle correlations in WDM, which are of particular importance for the correct behaviour at short distance. For example, the radial distribution function calculated in RPA leads to negative values for small distances, which indicates the limits of this approximation [Mahan, 2000].

To account for short distance correlations as well as exchange effects in the case of quantum plasmas, Hubbard suggested a correction factor for the RPA response function, the so called local-field correction (LFC) [Hubbard, 1957]. The LFC describes the differences between the interaction by a pure Coulomb potential and the interaction by a screened potential accounting for density fluctuations due to correlation effects in the full many-body system. The response of such a system is then given by [Ichimaru, 2004b]

$$\chi(\mathbf{k},\omega) = \frac{\chi^0(\mathbf{k},\omega)}{1 - V(\mathbf{k})\left[1 - G(\mathbf{k},\omega)\right]\chi^0(\mathbf{k},\omega)} \,. \tag{5.16}$$

$G(\mathbf{k},\omega)$ denotes the dynamic local field corrections (DLFC). By setting $G(\mathbf{k},\omega) = 0$, the RPA response function can be recovered. Many approaches were suggested to find approximative solutions for the calculations of the LFC (e.g. see Refs. [Ichimaru, 2004b; Mahan, 2000]). With such correction factors, the collective behaviour in moderately coupled systems can then be approximately described. As the electrons in WDM are often only weakly coupled, these corrections should only have a small effect on the dynamic structure between the free electrons. Nevertheless, it could be considered for further work to improve the description.

Due to the neglect of higher-order correlations, the RPA can only described collisionless plasmas, as higher-correlation terms are essential to incorporate collisions. Following the idea of Mermin, a modified response function can be derived which accounts for electron-ion collisions [Mermin, 1965; Höll et al., 2007; Kremp et al., 2005]

$$\chi^{\mathrm{M}}(\mathbf{k},\omega) = \left(1 - \frac{i\omega}{\nu_{ei}}\right)\left(\frac{\chi^0(\mathbf{k},z)\chi^0(\mathbf{k},0)}{\chi^0(\mathbf{k},z) - \frac{i\omega}{\nu_{ei}}\chi^0(\mathbf{k},0)}\right) \tag{5.17}$$

with $z = \omega - \operatorname{Im}\nu_{ei}(\omega) + i\operatorname{Re}\nu_{ei}(\omega)$. For the calculation of the collision frequency $\nu_{ei}(\omega)$, the Born approximation can be used leading to the Born-Mermin approach [Thiele et al., 2008; Fortmann et al., 2009]. This description was successfully applied for the analysis of the x-ray scattering signal in beryllium [Thiele et al., 2008].

It could be shown, that the inclusion of electron-ion collisions leads to additional damping and broadening of the plasmon resonances. Thus, the description with RPA would overestimate the plasma parameters extracted from the experimental spectrum. An extended Mermin approach which also incorporates static LFC was published by Fortmann *et al.* to account for correlation effects and collisions in a two-component plasma simultaneously [Fortmann et al., 2010].

The expansion of the current description of the free electron feature by the Born-Mermin approach would be worthwhile for future work. In particular, the use of free electron laser facilities will deliver high precision measurements for more accurate spectrally resolved x-ray scattering spectra and a much improved signal-to-noise ratio. In such experiments, small changes will be measurable which require a better theoretical description to extract the correct plasma parameters.

For current x-ray sources, the results obtained in RPA are, however, often sufficient to yield the plasma parameters from the scattering signal. Furthermore, the data obtained by RPA are still applicable for higher coupling strength in case of non-collective scattering [Gregori et al., 2003].

5.2 Description of the bound electrons

The bound electrons are described by the atomic/ionic form factor which is defined by the Fourier transformed charge density $\varrho_b(\mathbf{r})$ around an atom/ion

$$f(k) = \int \mathrm{d}\mathbf{r}\varrho_b(\mathbf{r}) \exp\left(-i\mathbf{k}\cdot\mathbf{r}\right) . \tag{5.18}$$

The density distribution can be calculated by the wave functions of the electrons as $\varrho_b(\mathbf{r}) = |\psi(\mathbf{r})|^2$. In the case of a hydrogen plasma, the wave functions of the ground state $1s$ electrons are well-known yielding

$$\begin{aligned} f_{i,H}(k) &= \int \mathrm{d}\mathbf{r} \left| \frac{2}{\sqrt{4\pi}} a_B^{-3/2} \exp\left(-\frac{r}{a_B}\right) \right|^2 \exp(-i\mathbf{k}\cdot\mathbf{r}) \\ &= \left[1 + (ka_B/2)^2\right]^{-2} . \end{aligned} \tag{5.19}$$

For other elements, the wave function of the many-particle system can be approximated through the mean-field approximation of Hartree [Fehske et al., 2008]. This approach reduces the many-particle problem to a one-electron Schrödinger equation, where each electron is presented by its own single-particle wave function with its own energy. Then, the single electron is moving in the force field produced by the nuclei and an average potential caused by the other electrons. This

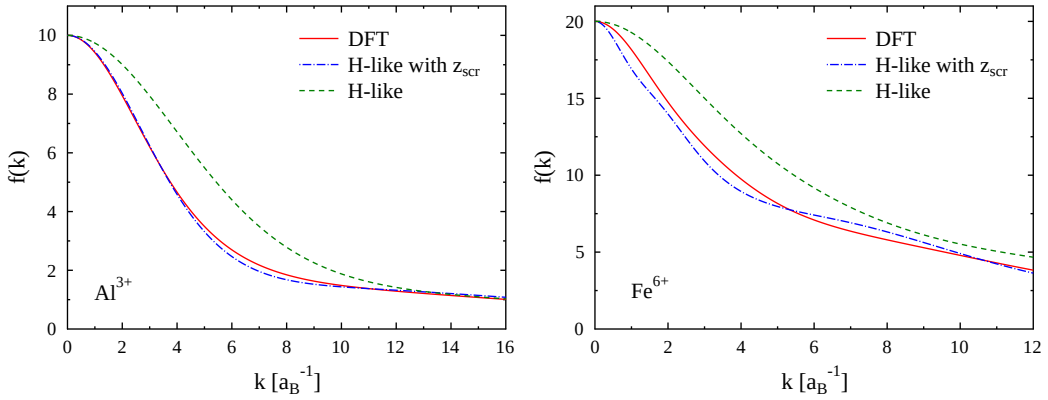

(a) aluminium (b) iron

Figure 5.5: Comparisons of different calculations for the ionic form factors for threefold charged aluminium ions and sixfold charged iron ions using pure hydrogen-like wave functions (labelled H-like), hydrogen-like wave functions with a screening constants (labelled H-like with Z_{scr}) and results from DFT calculations.

potential depends on the density distribution which is, however, calculated from the electron wave functions themselves. Now, in a self-consistent manner, the wave functions build the density distribution which yield the average potential to solve the Schrödinger equation to obtain an improved wave function. This iterative process continues until a self-consistent wave function is achieved. The final wave function of the N-particle system is then given by a product of the single-electron wave functions. Later, Fock improved this method by including the exchange effect due to antisymmetrised wave functions (Hartree-Fock calculations).

Here, the density distributions and the wave functions are calculated by means of density functional theory [Soler et al., 2002] performed by J. Vorberger [Wünsch et al., 2008b]. Thereby, the electron-electron correlations are approximated by an exchange-correlation term which is considered within the GGA approximation (see section 4.1.5). Work by Dharma-wardana showed that the electron density distribution in a plasma can often be well approximated by those of isolated atoms [Dharma-wardana and Perrot, 1992; Wünsch et al., 2008b]. This limits the numerical effort significantly.

Another, fully analytical approach for the determination of the form factor was suggested by Pauling who described the bound states by hydrogen-like wave functions which include a screening constant, z_{scr}, to account for other bound electrons [Pauling and Sherman, 1932; Hubbel et al., 1975]. Pauling and Sherman calculated the screening constant for several ion species which is, of course, different

for each element [Pauling and Sherman, 1932]. Following this idea, the form factor for elements with $1s$ electrons can then be evaluated analytically by

$$f_{I,1s} = \left[1 + (ka_s/2)^2\right]^{-2} \tag{5.20}$$

where $a_s = a_B/(Z_A - z_{scr})$ is the effective bound state radius with the screening constant, z_{scr}, and the nuclear charge, Z_A.

A comparison of this approximate treatment to DFT results is presented in Fig. 5.5 for aluminium ions and for iron ions with charge states of Z=3 and Z=6, respectively. The results following from hydrogen-like wave functions without further corrections overestimate the ion form factor due to the neglect of the internal screening effects. By including the screening constant as suggested by Pauling and Sherman [Pauling and Sherman, 1932], the resulting ionic form factor is in good agreement with DFT calculations for aluminium. Even for a high Z material, such as iron, the approximate treatment still yields fairly accurate results in comparison with DFT.

5.3 Description of the electron screening cloud

Following the idea of Chihara, the electrons in a plasma can be decomposed into bound and free electrons. The latter are considered kinetically free and give rise to the free electron feature in the spectrum as well as form the screening cloud. The free electron feature is independent of the ions and can be described by the RPA approximation as presented in the first section of this chapter. The screening cloud is co-moving with the ion motion. As current x-ray sources cannot resolve the low frequency part of the ion dynamics, a static treatment of the screening function is sufficient.

To describe the x-ray scattering signal, the Fourier transformed density of the screening electrons is required. This density is defined by the static structure factors in a two-component system (see Eq. (3.60b))

$$q(k) = \sqrt{Z_f}\frac{S_{ei}(k)}{S_{ii}(k)} \,. \tag{5.21}$$

Here, $S_{ei}(k)$ is the electron-ion structure factor which contains only kinetically free electrons. Thus, a method that can describe the electron-ion structure in a moderately to strongly coupled, partial degenerate system is required for the calculation of $q(k)$. The challenge of such a task was already discussed based on the unknown-

effective inter-particle potential in such a highly non-ideal system.

Another approach to calculate this quantity approximately is based on the linear response theory. The screening density is then given by [Gericke et al., 2010]

$$q(k) = \chi_{ee}(k) V_{ei}(k) \tag{5.22}$$

with the susceptibility of the free electrons in the static limit, that is $\omega \to 0$. The electron response function is given in the random phase approximation by $\chi_{ee}^{\mathrm{RPA}}(k) = \chi_{ee}^{0}(k)/\varepsilon^{\mathrm{RPA}}(k)$ (see Eq. (5.2)). In the static limit, the susceptibility of the uncorrelated system is $\chi_{ee}^{0}(k) = \kappa_e^2/4\pi e^2$ and the dielectric function can be expressed as $\varepsilon^{\mathrm{RPA}}(k) = (k^2 + \kappa_e^2)/k^2$ with the electron screening parameter κ_e [Ichimaru, 2004a]. $V_{ei}(k) = 4\pi Z e^2/k^2$ is the pure Coulomb potential between electrons and ions. Using these expressions in the definition of the screening function (5.22) yields

$$q^{\mathrm{RPA}}(k) = Z \, \frac{\kappa_e^2}{k^2 + \kappa_e^2} \, . \tag{5.23}$$

This approximate expression is derived in RPA for Coulomb fields as in fully ionised plasmas. It leads to the correct long wavelength limit, that means, $\lim_{k\to 0} q(k) = Z$.

The bare Coulomb potential can only be applied in this description if the ions are fully ionised. For partially ionised systems, the interaction between the free electrons and the nuclei is influenced by the bound states which cause an additional repulsion for small distances. This effect might be described by an effective electron-ion potential which is modified near the nucleus and merges in the Coulomb potential for large distances.

A simple form for such a pseudo-potential, often used in solid state physics where it approximately describes the properties of the electrons, is known as empty-core potential [Ashcroft, 1966]

$$V_{ei}^{\mathrm{ec}}(r) = \begin{cases} \frac{Ze^2}{r} & \text{for} \quad r > r_{cut} \\ 0 & \text{otherwise} \end{cases} \, . \tag{5.24}$$

Here, r_{cut} defines the cut-off radius which classifies the area occupied by the nucleus with its bound states. Outside of this radius, the inter-particle force is the Coulomb potential. The core radius is a free parameter which can be varied to match experimental data on transport and optical properties of the material under consideration [Hafner and Heine, 1983; Balbas et al., 1984; Vora, 2007]. Applying the Fourier transformation of this potential and inserting the result in Eq. (5.22) leads, within

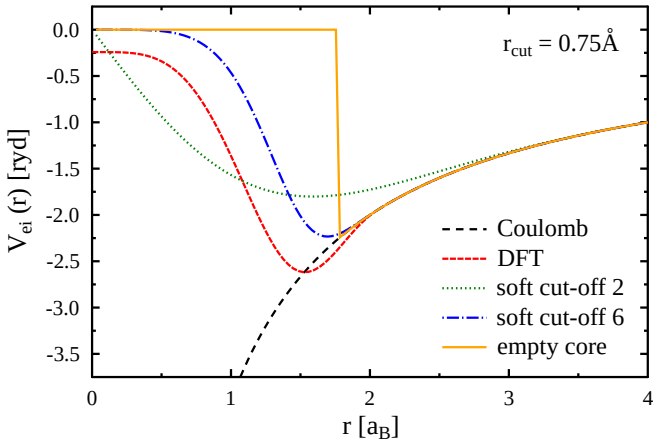

Figure 5.6: Effective electron-ion potentials used for the linear response description of the screening function. The soft-core potential, defined by Eq. (5.26), is shown for exponents $\alpha = 2$ and $\alpha = 6$. The curve labelled DFT gives the norm-conserving potential for beryllium used in the DFT-MD simulation when the $1s$ electrons are frozen out.

the linear response theory, to a screening function of the form

$$q(k) = Z \, \frac{\kappa_e^2}{k^2 + \kappa_e^2} \, \cos(k r_{cut}) \; . \tag{5.25}$$

The hard cut-off at r_{cut} yields several unphysical properties. These issues can be mitigated by a soft cut-off of the form [Gericke et al., 2010]

$$V_{ei}^{\text{soft}}(r) = \frac{Ze^2}{r} \left[1 - \exp\left(-\frac{r^\alpha}{r_{cut}^\alpha} \right) \right] \; . \tag{5.26}$$

The parameter, α, controls the steepness of the core edge whereas the cut-off radius, r_{cut}, determines the depth of the minimum. α can also be seen as a further fitting parameter. To determine the screening function, the Fourier transform of this potential is required, which was done numerically using an FFT from Numerical Recipes [Press et al., 1994].

Fig. 5.6 presents the pseudo-potential to be used in the analysis. Furthermore, a norm-conserving pseudo-potential is displayed, which was created to describe the effective interaction between valence electrons and partially charged ions in density functional calculations. The benefit of such a potential lies in the reduction of the numerical computational effort as less electrons have to be considered explicitly. The potential shown as the red curve in Fig. 5.6 is for simulations with the VASP package

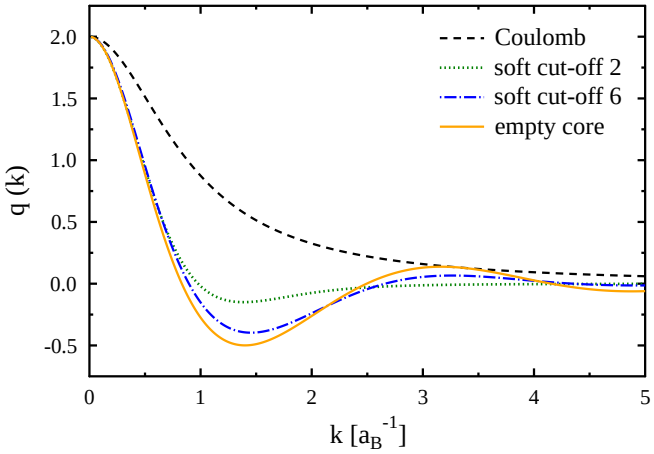

Figure 5.7: Screening function $q(k)$ obtained in linear response theory applying different effective potentials. The plasma parameters were taken for beryllium at solid density ($\varrho = 1.848\,\mathrm{g/cm^{-3}}$) and $T = 12\,\mathrm{eV}$. The ion charge state is $Z = 2$. The free cut-off parameter in the pseudo-potentials is set to be $r_{cut} = 1\,\text{Å}$.

(see section 4.1.5) containing double charged beryllium ions, where the $1s$ electrons are frozen out.

Fig. 5.6 shows the hard jump in the empty core potential at the cut-off radius and the softening of the edge due to the exponential function in the soft-core potential (5.26). A small value of α leads to a very soft pseudo-potential, whereas for $\alpha \to \infty$ the empty-core potential can be reproduced. The potential used in DFT-MD can be matched reasonable well by the soft-core potential with $\alpha = 6$ and a cut-off radius of $r_{cut} = 0.75$ Å.

In the following, a beryllium plasma with solid density, $\varrho = 1.848\,\mathrm{g/cm^{-3}}$, a temperature of $T = 12\,\mathrm{eV}$ and double charge ions will be considered. Such a system was experimentally investigated in recent scattering experiments [Glenzer et al., 2003a, 2007]. Fig. 5.7 presents the associated screening functions obtained in linear response theory applying the different effective potentials described above. For comparison, the black curve in the figure presents the calculation using a Coulomb potential, that is, Eq. (5.23). It can be seen, that the screening function calculated with the pseudo-potentials is significantly reduced for wavelengths $k < 3\,\mathrm{a_B^{-1}}$. Even negative values can be observed for intermediate wavelengths, which is a well-known feature from solid state physics [Louis and Ashcroft, 1998]. The electron density in real space must be positive. However, the screening charge can be negative in Fourier space. The reason for the different behaviours lies in the fact that bound

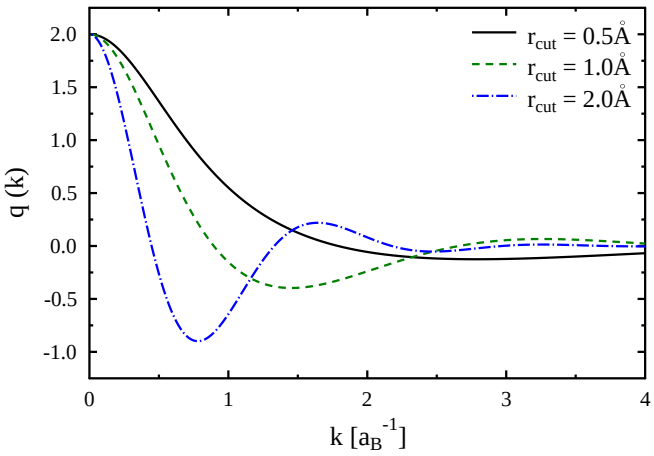

Figure 5.8: Influence of the cut-off radius r_{cut} on the screening function $q(k)$ using the soft-core potential (5.26) with $\alpha = 6$. Plasma conditions as in Fig. 5.7.

electrons cause a strong repulsion at short distances. This leads to a reduction of screening near the nucleus as the valence electrons cannot enter this space. Due to charge neutrality in a plasma, the screening needs to be compensated at larger distances causing negative values of the Fourier component of the screening charge at intermediate k values.

The qualitative form of the screening function depends on the functional form of the pseudo-potential used as well as on the choice of the cut-off radius. In Fig. 5.8, the screening function calculated with the soft-core potential (5.26) with $\alpha = 6$ is displayed applying various cut-off radii. A small cut-off radius leads to a Coulomb-like behaviour whereas a large cut-off radius causes strong oscillations yielding a significant reduction of screening effects for intermediate wavelengths. In the literature, a wide variety of cut-off radii was proposed due to various experimental techniques to fit the parameter. The presented cut-off radii in the Fig. 5.8 are within the range found in published papers [Hafner and Heine, 1983; Balbas et al., 1984; Vora, 2007].

The influence of tightly bound electrons on the screening of ionic cores in partially ionised plasmas can be studied by applying effective pseudo-potentials. Even for low-Z materials, such as beryllium, this treatment causes significant changes in the description of the screening function leading up negative values at intermediate k values in extreme cases. Nevertheless, an evaluation of this effects requires further work and comparisons with more accurate theories or experimental results.

Chapter 6

Theoretical predictions for the x-ray scattering process

After a detailed discussion of methods to describe the various scattering features in the previous chapters, the theoretical framework is now available to calculate a complete synthetic x-ray scattering spectrum for a wide range of plasma parameters. However, to generate a theoretical spectrum for a scattering process comparable to experimental results, some experimental constraints have to be considered. For example, the finite bandwidth of the probe beam, the finite resolution of the detector and the finite sample size modify the measured signal [Urry et al., 2006]. All these effects can be approximately included in an instrumental response function, which will be introduced in the beginning of this chapter. Afterwards, the sensitivity of the scattering signal to the plasma parameters will be investigated which allows the specification of the probed sample. In the non-collective scattering regime, the main plasma parameters can be extracted from the electron response alone, whereas the ionic structure is required as well to characterise the system in the collective mode.

The elastic Rayleigh peak, which will be discussed in detail in the second section, arises from the microscopic ion structure and the electron density around the ions. The elastic scattering feature can be treated statically as current x-ray experiments cannot resolve the small frequencies of the ion motion. It will be demonstrated how the various theoretical models for the ionic structure as well as for the free electrons forming the screening cloud significantly affect the elastic part of the scattering feature. Thereby, the conditions under which these differences can be tested by experimental measurements will be highlighted.

Based on the novel decomposition of the electron structure factor in multi-component systems, as derived in section 3.2.2, it will be demonstrated at the end of

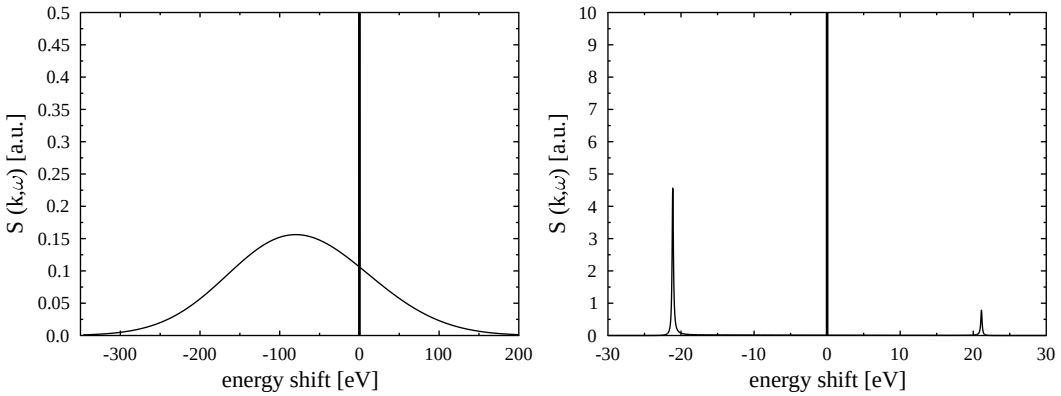

(a) non-collective regime (b) collective regime

Figure 6.1: Synthetic scattering spectra for a beryllium plasma at solid density in the (a) non-collective and the (b) collective scattering regime. The parameters applied are given in Tab. 6.1. As the elastic scattering feature is only treated statically the Rayleigh peak appears as a delta peak at $\hbar\omega = 0$.

this section that the Rayleigh peak is very sensitive to the ratio of different elements in the probe volume. Thus, x-ray Thomson scattering is a viable method for probing mixing properties of material in the WDM region. Important implementations for inertial confinement fusion (ICF) research and planetary physics will be presented.

6.1 Synthetic x-ray scattering spectrum

In the preceding sections, the theoretical models to describe the various quantities needed to describe the scattering process were discussed in detail. Based on these approaches, the complete x-ray scattering spectrum for arbitrary scattering angles and initial photon energies can now be generated. To ensure that the entire dynamic response to the probe beam is considered, the energy range required is estimated by the Compton shift or the plasmon position in the vicinity of the plasma frequency, in the case of a non-collective or collective scattering regime, respectively. Furthermore, the step width in the energy scale needs to be accurate enough to resolve all features. This is particularly relevant for small scattering angles, where plasma oscillations can be observed. The code, developed for this work, automatically calculates the energy range required and the approximate width of the peaks arising in the free electron contribution. The program is efficient for this application as the energy grid is then sufficient to resolve the sharp peaks of the plasma oscillations with only minimal computer resources needed.

Synthetic scattering spectra are shown in Fig. 6.1 for a beryllium plasma

Table 6.1: A detailed list of the plasma parameters used for the calculation of the synthetic scattering spectra presented in Fig. 6.1 and Fig. 6.2.

	non-collective	**collective**
mass density ϱ	$1.848\,\mathrm{g/cm^{-3}}$	$1.848\,\mathrm{g/cm^{-3}}$
temperature T	53 eV	13 eV
charge state Z	2.7	2
photon energy E_i	4.75 keV	2.96 keV
scattering angle θ	120°	20°
scattering parameter α	0.24	3.19
degeneracy parameter $n_e\Lambda_e^3$	0.28	1.97
coupling parameter Γ	0.3	1.2
FWHM ΔE	45 eV	6 eV

for conditions similar to experiments performed in backward and forward scattering geometry by Glenzer *et al.* to access the non-collective Compton regime and the collective scattering mode, respectively [Glenzer et al., 2003a, 2007]. A detailed list of the plasma parameters used is given in table 6.1 for both cases. As the elastic ion feature is treated statically, that is $S_{ii}(k,\omega) = S_{ii}(k)\delta(\omega)$, the Rayleigh peak appears as a delta function at $\hbar\omega = 0$. Obviously, such a spectrum cannot be used for comparisons with experimental data as the finite x-ray probe bandwidth and the finite spectrometer resolution cause a broadening of the spectra which is not yet accounted for in the theoretical profile [Glenzer and Redmer, 2009]. Therefore, the dynamic structure factor, $S_{ee}^{\mathrm{tot}}(k,\omega)$, will be convolved with a weighting function to account for these experimental constraints.

6.1.1 Instrument response function

The x-ray source spectrum has a finite bandwidth in ω-space and the spectrometer possesses a finite resolution. Both effects will be combined in an instrument response function, $g(\omega)$, which will be used for the convolution with the spectrum generated theoretically. Thus, the dynamic structure factor, applicable for comparisons with experimental results, is calculated by [Glenzer and Redmer, 2009]

$$S_{ee}^{\mathrm{exp}}(k,\omega) = S_{ee}(k,\omega) * g(\omega)\ . \tag{6.1}$$

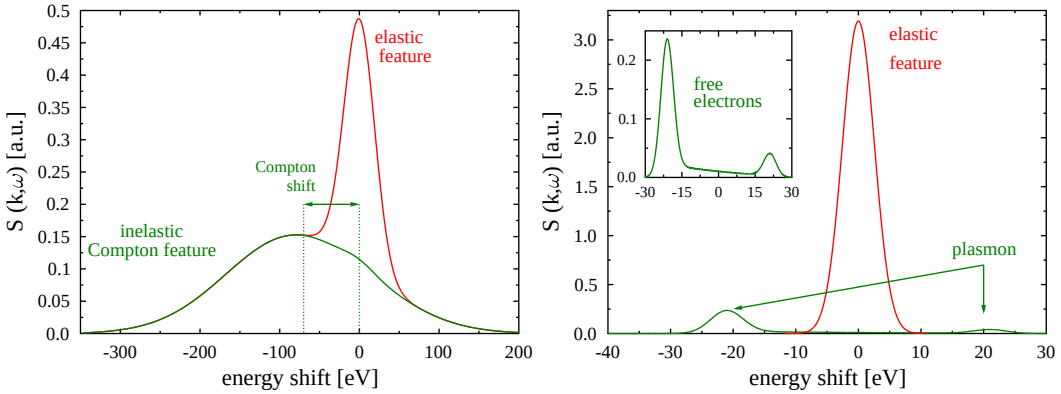

(a) non-collective regime (b) collective regime

Figure 6.2: Synthetic scattering spectra for a beryllium plasma as a function of the frequency shift, $\hbar\omega$, convolved with a Gaussian instrument response function with a bandwidth of (a) $\Delta E/E = 0.01$ and (b) $\Delta E/E = 0.002$ for the non-collective and the collective scattering regime, respectively. The plasma parameters are listed in Tab. 6.1.

Here, a normalised Gaussian distribution of the form

$$g(\omega) = \frac{1}{\sqrt{2\pi}\sigma} \exp\left(-\frac{\omega^2}{2\sigma^2}\right) \tag{6.2}$$

is used as an instrument response function. The standard variance is given by $\sigma = 0.425 \cdot \mathrm{FWHM}$ with a full width at half maximum (FWHM) of the Gaussian function incorporating the finite bandwidth of the probe beam and the finite resolution of the detector. As the elastic ion feature is only calculated in the static limit, the convolution simplifies here to a multiplication with the weighting function. Finally, the generated spectrum is calculated for a single ion system as

$$S_{ee}^{\mathrm{exp}}(k,\omega) = \frac{1}{\sqrt{2\pi}\sigma} \left\{ |f(k)+q(k)|^2 \, S_{ii}(k) \exp\left(-\frac{(\omega-\omega_i)^2}{2\sigma^2}\right) + Z_f \int \mathrm{d}\omega' S_{ee}^0(k,\omega') \exp\left(-\frac{(\omega-\omega_i-\omega')^2}{2\sigma^2}\right) \right\} , \tag{6.3}$$

where ω_i denotes the initial photon energy. In the second term the complete convolution integral has to be evaluated. Here, a convolution using a Fast Fourier Transformation (FFT) from the Numerical Recipes was applied [Press et al., 1994].

Schematic scattering spectra for both the non-collective and the collective scattering regime convolved with a Gaussian instrument response function are shown in Fig. 6.2. The plasma parameters are listed in Tab. 6.1. The non-collective scatter-

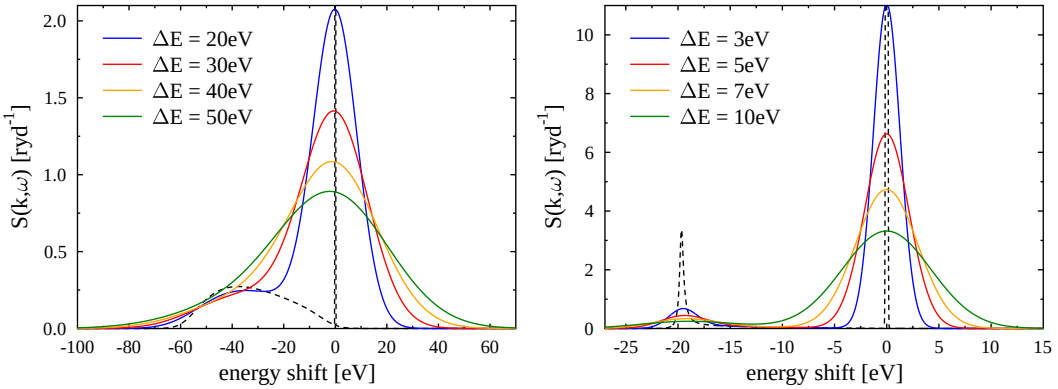

(a) non-collective regime (b) collective regime

Figure 6.3: Synthetic scattering spectra for a lithium plasma in the collective and the non-collective regime convolved with a Gaussian function with various FWHM in the energy (ΔE). The plasma parameters are $T = 1.7\,\mathrm{eV}$, $n_i = 1.6 \times 10^{23}\,\mathrm{cm}^{-3}$ and $Z = 1$ with the initial photon energy $E_i = 2.96\,\mathrm{keV}$ and the scattering angles (a) $\theta = 40°$ and (b) $\theta = 120°$. The corresponding bandwidths are listed in Tab 6.2.

ing regime presents the incoherent scattering by the free electrons yielding a down-shifted peak due to the Compton effect which is furthermore broadened by their thermal motion. The unshifted peak reflects the elastic scattering by weakly and tightly bound electrons. Its intensity depends on Z_B, the number of bound electrons. This low-frequency resonance of the Rayleigh feature is also present in the collective scattering mode, see Fig. 6.2b. In the high-frequency part, collective oscillations arise from the free electrons yielding a red ($\hbar\omega < 0$) and a blue ($\hbar\omega > 0$) shifted plasmon peak in the vicinity of the plasma frequency under these conditions. The resonance frequency is given by Eq. (5.13). The inset on the upper left in Fig. 6.2b magnifies the collective scattering by the free electrons to highlight the asymmetric behaviour of the blue and red-shifted plasmon peaks due to the detailed balance (see Eq. (5.14)).

For spectrally resolved x-ray scattering experiments certain constraints are required for the bandwidth of the x-ray sources and the resolution of the detectors used. To fully resolve all the scattering features, bandwidths of $\Delta E/E \simeq 0.01$ for the non-collective and $\Delta E/E \simeq 0.002$ for the collective mode are required [Glenzer and Redmer, 2009; Urry et al., 2006; Landen et al., 2001]. Furthermore, the number of scattered x-ray photons needs to be high enough to get a reasonable signal-to-noise ratio, which is particular important to access the collective plasmon peaks. Fig. 6.3 presents theoretical scattering spectra in the collective and the non-collective regime convolved with a Gaussian function with various FWHM in the energy scale (ΔE)

Table 6.2: The FWHM of the Gaussian instrument response function ΔE and the associate bandwidth $\Delta E/E$ for the scattering spectra plotted in Fig. 6.3

non-collective		**collective**	
ΔE	$\Delta E/E$	ΔE	$\Delta E/E$
20 eV	0.0067	3 eV	0.0010
30 eV	0.0101	5 eV	0.0017
40 eV	0.0135	7 eV	0.0023
50 eV	0.0169	10 eV	0.0034

to study the spectral blurring due to the finite resolution of the probe beam and the detector. As an example, a lithium plasma with single charged ions at solid density is considered. The initial photon energy is $E_i = 2.96\,\mathrm{keV}$ and the scattering angles are chosen in such a way that Fig. 6.3a presents the non-collective mode ($\theta = 120°$) and Fig. 6.3b the collective regime ($\theta = 40°$). To generate the Rayleigh feature, the static ionic structure factor, $S_{ii}(k)$, the screening function, $q(k)$, and the form factor, $f(k)$, are required. Here, a HNC approach, applying the Debye potential, was used to obtain $S_{ii}(k)$. $q(k)$ was calculated in linear response theory using equation (5.23) and the form factor describes the remaining $1s^2$ electrons. The dynamic response of the free electrons is calculated in RPA.

The black dashed curves present in both cases the unconvolved theoretically generated scattering spectrum. In table 6.2 the bandwidth $\Delta E/E$ for each presented curve is listed. It can be seen from the figure that a bandwidth of $\Delta E/E \lesssim 0.01$ is sufficient to separate the down-shifted Compton line from the Rayleigh peak in the non-collective scattering regime. To experimentally access the plasmon peak in the collective scattering mode a $\Delta E = 7eV$ or less is required. Here, the plasmon peak can be clearly separated from the Rayleigh peak. However, due to the small Thomson cross section and thus the small number of scattered x-ray photons, the signal-to-noise ratio is too low to experimentally measure the plasmon peak, in particular for the blue-shifted plasmon. To get a strong scattering signal from the collective oscillations, a low Z material should be chosen, as the Rayleigh peak will be comparatively small.

Furthermore, the uncertainty regarding the scattering angle and thus the wavenumber has to be considered. To incorporate such k-vector blurring, the scattering spectrum is convolved again with a function representing the range of scat-

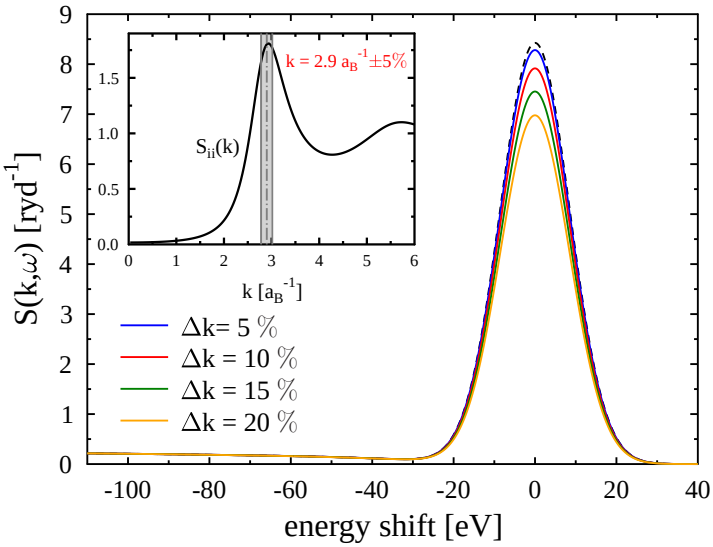

Figure 6.4: Synthetic scattering spectra for a carbon plasma convolved with a Gaussian function with various FWHM for the wavenumber (Δk). The plasma parameters are $T = 1\,\mathrm{eV}$, $n_i = 5 \times 10^{23}\,\mathrm{cm}^{-3}$ and $Z = 4$ with the initial photon energy of $E_i = 8\,\mathrm{keV}$, the scattering angle of $\theta = 85°$ and a bandwidth of $\Delta E/E = 2.5 \times 10^{-3}$. The black dashed line presents the theoretical generated scattering spectrum with no k-vector blurring effects.

tering angles. Often it is sufficient to use a Gaussian function for the wavenumber. Then the spectrum is given by

$$S_{ee}^{\mathrm{tot}}(k,\omega) = \frac{1}{2\pi\sigma_k} \int \mathrm{d}k'\, S_{ee}(k',\omega) \exp\left(-\frac{(k-k')^2}{2\sigma_k}\right). \tag{6.4}$$

To demonstrate the effect of the k-vector blurring, Fig. 6.4 shows a theoretical scattering spectrum for a carbon plasma convolved with a Gaussian function with various widths Δk. The static structure factor, which was obtained by HNC calculations applying the Yukawa model, is also shown as inset in Fig. 6.4 highlighting the wave vectors measured in the case where $k = 2.9 \pm 0.12\,\mathrm{a_B^{-1}}$, corresponding to 10% uncertainty in the scattering angle. The free electron scattering contribution was calculated in RPA. The black dashed line presents the theoretically generated scattering spectrum where no k-vector smearing is considered.

The k-vector blurring affects mainly the Rayleigh peak. Here, with increase of the uncertainty in the wavenumber probed (Δk) the intensity of the Rayleigh peak decreases. The relevance of this effect is, however, strongly dependent on the chosen scattering angle. For $\theta = 85°$, that is, $k = 2.9\,\mathrm{a_B^{-1}}$, the static structure factor

has a maximum. Thus, the static structure factor significantly declines for slightly smaller or larger wavenumbers. This fact causes the decrease of the elastic scattering intensity, which can be measured. For other wavenumbers probed, the effect of the k-vector blurring can be much less significant, especially, when increasing and decreasing contributions cancel for nearly linear increase/decrease in the structure factor.

6.1.2 Sensitivity of scattering profile from plasma parameters

To extract the plasma parameters from the measured scattering signal, theoretically generated spectra are fit to the experimentally measured data by changing temperature, density and ionisation degree. The best fit is then considered to yield the conditions within the sample. Therefore, it is important to understand the sensitivity of the various plasma features of the scattering signal to the plasma parameters, which will be discussed in this section for different plasma regimes.

Non-collective scattering regime

Firstly the non-collective scattering regime will be considered, that is, conditions with $\alpha < 1$. Taking a beryllium target as an example, synthetic scattering spectra are generated for various electron densities, temperatures and ionisation degrees. To generate the scattering profile, RPA is applied for the response of the free electrons. To evaluate the scattering contribution of the weakly and tightly bound electrons, ionic structure factors of the HNC approach are applied in the Yukawa model. The screening functions are used in linear response to a Coulomb field given by Eq. (5.23) and the form factors are taken from DFT calculations for isolated beryllium ions.

Fig. 6.5 presents synthetic scattering profiles for a beryllium plasma at various electron temperatures. The variation of the temperature mainly affects the Compton down-shifted line, which gets broadened and lower for higher temperatures due to the increase of the thermal motion of the free electrons. As the plasma parameters considered describe a non-degenerate system with $n_e\Lambda_e^3 < 0.1$ for all temperatures, the inelastic Compton line reflects the Gaussian form of the Maxwell-Boltzmann velocity distribution of the electrons. Therefore, the width of the Compton line is directly related to the electron temperature in the system.

In degenerate plasmas, however, Fermi distributions have to be applied to describe the velocity distribution of the free electrons. Therefore, the width of the Compton down-shifted line is now proportional to $(\epsilon_F)^{1/2}$, the Fermi energy (1.3), which provides the electron density [Landen et al., 2001]. To describe a degenerate

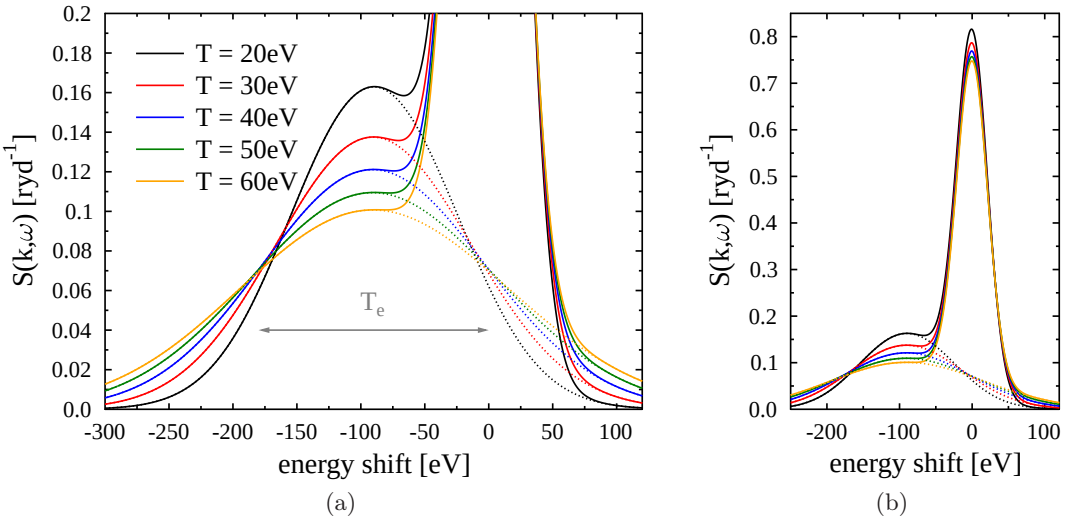

Figure 6.5: Synthetic scattering spectra for a beryllium plasma for various temperatures with $n_i = 10^{23}\,\mathrm{cm}^{-3}$ and $Z = 2$. The initial photon energy is $E_i = 4.75\,\mathrm{keV}$, the bandwidth is $\Delta E/E = 0.01$ and the scattering angle is $\theta = 160°$ probing at $k = 2.5\,\mathrm{a_B^{-1}}$. The main figure (a) magnifies the Compton down-shifted line whereas (b) presents the scattering spectrum over the entire energy scale.

plasma, the electron temperature was decreased to $T = 5\,\mathrm{eV}$ yielding a degeneracy parameter of $n_e\Lambda_e^3 > 6$ for all densities considered. The resulting scattering profiles are displayed in Fig. 6.6. To demonstrate the density dependence, the ion density was varied from $n_i = 10^{23}\,\mathrm{cm}^{-3}$ to $n_i = 10^{24}\,\mathrm{cm}^{-3}$ while the charge state of the beryllium ions stays constant. With the highest density the plasma is highly degenerate with $n_e\Lambda_e^3 = 59$. The inelastic scattering spectrum gets broadened and the intensity decreases with the increasing electron density. The Compton down-shifted line also shows the parabolic form due to the Fermi distribution.

The effect of the charge state of the ions on the x-ray scattering signal can be seen in Fig. 6.7 for a beryllium plasma. In the case of non-integer degrees, like $Z = 2.3$, the full multicomponent version of the x-ray scattering formula derived in chapter 3 (see Eq. (3.73)) is used. Then two ion species accounting for double and threefold charged beryllium ions are taken as basic species. The increase of the charge state causes an increase of the inelastic scattering feature whereas the intensity of the Rayleigh peak decreases. For large k-values, the contribution of the screening function is small and the ionic structure factor is around unity. Thus, the intensity of the Rayleigh peak is directly related to the form factor and thus to the number of bound electrons, that is, $I_{\mathrm{elast}} \sim Z_b^2$. In contrast, the intensity of the inelastic scattering feature is directly related to the number of free or weakly

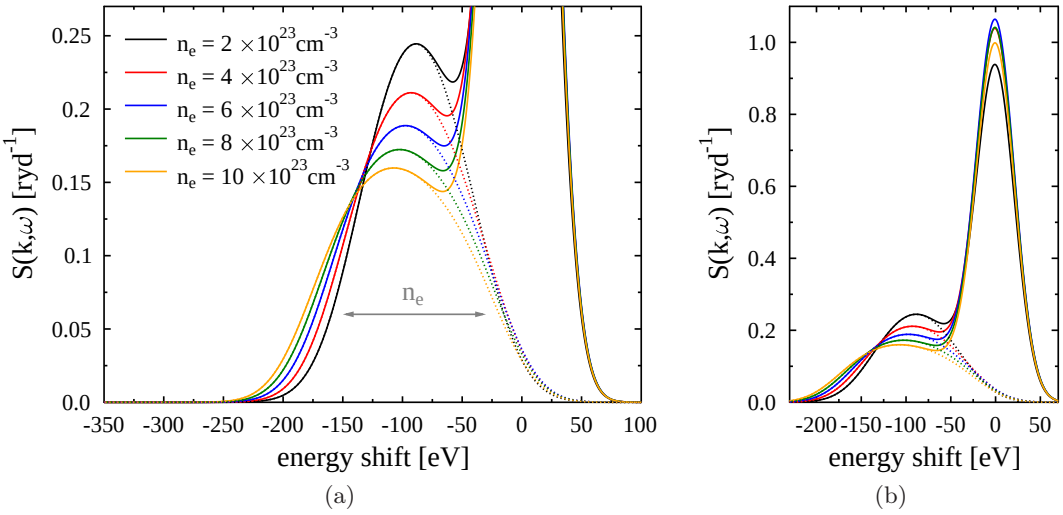

Figure 6.6: Synthetic scattering spectra for a beryllium plasma for various electron densities. with $T = 5\,\mathrm{eV}$ and $Z = 2$. The initial photon energy is $E_i = 4.75\,\mathrm{keV}$, the bandwidth is $\Delta E/E = 0.01$ and the scattering angle is $\theta = 160°$. The main figure (a) magnifies the Compton down-shifted line whereas (b) presents the scattering spectrum over the entire energy scale.

bound electrons, that is, $I_{\mathrm{inelast}} \sim Z_f$ [Gregori et al., 2003]. It should be mentioned, that this number does not necessarily reflect the ionisation degree of the material under investigation. It accounts for all electrons for which binding energy is smaller than the Compton energy, that is, $E_b < E_C$. In cases of large scattering angles the Compton energy is often larger than the binding energies of the outer shell electrons. Consequently, these electrons give contributions shifted according to the Compton energy and, thus, contributing to the inelastic scattering feature. However, the number of weakly bound electrons gives an upper limit of the ionisation degree Z. Nevertheless, the ratio between the inelastic to elastic scattering intensity can be used to infer the ionisation ion charge state, Z. In isochorically heated matter with known mass density, the measurement of the free electron density also leads directly to the charge state of the ions.

In most scattering experiments, the plasma is partially degenerate, causing the inelastic scattering feature to have a temperature and density dependency. In highly degenerate systems, the electron feature is, however, roughly temperature independent and other methods are required to reveal the temperature of the system. In summary, several plasma parameters can be inferred from the scattering signal in the non-collective scattering regime without further information about the ionic structure, and thus, relatively free from theoretical uncertainties.

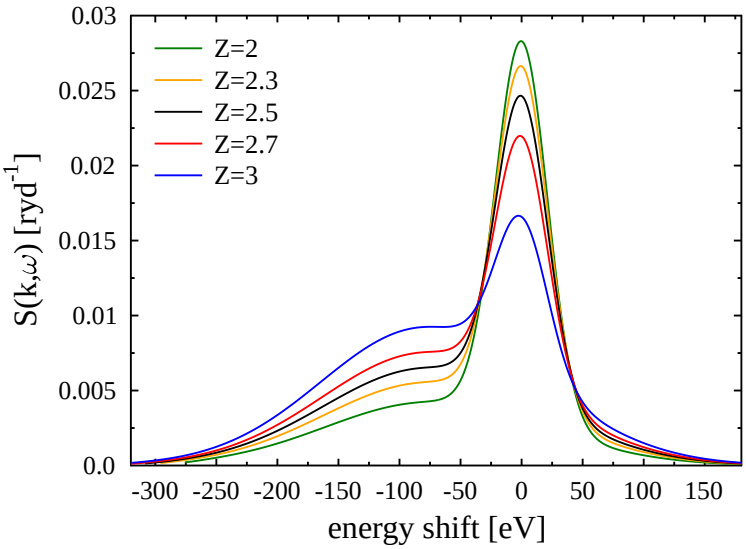

Figure 6.7: Synthetic scattering spectra for a beryllium plasma for various ionisation degrees with $n_i = 1.23 \times 10^{23}\,\mathrm{cm}^{-3}$ and $T = 53\,\mathrm{eV}$. The initial photon energy is $E_i = 4.75\,\mathrm{keV}$, the bandwidth is $\Delta E/E = 0.01$ and the scattering angle is $\theta = 160°$. In the case of non-integer ionisation degrees the full multicomponent version of the x-ray scattering formula (3.73) is used.

Collective scattering regime

To study the sensitivity of the plasma parameters on the x-ray scattering profiles in the collective scattering regime, the scattering angle was set to $\theta = 25°$ whereas the other parameters are unchanged to the cases presented previously. The same theories as in the non-collective regime were implemented to generate the synthetic scattering spectra. However, the FWHM of the Gaussian instrument response function is now reduced to $\Delta E = 7\,\mathrm{eV}$ to separate the plasmon peak from the Rayleigh peak.

In the forward scattering geometry the signal of collective oscillations arise in the scattering spectrum. The position of the plasmon resonance is density dependent, which is presented in Fig. 6.8 for solid density beryllium. The temperature is here set to be $T = 5\,\mathrm{eV}$ yielding a scattering parameter of $\alpha = 1.8 \ldots 2.35$, depending on the density. For an ion density of $n_i = 10^{23}\,\mathrm{cm}^{-3}$ the plasmon is red-shifted by $\Delta E_{\mathrm{Pl}} = 22.6\,\mathrm{eV}$ as highlighted in the figure. The exact position of the plasmon resonance is given by the dispersion relation, (5.13), where the main contribution is given by the plasma frequency at $\hbar\omega_{Pl} = 16.6\,\mathrm{eV}$. The difference between these numbers reflects the thermal motion of the electrons as well as corrections due to the fact that the system is partially degenerate with $n_e\Lambda_e^3 = 5.9$. The latter effect was included in an enhanced dispersion relation given by Thiele *et al.* [Thiele et al.,

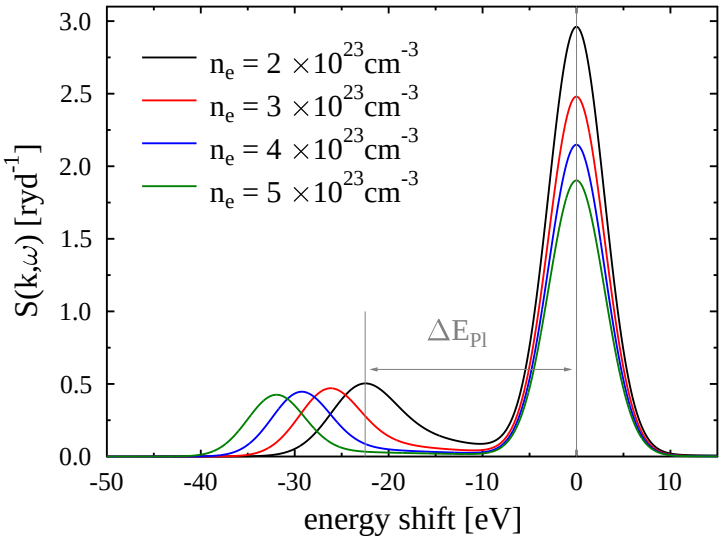

Figure 6.8: Synthetic scattering spectra calculated for a beryllium plasma with $T = 5\,\mathrm{eV}$ and $Z = 2$ for various electron densities in the collective scattering regime. The initial x-ray energy is $E_i = 4.75\,\mathrm{keV}$ and the scattering angle is $\theta = 25°$ probing at $k = 0.55\,\mathrm{a_B^{-1}}$. The plasmon frequency shifts and the corresponding plasma frequencies are listed in table 6.3 for each density.

2008]. A detailed list of the plasma frequency shifts and the plasma frequencies for all densities considered is given in table 6.3. With the increase of the density, the plasma frequency shift gets larger yielding a sensitive method to extract the electron density in the system. An enhancement of the accuracy for the extraction of the electron density from the plasmon frequency shift is discussed, for example, in the work of [Thiele et al., 2008]. Here, an improved description of the dynamic response of the free electrons due to the inclusion of collision effects via the Born-Mermin approach was applied as well.

The plasmon signal also contains a temperature dependency [Döppner et al., 2009] as the increase of the thermal motion of the electrons yields a further broadening of the plasmon peaks. Thus, the shape of the plasmon signal can be used to infer the temperature. However, further effects influence the shape, such as damping due to collisions which are not included in the RPA description [Neumayer et al., 2010].

Another temperature dependence is given by the ratio of the intensities of the blue- and red-shifted plasmons (detailed balance Eq. (5.14)). To emphasise this effect, the scattering angle was adjusted to $\theta = 15°$ as this effect becomes more pronounced for smaller wavenumbers where the plasmon peaks are more distinct. Fig. 6.9 presents calculated synthetic scattering spectra for a beryllium plasma at

Table 6.3: The plasmon frequency shifts ΔE_{Pl} and the corresponding plasma frequencies, ω_{Pl}, for a solid density beryllium target with $T = 5\,\mathrm{eV}$ and $Z = 2$ for various electron densities, n_e, according to the dynamic structure factor presented in Fig. 6.8.

$n_e\,[\mathrm{cm}^{-3}]$	$\Delta E_{\mathrm{Pl}}\,[\mathrm{eV}]$	$\hbar\omega_{\mathrm{Pl}}\,[\mathrm{eV}]$
2×10^{23}	22.6	16.6
3×10^{23}	26.5	20.3
4×10^{23}	29.5	23.4
5×10^{23}	31.8	26.3
6×10^{23}	34.4	28.7

various temperatures. Due to the scattering angle chosen, the system is probed at $k = 0.33\,\mathrm{a_B^{-1}}$ yielding scattering parameters of $\alpha = 2.6 \ldots 3.0$. With the increase of the temperature in the system, the intensity of the blue-shifted plasmon peak increases whereas the intensity of the red-shifted plasmon signal decreases. In Fig. 6.9, the required quantities to apply the detailed balance relation, that is, the energy transfer, $\hbar\omega$, of the scattered photon and the intensities of the red- and blue-shifted plasmon signal, are highlighted for the case $T = 25\,\mathrm{eV}$.

The detailed balance relation can provide an accurate technique to infer the electron temperature of the system considered as it does not rely on any other assumption except that the system has to be in a thermodynamic equilibrium. However, the experimental access to the blue-shifted plasmon peak is challenging as the scattering intensity is low and thus this feature lies mostly below the noise level. First measurements with sufficiently high temperatures could be achieved in recent scattering experiments on a beryllium target, which allow the application of the detailed balance to extract the electron temperature [Döppner et al., 2009].

A third option to infer the temperature from the scattering signal is given by the ratio of the red-shifted plasmon intensity to the intensity of the Rayleigh peak as the elastic scattering feature is directly related to the ionic structure and, thus, affected by the ion temperature. In Fig. 6.10b, synthetic scattering spectra generated for 4.75 keV x-rays scattered on beryllium at solid density under an scattering angle of $\theta = 25°$ are shown for various temperatures. It can be seen that the increase of the temperature leads to an increase of the intensity of the Rayleigh feature. The differences are caused mainly by the changes in the microscopic structure of the ionic subsystem characterised by the static ion-ion structure factors. This quantity

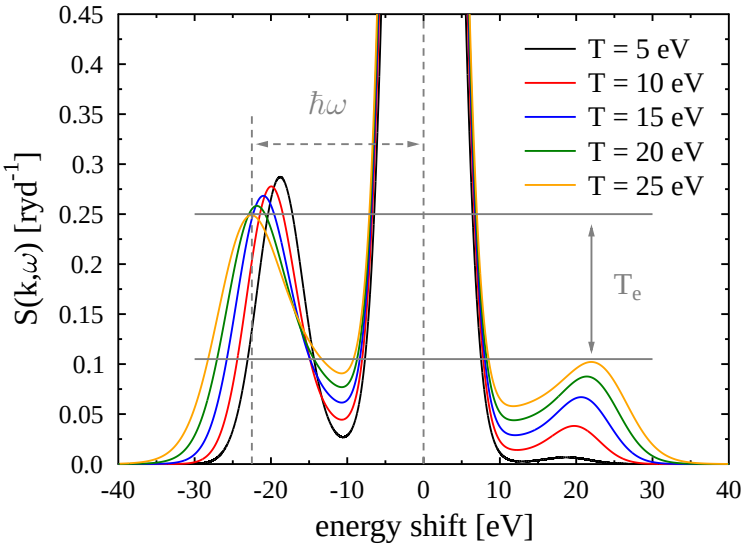

Figure 6.9: Synthetic scattering spectra calculated for a beryllium plasma with solid density $n_i = 10^{23}\,\mathrm{cm}^{-3}$ and ionisation state $Z = 2$ for various temperatures. The initial x-ray energy is $E_i = 4.75\,\mathrm{keV}$ and the scattering angle is $\theta = 15°$ probing at $k = 0.33\,\mathrm{a_B}^{-1}$. $\hbar\omega$ denotes the energy transfer of the scattered photon.

is shown in the left panel of Fig. 6.10. With an increase of the temperature from $T = 1\,\mathrm{eV}$ to $T = 9\,\mathrm{eV}$, the intensity of the Rayleigh feature increases by a factor of around 2.5. The same increase can be observed in the static structure factors for the wave vector probed.

The latter approach to infer the temperature relies heavily on a correct theoretical model for the ionic structure and the electron density around the ions characterised by the screening function, $q(k)$, and the form factor, $f(k)$. As already discussed in chapter 4 as well as in section 5.3, these quantities are strongly depending on the effective inter-particle potential applied which is still a topic of ongoing research in warm dense matter. Vice versa, accurate measurement of plasma parameters and the spectra can be used to validate theoretical predictions and, thus, improve the understanding of the microscopic structure in warm dense matter.

6.2 Elastic scattering feature

The electron density fluctuations due to the form factor (bound states) and the screening cloud scatter light elastically. The corresponding scattering feature is the Rayleigh peak at the initial photon energy. This contribution is directly related to the ionic microscopic structure, characterised by the ion-ion structure factor, describing

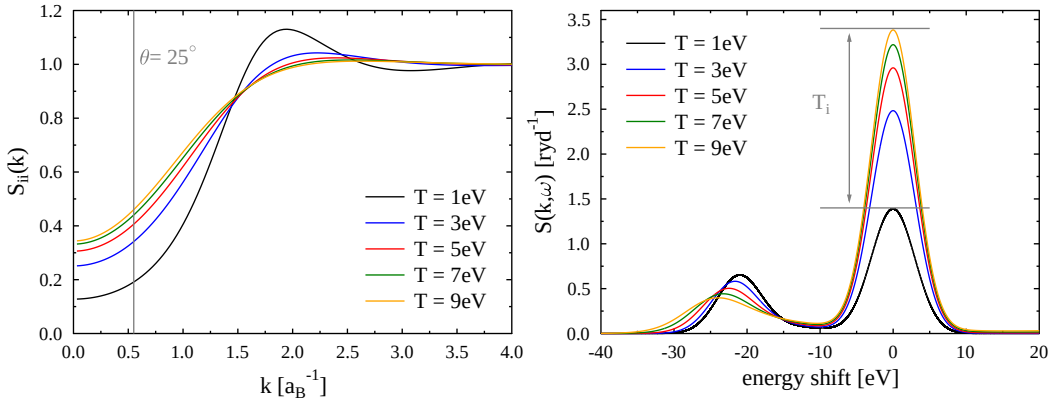

(a) static structure factor (b) x-ray scattering spectrum

Figure 6.10: Synthetic scattering spectra calculated for a beryllium target with solid density $n_i = 10^{23}\,\mathrm{cm}^{-3}$ and ionisation state $Z = 2$ for various temperatures. The initial x-ray energy is $E_i = 4.75\,\mathrm{keV}$ and the scattering angle is $\theta = 25°$ probing at $k = 0.55\,\mathrm{a_B^{-1}}$. The left picture presents the associated static structure factors obtained by HNC method applying a screened Coulomb potential. The gray line indicates the position of the probed k-vector.

the spatial arrangement and the thermal motion of the ions. The elastic part of the scattering spectrum can be treated statically as typical laser-driven x-ray sources and also current free-electron lasers have a bandwidth that cannot resolve the dynamics of the ion motion. In this case, the measured elastic feature is fully characterised by the frequency integrated area under the Rayleigh peak. Theoretically, this quantity is described by the weight of the Rayleigh peak (see Eq. (3.62))

$$W_R(k) = [f_i(k) + q(k)]\, S_{ii}(k)\ , \tag{6.5}$$

where the form factor, $f(k)$, and the screening cloud, $q(k)$, account for the tightly bound and the free electrons, respectively, and $S_{ii}(k)$ is the static ion-ion structure factor.

Due to the connection with the structure factor, the Rayleigh peak contains information of the ionic subsystem, such as, ion density, ion temperature and ionisation degree. In the case of collective scattering, the plasmon frequency shift leads to the electron density and the temperature can be revealed from the weight of the Rayleigh peak. The latter also yields information of the coupling strength which leads to the ion charge state and, via the electron density obtained by the plasmon frequency shift, to the mass density.

To fully extract the plasma parameters from the x-ray scattering signal, in

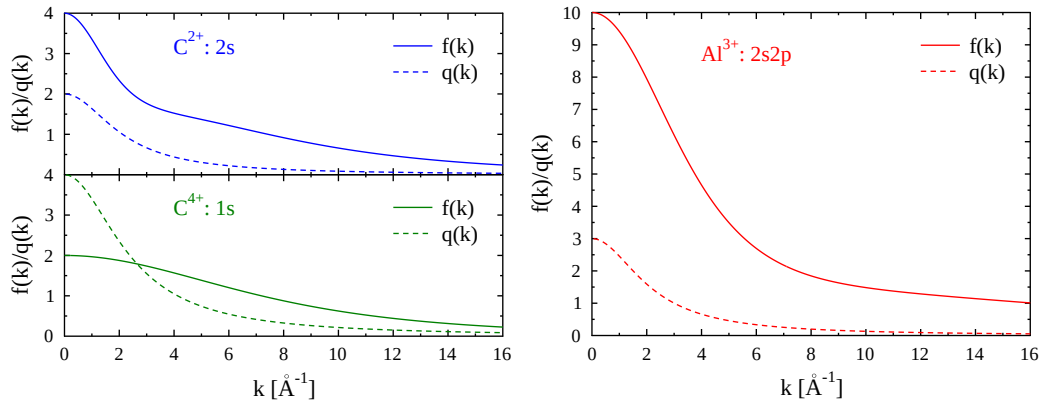

(a) carbon (b) aluminium

Figure 6.11: Form factors, f(k) (solid lines), obtained by DFT simulations and screening functions, q(k) (dashed lines), calculated in linear response to a Coulomb field (5.23) for (a) a carbon and (b) an aluminium plasma at $T = 1\,\mathrm{eV}$. The mass density of carbon is $\varrho_C = 2.2\,\mathrm{g/cm^3}$ yielding the inverse screening length of $\kappa_s = 1.12\,\mathrm{a_B^{-1}}$ for double charged (upper panel) and $\kappa_s = 1.26\,\mathrm{a_B^{-1}}$ for fourfold charged ions (lower panel). The mass density of aluminium is $\varrho_{Al} = 3.4\,\mathrm{g/cm^3}$ leading to $\kappa_s = 1.12\,\mathrm{a_B^{-1}}$ with an ionisation degree of $Z = 3$.

particular from the Rayleigh peak, an excellent theoretical description of all quantities involved is required. In chapter 4 and chapter 5, different methods were introduced to calculate these quantities, namely, the structure factor, $S(k)$, the ionic form factor, $f(k)$, and the screening function, $q(k)$. This section will study the influence of these models on the elastic part of the x-ray scattering signal. Thereby, conditions will be discussed which might allow for an experimental verification of the various theoretical models available.

6.2.1 Electron density around the ions

For the evaluation of the Rayleigh peak, the electron density around the ions in the Fourier space is required, that is, the form factor, $f(k)$, and the screening function, $q(k)$. The form factor describing the tightly bound electrons is obtained from DFT simulations of an isolated ion. The contribution of the electrons forming the screening cloud is calculated in linear response to a Coulomb field after Eq. (5.23). Fig. 6.11 shows the results for the electronic structure for warm dense carbon with double (upper panel of Fig. 6.11a) and fourfold (lower panel of Fig. 6.11a) charged ions as well as for an aluminium plasma.

The bound electrons are closely localised around the nuclei yielding a function which is widely spread in the Fourier space. In contrast, the electrons forming the

screening cloud are less localised in real space so that their contribution in Fourier space is mainly concentrated at small k-values. In the long wavelength limit, that is, $k = 0$, the form factor reflects the number of bound electrons, Z_b, whereas the screening functions present the charge state of the ions.

For double ionised carbon (upper panel of Fig. 6.11a), two electrons form the screening cloud and the remaining $2s$ electrons contribute to the form factor. Obviously, the contribution of the bound electrons to the scattering process is higher than that of the screening cloud. In contrast, in the case of fourfold ionised carbon (lower panel of Fig. 6.11a), the contribution of the screening function for small wavenumbers is larger than from the bound electrons. This is caused by the fact that all electrons except the K-shell are ionised and, thus, contribute to the screening cloud. If accurately measured, the slope of $W_R(k)$ in k-space can give information on the charge state distribution in the sample investigated.

In the case of threefold ionised aluminium, see Fig. 6.11b, the scattering contribution of the bound electrons clearly dominates, as only 3 electrons account for the screening cloud whereas all remaining 10 electrons of the K- and $L-$shell are included in the form factor. Therefore, for elements with a large number of bound electrons, the contribution of the screening function is less important and will only be relevant for small k-values as for the evaluation of the Rayleigh peak both terms need to be added.

6.2.2 Influence of various models for the ionic structure

In chapter 4, the effect of different inter-particle potentials on the ionic structure in warm dense matter was discussed. Now, the influence of the various models on the elastic scattering feature will be studied. Here, three models will be considered: (i) the one component plasma (OCP) model (ii) the Yukawa model (Y) and (iii) the Yukawa model with an additional short range repulsion (Y+SRR). The first two model systems are widely used. The OCP model, which considers the ions interacting by a pure Coulomb potential (see section 4.2), often yields similar results as an electron-ion system when the electron-ion interaction is described by a weak pseudo-potential (see section 4.3). In the second model, the electrons are taken into account and a linearly screened ion-ion Coulomb potential is used. The third model includes an additional short-range repulsion term to the Debye potential to mimic the effect of bound electrons in partially ionised systems (see section 4.4).

Fig. 6.12 shows the weight of the Rayleigh peak, $W_R(k)$, for a silicon plasma calculated in the three different model systems described above. In the upper right panel of the figure, the related ion-ion structure factors are presented. Here, the

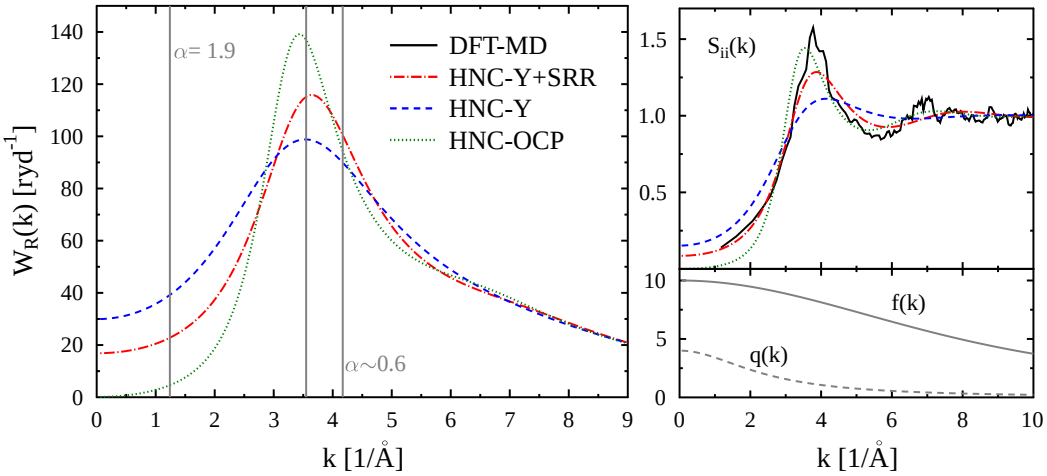

Figure 6.12: The weight of the Rayleigh peak, $W_R(k)$, for a silicon plasma with $T = 4.7\,\mathrm{eV}$, $\varrho = 2.33\,\mathrm{g/cm^3}$ and $Z = 4$ calculated for three different model systems applied in the HNC approach, namely, the OCP, the Yukawa (Y) and the Yukawa model with a short-range repulsion (Y+SRR). The related ion-ion structure factors are displayed in the top right panel, showing furthermore the structure obtained by DFT-MD simulations. The electronic structure, that is, the form factor, $f(k)$, and the screening function, $q(k)$, are presented in the bottom right picture for the system considered. The first quantity is obtained from DFT simulations of an isolated ion and the second is calculated after Eq. (5.23). The gray lines in $W_R(k)$ indicate the wave vectors which will be used to discuss the behaviour of the x-ray scattering signal in the non-collective and collective regime.

results from the HNC approach are compared with data obtained by DFT-MD simulations. It can be seen, that the HNC calculations applying the OCP model can reproduce the first peak in the ionic structure as shown in the data gained by the simulations. However, the small k-behaviour is not correctly described as screening effects are neglected in this model. The use of the Debye potential in the HNC method (line labelled HNC-Y), however, cannot described the correct spatial correlations in this strongly coupled system. Following the discussions of section 4.4, the bound electrons of the fourfold charged silicon ions cause a further repulsion for small distances which can be mimicked by an additional short-range repulsion term added to the Debye potential. Applying this model potential in the HNC code can reproduce the ionic structure obtained by DFT-MD very well.

The electron distribution around the silicon ions is displayed in the lower right panel of the Fig. 6.12. Here, the form factor, $f(k)$, which is obtained by DFT simulations, describes the tightly bound $2s$ and $2p$ electrons of the K- and L-

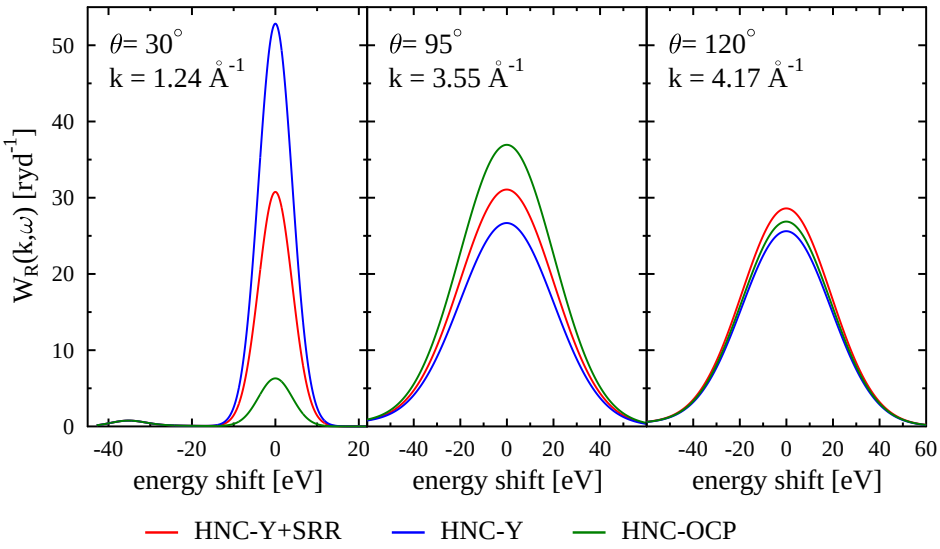

Figure 6.13: Calculated Rayleigh peak for the silicon system as described in Fig. 6.12 broadened by a Gaussian response function for various wavenumbers as indicated in $W_R(k)$. The incident photon energy is $E_i = 4.75\,\mathrm{keV}$. The bandwidths of the instrument function are set to $\Delta E/E = 0.002$ and $\Delta E/E = 0.01$ for the collective and the non-collective scattering regime, respectively.

shell, respectively. The screening function, $q(k)$, describes the four valence electrons contributing to the screening cloud. The latter one is calculated in linear response to a Coulomb field (5.23).

The weight of the Rayleigh peak varies significantly for the different models applied. For experimental verifications, the wave vectors probed should be chosen at the positions where the most discrepancies arise. These positions are given for small distances around $k = 1.24\,\text{Å}^{-1}$ and around the peak position at $k = 3.55\,\text{Å}^{-1}$ (corresponding to the first gray lines in $W_R(k)$ presented in Fig. 6.12). The first wave vector probes the system in the collective mode with a scattering parameter of $\alpha = 1.9$ whereas the second wavenumber yields $\alpha = 0.6$, that is, probing occurs at the border of the non-collective scattering regime.

To compare with experimental results, the Rayleigh peak has to be broadened with an instrument response function to account for the energy blurring (see section 6.1.1). Fig. 6.13 presents the resulting elastic Rayleigh peak for the three different wave vectors highlighted as gray lines in Fig. 6.12. The discrepancies between the different models for the ion structure are small for the largest wave vector at $k = 4.17\,\text{Å}^{-1}$ and will lie below the experimental noise level. This characteristic can be traced back to the form of the related ion-ion structure factors which show a

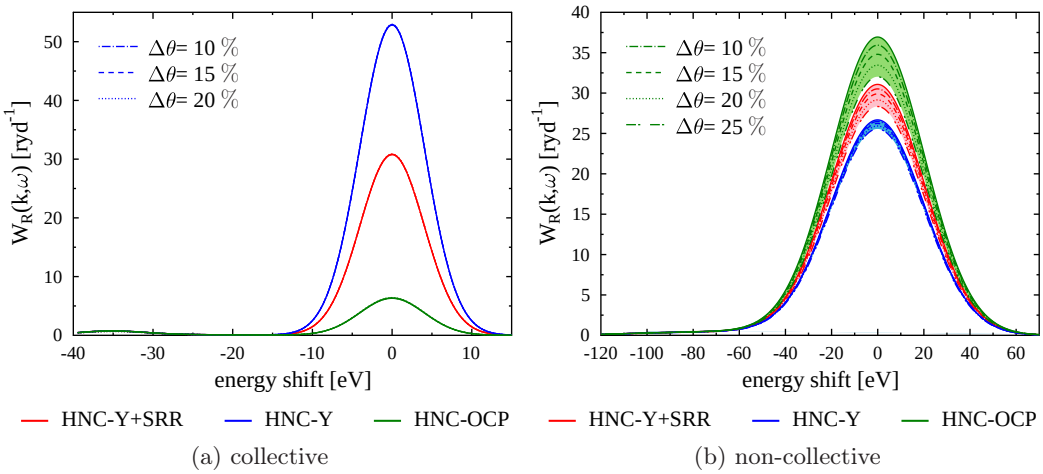

(a) collective (b) non-collective

Figure 6.14: The theoretically generated dynamic Rayleigh peak for the silicon system as described in Fig. 6.12 and Fig. 6.13 now convolved furthermore with a Gaussian instrument response function with various FWHM for $\Delta\theta$ to include the k-vector blurring. The scattering angles are $\theta = 30\,^\circ$ and $\theta = 95\,^\circ$ to access the collective and non-collective regime, respectively.

similar behaviour for all models considered at this wavenumber.

Directly on the position with the peak in the ion-ion structure factor at $k = 3.55\text{Å}^{-1}$, the differences between the various models can be clearly seen. It still might be challenging for current experimental accuracy to distinguish the various models as the height of the Rayleigh peak varies around 15%. However, between the Yukawa model, which predicts the smallest peak, and the OCP model, which leads to the largest value, differences of 30% arise which might allow the experimental validation of the influence of screening effects in WDM.

In the collective scattering regime, under a scattering angle of $\theta = 30°$, the influence of the various ionic models strongly affects the predictions of the scattering signal. Here, discrepancies up to 75% arise between the OCP model and the Y+SRR model and differences of 50% between the Y+SRR model and the pure Yukawa model. These effects are caused by the different small k-behaviour of the related ion-ion structure factors whose absolute values vary by a factor of two between the models in the selected scattering regime. These large differences in the Rayleigh peak makes the different theories experimentally testable.

Besides the broadening in the energy space, an uncertainty in the scattering angle needs to be considered for experimental comparisons. Therefore, the theoretical scattering spectra from Fig. 6.13 will be further convolved with a Gaussian function to account for the k-vector blurring. The results are presented in Fig. 6.14

for the two scattering angles with the largest discrepancies between the various ionic models, that is, $\theta = 30\,^\circ$ and $\theta = 95\,^\circ$. Here, errors up to $\pm 12.5\%$ (or $\Delta\theta = 25\%$) are investigated, as these uncertainties might occur in current x-ray experiments [Glenzer and Redmer, 2009]. Interestingly, the k-vector blurring does not change the scattering signal in the collective regime. The reason for such a behaviour lies in the characteristics of the weight of the Rayleigh peak, which is approximately linear around the wave vector considered. Therefore, the k-vector blurring causes no significant contribution. In contrast, $W_R(k)$ is strongly non-linear around the peak position. Here, the k-vector blurring yields a reduction of the elastic Rayleigh peak, most significantly for the data applying the OCP model. An error up to $\pm 12.5\%$ in the determination of the scattering angle, that means, $\theta = 95 \pm 12\,^\circ$, can smear out the results in such a way, that the previous differences of 30% between the OCP and the Yukawa model will be reduced to 15%. Obviously this fact, will make an experimental verification even more challenging.

In summary, the different ion structure models significantly change the theoretically predicted scattering spectra and, thus, the interpretation of the experimental data. This is particularly important in the collective scattering regime, as the height of the elastic Rayleigh peak is currently used to extract the temperature and the ionisation degree of the system. Therefore, an experimental verification of the various theories is highly desirable for the advanced development of x-ray Thomson scattering as a reliable diagnostics tool in WDM. For an optimal testing ground, a strongly coupled, partially ionised system should be considered as the different theories will predict the largest differences. Furthermore, the wave vector probed should be chosen carefully to access the regions with the most discrepancies under consideration of experimental uncertainties due to sample size, scattering geometry, bandwidth of x-ray source and finite detector resolution.

6.2.3 Influence of various models for the screening cloud

In section 5.3 a pseudo-potential approach to investigate the effect of occupied core states on the interaction of free electrons was introduced. This model accounts for the screening cloud around an ion in a partially ionised plasma. Thereby, the contribution of the tightly bound electrons is condensed into an effective potential (see Eq. (5.24) and Eq. (5.26)) between electrons and nuclei. As a main result, it could be shown that the corresponding screening function, $q(k)$, is strongly modified with respect to the Debye result (5.23). Now, the impact of these discrepancies between the different theoretical approaches on the interpretations of the elastic x-ray scattering feature will be discussed.

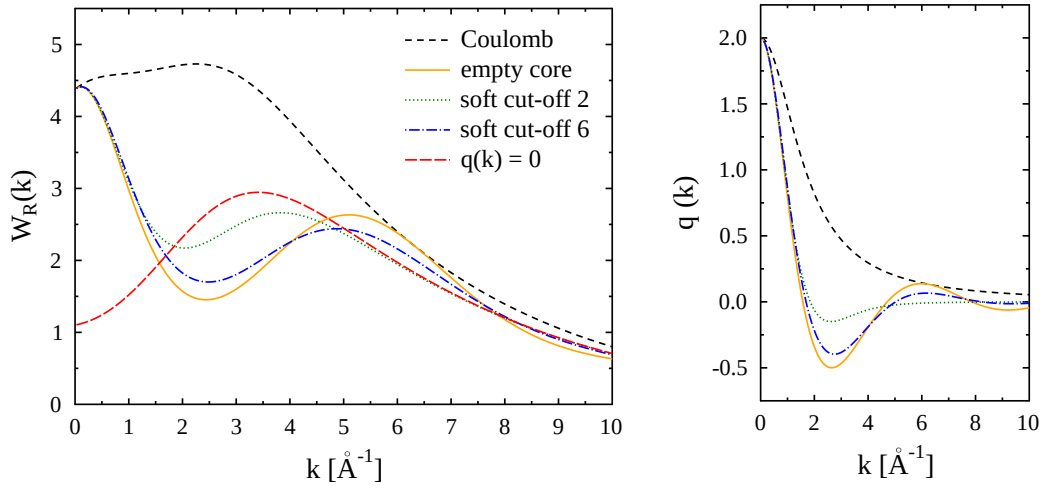

(a) weight of the Rayleigh peak

(b) screening function

Figure 6.15: Weight of the Rayleigh peak for a beryllium plasma at solid density with $T = 12\,\mathrm{eV}$ and $Z = 2$. The ion-ion structure factor was obtained by HNC calculations applying a Yukawa model with an additional short-range repulsion (see Fig. 4.8) and the form factor is taken from DFT simulations. The used screening function, $q(k)$, shown in the right panel, applies several pseudo-potentials (see Eq. (5.24) and Eq. (5.26)) in linear response. The soft-core potential (labelled soft cut-off) is shown for exponents 2 and 6, respectively. The free cut-off parameter in the pseudo-potentials is set to be $r_{cut} = 1$Å. For comparison, $W_R(k)$ is also shown for the case where the screening function is set zero.

The weight of the Rayleigh peak was calculated applying various models to describe the screening cloud for a beryllium plasma. The results are shown in Fig. 6.15. For a better understanding, the right picture shows the related screening functions obtained by the pseudo-potential approach, as already presented in Fig. 5.7. The labels in the figure refer to the used potentials: a pure Coulomb potential (1.14), an empty core potential (5.24) and a soft-core potential (5.26). For comparison, the weight of the Rayleigh peak is also presented for the case where the screening function is set zero. Fig. 6.15 shows that the intensity of the Rayleigh scattering is strongly reduced for $k < 5\,\text{Å}^{-1}$ if pseudo-potentials are applied. It increases, however, again for small wavenumbers $k < 2\,\text{Å}^{-1}$ merging finally in the result applying the Coulomb potential for the long wavelength limit, that is, $k = 0$. This rise in the intensity of the Rayleigh peak cannot be reproduced if the screening function is neglected completely, that is, $q(k) = 0$.

The possibility of a significantly reduced Rayleigh peak due to the screening function has important implications for the development of x-ray Thomson scattering as a reliable diagnostic tool. The intensity of the Rayleigh peak in the collective

scattering regime has often been found to be much lower then predicted by the theory obtained from linearly screened interactions [Döppner et al., 2009; Glenzer and Redmer, 2009]. However, structure factors which were obtained by HNC calculations applying these screened ion-ion potentials yield very good agreements in comparisons with *ab initio* simulations [Wünsch et al., 2009a]. Therefore, the observed, reduced intensity might indicate a small or even negative screening function.

Although the simple description with pseudo-potentials needs improvements, the trend of the effect is in agreement with experimental findings. It shows also qualitative agreement with DFT-MD simulations [Desjarlais, 2011]. Further work is required to obtain more realistic electron-ion pseudo-potentials to allow for a quantitative comparison with experiments and improve the understanding of the electronic structure in warm dense matter.

6.3 Warm dense mixtures

Recent x-ray scattering experiments have moved from studying simple elements, such as, beryllium [Glenzer et al., 2003a, 2007] and lithium [García Saiz et al., 2008], to investigate more complex, composite materials, such as lithium-hydride, LiH [Kritcher et al., 2008, 2009], and plastics, CH [Sawada et al., 2007; Barbrel et al., 2009]. For the analysis of their x-ray scattering signals several components must be included in the description to account for all mutual correlations between the ion species considered. The corresponding theoretical framework was derived in detail in section 3.2.2. In the following, the main focus will lie on the elastic scattering feature, as the free electron feature is not affected by the different ion species. The corresponding weight of the Rayleigh peak is defined in a multicomponent system as (see Eq. (3.73))

$$W_R(k) = \sum_{\alpha,\beta} \frac{\sqrt{n_\alpha n_\beta}}{n_i} \left[f_\alpha(k) + q_\alpha(k)\right] \left[f_\beta(k) + q_\beta(k)\right] S_{\alpha\beta}(k) \; . \tag{6.6}$$

The summation runs over the different ion species, α and β, with the corresponding ion densities, n_α. n_i denotes the total ion density in the system. In this generalised version, the form factors, $f_\alpha(k)$, and the screening functions, $q_\alpha(k)$, associated with the specific ion species α are required. The partial structure factors, $S_{\alpha\beta}(k)$, contain all the structural information of the ionic subsystem and, thus, all the mutual correlations between the different ion species. Methods to calculated these structure factors were introduced in section 4.5.

Fig. 6.16 presents the ionic structure as well as the weight of the Rayleigh peak

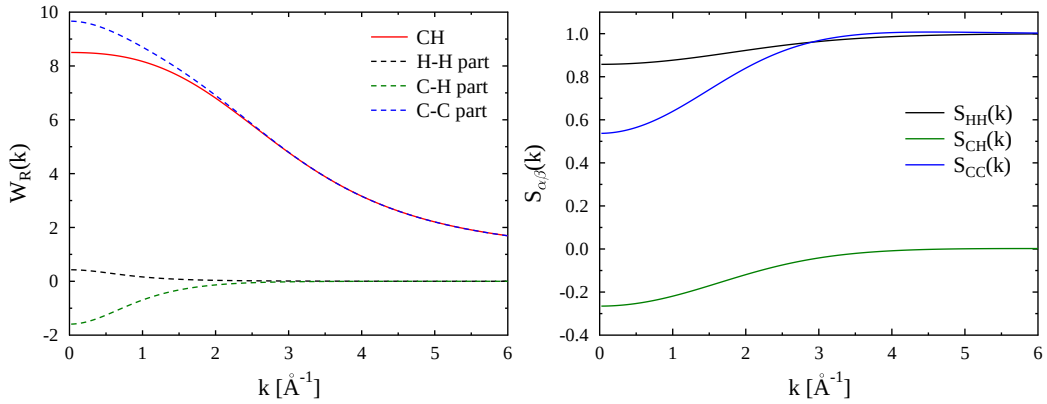

(a) weight of the Rayleigh peak (b) partial structure factors

Figure 6.16: Structure factors and weight of the Rayleigh peak for a CH plasma with $n_C = n_H = 5 \times 10^{22}\,\mathrm{cm}^{-3}$ and a temperature of $T = 8\,\mathrm{eV}$. The ion charge states are $Z_H = 1$ and $Z_C = 2$. The left panel shows the weight of the Rayleigh peak, $W_R(k)$ (solid line), and its three contributions (dashed lines). The right panel presents the associated partial structure factors obtained by a two-component HNC approach applying the Yukawa model. The screening functions are calculated in linear response to a Coulomb field and the form factor for C^{2+} is taken from DFT simulations.

for a dense CH plasma. In the right picture the partial structure factors are shown which are obtained by a two-component HNC approach applying a linearly screened Coulomb potential between the ions. For the plasma parameters considered, the higher charged carbon ions exhibit a more distinct structure than the protons or the cross term. In fact, the protons are only moderately coupled with a classical coupling parameter of $\Gamma = 1.3$. They can nearly be described as a uniform background as demonstrated by the almost constant structure factor that is typical for weakly coupled systems. Note, that the partial structure factor, $S_{CH}(k)$, presents the typical characteristics of the cross terms. As unity is not added in the definition (2.48), it yields negative values for small wavenumbers, k, and the long-range limit is zero. The total structure factor, however, is positive definite.

Fig. 6.16a shows the weight of the Rayleigh peak calculated by Eq. (6.6) for a CH plasma. The required form factor for the double charged carbon ions is taken from DFT simulations. Due to the fact that hydrogen is fully ionised, only the screening function and no atomic form factor has to be considered. The contributions of the screening clouds are calculated in linear response (5.23) for the carbon and for the hydrogen ions separately. The resulting weight of the Rayleigh peak is shown as a red solid line in the figure. Furthermore, the three contributions related to the

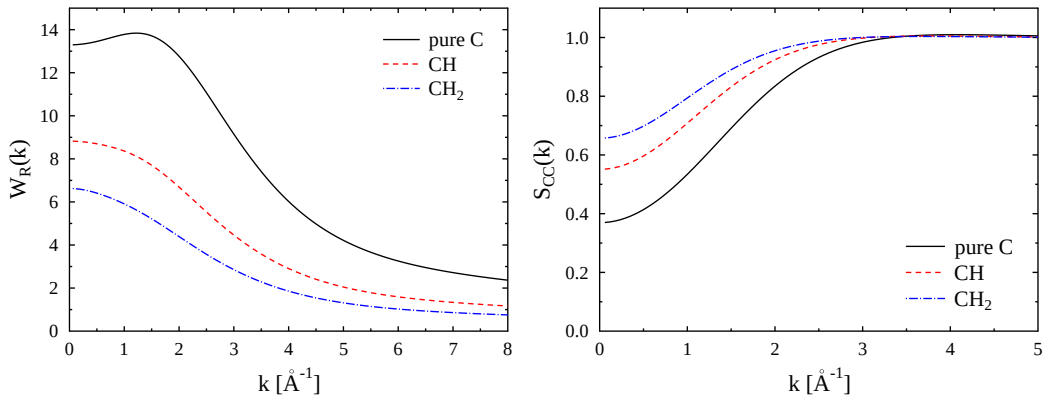

(a) weight of the Rayleigh peak (b) partial structure factors

Figure 6.17: Comparisons of the weight of the Rayleigh peak for a pure carbon, a CH and a CH_2 plasma with a constant ion density of $n_i = 5 \times 10^{22}\,\mathrm{cm}^{-3}$. The related carbon-carbon structure factors are shown in the right picture obtained by the HNC approach. The ionisation degree of carbon, $Z_C = 2$, and the temperature of $T = 8\,\mathrm{eV}$ are fixed for all systems. For the calculations of CH and CH_2 fully ionised hydrogen is assumed. The required electron distribution, $f(k)$ and $q(k)$, are calculated as described in Fig. 6.16.

different combinations of C and H ions are plotted as dashed lines in the figure. This comparison makes it clearly visible that the elastic ion peak is mainly given by the scattering on the C^{2+} ions due to the higher number of electrons, bound as well as valence electrons. The contribution of the C−H term is negative for small wavenumbers, k, due to the behaviour of the related structure factor $S_{CH}(k)$.

To investigate the influence of a second material in the system, a pure carbon, a CH and a CH_2 plasma will be compared in the next example. Fig. 6.17 shows the weight of the Rayleigh peak as well as the structure factors for the different cases. To gain the partial structure factor, $S_{CC}(k)$, a one- and a two-component HNC code with a screened Coulomb interaction was used. The pure carbon plasma shows the most pronounced structure. With the increase of the proton density, the associated structure factor rises for small k values. This is due to the fact that the protons in the system contribute to further screening between the carbon ions yielding a decrease of the carbon-carbon coupling. Obviously, this effect becomes more significant with a higher proton density in the case of CH_2.

A significant modification of the weight of Rayleigh peak due to the protons can be seen in Fig. 6.17a. For a pure carbon system, the Eq. (6.6) simplifies to $W_R(k) = [f_C(k) + q_C(k)]^2 S_{CC}(k)$, whereas three contributions have to be considered for the two cases of plastics. With the occurrence of protons in the system, the ion

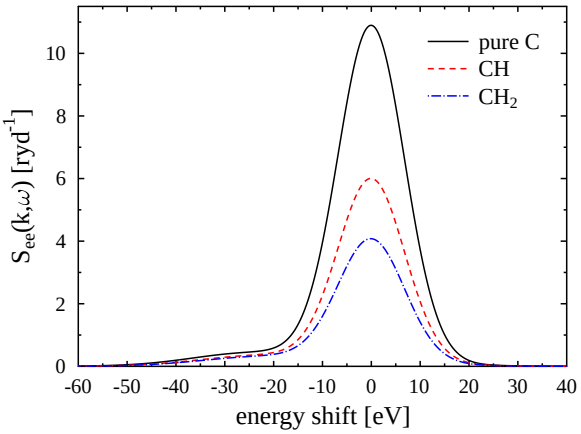

Figure 6.18: The total dynamic structure factor for warm dense carbon, a CH and a CH_2 plasma as considered in Fig. 6.17. The initial photon energy is $E_i = 8\,\mathrm{keV}$, the FWHM of the Gaussian instrument function is $\Delta E = 16\,\mathrm{eV}$ and the scattering angle is $\theta = 25°$ leading to a scattering parameters of $\alpha = 0.76$.

peak decreases nearly by a factor of two. This reflects the change in the partial structure factor due to the multicomponent description. Even though the weight of the Rayleigh peak is dominated by the scattering on the carbon ions, the full multicomponent description is necessary to get the correct statistical weight given by the densities of the elements considered. An increase of the proton density, like given with CH_2, leads to a further reduction of the elastic scattering feature $W_R(k)$.

The effects on the weight of the Rayleigh peak can be also observed in the scattering intensity characterised by the dynamic electronic structure factor. Fig. 6.18 clearly shows that the Rayleigh peak is very sensitive to the elements in the probe volume. The occurrence of protons in the CH plasma leads to an almost 50% reduction in the intensity of the elastic scattering feature in comparison with a pure carbon system. A further increase of the proton density by a fixed total ion density causes another 30% decline in the intensity. These differences should exceed the experimental uncertainties and, thus, indicate that x-ray Thomson scattering is capable of probing mixing properties in warm dense matter.

6.3.1 Approximation based on an average state of the system

To apply the full multicomponent description of the x-ray scattering signal presented in Eq. (3.73), all partial structure factors as well as the associated electron densities around each ion species considered are required. An approximate treatment for x-ray scattering experiments with multiple ion species was published by G. Gregori

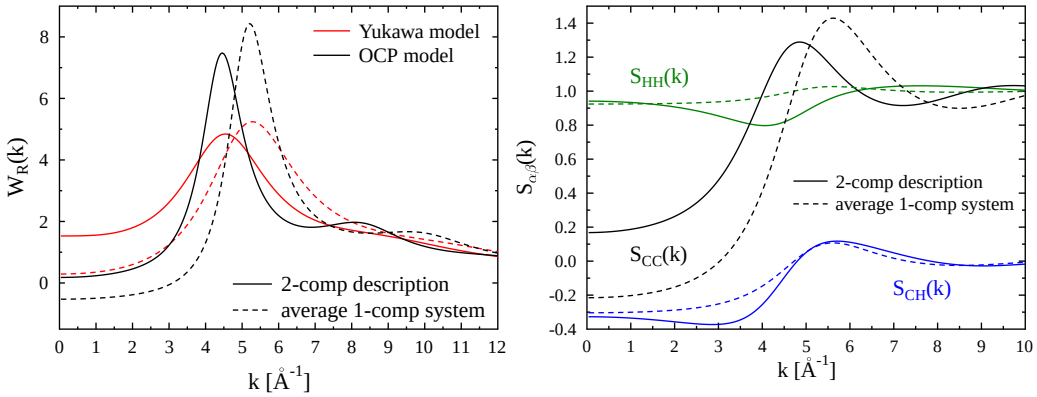

(a) weight of the Rayleigh peak

(b) partial structure factors

Figure 6.19: Comparison of the weight of the Rayleigh peak for a CH plasma calculated by an approximation published by G. Gregori *et al.* [Gregori et al., 2006] that is based on an average state of the system (dashed lines) with results from a two-component description applying Eq. (3.73) (solid lines). Results for $W_R(k)$ are presented for a Yukawa (red lines) and a OCP model (black lines). The partial structure factors shown in the right panel are results from HNC calculations in the Yukawa model only. Considered is a CH plasma with $n_\mathrm{C} = n_\mathrm{H} = 2.3 \times 10^{23}\,\mathrm{cm}^{-3}$, $T = 1\,\mathrm{eV}$, $Z_\mathrm{C} = 4$ and $Z_\mathrm{H} = 1$.

et al. [Gregori et al., 2006]. This description is based on a structure factor for ions with an average state of the system. Here, the required partial structure factors are generated from an effective one-component system with an average ion charge state via Eq. (4.45). As already discussed in section 4.5, this expression is only correct in the limit of weakly coupled plasmas where the random phase approximation is applicable. Although it yields good agreements in comparisons with full multicomponent methods up to moderate coupling strengths, see Fig. 4.13, this approximation is unable to describe the highly non-linear effects in the structure of strongly coupled ions. A further simplification applied in the method of Ref. [Gregori et al., 2006] is the use of an averaged screening cloud for all ion species. This assumption will be applicable as long as the ion charges of the various ion species are similar. In cases where ions occur with strongly dissimilar charge states, as $Z_1 = 1$ and $Z_2 = 4$, the simplification is causing error.

The differences that arise in the weight of the Rayleigh peak, by applying the approximate treatment of Ref. [Gregori et al., 2006] in comparison with the full multicomponent formula (3.73), are presented in Fig. 6.19a. The required structure factors are obtained by HNC calculations applying a pure Coulomb potential and a linearly screened Coulomb potential, that is, the OCP and the Yukawa model,

respectively. For the effective one-component system an average ionisation degree of $Z_f = 2.5$ is used for the CH plasma. For a better understanding, the related partial structure factors are presented in Fig. 6.19b for the Yukawa model. For their calculation, Eq. (2.48) is applied for the two-component description whereas Eq. (4.45) is used in the case of the effective average one-component system.

For both, the unscreened and the screened ion systems, the maximum of the Rayleigh peak is shifted resulting in more than 100% difference in the scattering signal for $k < 3\,\text{Å}^{-1}$ which allows for an experimental distinction between the theories. This small k behaviour reflects the fact that the higher charged carbon ions imprint their structure onto the proton subsystem which cannot be described by the one-component calculation (see Fig. 6.19b). The mutual screening of the ions is also neglected in the reduced model of [Gregori et al., 2006] which results in a strongly underestimated Rayleigh peak. In the OCP case, the Rayleigh peak, obtained by the approximate treatment, predicts even negative values, which is an unphysical behaviour. Thus, in agreement with comparisons presented in section 4.5, for strongly coupled, multicomponent systems, the analysis of the x-ray scattering signal should be based on the full multicomponent expression (3.73) derived in section 3.2.2.

6.3.2 Applications to ICF and astrophysics

The possibility of probing mixtures and composite materials under extreme conditions can have important applications for ICF research and planetary physics. In both cases, mixing properties play a crucial role, for instance, for the energy balance of planets or for the performance of ICF capsule. Here, it will be shown on two examples that elastic x-ray scattering is capable of providing information about the degree of mixing in strongly compressed samples.

First, a mixture of beryllium and hydrogen will be considered as it might be relevant in experiments related for ICF research. Here, beryllium is considered as possible shell material in the ICF capsule. During the compression of the target, the outer layer of the fuel and the ablator will mix due to Rayleigh Taylor instabilities. In this region, beryllium and hydrogen will occur as two fluids which will later microscopically mix due to diffusion. The degree of mixing as well as the existence of both materials as either hydrodynamic or microscopic mixtures is highly relevant for the performance of the target [Regan et al., 2002, 2004].

Fig. 6.20 presents the weight of the elastic Rayleigh peak and the related beryllium-beryllium structure factors for beryllium-hydrogen mixtures with various mixing ratios. The plasma parameters were taken from recent x-ray scattering experiments on pure, shock compressed beryllium [Lee et al., 2009] to demonstrate

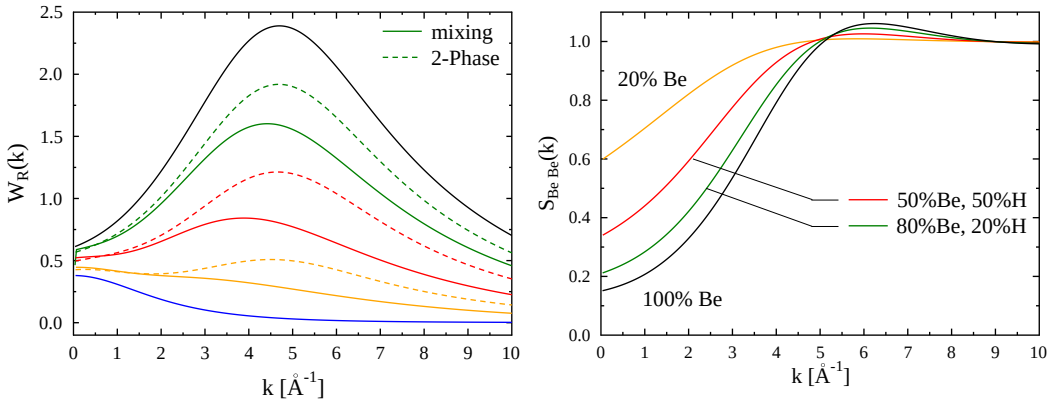

(a) weight of the Rayleigh peak

(b) partial structure factors

Figure 6.20: The weight of the Rayleigh peak, $W_R(k)$, for microscopic mixtures of beryllium and hydrogen (solid lines) and also for systems that contain both materials in two pure phases (dashed lines). The concentrations of beryllium are (from top to bottom): 100%, 80%, 50%, 20%, and 0%. The temperature of the system is $T = 13\,\mathrm{eV}$. The total densities were arranged in a way that the system is in pressure equilibrium with pure beryllium at $\varrho_{\mathrm{Be}} = 5.544\,\mathrm{g/cm^3}$. The right picture displays the related partial beryllium-beryllium structure factor.

that the conditions required can be reached with existing experimental set-ups. As beryllium scatters more efficiently than hydrogen, the pure beryllium (black line in Fig. 6.20) presents the highest value in the elastic Rayleigh peak for intermediate wavenumbers. With the occurrence of protons, the intensity of the Rayleigh peak decreases. Thereby, the strength of the peak is determined by the degree of mixing in the probe volume. An incorporation of 20% hydrogen leads to a decrease of roughly 30% in the weight of the Rayleigh peak at $k = 4.5\,\mathrm{Å}^{-1}$ if microscopic mixing is considered. A mixture of 50% Be and 50% H yields a scattering signal which is reduced by up to 70% in comparison with the signal obtained from pure beryllium. This behaviour can be understood if one considers the changes in the partial structure factors between the beryllium ions due to the occurrence of protons in the system. As already discussed for a CH plasma in the previous section, the coupling strength between the beryllium ions is reduced by the increasing hydrogen concentration. This causes the increase of the related structure factor, $S_{\mathrm{BeBe}}(k)$, for small k-values. Furthermore, no form factor needs to be considered as the hydrogen ions are fully ionised. However, the double charged beryllium ions still possesses tightly bound electrons from the K-shell, which are described by the associated form factor, $f_{\mathrm{Be}^{2+}}(k)$. This contribution is added, according the ratio of the beryllium content, to generate the weight of the Rayleigh peak and causes a significant contribution for

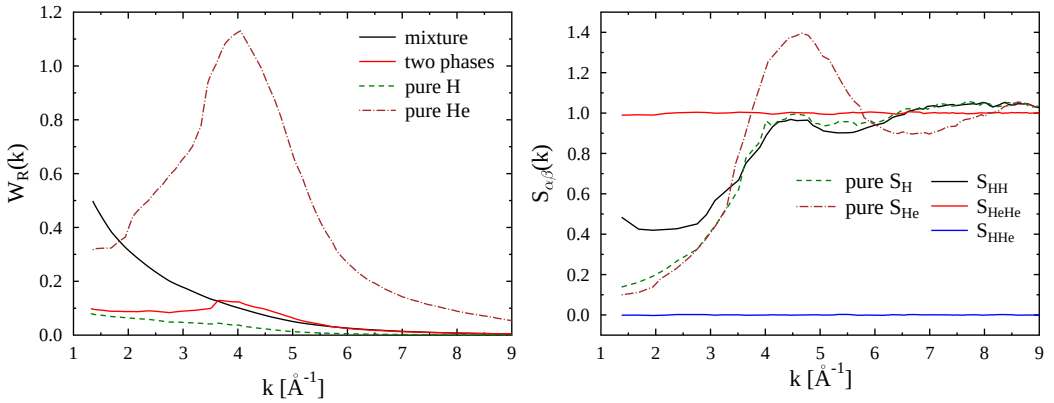

(a) weight of the Rayleigh peak

(b) partial structure factors

Figure 6.21: The weight of the Rayleigh peak for pure hydrogen, pure helium, and a mixture of both elements at a temperature of $T = 5000\,\mathrm{K}$. The mixture consists of 7.6% atomic helium and 92.4% fully ionised hydrogen. All systems have an electron density of $n_e = 4.7 \times 10^{23}\,\mathrm{cm}^{-3}$. The partial structure factors of the three systems are obtained by DFT-MD simulations.

intermediate wavenumbers.

The elastic scattering feature also provides information about the kind of mixing of the region probed. Whereas both microscopic mixtures and two-phase systems scatter very similar at small wavenumbers, significant differences arises in the weight of the Rayleigh peak for larger k-values. Thus, hydrodynamic and microscopic mixing can be distinguished if the matter is probed under different angles.

The observed differences in the weight of the Rayleigh peak are large enough for intermediate wavenumbers to allow experimental investigations of the mixing properties. In particular, backscattering geometry is required to access intermediate wavenumbers, that means, probing in the non-collective scattering regime. As discussed in section 6.1.2, the scattering signal in this regime is less dependent on the ionic structure which simplifies the theoretical analysis of the scattering signal.

As a second example, the mixture of hydrogen and helium is investigated for conditions similar to those found in the interior of giant gas planets like Jupiter [Guillot, 1999]. Under the selected plasma conditions, hydrogen is fully ionised whereas the helium occurs in the atomic phase. To describe the neutral atoms correctly within the system, DFT-MD simulations were performed by J. Vorberger leading to the structure factors presented in Fig. 6.21b. Here, the structure factors of the mixture are compared to results for pure hydrogen and helium gas. The mixing process can lead to either a microscopic mixture or a phase separation into a helium-poor and a helium-rich phase [Militzer et al., 2008; Lorenzen et al., 2009]. Depending

on the scattering volume, x-rays could scatter only on the pure substances in the phase-separated case. The associate weights of the Rayleigh peaks for all cases are shown in Fig. 6.21a. As hydrogen is fully ionised only the atomic form factor of helium is required in addition to the screening function for the hydrogen ions, which was evaluated in linear response to a Coulomb field (5.23).

It can be seen that the weight of the Rayleigh peak shows large differences between the pure substances and the mixtures. The elastic scattering signal for pure helium features a maximum around $k = 4\,\text{Å}^{-1}$, whereas $W_R(k)$ is nearly featureless for the scattering on a pure hydrogen gas. Due to the ratio of the mixture, the two-phase system is dominated by the properties of hydrogen, yielding an almost featureless weight of the Rayleigh peak, too. The elastic Rayleigh peak of the mixture, however, shows a monotonic decrease for small wavenumbers.

The reason for the large discrepancies lies not only in the fact that the helium atoms scatter x-rays more efficiently. The different structure factors play an essential role, too. Pure helium has a strong peak in the structure factor which is also imprinted in the related strength of the elastic feature. This feature disappears in the mixture where, due to the concentrations selected, the helium density is too low to significantly influence the behaviour. Nevertheless, the small fraction of helium affects the coupling strength in the hydrogen subsystem leading to an increased weight of the Rayleigh peak for small k-values.

The distinction between microscopic mixture and phase-separation can enhance the understanding of the structure of giant gas planets as phase separation of the hydrogen-helium mixture leads to further layers in the mantle of giant gas planets. Also the evaluation of planets is strongly influenced by mixing/demixing of the components. Best example is probably Saturn, where the best explanation of the measured surface temperature is an additional heat source in the planet due to demixing of hydrogen and helium. Thus, laboratory experiments are needed to investigate mixing properties of material under extreme conditions. Elastic x-ray scattering will be an excellent diagnostic for this task.

Chapter 7

Application of the theory to x-ray scattering experiments

The application of light scattering to investigate the structural properties of matter is widely spread in physics. Thomson scattering was successfully applied in low-density plasmas to accurately extract the plasma conditions [Evans and Katzenstein, 1969; Sheffield, 1975]. With the development of powerful laser-driven x-ray sources and free electron lasers (FEL), it is nowadays possible to use this diagnostics for the investigation of high-density matter as well. In this chapter, the theory presented is used to describe some recent scattering experiments performed to investigate the various states of dense matter.

At the beginning of the chapter, the first x-ray Thomson scattering experiments probing solid-density beryllium isochorically heated will be discussed. Here, spectrally resolved scattering signals were obtained which were used to analyse the material under investigations. While the extraction process of the plasma conditions is well-understood in the non-collective scattering regime, problems arise in the analysis of the collective scattering signal. The complexity of the analysis will be highlighted where special care is taken with respect to the ionic properties in strongly coupled, dense plasmas.

The second example considers a lithium target which was compressed above solid density by a laser-driven shock wave. Due to the compression, the mass density of the system is unknown and needs to be extracted as well from the scattering signal. This experiment directly addressed the ionic structure in compressed matter. Due to the combination of experimental analysis and quantum simulations, it was possible to extract the ion-ion structure factor directly from the scattering signal without any assumption from theoretical models. This allowed the investigation of the long

wavelength limit of the ion response in shock-compressed matter.

As a last example, a scattering experiment on warm dense lithium hydride will be studied. Here, the effect of multiple ion species will be demonstrated. In particular, the differences arising between the single-ion model and the full multi-component treatment will be highlighted. Even for a multicomponent treatment, the experimentally obtained data still show discrepancies when compared with the theoretical predictions. Thus, the need for further studies addressing the structural properties in high-density matter becomes obvious.

7.1 Isochorically heated beryllium

The first experiments demonstrating the use of x-ray Thomson scattering to probe solid density matter were performed by the research group of S.H. Glenzer using the Omega laser facilities in Rochester, USA [Glenzer et al., 2003a, 2007]. In 2003, laser-produced x-rays were successfully applied to measure basic thermodynamic properties of isochorically heated, solid-density beryllium in backscattering geometry [Glenzer et al., 2003a]. The spectrally resolved scattering profile shows the inelastic Compton feature. Its line shape was used to reveal the electron temperature within an error range of $10-20\%$ in the case of non-degenerate systems. Furthermore, the ionisation degree was inferred using the ratio of the Compton scattering intensity to the intensity of the Rayleigh peak. The mass density was constant due to isochoric heating. The entire system could thus be fully determined from the analysis of the x-ray scattering signal.

In a second campaign of experiments published 2007, the collective scattering regime was investigated and the first measurements of plasma oscillations in warm dense matter could be presented [Glenzer et al., 2007]. The scattering spectrum of isochorically heated beryllium demonstrates that the plasmon frequency shift can be used to infer the electron density within 20%. Thus, in principle, all basic plasma parameters of solid-density matter can be obtained from the x-ray scattering signal if different geometries, that means, a combination of forward and backward scattering, are applied as demonstrated in these proof-of-principle experiments.

7.1.1 Experiment

The target material for these x-ray scattering experiments was beryllium at normal density. Beryllium is of particular interest for the ICF research as it might be used as shell material in the fusion capsule. Furthermore, beryllium is a low-Z material

with two conduction electrons. This combination has the effect that the intensities of the elastic and inelastic scattering feature are comparable in magnitude.

For the heating of the target, the beryllium sample is wrapped into a rhodium or silver foil which was illuminated by the laser system of the Omega facility. To heat the sample up to 50 eV, as required for the first scattering experiment, 30 laser beams with wavelength $\lambda_i = 351\,\mathrm{nm}$, a duration of 1 ns and a total energy of 15 kJ were used. The rhodium laser plasma converts $5-10\%$ of the laser energy into L-shell radiation which heats the target. The absorption length is reflected in the geometry of the beryllium sample which has a cylindric form with 600 µm diameter and a length of 750 µm. The heating process is isochoric and homogeneous in the center of the sample. This was verified by radiation-hydrodynamic modelling which predicts densities of $2-3\times10^{23}\,\mathrm{cm}^{-3}$ and temperatures in the order of 30 eV. For the x-ray scattering experiment in the collective regime, a silver foil and 20 pump lasers from the Omega facility with a total energy of 10 kJ were used. Here, the temperature was of the same magnitude as the Fermi energy, that is, $T_e = 10-15\,\mathrm{eV}$. The advantage of isochoric heating lies in the constant mass density which allows the extraction of the ionisation degree directly from the measured electron density or vice versa. This obviously simplifies the analysis of the x-ray scattering spectrum significantly, as one thermodynamic quantity is already known.

For these first scattering experiments, laser-produced x-rays from line radiation were applied. The energy has to be sufficiently high to penetrate the solid-density target. In the case of the experiment in 2003, a titanium foil was irradiated with 15 laser beams with a total energy of 7 kJ for 1 ns yielding an intensive He-α radiation at $E_i = 4.75\,\mathrm{keV}$. The second laser system was delayed by 1 ns with respect to the heating beams, which allowed the system to be probed at the highest electron temperature. The bandwidth of the probe beam is $\Delta E/E \approx 0.005$ which is within the limit for spectrally resolving the inelastic Compton feature from the elastic Rayleigh peak. For the second class of experiments, Saran foils were used to produce x-rays with an energy of $E_i = 2.96\,\mathrm{keV}$ by the chlorine Ly-α emission line. To maximise the number of photons in the detector, the x-rays needs to be produced close to the target as the laser x-ray source emits into 4π steradians.

The scattered photons are observed under a scattering angles of $\theta = 125^\circ$ and $\theta = 40^\circ$ in the case of non-collective and collective scattering, respectively. To spectrally disperse the scattered photons, a high efficiency Bragg crystal is applied. The x-rays are finally detected by a CCD camera. The resolution of the Bragg crystal detector is around $\Delta E/E \approx 0.003$ yielding, together with the narrow bandwidth of the x-ray sources, a total spectral resolution of 50 eV and 7.7 eV for the scattering

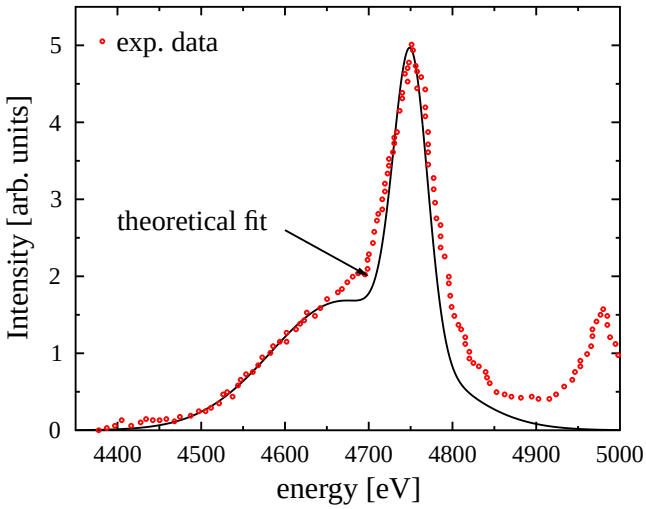

Figure 7.1: Experimental scattering spectrum of isochorically heated solid-density beryllium in backscattering geometry: data taken from [Glenzer et al., 2003a]. The theoretical fit was generated with Eq. (6.3) using the plasma parameters given in the publication, that is, $T_e = 53\,\mathrm{eV}$, $n_e = 3.3 \times 10^{23}\,\mathrm{cm}^{-3}$ and $Z = 2.7$. The electronic feature was calculated in RPA, the ion feature uses structure factors obtained by HNC and form factors are taken from DFT simulations. A bandwidth of $\Delta E/E = 0.01$ is considered in the instrument response function.

experiment in the non-collective and collective regime, respectively.

A more detailed description of the experiments with schematic pictures of the target and the set-ups can be found in the related publications of Glenzer *et al.* [Glenzer et al., 2003a,b, 2007; Glenzer and Redmer, 2009]

7.1.2 Results for the non-collective scattering regime

An experimentally obtained scattering spectrum in backscattering geometry is shown in Fig. 7.1 [Glenzer et al., 2003a]. The scattering profile shows two peaks according to the radiation lines from the titanium foil at 4.75 keV and 4.92 keV. The latter corresponds to the low intensity Ly-α radiation line. The photons scatter on both lines elastically causing a Rayleigh peak at the initial photon energies. As the Ly-α emission is lower in intensity, the related scattering spectra is also reduced in comparison with the scattering contribution at the strong He-α radiation line. The latter line also produces a clearly visible inelastic Compton shifted feature. In the original publication, a scattering spectrum of cold beryllium was also presented highlighting the broadening of the Compton feature with the increase of the temperature and thus the increase of the thermal motion of the electrons in the case of heated beryllium.

To extract the plasma parameters, one generates synthetic scattering profiles taking the probe spectrum and the finite resolution of the detector into account. These profiles will then be matched to experimentally measured data by adjusting the plasma parameters. The best fit is then considered to yield the conditions of the material investigated. The applied theory is presented in Ref. [Gregori et al., 2003], which is based on the RPA approximation. Following this routine, the sample is characterised by $T_e = 53\,\mathrm{eV}$, $Z = 2.7$, $n_e = 3.3 \times 10^{23}\,\mathrm{cm}^{-3}$ and the known mass density of $\varrho = 1.85\,\mathrm{g/cm}^3$. An error range for the temperature of $10 - 20\%$ and for the density of 20% is given for the heated beryllium.

Based on these plasma parameters, a theoretical scattering spectrum based on Eq. (6.3) was generated here as well. This spectrum applies the theories presented in this thesis. That is, the free electron feature is described in RPA and the inelastic excitations are neglected as their contribution is small in comparison with the free electron dynamic structure factor [Gregori et al., 2003; Glenzer et al., 2003b]. To calculate the elastic Rayleigh peak, an ion structure factor obtained by the HNC approach is used. Here, the applied effective inter-particle potential is less relevant, as the structure factor is already close to unity (wavenumber of $k = 4.27\,\mathrm{Å}^{-1}$) for all ionic structure models. The form factor is obtained from the simulations, averaged to the non-integer ionisation degree of $Z = 2.7$ from results for double and threefold charged beryllium ions. The contribution of the screening cloud can be neglected for the large wave vector considered. The result of this procedure is shown in Fig. 7.1 comparing it with the experimental data. Obviously, the synthetic scattering spectrum agrees very well with the experimental results. As only the He-α line at 4.75 keV is considered, the second peak is not fitted by this approach.

The used theories are similar to those applied in the original publication [Glenzer et al., 2003a]. Although the method for the calculation of the ion structure factor is different, the results are insensitive to these changes in the backscattering geometry (see section 6.2.2).

In the following, the fitting process to extract the plasma parameters will be considered in more detail. As discussed in section 6.1.2, the Compton down-shifted line is sensitive to the electron temperature as long as the system is in a non- or partially degenerate state. This condition is fulfilled here as the degeneracy parameter is $n_e\Lambda_e^3 \approx 0.28$ for the plasma conditions considered. In Fig. 7.2, the experimentally measured Compton feature is compared with several synthetic scattering spectra generated for various temperatures. It can be seen that the shape of the Compton feature is sensitive to the temperature of the system. For instance, the slope for $T = 30\,\mathrm{eV}$ is too steep to fit the experimental data, whereas the slope for $T = 70\,\mathrm{eV}$

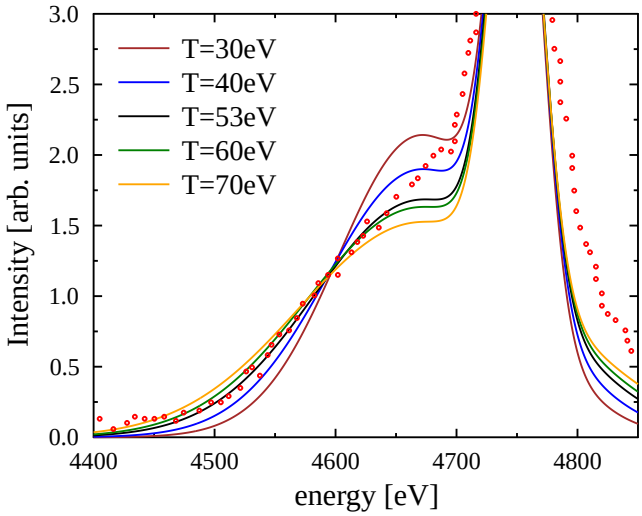

Figure 7.2: Experimentally measured inelastic Compton feature from Fig. 7.1 and theoretical scattering profiles calculated for various temperatures. The electron density of $n_e = 3.3 \times 10^{23}\,\mathrm{cm}^{-3}$ and the ionisation degree of $Z = 2.7$ are fixed. The same methods of generating the synthetic scattering spectra are applied as in Fig. 7.1.

is too shallow. In the case of cold beryllium, the extraction of the temperature is less accurate as the system is in a highly degenerate state with $n_e\Lambda_e^3 \approx 23$ if a temperature of $T = 2.5\,\mathrm{eV}$ is assumed. In this state, the Compton feature presents the parabolic Fermi distribution which is roughly temperature independent.

Furthermore, the ionisation degree can be inferred by comparing the ratio of the intensities of the inelastic to the elastic scattering feature as discussed in section 6.1.2. Fig. 7.3 displays several synthetic scattering profiles calculated for various ionisation degrees and compares them with the experimental data. The Rayleigh peak significantly changes by varying the ionisation degree. This can be understood as the Rayleigh peak reflects the scattering on bound electrons characterised by the form factor, which are shown in Fig. 7.3b for different charge states of the beryllium ions. The best fit yields $Z = 2.7$ and, as the mass density is known, the electron density can be determined to be $n_e = 3.3 \times 10^{23}\,\mathrm{cm}^{-3}$.

To accurately describe a system with a non-integer ionisation degree, a two-component model is required. Here, the double and threefold charged beryllium ions are taken into account as individual components. However, as the charge states are similar and the system is in a weakly coupled state with a classical electron coupling parameter of $\Gamma_{ee} = 0.3$, the outcome of the two-component approach is barely different from results applying an average state of the system (see section 6.3.1).

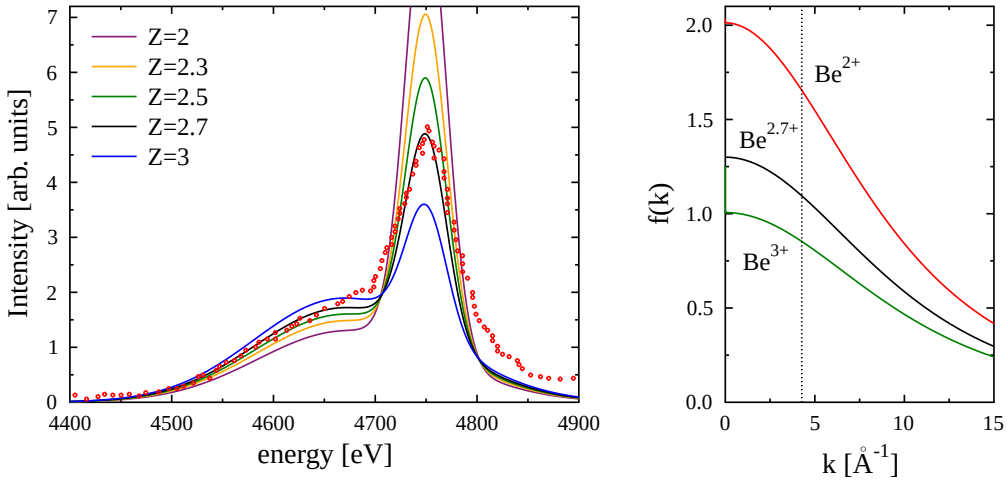

(a) scattering spectrum (b) form factor

Figure 7.3: Experimentally measured x-ray scattering profile from Fig. 7.1 and theoretical scattering profiles calculated for various ionisation degrees. An ion density of $n_i = 1.23 \times 10^{23}\,\mathrm{cm}^{-3}$ and temperature of $T = 53\,\mathrm{eV}$ are used. The same methods to generate the synthetic scattering spectra are applied as in Fig. 7.1. The small panel presents the form factors for the different charge states of the beryllium ions.

As shown above, the plasma parameters can be extracted with an accuracy of $10 - 20\%$ from the non-collective scattering spectrum for isochorically heated beryllium in the warm dense matter region. However, in a system with highly degenerate electrons, the x-ray scattering spectra is roughly temperature independent and, thus, further methods are required to fully determine the state of the system. The analysis is also more complicated in the case of unknown mass density. Here, it might be likely that several sets of basic plasma parameters, that is, electron density, temperature and ionisation degree, can be fitted to the experimental x-ray scattering spectrum and further investigations are required to accurately extract the plasma conditions.

7.1.3 Results for the collective scattering regime

In a second class of experiments, x-ray scattering was performed on solid-density beryllium in forward scattering geometry. According to the initial photon energy of $E_i = 2.96\,\mathrm{keV}$ and a scattering angle of 40°, the scattering parameter is $\alpha = 1.7$. That means, the collective regime was probed. The obtained scattering spectrum is shown in Fig. 7.4 (data from Ref. [Glenzer et al., 2007]). The measured profile presents the elastic Rayleigh peak, caused by electrons co-moving with the ions, as well as the plasmon peak from scattering on kinetically free electrons. These

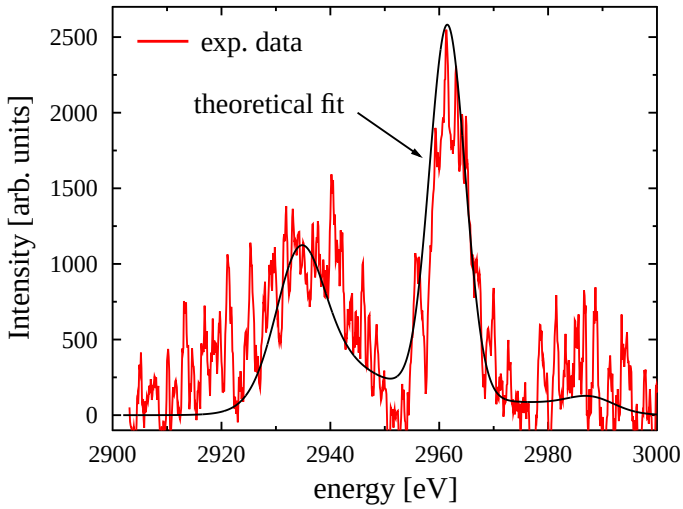

Figure 7.4: Experimental scattering spectrum of isochorically heated solid-density beryllium in forward scattering geometry as published in Ref. [Glenzer et al., 2007]. The theoretical fit was generated after Eq. (6.3) using the plasma parameters ($T_e = 12\,\mathrm{eV}$, $n_e = 3 \times 10^{23}\,\mathrm{cm}^{-3}$ and $Z = 2.3$) as well as the theories described in the publication. A spectral resolution of $\Delta E = 7.7\,\mathrm{eV}$ is applied in the instrument response function.

experiments demonstrated the possibility to investigate collective oscillations in the WDM regime.

For fitting the spectrum and thus extracting the plasma conditions of the beryllium plasma, the free electron feature was calculated originally in the Born-Mermin approach (see section 5.1.3) to account for collision effects between electrons and ions. This theory yields an electron density of $n_e = 3 \times 10^{23}\,\mathrm{cm}^{-3}$ with an accuracy of 20%. As the mass density is constant for isochoric heating, the ionisation degree can be derived as $Z = 2.3$. Furthermore, an upper limit of the temperature could be revealed from the detailed balance relation to be $T_e < 25\,\mathrm{eV}$. A more accurate measurement based on this method requires higher precision scattering signals, in particular of the up-shifted plasmon peak. The width of the plasmon peak is also sensitive to the electron temperature yielding $T_e = 12\,\mathrm{eV}$ from the best fit. For the evaluation of the Rayleigh peak, structure factors were taken from HNC calculations applying the Klimontovich-Kraeft potential (4.42), which is an effective quantum potential. The form factor was calculated with hydrogen-like wave functions for the electrons that feel an effective ion charge (see Eq. (5.20)) and the screening function was determined according to Eq. (5.21) with partial structure factors obtained by the two-component HNC method. The height of the Rayleigh

peak can be used to infer the ion temperature, yielding $T_i = 12\,\mathrm{eV}$ as well. The entire theoretical spectrum takes the spectral resolution of 7.7 eV and scattering angles in the range of $25^\circ < \theta < 55^\circ$ into account.

Based on the descriptions published [Glenzer et al., 2007; Glenzer and Redmer, 2009], a theoretical scattering profile is generated here using the extracted plasma conditions, that is, $T = 12\,\mathrm{eV}$, $n_e = 3 \times 10^{23}\,\mathrm{cm}^{-3}$ and $Z = 2.3$. The result is shown in Fig. 7.4 in comparison with the measured signal. The discrepancies in the width of the down-shifted plasmon peak may be caused by the use of RPA to described the free electron feature. This approach neglects collision effects which cause damping and, thus, a further broadening of the plasmon peak. However, the plasmon position is not effected by this improvement which allows the electron density to be inferred with the same accuracy.

As already mentioned in section 6.1.2, the description of the collective scattering signal strongly depends on the theoretical modelling, in particular for the elastic Rayleigh peak. Therefore, DFT-MD simulations were performed by J. Vorberger to investigate the microscopic structure of beryllium under the suggested plasma conditions. The resulting static structure factor as well as the electron density around the ions in real space are shown in Fig. 7.5b and 7.5c, respectively. Following the discussions from section 4.4, the static ion-ion structure factor, obtained by the HNC approach applying the Yukawa model with an additional short range repulsion (labelled HNC-Y+SRR) to account for bound electrons, agrees very well with results from *ab initio* simulations. In contrast, the use of quantum potentials (here the Klimontovich-Kraeft (KK) potential) in the HNC equations underestimates the screening between the ions due to a weak electron-ion interaction yielding results equal to HNC calculations applying the OCP model. The wave vector k probed in the experiment is highlighted as the dotted line in the picture showing the structure factors (Fig. 7.5b). Here, the differences between the various models for the ion structure are significant. In particular, models that take screening into account (Yukawa or Yukawa+SRR) and those which neglect or approximate screening (OCP or KK) strongly differ. The long wavelength limit of the static ion-ion structure factor, that is $\lim_{k\to 0} S_{ii}(k)$, can be calculated using the compressibility sum rule [Schwarz et al., 2010]. This limiting case was evaluated for the plasma conditions of this experiment, yielding a value around $\lim_{k\to 0} S_{ii}(k) \approx 0.4$ which is in fair agreement to the HNC-Y+SRR results.

The electron density around the ions can be derived from DFT-MD simulations as well. Comparing the outcome with the electron distributions of double and threefold charge beryllium ions, as presented in Fig. 7.5c, indicates that the

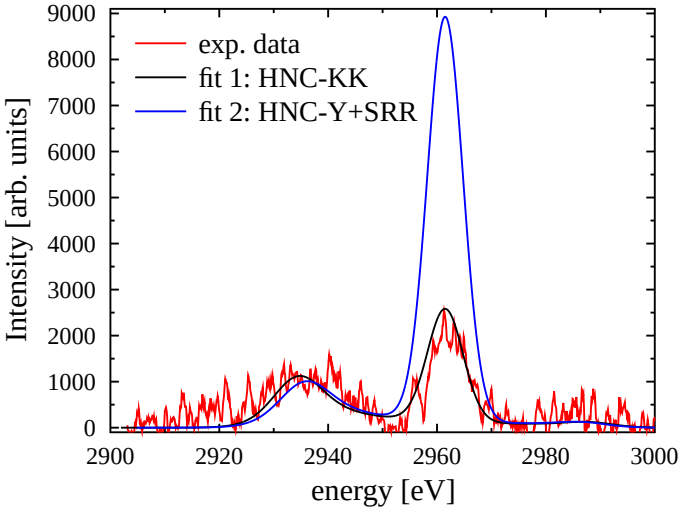

(a) scattering spectrum

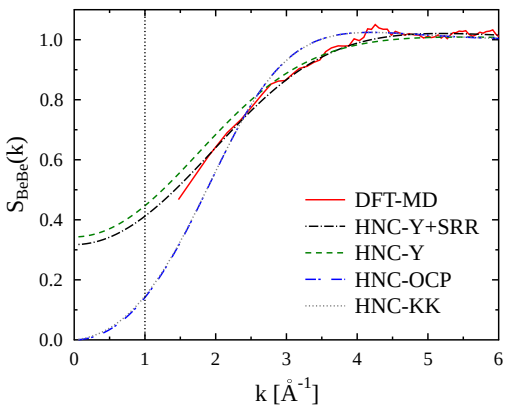

(b) static structure factor

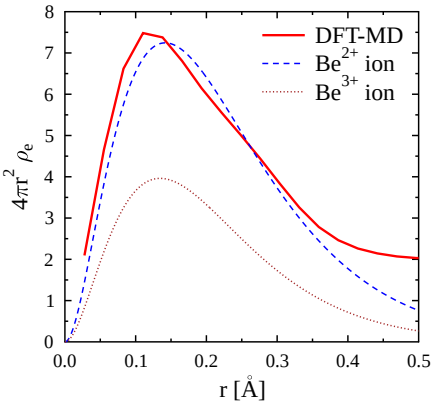

(c) electron density around ion

Figure 7.5: The experimental scattering spectrum for solid-density beryllium from Fig. 7.4 with two theoretical fits. Furthermore, the structure of beryllium is shown: (b) the static ion-ion structure factor comparing the different interaction potentials applied in HNC with results from DFT-MD and (c) the electron density around the ions comparing double and threefold charge beryllium ions with results from DFT-MD. The first theoretical fit (labelled as HNC-KK) applies the theories described in Ref. [Glenzer et al., 2007] whereas the second theoretical fit (labelled as HNC-Y+SRR) uses theories which match best the results obtained by DFT-MD. The dotted line in the panel presenting $S_{\mathrm{BeBe}}(k)$ indicates the wave vector probed.

charge state of the beryllium ions is $Z_f = 2$ for the conditions considered. Taking these parameters for the evaluation of the synthetic scattering spectrum leads to the second theoretical fit presented in Fig. 7.5a (labelled with HNC-Y+SRR according to the method used to obtain $S_{\mathrm{BeBe}}(k)$). It can be seen, that the use of the Y+SRR

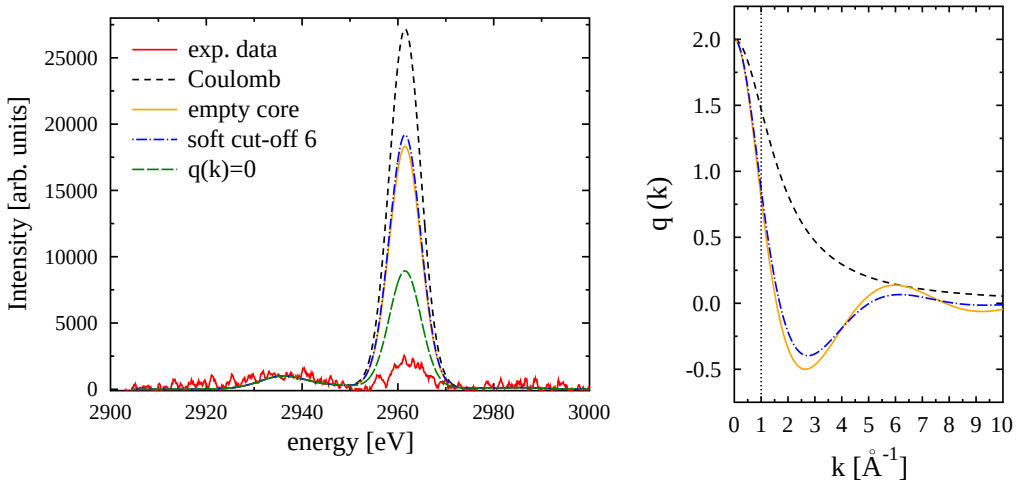

(a) scattering spectrum (b) screening function

Figure 7.6: The experimental scattering spectrum for solid-density beryllium from Fig. 7.4 and theoretical scattering profiles calculated with various theories for the screening functions. The related $q(k)$ are shown in the right panel which was already described in section 6.2.3 in detail. The labels correspond to the pseudo-potentials used to calculate $q(k)$ (see Eq. (5.24) and Eq. (5.26)). The cut-off radius is set to $r_{\text{cut}} = 1\,\text{Å}^{-1}$. Results are also shown for the case where the screening function is set to zero (green curve).

model, which correctly describes the ionic structure of the system in comparisons with DFT-MD simulations, highly overestimates the height of the elastic Rayleigh peak. This discrepancy might be explained by modifications to the distribution of free electrons around the ions which are described by the screening function, $q(k)$.

In section 6.2.3, the influence of various models to calculate the screening function are described. It could be shown, that the use of pseudo-potentials, that account for the effect of core electrons, significantly changes the weight of the Rayleigh peak, $W_R(k)$, in particular for small wavenumbers, k, (see e.g. Fig. 6.15). Here, the newly introduced pseudo-potentials, that is, the empty core potential,(5.24), and the soft-core potential, (5.26), will be used to generate theoretical scattering spectra with static ion-ion structure factors obtained by HNC applying the Y+SRR model. The results are shown in Fig. 7.6. The use of pseudo-potentials in the calculation of $q(k)$ reduces the height of the Rayleigh peak by around 30%, whereas no significant changes arise between the calculations with the empty-core or the soft-cut-off potential. Furthermore, the outcome is shown for the case where the screening function is set to zero, which could be realised by a screening cloud that is infinitely spread in real space resulting in a function whose main contributions are for very small wave vectors only, that is, $k < 1\,\text{Å}^{-1}$. This assumption reduces the Rayleigh peak by 75%

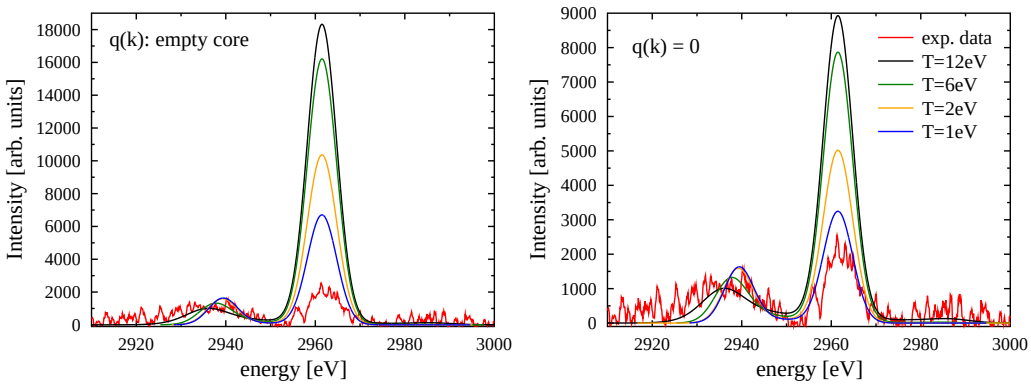

(a) $q(k)$ applying empty core potential

(b) screening function set to zero

Figure 7.7: The experimental scattering spectrum for solid-density beryllium from Fig. 7.4 and theoretical scattering profiles calculated for various temperatures. In the left picture, the empty core potential is used for the calculation of the screening function, whereas in the right picture the screening function is set to zero. The ionic structure is taken from HNC with the Y+SRR model and $Z_f = 2$ is assumed.

in comparison with the linear response approximation applying a pure Coulomb field (5.23). However, even this quite drastic assumption still leads to an overestimation of the strength of the elastic Rayleigh peak by a factor of around 3. As already emphasised, the presented model potentials are quite simple and further studies are required to fully understand the modification of the electron distribution around the ions in partially ionised, solid-density matter.

Another possible explanation for the discrepancies found is related to the temperature extracted from the fitting process. The ion temperature is inferred from the height of the Rayleigh peak and, thus, strongly depends on the theoretical models applied. Using the temperature as a fitting parameter to match the experimental results yields temperatures far below the suggested $T = 12\,\mathrm{eV}$, as can be seen in Fig. 7.7. Given the total energy deposited in the system by the heating beam, a temperature of $\sim 1\,\mathrm{eV}$ is highly questionable. Nevertheless, it might indicate that the system is not in an equilibrium state and, thus, adjustments need to be done for the theoretical modelling of the scattering signal. Recent studies by D.A. Chapman demonstrate that even a small fraction of highly energetic electrons can significantly influence the synthetic scattering signal [Chapman and Gericke, 2011].

In summary, the differences between the theoretical models, the quantum simulations and the experimental data highlight that further studies are required to understand the microscopic structure in WDM. In particular, first principle methods, such as, temperature measurements through the detailed balance, would be very

valuable to validate theoretical predicts.

Nevertheless, the plasma parameters can be inferred from the x-ray scattering signal with a reasonable accuracy, in particular if forward and backward scattering geometry are combined. For isochorically heated matter, the electron density can be derived from the plasmon frequency shift and checked by the shape of the inelastic Compton shift in non-collective scattering regime in the case of partially degenerate systems. Furthermore, the ionisation degree can be tested via the ratio of the intensities of the inelastic to elastic scattering peak in the non-collective regime. In a similar manner, the electron temperature could be revealed from the Compton shape and checked by the width of the plasmon peak. The determination of the ion temperature, however, still presents challenges. As the Rayleigh peak is less sensitive to the ionic structure and, thus, to the ion temperature in the non-collective regime, the temperature required needs to be revealed from the collective scattering spectrum. However, the microscopic structure in the collective regime is still an ongoing research topic.

7.2 Shock-compressed lithium

One way to create a warm dense matter state is laser-driven compression launching a shock wave and creating warm matter with densities above solid density. The analysis of the x-ray Thomson scattering signal in shock-compressed materials is challenging, as the mass density is now an additional unknown variable. This quantity is directly connected to the elastic Rayleigh peak and, thus, to the structural properties of the material under investigation. García Saiz *et al.* performed a scattering experiment which was designed to investigate the long-wavelength limit of the ion structure in shock-compressed matter [García Saiz et al., 2008]. By combining experimental results and quantum simulations, the structural properties for the wave vector range with the largest discrepancies between the various ionic structure models could be studied.

Our group was actively involved in the theoretical support and the analysis of the experimental results by performing DFT-MD simulations and HNC modelling.

7.2.1 Experiment

The experiment was performed at the Vulcan laser facility, Rutherford Appleton Laboratory. The target material was lithium, a simple material with an electron configuration $1s^2\,2s^1$, i.e., it has only a single valence electron. Inner excitations can

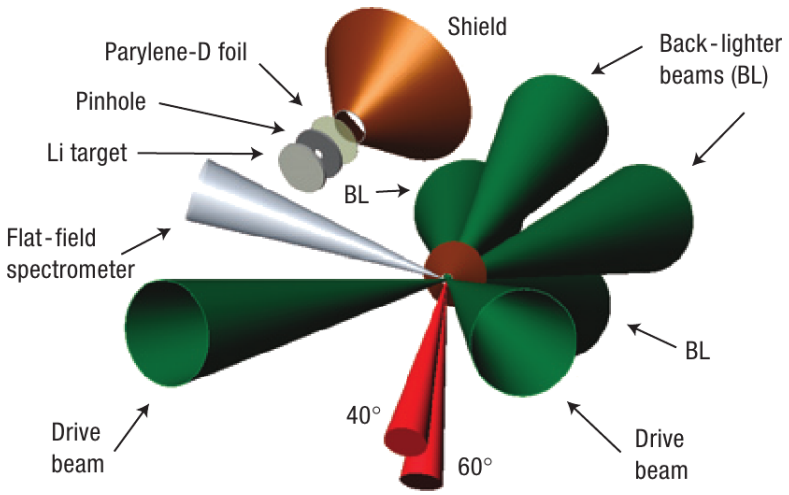

Figure 7.8: A schematic set-up of the x-ray scattering experiment on shock-compressed lithium as published in Ref. [García Saiz et al., 2008]. It shows the two drive and the four back-lighter beams as well as an image enlargement of the target assembly with the Cu shield, the Parylene-D foil generating the x-ray radiation, the Ag pinhole to collimate the probe beam and the Li sample. Furthermore, the direction of the detector for the scattered photons is highlighted.

be neglected as the average energy transfer during the scattering process is much less than the ionisation energy of the K-shell electrons.

To compress the 250 μm thick lithium foil, two drive beams directly illuminated the foil for a duration of 1 ns with a total energy of around 50 J. This leads to an average irradiance of around $3 \times 10^{13}\,\mathrm{W/cm^2}$ on a 400 μm focal spot which creates a shock wave. One-dimensional radiation hydrodynamic simulations were performed using the HELIOS code [García Saiz et al., 2008]. The code predicts around $(2-3)$ times compressed lithium with an electron temperature of $T_e < 10\,\mathrm{eV}$ at peak compression.

The x-ray probe beam was generated by illuminating a Parylene-D foil with four back-lighter beams of around 100 J for 1 ns yielding a chlorine Ly-α emission line with photon energy of $E_i = 2.96\,\mathrm{keV}$. The time delay between the drive beams and the back-lighter beams is around 3 ns. The scattered photons are detected in forward scattering geometry under 40° and 60°. Thus, the experiment probes the collective scattering regime with $\alpha = 2.0$ and $\alpha = 1.37$, respectively. To spectrally resolve the scattered photons, a highly efficient graphite crystal coupled to a CCD camera is applied. To avoid unwanted observation of photons from the x-ray source, a copper shield cone was attached over the Parylene-D foil. Furthermore, a silver pinhole with

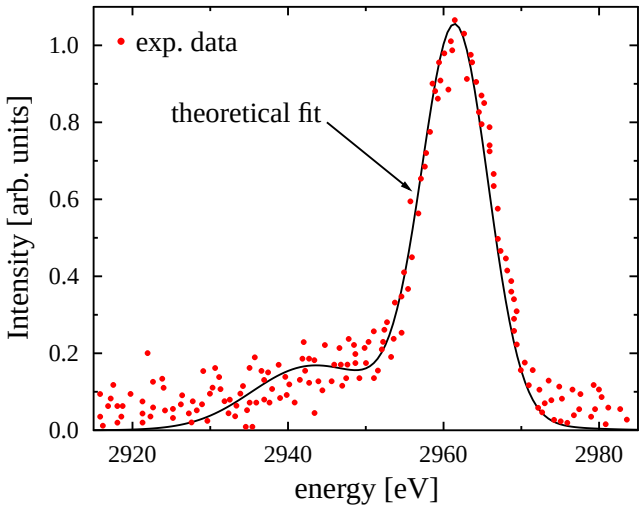

Figure 7.9: Experimental scattering spectrum of shock-compressed lithium observed under a scattering angle of 60° as published in Ref. [García Saiz et al., 2008]. The theoretical fit was generated with the use of Eq. (6.3) using the plasma parameters ($T_e = 4.5\,\mathrm{eV}$, $\varrho = 0.6\,\mathrm{g/cm^3}$ and $Z = 1.35$) as given in the original publication. The free electron feature is calculated in RPA. The ion feature uses a structure factor obtained by the HNC approach applying a linearly screened Coulomb potential. The screening function is calculated in linear response to the Coulomb field (5.23) and the form factor is taken from DFT simulations. A spectral resolution of $\Delta E = 9\,\mathrm{eV}$ is applied in the instrument response function.

a diameter of 170 μm is located between the Li target and the Parylene-D foil. This part allows the collimation of the x-rays and ensures that only the compressed center of the target is probed.

A schematic set-up of the experiment, as published in Ref. [García Saiz et al., 2008], is displayed in Fig. 7.8. It shows the target design and the distribution of the various laser systems. A more detailed description of the experimental design can be found in the corresponding Ref. [García Saiz et al., 2008] or in the thesis of E. García Saiz [García Saiz, 2008].

7.2.2 Results and discussions

The experimentally obtained scattering spectrum observed at a scattering angle of 60° is shown in Fig. 7.9 (data from Ref. [García Saiz et al., 2008]). The signal shows the typical picture of the collective scattering regime, namely, the elastic Rayleigh peak at the initial photon energy and the inelastic plasmon feature.

Table 7.1: Different plasma parameter sets which fit the experimental scattering spectrum from Fig. 7.9 equally well. The values are taken from the thesis of E. Garcia Saiz [García Saiz, 2008]. Synthetic scattering spectra generated from these plasma conditions are presented in Fig. 7.10a.

theoretical fit #	ϱ [g/cm^3]	T [eV]	Z
1	0.45	5.0	1.45
2	0.55	4.5	1.40
3	0.60	4.5	1.35
4	0.65	4.0	1.30
5	0.70	3.5	1.25
6	0.75	3.0	1.15

To determinate the state of the system, synthetic scattering spectra can be fitted to the experimental data and adjusted by varying temperature, density and ionisation degree until a match is found. This procedure, however, requires high-quality experimental data and an excellent theoretical description of all quantities needed. The free electron feature is well described within RPA. Thus, the plasmon frequency shift provides a robust value for the electron density with an accuracy of around 20% [Glenzer et al., 2007]. To infer the ionic properties, the ion-ion structure factor $S_{ii}(k)$ is required which varies significantly between different theories in the WDM regime for the wave vectors considered. Therefore, another approach was applied here in using $S_{ii}(k)$ as another free fit parameter. This makes the measurements more independent of the partially uncertain theories.

Following this idea, a certain mass density was assumed while the other parameters (T and Z) were determined by a fitting procedure of theoretical to measured spectra. Afterwards, the entire process was repeated for other mass densities leading to different temperatures and ionisation states. To take the various ionic structure models into account, the fitting process was performed for a screened and an unscreened system, that is, a Yukawa and an OCP model, respectively (see section 1.3). The error analysis was carried out by E. García Saiz and a more detailed description can be found in her thesis [García Saiz, 2008]. Following the fitting process, several sets of plasma parameters could be extracted which equally match the experimental results. A possible set of conditions is listed in table 7.1 (taken from the thesis of E. García Saiz [García Saiz, 2008]). Synthetic scattering spectra generated with

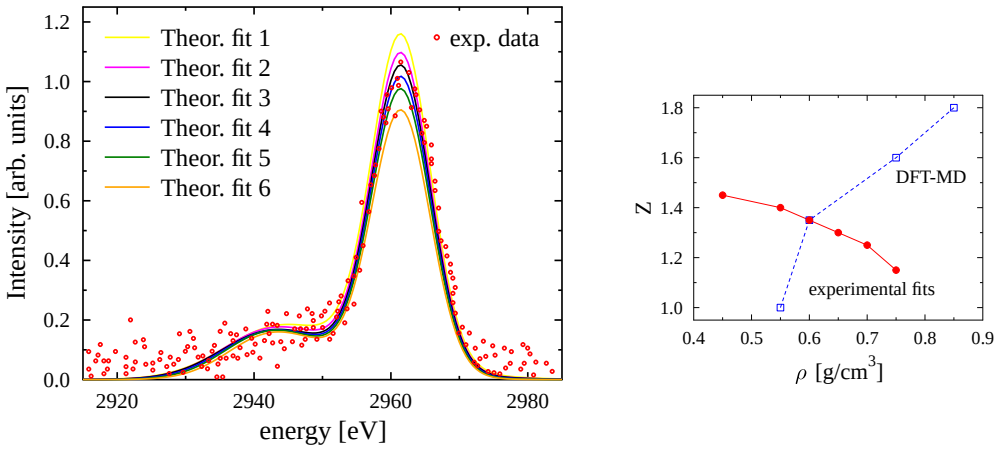

(a) scattering spectrum (b)

Figure 7.10: The experimental scattering spectrum from shock-compressed lithium from Fig. 7.9 and theoretical scattering profiles calculated for various plasma parameters as listed in table 7.1. The same theories, as described in Fig. 7.9, are used for the evaluation of the elastic Rayleigh peak. In the right picture the experimental and theoretical values for mass density and charge state are displayed for the related plasma conditions.

these plasma parameters can be seen in Fig. 7.10a in comparison with the experimentally observed signal. Here, a screened system is considered for the evaluation of the Rayleigh peak. All theoretically generated scattering spectra can be seen as suitable fits by taking the experimental uncertainties into account.

To finally determine a unique set of plasma parameters, an additional source of information is required. Here, information on the electron states from DFT-MD simulations were used to complement the experimental analysis. For several plasma conditions, DFT-MD runs were performed yielding various pair distribution functions, $g_{ii}(r)$. To extract the ionisation degree from DFT-MD, the effective pair potentials were extracted from the simulations [Ercolessi and Adams, 1994] which were then used to perform classical Monte Carlo (MC) simulations. The latter require the ionisation degree, Z, as an input parameter. Thus, by varying Z in the MC runs to match the pair distribution functions, $g_{ii}(r)$, to the DFT-MD results, the ionisation state could be determined.

A comparison of the experimentally and theoretically extracted values for mass density and charge state can be seen in Fig. 7.10b. Clearly, the charge states derived from the experimental fitting process show an opposite behaviour than those obtained by simulations: while the experimental results lead to a decrease of Z for rising mass densities, the simulations predict an increase of the ionisation state.

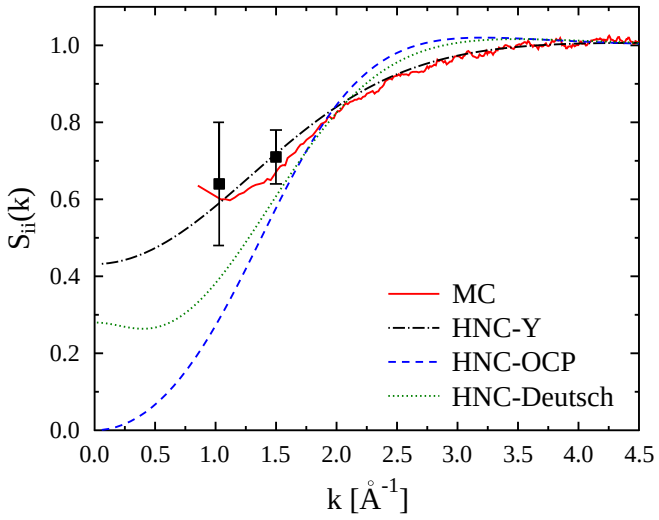

Figure 7.11: The experimentally obtained ion-ion structure factor (black squares) compared to various theoretical models for the ionic structure in warm dense lithium as published in Ref. [García Saiz et al., 2008]. The MC simulation applies an effective ion-ion potential extracted from DFT-MD simulations. The HNC method uses various inter-particle potentials, namely, a linear screened Coulomb potential (labelled HNC-Y), a pure Coulomb potential (HNC-OCP) and the Deutsch potential (4.43) (labelled HNC-Deutsch).

The behaviour of the experimentally extracted values can be understood by the fact that the inelastic scattering feature is previously well fitted, yielding the electron density. This quantity stays constant during the fitting process of the Rayleigh peak. Therefore, to fulfil the quasi-neutrality in the plasma, the charge state needs to decrease for increasing mass densities. Only one (Z–ϱ–T)-set is consistent with both, the experimental results and the quantum simulations. This is considered as the plasma conditions of the lithium sample investigated, that is, $\varrho = 0.6 \pm 0.025\,\mathrm{g/cm^2}$, $T_e = 4.5 \pm 1.5\,\mathrm{eV}$ and $Z = 1.35 \pm 0.1$. The theoretical fit in Fig. 7.9 is generated using these plasma conditions, yielding an excellent agreement to the experimental data. The extracted mass density and electron temperature are also consistent with prediction of the hydrodynamic code, HELIOS [García Saiz et al., 2008].

Finally, the ion-ion structure factor can be directly extracted from the measured scattering signal. Using the ionisation charge, the form factor and the screening function can be calculated for the plasma parameters considered. The experimentally obtained ion-ion structure factors for the two measured wave vectors ($k = 1.0\,\mathrm{Å^{-1}}$ and $k = 1.5\,\mathrm{Å^{-1}}$) can be seen in Fig. 7.11. For comparisons, the ion-ion structure

factor obtained by MC simulations applying the effective ion-ion potential, which was directly extracted from DFT-MD simulations, is also shown in the picture. The agreement of the simulations with the measured data is a further check for the consistency of the analysis using the combination of quantum simulations and experimental fitting process.

Furthermore, HNC calculations were performed using various inter-particle potentials to investigate the effective interaction in warm dense lithium. The comparison demonstrates that the HNC result applying a linearly screened potential can reproduce the measured values well. In contrast, the models which assume either a weak electron-ion potential (like the Deutsch potential, see Eq. (4.43)) or completely neglect screening effects (like the OCP model) cannot describe the small k-behaviour of the ion-ion structure factor, $S_{ii}(k)$. Therefore, we can conclude that screening effects are essential to describe the structural properties in warm dense lithium.

7.3 Ionic structure of shock-compressed lithium hydride

As an example for a scattering experiment on warm dense mixtures, an experiment performed by Kritcher *et al.* will be discussed [Kritcher et al., 2009]. Here, a lithium hydride target was compressed by a laser-driven shock up to around 2.7 times solid density, that is, $\varrho \approx 2.7 \times 0.78\,\mathrm{g/cm^3}$, yielding a strongly coupled, Fermi degenerate plasma with the classical coupling parameter for the ions of $\Gamma_{ii} = 7.4$ and the electron degeneracy parameter of $n_e\Lambda_e^3 = 24$. Our group supported the experimental team with analytical models and simulations for the structural properties.

The experiment was performed at the Titan laser facility at the Lawrence Livermore National Laboratory, USA. The required x-ray probe was generated by illuminating a titanium foil yielding K-α emission with a photon energy of $E_i = 4.51\,\mathrm{keV}$ and a bandwidth of $\Delta E/E = 0.003$. This allows the material to be probed spectrally and angularly resolved in the non-collective and in the collective scattering regime. The target assembly enabled the probing of the shock-compressed LiH under various scattering angles in the range of $\theta = 35^\circ \ldots 105^\circ$ leading to $\alpha = 1.44 \ldots 0.54$.

To extract the plasma conditions of the material under investigation, the scattering signal in backscattering geometry was selected to avoid additional errors from the uncertainties of the theoretical models applied. The fitting process yields $n_e = 1.6 \times 10^{23}\,\mathrm{cm^{-3}}$ and $T_e = 1.7\,\mathrm{eV}$, both with an accuracy of 20%. The ionisation state of the mixture with single charged lithium ions and neutral hydrogen atoms was inferred by a previous experiment of the same material as published

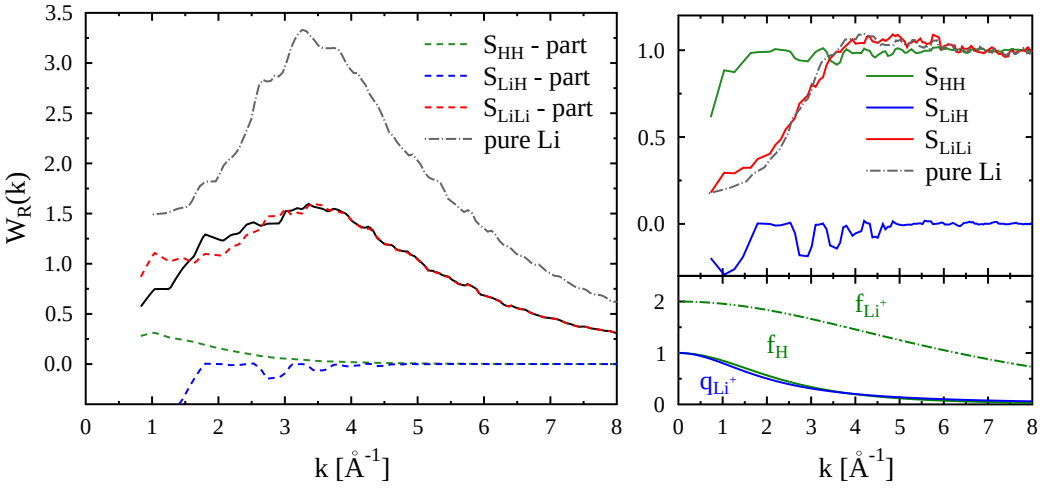

Figure 7.12: The weight of the Rayleigh peak for a LiH mixture with the mass density $\varrho_{\mathrm{LiH}} = 2.25\,\mathrm{g/cm^3}$ and the temperature $T = 2.2\,\mathrm{eV}$ calculated after Eq. (7.1). The dashed lines present the three scattering contributions of the different combinations between Li^+ ions and H according to the labels. The related structure factors, which were obtained by DFT-MD simulations, are displayed in the right top panel. The lower right panel presents the electron distribution around the nuclei, that is, the form factors for atomic hydrogen and single charge lithium ions as well as the screening function of Li^+. $f(k)$'s are taken from DFT simulations and $q(k)$ is calculated using Eq. (5.23). For comparison, a calculation for a pure lithium plasma was performed. The mass density is here set to $\varrho_{\mathrm{Li}} = 2.0\,\mathrm{g/cm^3}$, yielding the same lithium density like in the mixture, that is, $n_{\mathrm{Li}} = 1.7 \times 10^{23}\,\mathrm{cm}^{-3}$.

in Ref. [Kritcher et al., 2008]. The plasma parameters extracted are also consistent with results from radiation-hydrodynamic simulations applying the HELIOS code [Kritcher et al., 2008, 2009].

To analyse the scattering signal in a multicomponent system, the generalised Chihara formula Eq. (3.73) is used. The free electron feature is not affected by the different ion species. Thus, we will concentrate on the weight of the Rayleigh peak for a two ion system (6.6). For the LiH mixture, the hydrogen is neutral, yielding $q_{\mathrm{H}}(k) = 0$. Therefore, the equation simplifies to

$$W_R(k) = \frac{n_{\mathrm{H}}}{n_i} f_{\mathrm{H}}(k)^2 S_{\mathrm{HH}}(k) + \frac{n_{\mathrm{Li}}}{n_i} \left[f_{\mathrm{Li}}(k) + q_{\mathrm{Li}}(k)\right]^2 S_{\mathrm{LiLi}}(k) + 2\frac{\sqrt{n_{\mathrm{H}} n_{\mathrm{Li}}}}{n_i} \left[f_{\mathrm{H}}(k) f_{\mathrm{Li}}(k) + f_{\mathrm{H}}(k) q_{\mathrm{Li}}(k)\right] S_{\mathrm{LiH}}(k)\,. \quad (7.1)$$

The required partial structure factors were obtained by DFT-MD simulations, as the HNC model cannot account for the neutral hydrogen atoms. The effect of the

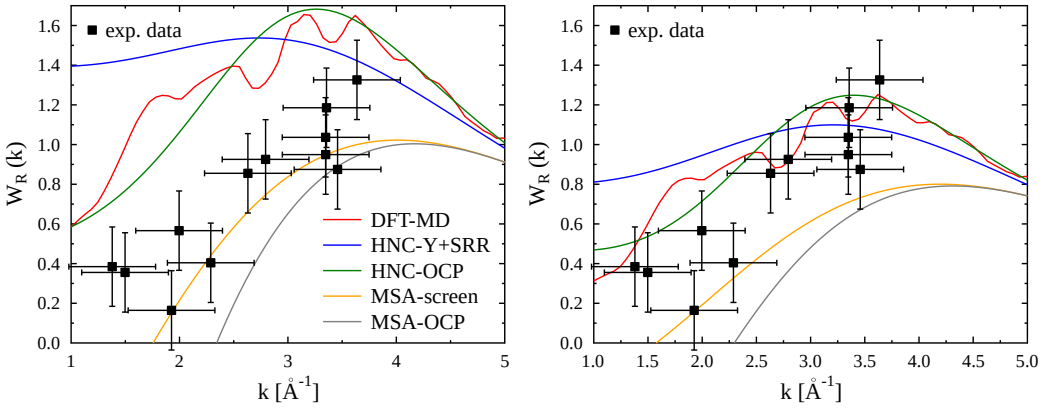

(a) screening function in linear response

(b) screening function set to zero

Figure 7.13: Experimentally measured weight of the Rayleigh peak as a function of wave vectors for the LiH plasma as published Ref. [Kritcher et al., 2009] compared with various theoretical models. The models use the plasma conditions of $T = 1.8\,\mathrm{eV}$, $\varrho = 2.0\,\mathrm{g/cm^3}$ and single charged lithium ions. The required ionic structure is calculated either by DFT-MD, HNC or MSA method where a screened (Y) and an unscreened (OCP) system is considered according to the labels. In the left panel, the screening function, $q_{\mathrm{Li}}(k)$, was calculated in linear response to a Coulomb field (5.23) whereas in the right panel $q_{\mathrm{Li}}(k)$ is set to zero.

multicomponent treatment can be seen in Fig. 7.12 where the weight of the Rayleigh peak is shown for LiH and a pure lithium plasma with the same lithium density. The plasma conditions chosen are similar to those extracted from the experiment. The presented scattering contributions from the different combinations of the Li^+ and the H particles demonstrate that the scattering process is dominated by the lithium ions. Nevertheless, a full multicomponent description is required to obtain the correct statistical weight given by the contributions of the elements in the mixture (see section 6.3). Thus, the single-ion model overestimates the weight of the elastic Rayleigh peak for the entire wave vector range considered, although the ion-ion structure factor, $S_{\mathrm{LiLi}}(k)$, is similar in the mixture and in the corresponding pure lithium plasma (gray line in Fig. 7.12).

In the experiment, the frequency-integrated elastic Rayleigh peak, that is, $W_R(k)$, could be extracted as a function of wave vectors. The results are presented in Fig. 7.13 (see Ref. [Kritcher et al., 2009]). The given horizontal error bars account for the uncertainties of the scattering angle measurements (around $\pm 10°$) due to the scattering geometry, the finite sample size and the finite exception angle of the spectrometer. Several theoretical models were applied to fit the experimentally measured data. As the plasma conditions (temperature and density) slightly vary during the

different shots, the average plasma conditions $T = 1.8\,\mathrm{eV}$ and $\varrho = 2.0\,\mathrm{g/cm^3}$ are used for the calculations. The theoretical models considered are DFT-MD simulations, HNC calculations using the unscreened OCP and the screened Yukawa model with additional short range repulsion (Y+SRR) to account for the remaining bound electrons and MSA results for a screened (MSA-screen) and an unscreened ion system (MSA-OCP). In the latter cases, the partial structure factors are obtained by an approximate treatment (see Eq. (4.45)).

As the description of the electrons forming the screening cloud is still problematic (see discussion for beryllium in section 7.1.3), the weight of the Rayleigh peak was calculated a) using a screening function calculated in linear response to a Coulomb field, Eq. (5.23), and b) without a screening function. In the first case, when the screening function is considered, the MSA-screen model fits the experimental data best. However, the model predicts negative values for $W_R(k)$ for small wave vectors k which is an unphysical behaviour. This behaviour is related to the way the partial structure factors are generated, as discussed in section 4.5. DFT-MD simulations are able to describe the structural properties in WDM, but the results obtained by the quantum simulations overestimate the measured values. In the case where the screening function is set to zero, the outcome of DFT-MD agrees well with the experimental data.

In general, all theories can fit the measured values within the error bars for larger wave vectors. Significant discrepancies can be observed for smaller k-values. Here, the various theories also predict different qualitative behaviours. A similar outcome was already reached in the discussions in the beryllium experiments: whereas the large k-behaviour is reasonable well-understood, the description of the structural properties, ionic as well as electronic, are still problematic in the area where correlations and, thus, screening effects are highly relevant. Further experimental and theoretical studies are required to investigate the structural behaviour in strongly coupled, shock compressed matter to explain this behaviour.

Chapter 8

Summary and future work

The main objective of this thesis was the development of a theoretical description of x-ray Thomson scattering (XRTS) in warm dense matter consisting of several ion species. XRTS is one of the few diagnostic tools capable of delivering basic plasma parameters as well as dynamic and structural properties of WDM. However, the analysis of the measured scattering signal and its interpretation strongly relies on theoretical modelling. Therefore, improved theoretical techniques, that must consider the complex interplay of strong correlations and quantum effects in WDM, must be developed to enhance the capabilities of XRTS. In particular, the generalisation for systems with multiple ion species presented here enables the investigation of mixtures typically found in nature and technical applications.

The scattering spectrum contains two distinct features: the frequency shifted part, related to the inelastic scattering on free electrons and bound-free transitions and the unshifted Rayleigh peak caused by elastic scattering from electrons co-moving with the ions. The main focus of this work has been the latter contribution which contains information of the ion properties. To this end, the ionic structure and the electron density around the ions, that is, the bound state wave function and the screening cloud, has been investigated. The ion structure has been determined by classical integral equations and quantum simulations. Special focus has been given to the effects of multiple ion species and partial ionisation in this thesis.

A further objective of this work was the support of XRTS experiments as well as to assess the quality of theoretical models against experimentally obtained data. It could be shown that we have developed a good understanding of XRTS in the non-collective scattering regime, whereas the interpretation of the profile in the collective scattering mode still presents challenges. Possible explanations and extensions of the theory have been discussed.

In more detail, the results obtained in this thesis can be summarised as:

- The scattering intensity is directly related to the microscopic electron structure in the system. Following ideas of Chihara, this structure factor can be decomposed into three parts associated with elastic scattering on electrons following the ion motion, inelastic scattering on free electrons and excitations of bound electrons. This description has been generalised to multicomponent systems. The novel decomposition includes partial structure factors which account for all mutual correlations between the different ions. In contrast to approximate treatments applying an average ion charge state, the new theoretical description also describes the non-linear interplay between differently correlated ion species. Furthermore, the screening functions are now Z-dependent, whereas an average screening cloud is assumed in the approximate treatment.

- To investigate the structure in strongly coupled plasmas, classical hypernetted-chain (HNC) equations were used. By generalising the approach to multiple species, it has been demonstrated that mutual correlations between the different ion species highly affect the structural properties in strongly coupled systems. For instance, the ions with the highest charge state can imprint their structure on the less strongly coupled species. Such a behaviour cannot be explained by an approximate treatment that assumes an average charge state for all ions in the system.

- To directly account for the electron component within the HNC approach, quantum pseudo-potentials, which were derived to mimic quantum behaviour in classical systems, have been implemented in the HNC approach. However, the applicability of these potentials is limited to weakly coupled and weakly degenerate systems which makes their application in WDM highly questionable. Moreover, comparisons with *ab initio* simulations and experimental data have demonstrated that this approach is inapplicable for WDM conditions. Particularly, deviations were found in the long wavelength limit.

- A simple approximation for the determination of the ion structure is given by the mean spherical approximation (MSA), which has the advantage of an analytical solution. Furthermore, many XRTS experiments were analysed using the MSA approach to model the ionic structure in the system. To assess the quality of such a treatment, a comparison of MSA and HNC results has been performed. The results show small differences when either the ions are weakly

coupled or the screening is weak. However, the MSA approach fails to incorporate the screening correctly for strongly coupled systems. Thus, the use of MSA should be limited to moderately coupled or weakly screened plasmas.

- The HNC approach is known to yield reasonably accurate results for classical systems with known interactions. However, WDM is characterised by degenerate electrons and often partial ionisation. In order to test different models under these conditions, comparisons with full quantum simulations (DFT-MD) were performed. First, it was shown that an approximate treatment of the quantum effects by weak quantum potentials fails to described WDM correctly. However, a simple linearly screened Coulomb potential used in the HNC approach for the ions only, agrees well with DFT-MD results for most cases. The results can be further improved by adding a short-range repulsion term to account for bound electrons in partially ionised systems. With these modifications, the highly efficient HNC method can be applied to determine the ion structure in WDM.

- The accurate description of the electrons forming the screening cloud around an ion is still an unresolved research topic. Here, a pseudo-potential approach has been used to investigate the effect of tightly bound electrons on the interaction of free electrons with the ions in partially ionised plasmas. It could be shown, that the remaining bound electrons strongly modified the screening cloud. These modifications lead to a significant reduction of the intensity of the elastic Rayleigh peak. This fact highly affects the interpretation of the XRTS signal for small wavenumbers. Although the pseudo-potential description requires further improvements, we were able to show that the trend of the effect is in agreement with experimental findings.

- With the novel decomposition of the total electron structure factor for multicomponent systems, it was possible to investigate the effects of multiple ion species on the x-ray scattering signal. It has been shown, that the scattering signal differs significantly between single species, microscopic mixtures and phase-separate fluids. As the differences arising clearly exceed the experimental uncertainties, x-ray scattering can now be used to investigate mixing properties of materials in the WDM regime. Furthermore, it was found that the multicomponent description is also necessary for cases where scattering is dominated by a single ion species. These results can have important implementations for experiments related to inertial confinement fusion research and planetary physics as presented in two examples.

- In the last decade, several XRTS experiments have been performed. These data allowed for a comparison of the theoretical models which has already led to an improved theoretical description. Furthermore, the derived framework was used to support the analysis of XRTS signals. Most prominent documents of these collaborations are the articles of Garcia Saiz *et al.* in Nature Physics [García Saiz et al., 2008] and the Physical Review Letters by Barbrel *et al.* [Barbrel et al., 2009] and Kritcher *et al.* [Kritcher et al., 2009].

  The first work investigated the long wavelength limit of the ion structure factor of shock-compressed lithium. Comparing HNC results for various inter-particle potentials with experimentally extracted data, it could be shown that screening is essential to describe the properties of warm dense lithium.

  The other two experiments investigated warm dense mixtures, namely, CH and LiH, both using shocks to compress and heat the sample. In the work of Barbrel *et al.*, the analysis of the HNC method indicated that multicomponent effects barely affect the ion structure in the wave vector range considered. In LiH, the strength of the Rayleigh peak was measured as a function of the wave vector. Whereas all theories agree with the measured data within the error bars for large wave vectors, significantly discrepancies arise for smaller k-values. However, further studies with higher accuracy are required before a conclusive result of the small k-vector behaviour can be reached.

Further work:

The theoretical approaches and models developed in this thesis have been implemented into a number of computer codes. One objective for future work will be to condense these models into a user-friendly tool that will be made accessible to the worldwide XRTS community. This program should include all the relevant physics to describe the XRTS signal for strongly coupled, multicomponent systems. It should also have a user interface that can easily be operated without knowledge of the details of the theoretical models involved. This development will benefit two main streams of research activities: the urgently needed benchmarking of theory against experimental data, and the application of XRTS as a diagnostic method. This software will thus strongly enhance the future research prospects of the XRTS community.

The second natural extension of this work is the application of the developed theories to the interpretation of ongoing and future experiments. As emphasised in chapter 7, the interpretation of the scattering signal in the collective scattering regime is still challenging as the microscopic structure is still unknown in this limit

where correlations and screening effects are highly relevant. The ongoing theoretical effort that is required to fully understand the small k-behaviour will be combined with an experimental investigation: a team, including our group, suggested an experiment at the Linac Coherent Light Source (LCLS) at Stanford, USA, to specifically investigate the long-wavelength limit [Fletcher et al., 2011]. As free electron lasers have much better beam quality than laser-generated sources, one can expect strongly reduced statistical errors in the experimental data and can furthermore investigate much smaller scattering angles. In turn, these data can be used to advance and restrict theoretical approaches. Our group also participates in a x-ray diffraction experiment on warm dense iron at the Vulcan laser facility. It is expected that the data show significant effects of bound electrons for this heavy element. The theories presented here are also used for the design and interpretation of investigations of warm dense carbon supported by beam time at the Rutherford Appleton laboratory and at GSI-Darmstadt, Germany. These experiments will advance our understanding of the high pressure melting behaviour of carbon and its transition into a warm dense fluid.

Appendix A

Density response for multicomponent systems

A plasma consisting of free electrons and several ion species is considered. The dynamical direct correlation function can be expressed by means of the dynamical density response functions [Chihara, 1987]

$$\sqrt{\underline{\underline{\mathcal{D}}}}\,\underline{\underline{\mathcal{C}}}(\mathbf{k},\omega)\sqrt{\underline{\underline{\mathcal{D}}}} = \left(\underline{\underline{\chi}}^{0}(\mathbf{k},\omega)\right)^{-1} - \left(\underline{\underline{\chi}}(\mathbf{k},\omega)\right)^{-1} . \tag{A.1}$$

$\chi(k,\omega)^0$ and $\chi(k,\omega)$ describe the density response function of the non-interacting and the interacting systems, respectively. For a two- or multicomponent system, the equation above is given in a matrix form with the components as following:

$$[\,\underline{\underline{\mathcal{D}}}\,]_{ab} = \delta_{ab} n_a,\ [\,\underline{\underline{\mathcal{C}}}\,]_{ab} = C_{ab}(\mathbf{k},\omega),\ [\,\underline{\underline{\chi}}\,]_{ab} = \chi_{ab}(\mathbf{k},\omega),\ \text{ and }\ [\,\underline{\underline{\chi}}^{0}\,]_{ab} = \delta_{ab}\chi^{0}_{a}(\mathbf{k},\omega)\ .$$

The indices a and b denote the species in the system, that is, electrons and several ion species. $\mathcal{D}$ describes the density matrix with the particle densities n_a, and $C_{ab}(\mathbf{k},\omega)$ characterises the dynamic direct correlation functions between the components.

To determine the response function for the interacting electron-ion system, Eq. (A.1) has to be rearranged to

$$\underline{\underline{\chi}}(\mathbf{k},\omega) = \underline{\underline{\chi}}^{0}(\mathbf{k},\omega)\left[\mathbb{1} - \sqrt{\underline{\underline{\mathcal{D}}}}\,\underline{\underline{\mathcal{C}}}(\mathbf{k},\omega)\sqrt{\underline{\underline{\mathcal{D}}}}\,\underline{\underline{\chi}}^{0}(\mathbf{k},\omega)\right]^{-1} , \tag{A.2}$$

where $\mathbb{1}$ describes the identity matrix. Eq. (A.2) is the compact form of [1]:

[1] For simplicity in the notation, the wave vector and the frequency arguments are suppressed.

$$\begin{pmatrix} \chi_{11} & \chi_{12} & \cdots & \chi_{1b} \\ \chi_{21} & \chi_{22} & \cdots & \chi_{2b} \\ \vdots & & \ddots & \\ \chi_{a1} & \chi_{a2} & \cdots & \chi_{ab} \end{pmatrix} = \begin{pmatrix} \chi_1^0 & 0 & \cdots & 0 \\ 0 & \chi_2^0 & \cdots & 0 \\ \vdots & & \ddots & \\ 0 & 0 & \cdots & \chi_{\mathbf{a}}^0 \end{pmatrix} \left[\mathbb{1} - \begin{pmatrix} \sqrt{n_1} & 0 & \cdots & 0 \\ 0 & \sqrt{n_2} & \cdots & 0 \\ \vdots & & \ddots & \\ 0 & 0 & \cdots & \sqrt{n_a} \end{pmatrix} \right.$$
$$\left. \times \begin{pmatrix} C_{11} & C_{12} & \cdots & C_{1b} \\ C_{21} & C_{22} & \cdots & C_{2b} \\ \vdots & & \ddots & \\ C_{a1} & C_{a2} & \cdots & C_{ab} \end{pmatrix} \begin{pmatrix} \sqrt{n_1} & 0 & \cdots & 0 \\ 0 & \sqrt{n_2} & \cdots & 0 \\ \vdots & & \ddots & \\ 0 & 0 & \cdots & \sqrt{n_a} \end{pmatrix} \begin{pmatrix} \chi_1^0 & 0 & \cdots & 0 \\ 0 & \chi_2^0 & \cdots & 0 \\ \vdots & & \ddots & \\ 0 & 0 & \cdots & \chi_a^0 \end{pmatrix} \right]^{-1} . \quad \text{(A.3)}$$

The required inversion of the matrix product leads to the mutual interaction of the cross correlations. Note, the symmetry of $C_{ab} = C_{ba}$ will be used in the following, which is valid in isotropic, translation invariant systems.

The density response function is connected to the structure factors of a many particle system with the aid of the fluctuation-dissipation theorem [Kubo, 1966] (see (2.66))

$$S_{ab}(\mathbf{k}, \omega) = \frac{1}{\pi} \frac{1}{\exp(-\beta\hbar\omega) - 1} \operatorname{Im} \chi_{ab}(\mathbf{k}, \omega) . \quad \text{(A.4)}$$

In the following, the results for a two- and a three-component system (i.e. one and two ion species, respectively) will be presented.

Results for a two-component system

For a single ion-component system, that is a two-component system with $a = e$ and $b = i$, the dynamical response functions are given by

$$\chi_{ee} = \frac{1}{\Delta} \left(1 - n_i C_{ii} \chi_i^0\right) \chi_e^0 , \quad \text{(A.5a)}$$

$$\chi_{ei} = \frac{1}{\Delta} \sqrt{n_e n_i}\, C_{ei} \chi_e^0 \chi_i^0 , \quad \text{(A.5b)}$$

$$\chi_{ie} = \frac{1}{\Delta} \sqrt{n_e n_i}\, C_{ei} \chi_e^0 \chi_i^0 , \quad \text{(A.5c)}$$

$$\chi_{ii} = \frac{1}{\Delta} \left(1 - n_e C_{ee} \chi_e^0\right) \chi_i^0 , \quad \text{(A.5d)}$$

with

$$\Delta = \left(1 - n_e C_{ee} \chi_e^0\right) \left(1 - n_i C_{ii} \chi_i^0\right) - n_e n_i C_{ei}^2 \chi_e^0 \chi_i^0 .$$

Thus, for example, the response function of the electrons (A.5a) depends on all three direct correlation functions as well as on the non-interacting response function of the electrons and the ions. This function can be rearranged to give two terms: a free

electron feature and a screening cloud around each ion

$$\begin{aligned}
\chi_{ee} &= \frac{1}{\Delta}\left(1 - n_i\, C_{ii}\chi_i^0\right)\chi_e^0 \\
\chi_{ee} &= \frac{\chi_e^0\left(1 - n_i\, C_{ii}\chi_i^0\right)\left(1 - n_e C_{ee}\chi_e^0\right) - \chi_e^0\left(n_e n_i C_{ei}^2 \chi_e^0\,\chi_i^0\right) + \chi_e^0\left(n_e n_i C_{ei}^2 \chi_e^0\,\chi_i^0\right)}{\Delta\left(1 - n_e C_{ee}\chi_e^0\right)} \\
\chi_{ee} &= \frac{(\chi_e^0)^2\left(n_e n_i C_{ei}^2 \chi_e^0\,\chi_i^0\right) + \chi_e^0\,\Delta}{\Delta\left(1 - n_e C_{ee}\chi_e^0\right)}\,.
\end{aligned}$$

Using the quasi-neutrality, i.e. $n_e = Z_f n_i$, where n_i characterises the total ionic density, calculated as sum over all ion species considered, leads to

$$\begin{aligned}
\chi_{ee} &= \frac{n_e^2 C_{ei}^2 (\chi_e^0)^2\,\chi_i^0\left(1 - n_e C_{ee}\chi_e^0\right)}{Z_f\Delta\left(1 - n_e C_{ee}\chi_e^0\right)^2} + \frac{\chi_e^0}{\left(1 - n_e C_{ee}\chi_e^0\right)} \\
\chi_{ee} &= \frac{1}{Z_f}\frac{n_e^2 C_{ei}^2 (\chi_e^0)^2}{\left(1 - n_e C_{ee}\chi_e^0\right)^2}\frac{\left(1 - n_e C_{ee}\chi_e^0\right)\chi_i^0}{\Delta} + \frac{\chi_e^0}{\left(1 - n_e C_{ee}\chi_e^0\right)} \\
\chi_{ee} &= \frac{q^2}{Z_f}\chi_{ii} + \frac{\chi_e^0}{\left(1 - n_e C_{ee}\chi_e^0\right)}\,. \qquad \text{(A.6)}
\end{aligned}$$

Here, a new quantity, $q(\mathbf{k},\omega)$, was introduced, that is, a screening cloud defined as

$$q(\mathbf{k},\omega) = \frac{n_e C_{ei}\,\chi_e^0}{1 - n_e C_{ee}\chi_e^0}\,. \qquad \text{(A.7)}$$

χ_e^0 characterises the response function of a free electron gas. Applying the fluctuation dissipation theorem leads to

$$\begin{aligned}
S_{ee}(\mathbf{k},\omega) &= \frac{1}{\pi}\frac{1}{\mathrm{e}^{-\beta\omega} - 1}\,\mathrm{Im}\,\chi_{ee} \\
S_{ee}(\mathbf{k},\omega) &= \frac{1}{\pi}\frac{1}{\mathrm{e}^{-\beta\omega} - 1}\,\mathrm{Im}\left(\frac{q^2}{Z_f}\chi_{ii}\right) + \frac{1}{\pi}\frac{1}{\mathrm{e}^{-\beta\omega} - 1}\,\mathrm{Im}\left(\frac{\chi_e^0}{1 - n_e C_{ee}\chi_e^0}\right) \\
S_{ee}(\mathbf{k},\omega) &= \frac{q^2(\mathbf{k})}{Z_f}S_{ii}(\mathbf{k},\omega) + S_{ee}^0(\mathbf{k},\omega)\,. \qquad \text{(A.8)}
\end{aligned}$$

In the last step, the approximation $q(\mathbf{k},\omega) \approx q(\mathbf{k},\omega \to 0)$ is used which allows the treatment of the screening function as a real function. This can be done as the frequency scales of electron and ion responses are very well separated. Indeed, the ion structure in frequency space is restricted to less than the ion plasma frequency. Thus, even for the lightest ions, that is protons, the frequency range is a factor of $\propto 1/\sqrt{m_p/m_e} \sim 1/42$ less than the one for electrons. Thus, the electron-electron structure factor, $S_{ee}(\mathbf{k},\omega)$, can be expressed via the ion-ion structure factor,

$S_{ii}(\mathbf{k},\omega)$, modulated by the screening function, $q(\mathbf{k})$, and the structure factor for a free electron gas, $S^0_{ee}(\mathbf{k},\omega)$.

The response function between electrons and ions, that is $\chi_{ei}(\mathbf{k},\omega)$, can also be rearranged to separate the electrons from the ions:

$$\chi_{ei} = \frac{1}{\Delta}\sqrt{n_e n_i}\, C_{ei}\chi^0_e\, \chi^0_i \ .$$

Applying the quasi-neutrality, $n_e = Z_f n_i$, yields

$$\begin{aligned}
\chi_{ei} &= \frac{1}{\Delta} C_{ei}\chi^0_e\, \chi^0_i \frac{n_e}{\sqrt{Z_f}} \frac{1 - n_e C_{ee}\chi^0_e}{1 - n_e C_{ee}\chi^0_e} \ , \\
\chi_{ei} &= \frac{1}{\Delta} \chi^0_i \left(1 - n_e C_{ee}\chi^0_e\right) \frac{1}{\sqrt{Z_f}} \frac{n_e C_{ei}\chi^0_e}{1 - n_e C_{ee}\chi^0_e} \ , \\
\chi_{ei} &= \chi_{ii} \frac{q}{\sqrt{Z_f}} \ . \qquad \text{(A.9)}
\end{aligned}$$

In the latter step the definition of the screening function, $q(\mathbf{k})$, are again introduced. The use of the fluctuation-dissipation theorem yields

$$S_{ei}(\mathbf{k},\omega) = \frac{q(k)}{\sqrt{Z_f}} S_{ii}(\mathbf{k},\omega) \ , \qquad \text{(A.10)}$$

that means, the correlations between the electrons and the ions is given by the microscopic structure of the ions modified by the screening functions describing the electrons forming the screening cloud.

In summary, the dynamical structure factors in a two-component electron-ion system are given by

$$S_{ee}(\mathbf{k},\omega) = \frac{q^2(k)}{Z_f} S_{ii}(\mathbf{k},\omega) + S^0_{ee}(\mathbf{k},\omega) \ , \qquad \text{(A.11a)}$$

$$S_{ei}(\mathbf{k},\omega) = \frac{q(k)}{\sqrt{Z_f}} S_{ii}(\mathbf{k},\omega) \ . \qquad \text{(A.11b)}$$

Results for a three-component system

If two ion species are considered within the system, the inversion of a three by three matrix has to be performed. The calculation leads to six different response functions, namely, two equations describing the interaction between the same ion species $(i_1 - i_1)$ and $(i_2 - i_2)$, one term for the mutual correlation between the different ion species $(i_1 - i_2)$, two contributions of the interaction electrons with ions,

that is $(e-i_1)$ and $(e-i_2)$, and the last term characterising the electron-electron correlation $(e-e)$:

$$\chi_{i_1i_1}(\mathbf{k},\omega) = \frac{1}{\Delta}\left[\chi^0_{i_1}\left(1-n_e\,C_{ee}\chi^0_e\right)\left(1-n_{i_2}C_{i_2i_2}\chi^0_{i_2}\right) - n_e n_{i_2}C^2_{ei_2}\chi^0_e\chi^0_{i_1}\chi^0_{i_2}\right] ,$$

$$\chi_{i_2i_2}(\mathbf{k},\omega) = \frac{1}{\Delta}\left[\chi^0_{i_2}\left(1-n_e\,C_{ee}\chi^0_e\right)\left(1-n_{i_1}C_{i_1i_1}\chi^0_{i_1}\right) - n_e n_{i_1}C^2_{ei_1}\chi^0_e\chi^0_{i_1}\chi^0_{i_2}\right] ,$$

$$\chi_{i_1i_2}(\mathbf{k},\omega) = \frac{1}{\Delta}\left[\sqrt{n_{i_1}n_{i_2}}\left(1-n_e\,C_{ee}\chi^0_e\right)C_{i_1i_2}\chi^0_{i_1}\chi^0_{i_2} + n_e\sqrt{n_{i_1}n_{i_2}}C_{ei_1}C_{ei_2}\chi^0_e\chi^0_{i_1}\chi^0_{i_2}\right] ,$$

$$\chi_{ei_1}(\mathbf{k},\omega) = \frac{1}{\Delta}\left[\sqrt{n_e n_{i_1}}C_{ei_1}\chi^0_e\chi^0_{i_1}\left(1-n_{i_2}C_{i_2i_2}\chi^0_{i_2}\right) + \sqrt{n_e n_{i_1}}n_{i_2}C_{ei_2}C_{i_1i_2}\chi^0_e\chi^0_{i_1}\chi^0_{i_2}\right] ,$$

$$\chi_{ei_2}(\mathbf{k},\omega) = \frac{1}{\Delta}\left[\sqrt{n_e n_{i_2}}C_{ei_2}\chi^0_e\chi^0_{i_2}\left(1-n_{i_1}C_{i_1i_1}\chi^0_{i_1}\right) + \sqrt{n_e n_{i_2}}n_{i_1}C_{ei_1}C_{i_1i_2}\chi^0_e\chi^0_{i_1}\chi^0_{i_2}\right] ,$$

$$\chi_{ee}(\mathbf{k},\omega) = \frac{1}{\Delta}\left[\chi^0_e\left(1-n_{i_1}C_{i_1i_1}\chi^0_{i_1}\right)\left(1-n_{i_2}C_{i_2i_2}\chi^0_{i_2}\right) - n_{i_1}n_{i_2}C^2_{i_1i_2}\chi^0_e\chi^0_{i_1}\chi^0_{i_2}\right] .$$

It can be seen that all partial density response functions are inter-connected. In a similar manner as for a two-component system, the electron-electron and the electron-ion structure factors can be decoupled which leads to

$$S_{ei_1}(\mathbf{k},\omega) = \frac{n_{i_1}}{Z_f n_i}q_{i_1}(\mathbf{k})S_{i_1i_1}(\mathbf{k},\omega) + \frac{n_{i_2}}{Z_f n_i}q_{i_2}(\mathbf{k})S_{i_1i_2}(\mathbf{k},\omega) , \tag{A.13a}$$

$$S_{ei_2}(\mathbf{k},\omega) = \frac{n_{i_2}}{Z_f n_i}q_{i_2}(\mathbf{k})S_{i_2i_2}(\mathbf{k},\omega) + \frac{n_{i_1}}{Z_f n_i}q_{i_1}(\mathbf{k})S_{i_1i_2}(\mathbf{k},\omega) , \tag{A.13b}$$

$$\begin{aligned} S_{ee}(\mathbf{k},\omega) = {} & \frac{n_{i_1}}{Z_f n_i}q^2_{i_1}(\mathbf{k})S_{i_1i_1}(\mathbf{k},\omega) + \frac{n_{i_2}}{Z_f n_i}q^2_{i_2}(\mathbf{k})S_{i_2i_2}(\mathbf{k},\omega) \\ & + \frac{\sqrt{n_{i_1}n_{i_2}}}{Z_f n_i}q_{i_1}(\mathbf{k})q_{i_2}(\mathbf{k})S_{i_1i_2}(\mathbf{k},\omega) + S^0_{ee}(\mathbf{k},\omega) , \end{aligned} \tag{A.13c}$$

with the definition of the screening cloud around ion i_1 and ion i_2:

$$q_{i_1}(\mathbf{k}) = \frac{n_e C_{ei_1}(\mathbf{k})\;\chi^0_e(\mathbf{k})}{1-n_e C_{ee}(\mathbf{k})\chi^0_e(\mathbf{k})} \qquad \text{and} \qquad q_{i_2}(\mathbf{k}) = \frac{n_e C_{ei_2}(\mathbf{k})\;\chi^0_e(\mathbf{k})}{1-n_e C_{ee}(\mathbf{k})\chi^0_e(\mathbf{k})} .$$

Here, the difference of the screening clouds arises due to the direct correlation functions, C_{ei_1} and C_{ei_2}. The total ion density is determined as $n_i = Z_1 \cdot n_1 + Z_2 \cdot n_2$.

In summary, the electron-ion structure factor, $S_{ei_1}(\mathbf{k},\omega)$, is defined by the microscopic properties of ion i_1 but contains also structural information associated with the other ion species i_2 as both ions species interact with each other as well as with their electrons which form the screening clouds. Likewise, the electron-electron structure factor is given by the structural properties of ion 1 and ion 2 as well as the cross term, $S_{i_1i_2}(\mathbf{k},\omega)$, to account for the correlation between the different ions and their screening clouds. These mutual correlations significantly affect the structure properties in a multicomponent system.

Bibliography

Abramowitz, M. and Stegun, I.A. *Handbook of Mathematical Functions, with formulas, graphs and mathematical tables*. Dover Publications, New York, 1965.

Als-Nielsen, J. and McMorrow, D. *Elements of Modern X-ray Physics*. Wiley, New York, 2001.

Altarelli, M., Brinkmann, R., Chergui, M., Decking, W., Dobson, B., Düsterer, S., Grübel, G., Graeff, W., Graafsma, H., Hajdu, J., Marangos, J., Pflüger, J., Redlin, H., Riley, D., Robinson, I., Rossbach, J., Schwarz, A., Tiedtke, K., Tschentscher, T., Vartaniants, I., Wabnitz, H., Weise, H., Wichmann, R., Witte, K., Wolf, A., Wulff, M., and Yurkov, M. (Eds.). *The European X-Ray Free-Electron Laser - Technical design report*. Hamburg, Germany, 2006. (`http://xfel.desy.de/tdr/tdr/`).

Anderson, M.H., Ensher, J.R., Matthews, M.R., Wieman, C.E., and Cornell, E.A. Observation of Bose-Einstein condensation in a dilute atomic vapor. *Science*, 269: 198, 1995.

Arthur, J. *et al. Linac Coherent Light Source (LCLS) - Conceptual Design Report*. Stanford, USA, 2002. (`http://www-ssrl.slac.stanford.edu/lcls/cdr/`).

Ashcroft, N.W. Electron-ion pseudopotential in metals. *Phys. Lett.*, 23:48, 1966.

Attwood, D. *Soft X-Rays and Extreme Ultraviolet Radiation: Principles and Applications*. Cambridge University Press, Cambridge, 1999.

Atzeni, S. and Meyer-ter-Vehn, J. *The Physics of Inertial Fusion*. Clarendon Press, Oxford, 2004.

Balbas, L.C., Vega, L.A., and Alonso, J.A. Density functional calculation of the electronegativity and other related properties of atoms and ions of the principal groups of the periodic table. *Z. Phys. A*, 319:275, 1984.

Barbrel, B., Koenig, M., Benuzzi-Mounaix, A., Brambrink, E., Brown, C.R.D., Gericke, D.O., Nagler, B., Rabec le Gloahec, M., Riley, D., Spindloe, C., Vinko, S.M., Vorberger, J., Wark, J., Wünsch, K., and Gregori, G. Measurement of short-range correlations in shock-compressed plastic by short-pulse x-ray scattering. *Phys. Rev. Lett.*, 102:165004, 2009.

Barriga-Carrasco, M.D. Proton stopping using a full conserving dielectric function in plasmas at any degeneracy. *Phys. Rev. E*, 82:046403, 2010.

Baus, M. and Hansen, J.-P. Statistical mechanics of simple Coulomb systems. *Phys. Rep.*, 59:1, 1980.

Blöchl, P.E. Projector augmented-wave method. *Phys. Rev. B*, 50:17953, 1994.

Bohm, D. and Gross, E.P. Theory of plasma oscillations. A. Origin of medium-like behavior. *Phys. Rev.*, 75:1851, 1949.

Bohm, D. and Pines, D. A collective description of electron interactions: III. Coulomb interactions in a degenerate electron gas. *Phys. Rev.*, 92:609, 1953.

Bose, S.N. Plancks Gesetz und Lichtquantenhypothese. *Z. Phys.*, 26:178, 1924.

Car, R. and Parrinello, M. Unified approach for molecular dynamics and density-functional theory. *Phys. Rev. Lett.*, 55:2471, 1985.

Chapman, D.A. and Gericke, D.O. Analysis of Thomson scattering from nonequilibrium plasmas. *Phys. Rev. Lett.*, 107:165004, 2011.

Chaturvedi, D.K., Rovere, M., Senatore, G., and Tosi, M.P. Liquid alkali metals and alloys as electron-ion plasmas. *Physica B*, 111:11, 1981.

Chávez-Rojo, M.A. and Medina-Noyola, M. Van hove function of colloidal mixtures: Exact results. *Physica A*, 366:55, 2006.

Chihara, J. Difference in x-ray scattering between metallic and non-metallic liquids due to conduction electrons. *J. Phys. F: Met. Phys.*, 17:295, 1987.

Chihara, J. Interaction of photons with plasmas and liquid metals - photoabsorption and scattering. *J. Phys.: Condens. Matter*, 12:231, 2000.

Compton, A.H. A quantum theory of the scattering of x-rays by light elements. *Phys. Rev.*, 21:483, 1923.

Council, National Research. Frontier in high energy density physics. The National Academy Press, Washington, 2003.

Daligault, J. and Dimonte, G. Correlation effects on the temperature-relaxation rates in dense plasmas. *Phys. Rev. E*, 79:056403, 2009.

Daligault, J. and Gupta, S. Electon-ion scattering in dense multi-component plasmas: Application to the outer crust of an accreting neutron star. *Astrophys. J.*, 703:994, 2009.

Danson, C.N., Collier, J., Neely, D., Barzanti, L.J., Damerell, A., Edwards, C.B., Hutchinson, M.H.R., Key, M.H., Norreys, P.A., Pepler, D.A., Ross, I.N., Taday, P.F., Toner, W.T., Trentelman, M., Walsh, F.N., Winstone, T.B., and Wyatt, R.W.W. Well characterized $10^{19}\mathrm{W\,cm^2}$ operation of VULCAN - an ultra-high power Nd:glass laser. *J. Mod. Optics*, 45:1653, 1998.

de Broglie, L. La mécanique ondulatoire et la structure atomique de la matière et du rayonnement (wave mechanics and the atomic structure of matter and radiation). *J. Phys. Radium*, 8:225, 1927.

Debye, P. and Hückel, E. Zur Theorie der Elektrolyte. *Z. Phys.*, 24:185, 1923.

Desjarlais, M. First-principles calculations for x-ray Thomson scattering in warm dense matter. Talk at International Workshop on Warm Dense Matter, Pacific Grove, California, 2011.

Deutsch, C. Nodal expansion in a real matter plasma. *Phys. Lett.*, 60A(4):317, 1977.

Dharma-wardana, M.W.C. and Perrot, F. Level shifts, continuum lowering, and the mobility edge in dense plasmas. *Phys. Rev. A*, 45:5883, 1992.

Dirac, P.A.M. On the theory of quantum mechanics. *Proc. Roy. Soc. A*, 112:661, 1926.

Döppner, T., Landen, O.L., Lee, H.J., Neumayer, P., Regan, S.P., and Glenzer, S.H. Temperature measurement through detailed balance in x-ray Thomson scattering. *High Energy Density Physics*, 5:182, 2009.

Drake, R.P. *High-Energy-Density Physics: Fundamentals, Inertial Fusion, and Experimental Astrophysics*. Springer, Berlin Heidelberg, 2006.

Dufour, P., Liebert, J., Fontaine, G., and Behara, N. White dwarf stars with carbon atmospheres. *Nature*, 450:522, 2007.

Edie, D.J., Vorberger, J., Rose, S.J., and Gericke, D.O. Alpha particle stopping in highly compressed ICF fuel. to be published.

Einstein, A. Quantentheorie des einatomigen idealen Gases. *Sitzungsber. Kgl. Preuss. Akad. Wiss.*, page 261, 1924.

Ercolessi, F. and Adams, J. B. Interatomic potentials from first-principles calculations: The force-matching method. *Europhys. Lett.*, 26:583, 1994.

Evans, D.E. and Katzenstein, J. Laser light scattering in laboratory plasmas. *Rep. Prog. Phys.*, 32:207, 1969.

Fehske, H., Schneider, R., and Weiße, A., editors. *Computational many-particle physics*. Springer, Berlin Heidelberg, 2008.

Fermi, E. Zur Quantelung des idealen einatomigen Gases. *Z. Phys.*, 36:902, 1926.

Fletcher, L., Falcone, R., Gregori, G., Gericke, D.O., Redmer, R., Döppner, T., Fortmann, C., Wünsch, K., Ma, T., Lee, H.J., and Neumayer, P. High-precision measurement of quasi-elastic x-ray scattering from strongly coupled dense plasmas - towards the long-wavelength limit. Proposal for LCLS Stanford, USA, 2011. Proposal number: L592.

Fortmann, C., Bornath, T., Redmer, R., Reinholz, H., Röpke, G., Schwarz, V., and Thiele, R. X-ray Thomson scattering cross-section in strongly correlated plasmas. *Laser and Particle Beams*, 27:311, 2009.

Fortmann, C., Wierling, A., and Röpke, G. Influence of local-field corrections on Thomson scattering in collision-dominated two-component plasmas. *Phys. Rev. E*, 81:026405, 2010.

French, M., Mattsson, T.R., Nettelmann, N., and Redmer, R. Equation of state and phase diagram of water at ultrahigh pressures as in planetary interiors. *Phys. Rev. B*, 79:054107, 2009.

French, M., Mattsson, T.R., and Redmer, R. Diffusion and electrical conductivity in water at ultrahigh pressures. *Phys. Rev. B*, 82:174108, 2010.

Froula, D.H., Glenzer, S.H., Luhmann, N.C. Jr., and Sheffield, J. *Plasma scattering of electromagnetic radiation.* Academic Press, Amsterdam, 2nd edition, 2011.

Fünfer, E., Kronast, B., and Kunze, H.-J. Experimental results on light scattering by a θ-pinch plasma using a ruby laser. *Phys. Lett.*, 5:125, 1963.

García Saiz, E., Gregori, G., Gericke, D.O., Vorberger, J., Barbrel, B., Clarke, R.J., Freeman, R.R., Glenzer, S.H., Khattak, F.Y., Koenig, M., Landen, O.L., Neely, D., Neumayer, P., Notley, M.M., Pelka, A., Price, D., Roth, M., Schollmeier, M., Weber, R.L., van Woerkom, L., Wünsch, K., and Riley, D. Probing warm dense lithium by inelastic x-ray scattering. *Nature Physics*, 4:940, 2008.

García Saiz, M.E. *X-ray scattering from warm dense matter.* PhD thesis, School of Mathematics and physics, Queen's University of Belfast, 2008.

Gauthier, P., Chaland, F., and Masse, L. Deflagration-to-detonation transition in inertial-confinement-fusion baseline targets. *Phys. Rev. E*, 70:055401(R), 2004.

Gericke, D.O., Vorberger, J., Wünsch, K., and Gregori, G. Screening of ionic cores in partially ionized plasmas within linear response. *Phys. Rev. E*, 81:065401 (R), 2010.

Gillian, M.J. A simple model for the classical one-component plasma. *J. Phys. C: Solid State Phys.*, 7:L1, 1974.

Glenzer, S.H., Gregori, G., Lee, R.W., Rogers, F.J., Pollaine, S.W., and Landen, O.L. Demonstration of spectrally resolved x-ray scattering in dense plasmas. *Phys. Rev. Lett.*, 90:175002, 2003a.

Glenzer, S.H., Gregori, G., Rogers, F.J., Froula, D.H., Pollaine, S.W., Wallace, R.S., and Landen, O.L. X-ray scattering from solid density plasmas. *Phys. Plasmas*, 10:2433, 2003b.

Glenzer, S.H., Landen, O.L., Neumayer, P., Lee, R.W., Widmann, K., Pollaine, S.W., and Wallace, R.J. Observations of plasmons in warm dense matter. *Phys. Rev. Lett.*, 98:065002, 2007.

Glenzer, S.H., MacGowan, B.J., Michel, P., Meezan, N.B., Suter, L.J., Dixit, S.N., Kline, J.L., Kyrala, G.A., Bradley, D.K., Callahan, D.A., Dewald, E.L., Divol, L., Dzenitis, E., Edwards, M.J., Hamza, A.V., Haynam, C.A., Hinkel, D.E., Kalantar, D.H., Kilkenny, J.D., Landen, O.L., Lindl, J.D., LePape, S., Moody, J.D., Nikroo, A., Parham, T., Schneider, M.B., Town, R.P.J., Wegner, P., Widmann, K., Whitman, P., Young, B.K.F., Wonterghem, B. Van, Atherton, L.J., and Moses, E.I. Symmetric inertial confinement fusion implosions at ultra-high laser energies. *Science*, 327:1228, 2010.

Glenzer, S.H. and Redmer, R. X-ray Thomson scattering in high energy density plasmas. *Rev. Mod. Phys.*, 81:1625, 2009.

Glosli, J.N., Graziani, F.R., More, R.M., Murillo, M.S., Streitz, F.H., Surh, M.P., Benedict, L.X., Hau-Riege, S., Langdon, A.B., and London, R.A. Molecular dynamics simulations of temperature equilibration in dense hydrogen. *Phys. Rev. E*, 78:025401, 2008.

Gonze, X., Amadon, B., Anglade, P.M., Beuken, J.-M., Bottin, F., Boulanger, P., Bruneval, F., Caliste, D., Caracas, R., Cote, M., Deutsch, T., Genovese, L., Ghosez, Ph., Giantomassi, M., Goedecker, S., Hamann, D., Hermet, P., Jollet, F., Jomard, G., Leroux, S., Mancini, M., Mazevet, S., Oliveira, M.J.T., Onida, G., Pouillon, Y., Rangel, T., Rignanese, G.-M., Sangalli, D., Shaltaf, R., Torrent, M., Verstraete, M.J., Zérah, G., and Zwanziger, J.W. ABINIT: first-principles approach to material and nanosystem properties. *Comp. Phys. Communications*, 180:2582, 2009.

Gonze, X., Beuken, J.-M., Caracas, R., Detraux, F., Fuchs, M., Rignanese, G.-M., Sindic, L., Verstraete, M., Zerah, G., Jollet, F., Torrent, M., Roy, A., Mikami, M., Ghosez, Ph., Raty, J.-Y., and Allan, D.C. First-principles computation of material properties: the ABINIT software project. *Comp. Mat. Science*, 25:478, 2002.

Gonze, X., Rignanese, G.-M., Verstraete, M., Beuken, J.-M., Pouillon, Y., Caracas, R., Jollet, F., Torrent, M., Zerah, G., Mikami, M., Ghosez, Ph., Veithen, M., Raty, J.-Y., Olevano, V., Bruneval, F., Reining, L., Godby, R., Onida, G., Hamann, D.R., and Allan, D.C. A brief introduction to the ABINIT software package. *Zeit. Kristallogr*, 220:558, 2005.

Gregori, G. and Gericke, D.O. Low frequency structural dynamics of warm dense matter. *Phys. Plasmas*, 16:056306, 2009.

Gregori, G., Glenzer, S.H., Chung, H.-K., Froula, D.H., Lee, R.W., Meezan, N.B., Moody, J.D., Niemann, C., Landen, O.L., Holst, B., Redmer, R., Regan, S.P., and Sawada, H. Measurement of carbon ionization balance in high-temperature plasma mixtures by temporally resolved x-ray scattering. *J. Quant. Spectrosc. Radidat. Transfer*, 99:225, 2006.

Gregori, G., Glenzer, S.H., Rozmus, W., Lee, R.W., and Landen, O.L. Theoretical model of x-ray scattering as a dense matter probe. *Phys. Rev. E*, 67:026412, 2003.

Gregori, G., Ravasio, A., Höll, A., Glenzer, S.H., and Rose, S.J. Derivation of the static structure factor in strongly coupled non-equilibrium plasmas for x-ray scattering studies. *High Energy Density Physics*, 3:99, 2007.

Grinenko, A. and Gericke, D.O. Nonlinear collisional absorption of laser light in dense strongly coupled plasmas. *Phys. Rev. Lett.*, 103:065005, 2009.

Grinenko, A., Gericke, D.O., Glenzer, S.H., and Vorberger, J. Probing the hydrogen melting line at high pressures by dynamic compression. *Phys. Rev. Lett.*, 101: 194801, 2008.

Guillot, T. Interiors of giant planets inside and outside the solar system. *Science*, 72:286, 1999.

Hafner, J. and Heine, V. The crystal structures of the elements: pseudopotential theory revisited. *J. Phys. F: Met. Phys.*, 13:2479, 1983.

Hamaguchi, S., Farouki, R.T., and Dubin, D.H.E. Triple point of Yukawa systems. *Phys. Rev. E*, 56:4671, 1997.

Hansen, J.P. and McDonald, I.R. Microscopic simulation of a hydrogen plasma. *Phys. Rev. Lett.*, 41:1379, 1978.

Hansen, J.P. and McDonald, I.R. Microscopic simulation of a strongly coupled hydrogen plasma. *Phys. Rev. A*, 23:2041, 1981.

Hansen, J.P. and McDonald, I.R. *Theory of simple liquids*. Academic Press, London, 1990.

Hohenberg, P. and Kohn, W. Inhomogeneus electron gas. *Phys. Rev. B*, 136(3):864, 1964.

Höll, A., Bornath, T., Cao, L., Döppner, T., Düsterer, S., Förster, E., Fortmann, C., Glenzer, S.H., Gregori, G., Laarmann, T., Meiwes-Broer, K.-H., Przystawik, A., Radcliffe, P., Redmer, R., Reinholz, H., Röpke, G., Thiele, R., Tiggesbäumker, J., Toleikis, S., Truong, N.X., Tschentscher, T., Uschmann, I., and Zastrau, U. Thomson scattering from near-solid density plasmas using soft x-ray free electron lasers. *High Energy Density Phys.*, 3:120, 2007.

Holst, B., French, M., and Redmer, R. Electronic transport coefficients from *ab initio* simulations and application to dense liquid hydrogen. *Phys. Rev. B*, 83: 235120, 2011.

Holst, B., Redmer, R., and Desjarlais, M.P. Thermophysical properties of warm dense hydrogen using quantum molecular dynamics simulations. *Phys. Rev. B*, 77:184201, 2008.

Hu, S.X., Militzer, B., Goncharov, V.N., and Skupsky, S. Strong coupling and degeneracy effects in inertial confinement fusion implosions. *Phys. Rev. Lett.*, 104: 235003, 2010.

Hubbard, J. The description of collective motions in terms of many-body perturbation theory. II. The correlation energy of a free-electron gas. *Proc. R. Soc. Lond. A*, 243:336, 1957.

Hubbel, J.H., Veigele, Wm.J., Briggs, E.A., Brown, R.T., Cromer, D.T., and Moverton, K.J. Atomic form factors, incoherent scattering functions, and photon scattering cross section. *J. Phys. Chem.*, 4:471, 1975.

Huser, G., Koenig, M., Benuzzi-Mounaix, A., Henry, E., Vinci, T., Faral, B., Tomasini, M., Telaro, B., and Batani, D. Temperature and melting of laser-shocked iron releasing into an LiF window. *Phys. Plasmas*, 12:060701, 2005.

Hutchinson, I.H. *Principles of Plasma Diagnostics*. Cambridge University Press, 2005.

Ichimaru, S. *Statistical Plasma Physics, Vol.1: Basic Principles*. Westview Press, Colorado, 2004a.

Ichimaru, S. *Statistical Plasma Physics, Vol.2 Condensed Plasmas*. Westview Press, Colorado, 2004b.

Issolah, A., Garreau, Y., Lévy, B., and Loupias, G. Experimental check of core Compton profiles, calculated using a quasi-self-consistent-field method. *Phys. Rev. B*, 44:11029, 1991.

Iyetomi, H., Ogata, S., and Ichimaru, S. Bridge functions and improvement on the hypernetted-chain approximation for classical one-component plasmas. *Phys. Rev. A*, 46:1051, 1992.

Jackson, J.D. *Classical Electrodynamics*. John Wiley & Sons, Inc., New York, 1999.

Kelbg, G. Quantenstatistik der Gase mit Coulomb-Wechselwirkung. *Ann. Phys.*, 12:354, 1964a.

Kelbg, G. Theorie des Quanten-Plasmas. *Ann. Phys.*, 12:219, 1964b.

Khairallah, S.A. and Militzer, B. First-principles studies of the metallization and the equation of state of solid helium. *Phys. Rev. Lett.*, 101:106407, 2008.

Klein, O. and Nishina, Y. Über die Streuung von Strahlung durch freie Elektronen nach der neuen relativistischen Quantendynamik von Dirac. *Z. Phys.*, 52:853 and 869, 1929.

Klimontovich, Y.L. *Kinetic theory of nonideal gases and nonideal plasmas (in Russian)*. Nauka, Moscow, 1975. (Engl. transl. Pergamon Press, 1982).

Klimontovich, Y.L. and Kraeft, W.-D. Pseudopotentil for a weakly nonideal plasma with allowance for polarization of the medium. *High. Temp. Phys. (USSR)*, 12: 212, 1974.

Koenig, M., Bennuzzi-Mounaix, A., Ravasio, A., Vinci, T., Ozaki, N., Lepape, S., Batani, D., Huiser, G., Hall, T., Hicks, D., MacKinnon, A., Patel, P., Parl, H.S., Boehly, T., Borghesi, M., Kar, S., and Romagnani, L. Progress in the study of warm dense matter. *Plasma Phys. Control. Fusion*, 47:B441, 2005.

Koenig, M., Benuzzi-Mounaix, A., Ozaki, N., Ravasio, A., Vinci, T., Lepape, S., Tanaka, K., and Riley, D. High energy density physics on LULI2000 laser facility. *AIP Conf. Proc.*, 845:1421, 2006.

Kohn, W. and Sham, L.J. Self-consistent equations including exchange and correlation effects. *Phys. Rev. A*, 140:1133, 1965.

Kraeft, W.-D., Kremp, D., Ebeling, W., and Röpke, G. *Quantum Statistics of Charged Particle Systems*. Akademie-Verlag, Berlin, 1986.

Kremp, D., Bonitz, M., Kraeft, W.-D., and Schlanges, M. Non-Markovian Boltzmann equation. *Ann. Phys.*, 258:320, 1997.

Kremp, D., Schlanges, M., and Kraeft, W.-D. *Quantum Statistics of Nonideal Plasmas*. Springer Verlag, Berlin Heidelberg New York, 2005.

Kresse, G. and Furthmüller, J. Efficiency of ab-initio total energy calculations for metals and semiconductors using a plane-wave basis set. *Comput. Mat. Sci.*, 6:15, 1996a.

Kresse, G. and Furthmüller, J. Efficient iterative schemes for ab initio total-energy calculations using a plane-wave basis set. *Phys. Rev. B*, 54:11169, 1996b.

Kresse, G. and Hafner, J. Ab initio molecular dynamics for liquid metals. *Phys. Rev. B*, 47:558, 1993.

Kresse, G. and Hafner, J. Ab initio molecular-dynamics simulation of the liquid-metal-amorphous-semiconductor transition in germanium. *Phys. Rev. B*, 49:14251, 1994a.

Kresse, G. and Hafner, J. Norm-conserving and ultrasoft pseudopotentials for first-row and transition-elements. *J. Phys.: Condens. Matter*, 6:8245, 1994b.

Kresse, G. and Joubert, D. From ultrasoft pseudopotentials to the projector augmented-wave method. *Phys. Rev. B*, 59:1758, 1999.

Kritcher, A.L., Neumayer, P., Brown, C.R.D., Davis, P., Döppner, T., Falcone, R.W., Gericke, D.O., Gregori, G., Holst, B., Landen, O.L., Lee, H.J., Morse, E.C., Pelka, A., Redmer, R., Roth, M., Vorberger, J., Wünsch, K., and Glenzer, S.H. Measurements of ionic structure in shock compressed lithium hydride from ultrafast x-ray Thomson scattering. *Phys. Rev. Lett.*, 103:245004, 2009.

Kritcher, A.L., Neumayer, P., Castor, J., Döppner, T., Falcone, R.W., Landen, O.L., Lee, H.J., Lee, R.W., Morse, E.C., Ng, A., Pollaine, S.W., Price, D., and Glenzer, S.H. Ultrafast x-ray Thomson scattering of shock-compressed matter. *Science*, 322:69, 2008.

Kubo, R. The fluctuation-dissipation theorem. *Rep. Prog. Phys.*, 29:255, 1966.

Kunze, H.J., Fünfer, E., Kronast, B., and Kegel, W.H. Measurement of the spectral distribution of light scattered by a θ-pinch plasma. *Phys. Lett.*, 11:42, 1964.

Landen, O.L., Glenzer, S.H., Edwards, M.J., Lee, R.W., Collins, G.W., R.C., Cauble., Hsing, W.W., and Hammel, B.A. Dense matter characterization by x-ray Thomson scattering. *J. Qant. Spectrosc. Radiat. Transfer*, 71:465, 2001.

Lee, H.J., Neumayer, P., Castor, J., Döppner, T., Falcone, R.W., Fortmann, C., Hammel, B.A., Kritcher, A.L., Landen, O.L., Lee, R.W., Meyerhofer, D.D., Munro, D.H., Redmer, R., Regan, S.P., Weber, S., and Glenzer, S.H. X-ray Thomson-scattering measurements of density and temperature in shock-compressed beryllium. *Phys. Rev. Lett.*, 102:115001, 2009.

Lindl, J.D. *Inertial Confinement Fusion*. Springer, New York, 1998.

Lindl, J.D., Amendt, P., Berger, R.L., Glendinning, S.G., Glenzer, S.H., Haan, S.W., Kauffman, R.L., Landen, O.L., and Suter, L.J. The physics basis for ignition using indirect-drive targets on the National Ignition Facility. *Phys. Plasmas*, 11:339, 2004.

Longman, I.M. On the numerical evaluation of Cauchy principal values of integrals. *Mathematical Tables and Other Aids to Computation*, 12:205, 1958.

Lorenzen, W., Holst, B., and Redmer, R. Demixing of hydrogen and helium at megabar pressures. *Phys. Rev. Lett.*, 102:115701, 2009.

Lorenzen, W., Holst, B., and Redmer, R. First-order liquid-liquid phase transition in dense hydrogen. *Phys. Rev. B*, 82:195107, 2010.

Louis, A.A. and Ashcroft, N.W. Extending linear response: Inferences from electron-ion structure factors. *Phys. Rev. Lett.*, 81:4456, 1998.

Mahan, G.D. *Many Particle Physics (Physics of Solids and Liquids)*. Springer, New York, 2000.

Martin, R.M. *Electronic structure: basic theory and practical methods*. Cambridge University Press, Cambridge, 2004.

Marx, D. and Hutter, J. Ab initio molecular dynamics: Theory and implementation. In Grotendorst, J., editor, *Modern Methods and Algorithms of Quantum Chemistry*, volume 3, page 329, Jülich, 2005. John von Neumann Institute for Computing.

Mayer, J.E. and Montroll, E. Molecular distribution. *J. Chem. Phys.*, 9:2, 1941.

Mermin, N.D. Thermal properties of the inhomogeneous electron gas. *Phys. Rev.*, 137:A1441, 1965.

Mie, G. Beiträge zur Optik trüber Medien, speziell kolloidaler Metallösungen. *Ann. Phys.*, 330:377, 1908.

Militzer, B. Path integral Monte Carlo and density functional molecular dynamics simulations of hot, dense helium. *Phys. Rev. B*, 79:155105, 2009.

Militzer, B., Hubbard, W.B., Vorberger, J., Tamblyn, I., and Bonev, S.A. A massive core in Jupiter predicted from first-principles simulations. *Astrophys. J. Lett.*, 688: L45, 2008.

Morita, T. Equation of state of high temperature plasma. *Prog. Theor. Phys.*, 22: 757, 1959.

Moses, E. and Wuest, C.R. The National Ignition Facility: Laser performance and first experiments. *Fusion Science and Technology*, 47:314, 2005.

Murillo, M.S. and Weisheit, J.C. Dense plasmas, screened interactions, and atomic ionization. *Phys. Rep.*, 302:1, 1998.

Nettelmann, N., Holst, B., Kietzmann, A., French, M., and Redmer, R. Ab initio equation of state data for hydrogen, helium, and water and the internal structure of Jupiter. *Astrophys. J.*, 683:1217, 2008.

Neumayer, P., Fortmann, C., Döppner, T., Davis, P., Falcone, R.W., Kritcher, A.L., Landen, O.L., Lee, H.J., Lee, R.W., Niemann, C., Le Pape, S., and Glenzer, S.H. Plasmons in strongly coupled shock-compressed matter. *Phys. Rev. Lett.*, 105: 075003, 2010.

Ornstein, L.S. and Zernike, F. *Proc. Akad. Sci. (Amsterdam)*, 17:793, 1914.

Palmer, R.G. and Weeks, J.D. Exact solution of the mean spherical model for charged hard spheres in a uniform neutralizing background. *J. Chem. Phys.*, 58: 4171, 1973.

Pauli, W. Über den Zusammenhang des Abschlusses der Elektronengruppen im Atom mit der Komplexstruktur der Spektren. *Z. Phys.*, 31:765, 1925.

Pauling, L. and Sherman, J. Screening constants for many-electron atoms. The calculation and interpretation of x-ray term values, and the calculation of atomic scattering factors. *Z. Kristallogr.*, 1:81, 1932.

Perdew, J.P., Burke, K., and Ernzerhof, M. Generalized gradient approximation made simple. *Phys. Rev. Lett.*, 77:3865, 1996.

Perdew, J.P., Burke, K., and Ernzerhof, M. Erratum: Generalized gradient approximation made simple. *Phys. Rev. Lett.*, 78:1396, 1997.

Perdew, J.P., Chevary, J.A., Vosko, S.H., Jackson, K.A., Pederson, M.R., Singh, D.J., and Fiolhais, C. Atoms, molecules, solids, and surfaces: Applications of the generalized gradient approximation for exchange and correlation. *Phys. Rev. B*, 46:6671, 1992.

Perdew, J.P., Chevary, J.A., Vosko, S.H., Jackson, K.A., Pederson, M.R., Singh, D.J., and Fiolhais, C. Erratum: Atoms, molecules, solids, and surfaces: Applications of the generalized gradient approximation for exchange and correlation. *Phys. Rev. B*, 48:4978, 1993.

Perdew, J.P. and Zunger, A. Self-interaction correction to density-functional approximations for many-electron systems. *Phys. Rev. B*, 23:5048, 1981.

Pines, D. A collective description of electron interactions: IV. Electron interaction in metals. *Phys. Rev.*, 92:626, 1953.

Press, W.H., Teukolsky, S.A., Vetterling, W.T., and Flannery, B.P. *Numerical Recipes in C: the Art of Scientific Computing*. Cambridge University Press, Cambridge, 1994.

Raman, C.V. and Krishnan, K.S. A new type of secondary radiation. *Nature*, 121: 501, 1928.

Ravasio, A., Gregori, G., Benuzzi-Mounaix, A., Daligault, J., Delserieys, A., Faenov, A.Ya., Loupias, B., Ozaki, N., Rabec le Gloahec, M., Pikuz, T.A., Riley, D., and Koenig, M. Direct observation of strong ion coupling in laser-driven shock-compressed targets. *Phys. Rev. Lett.*, 99:135006, 2007.

Rayleigh, L. On the light from the sky, its polarization and colour. *Scientific Papers*, 1:87, 1899.

Redmer, R., Reinholz, H., Röpke, G., Thiele, R., and Höll, A. Theory of x-ray Thomson scattering in dense plasmas. *IEEE Trans. Plasma Sci.*, 33:77, 2005.

Regan, S.P., Delettrez, J.A., Goncharov, V.N., Marshall, F.J., Soures, J.M., Smalyuk, V.A., Radha, P.B., Yaakobi, B., Epstein, R., Glebov, V.Yu., Jaanimagi, P.A., Meyerhofer, D.D., Sangster, T.C., Seka, W., Skupsky, S., Stoeckl, C., Haynes, D.A., Frenje, J.A., Li, C.K., Petrasso, R.D., and Séguin, F.H. Dependence of shell mix on feedthrough in direct drive inertial confinement fusion. *Phys. Rev. Lett.*, 92:185002, 2004.

Regan, S.P., Delettrez, J.A., Marshall, F.J., Soures, J.M., Smalyuk, V.A., Yaakobi, B., Epstein, R., Glebov, V.Yu., Jaanimagi, P.A., Meyerhofer, D.D., Radha, P.B., Sangster, T.C., Seka, W., Skupsky, S., Stoeckl, C., Town, R.P.J., Haynes, D.A., Golovkin, I.E., Hooper, C.F., Frenje, J.A., Li, C.K., Petrasso, R.D., and Séguin, F.H. Shell mix in the compressed core of spherical implosions. *Phys. Rev. Lett.*, 89:085003, 2002.

Reichl, L.E. *A modern course in statistical physics*. Wiley-VCH, 2nd edition, 2004.

Riley, D., Woolsey, N.C., McSherry, D., Weaver, I., Djaoui, A., and Nardi, E. X-ray diffraction from a dense plasma. *Phys. Rev. Lett.*, 84:1704, 2000.

Sahoo, S., Gribakin, G.F., Shabbir Naz, G., Kohanoff, J., and Riley, D. Compton scatter profiles for warm dense matter. *Phys. Rev. E*, 77:046402, 2008.

Salpeter, E.E. Electron density fluctuations in a plasma. *Phys. Rev.*, 120:1528, 1960.

Santra, R. PhD tutorial: Concepts in x-ray physics. *J. Phys. B: At. Mol Opt. Phys.*, 42:023001, 2009.

Sawada, H., Regan, S.P., Meyerhofer, D.D., Igumenshchev, I.V., Goncharov, V.N., Boehly, T.R., Epstein, R., Sangster, T.C., Smalyuk, V.A., Yaakobi, B., Gregori, G., Glenzer, S.H., and Landen, O.L. Diagnosing direct-drive, shock-heated, and compressed plastic planar foils with noncollective spectrally resolved x-ray scattering. *Phys. Plasmas*, 14:122703, 2007.

Schwabel. *Quantenmechanik*. Springer Verlag, Berlin Heidelberg New York, 6th edition, 2002.

Schwarz, V., Bornath, T., Kraeft, W.-D., Glenzer, S.H., Höll, A., and Redmer, R. Hypernetted chain calculations for two-component plasmas. *Contrib. Plasma Phys.*, 47:324, 2007.

Schwarz, V., Holst, B., Bornath, T., Fortmann, C., Kraeft, W.-D., Thiele, R., Redmer, R., Gregori, G., Lee, H.J., Döppner, T., and Glenzer, S.H. Static ion structure factor for dense plasmas: Semi-classical and *ab initio* calculations. *High Energy Density Physics*, 6:305, 2010.

Sheffield, J. *Plasma scattering of electromagnetic radiation*. Academic Press, New York, 1975.

Singh, H.B. and Holz, A. Structure factor of liquid alkali metals. *Phys. Rev. A*, 28: 1108, 1983.

Soler, J.M., Artacho, E., Gale, J.D., García, A., Junquera, J., Ordejón, P., and Sánchez-Portal, D. The Siesta method for *ab initio* order-N materials simulation. *J. Phys.: Condens. Matter*, 14:2745, 2002.

Soures, J.M., McCrory, R.L., Boehly, T.R., Craxton, R.S., Jacobs, S.D., Kelly, J.H., Kessler, T.J., Knauer, J.P., Kremens, R.L., Kumpan, S.A., Letzring, S.A., Seka, W.D., Short, R.W., Skeldon, M.D., Skupsky, S., and Verdon, C.P. Omega upgrade laser for direct-drive target experiments. *Laser and Particle Beams*, 11:317, 1993.

Springer, J.F., Pokrant, M.A., and Stevens Jr., F.A. Integral equation solutions for the classical electron gas. *J. Chem. Phys.*, 58:4863, 1973.

Thiele, R., Bornath, T., Fortmann, C., Höll, A., Redmer, R., Reinholz, H., Röpke, G., Wierling, A., Glenzer, S.H., and Gregori, G. Plasmon resonance in warm dense matter. *Phys. Rev. E*, 78:026411, 2008.

Urry, M., Gregori, G., Landen, O.L., Pak, A., and Glenzer, S.H. X-ray probe development for collective scattering measurements in dense plasmas. *J. Quant. Spectrosc. Radiat. Transfer*, 99:636, 2006.

van de Hulst, H.C. *Light scattering by small particles.* Dover Publications, New York, 1981.

van Hove, L. Correlations in space and time and Born approximation scattering in systems of interacting particles. *Phys. Rev.*, 95:249, 1954.

van Leeuwen, J.M.J., Groeneveld, J., and De Boer, J. New method for the calculation of the pair correlation function. I. *Physica*, 25:792, 1959.

Vanderbilt, D. Soft self-consistent pseudopotentials in a generalized eigenvalue formalism. *Phys. Rev. B*, 41:7892, 1990.

Vora, A.M. Study of driving forces for atomic migration in dilute alloys. *J. Condens. Matter*, 9:35, 2007.

Vorberger, J., Gericke, D.O., Bornath, Th., and Schlanges, M. Energy relaxation in dense, strongly coupled two-temperature plasmas. *Phys. Rev. E*, 81:046404, 2010.

Vorberger, J., Gericke, D.O., and Kraeft, W.-D. The hydrogen equation of state at high densities. *arXiv:1108.4826v1*, 2011. `http://arxiv.org/abs/1108.4826`.

Vorberger, J., Schlanges, M., and Kraeft, W.-D. Equation of state for weakly coupled quantum plasmas. *Phys. Rev. E*, 69:046407, 2004.

Vorberger, J., Tamblyn, I., Militzer, B., and Bonev, S.A. Hydrogen-helium mixtures in the interiors of giant planets. *Phys. Rev. B*, 75:024206, 2007.

Welser-Sherrill, L., Mancini, R.C., Koch, J.A., Izumi, N., Tommasini, R., Haan, S.W., Haynes, D.A., Golovkin, I.E., MacFarlane, J.J., Delettrez, J.A., Marshall, F.J., Regan, S.P., Smalyuk, V.A., and Kyrala, G. Spectroscopic determination of temperature and density spatial profiles and mix in indirect-drive implosion cores. *Phys. Rev. E*, 76:056403, 2007.

Wilson, H.F. and Militzer, B. Sequestration of noble gases in giant planet interiors. *Phys. Rev. Lett.*, 104:121101, 2010.

Wünsch, K., Hilse, P., Schlanges, M., and Gericke, D.O. Structure of strongly coupled, multi-component plasmas. *Phys. Rev. E*, 77:056404, 2008a.

Wünsch, K., Vorberger, J., and Gericke, D.O. Ion structure in warm dense matter: Benchmarking hypernetted-chain equations by first-principle simulations. *Phys. Rev. E*, 79:010201(R), 2009a.

Wünsch, K., Vorberger, J., Gregori, G., and Gericke, D.O. Ion structure in dense plasmas: MSA versus HNC. *J. Phys. A: Math. Theor.*, 42:214053, 2009b.

Wünsch, K., Vorberger, J., Gregori, G., and Gericke, D.O. X-ray scattering as a probe for warm dense mixtures and high-pressure miscibility. *EPL*, 94:25001, 2011.

Wünsch, K., Vorberger, J., Schlanges, M., and Gericke, D.O. Ion structure for x-ray thomson scattering in dense fusion plasmas. *J. Phys.: Conf. Series*, 112:032077, 2008b.